Università degli Studi di Palermo

AREA RICERCA E TRASFERIMENTO TECNOLOGICO
SETTORE DOTTORATI E CONTRATTI PER LA RICERCA
U. O. DOTTORATI DI RICERCA

Ph.D. Course in Mechanical, Manufacturing, Management and Aerospace Innovation
Department of Engineering
Applied Mechanics (ING-IND/13)

ANALYSIS, FUNCTIONAL DESIGN, AND ENERGY MANAGEMENT OF POWER-SPLIT HYBRID ELECTRIC VEHICLES

THE CANDIDATE
ANTONELLA CASTELLANO

THE COORDINATOR
PROF. GIOVANNA LO NIGRO

THE SUPERVISOR
PROF. MARCO CAMMALLERI

PH.D. CYCLE: XXXVI
YEAR OF AWARD OF THE PH.D. DEGREE: 2024

TABLE OF CONTENTS

NOMENCLATURE

ABBREVIATIONS:

CS	compound-split mode
CVT	continuously variable transmission
CVU	continuously variable unit
DOF	degree of freedom
EMS	energy management strategy
E-REV	extended-range electric vehicle
EV	electric vehicle
FHEV	full hybrid electric vehicle
FR	fixed-ratio mode (parallel mode)
HEV	hybrid electric vehicle
ICE	internal combustion engine
IS	input-split mode
MG	motor-generator
MPC	model predictive control
OOL	engine optimal operating line
OG	ordinary gear train
PG	planetary gear train
PH	prediction horizon
PHEV	plug-in hybrid electric vehicle
PS-CVT	power-split continuously variable transmission
PSU	power-split unit
RMSE	root mean square error
SOC	state of charge
TPM	three-port mechanism

SUBSCRIPTS:

C, R, S	carrier, ring gear and sun gear of a PG
in, out, i, o	main shafts of the PSU
x, y, z	external shafts of a TPM
X, Y, Z	external shafts of a PG

SYMBOLS:

a_{veh}	vehicle acceleration
A_f	vehicle frontal area
c_d	vehicle drag coefficient
[**K**]	constraints matrix
k_x	fixed-ratio of the OG on the *x*th branch of a TPM
m	vehicle mass

N_C	number of constructive constraints in the PSU
N_{TPM}	number of three-port mechanisms
P_j	ideal power through the *j*th shaft
$\bar{P}_j$	real power through the *j*th shaft
p_j	ideal power through the *j*th shaft as a fraction of the input power
p'_j	ideal power through the *j*th shaft as a fraction of the output power
$\bar{p}_j$	real power through the *j*th shaft as a fraction of the input power
$\bar{p}'_j$	real power through the *j*th shaft as a fraction of the output power
$P_j\big\vert_i$	ideal power through the *j*th shaft of the *i*th TPM
$\bar{P}_L$	overall meshing power losses
$\bar{p}_L$	overall meshing power losses as a fraction of the input power
$\bar{p}'_L$	overall meshing power losses as a fraction of the output power
T_j	ideal torque applied to the *j*th shaft
$\bar{T}_j$	real torque applied to the *j*th shaft
V_{veh}	vehicle speed
γ	road slope
η	PSU overall apparent efficiency
η_0	basic efficiency of a PG
ε	powertrain global efficiency (Chapter 5)
ε_{eq}	powertrain equivalent global efficiency (Chapter 5)
η_{ICE}	ICE efficiency
η_{MG1}	MG1 efficiency
η_{MG2}	MG2 efficiency
η^Z	fixed-*Z* apparent efficiency of a PG
$\eta_{X/x}$	efficiency of the OG on the shaft *x*
Θ	torque applied to the output shaft as a fraction of the input torque (overall torque ratio)
θ_j	ideal torque applied to the *j*th shaft as a fraction of the input torque
$\bar{\theta}_j$	real torque applied to the *j*th shaft as a fraction of the input torque
ρ_a	air density
τ	overall speed ratio
τ_j	speed ratio of the *j*th shaft
$\tau_{\#j}$	overall speed ratio for which the *j*th shaft is stationary (nodal ratio)
$\tau_{j\#k}$	speed ratio of the *j*th shaft when the *k*th shaft is stationary (corresponding speed ratio)
τ_*	overall speed ratio whereby a PG is synchronous
$\phi^Z_{x/y}$	generalised characteristic function for a TPM
Ψ	Willis ratio of a PG
$\psi^Z_{Y/X}$	fixed-*Z* speed ratio of a PG
$\bar{\psi}^Z_{X/Y}$	adjusted fixed-*Z* speed ratio of a PG (Section 2.4)
ω_j	rotational speed of the *j*th shaft
$\dot{\omega}_j$	angular acceleration of the *j*th shaft
$\{\boldsymbol{\omega}\}$	vector containing the speeds of the PSU shafts

MATRIX NOTATION:

$\mathrm{M}_{j_1,j_2,\ldots}^{k_1,k_2,\ldots}$	submatrix of the M matrix obtained by removing its j_1, j_2, ... columns and its k_1, k_2, ... rows
$\mathrm{M}_{(j_1,j_2,\ldots)}^{(k_1,k_2,\ldots)}$	submatrix of the M matrix that comprises its j_1, j_2, ... columns and its k_1, k_2, ... rows

PREFACE

To mitigate the ongoing escalation of global warming and air pollution, new regulations have been established in the transport sector in order to minimise greenhouse gases and toxic emissions. To this purpose, a transition from conventional vehicles powered by an internal combustion engine towards more sustainable solutions has been fostered by governments and regulatory bodies worldwide. In this regard, the hybrid electric powertrain appears as an effective alternative to be widely adopted in the short term.

The powertrain of a hybrid electric vehicle (HEV) includes an internal combustion engine and an electric unit. The synergy between these two power sources leads to a significant reduction of both fuel consumption and emissions, avoiding the most critical issues that affect pure electric vehicles, i.e., the low range and the need for significant enhancements to the electric infrastructure.

Among the available hybrid technologies, the power-split powertrain is the most versatile solution. The speed, torque and power ratios between the engine, the electric machines, and the wheels are established by the power-split continuously variable transmission (PS-CVT), consisting of a power-split unit (PSU) that includes one or more planetary gear trains (PGs) and, optionally, ordinary gear trains. The PSU enables two kinematic degrees of freedom, making the engine kinematically decoupled from the wheels, thus being able to always operate close to the best efficiency. The simplest power-split layout includes a single PG, but some solutions deploy two or more PGs. Moreover, a system of brakes and clutches can be embedded in a PSU to realise multi-mode PS-CVTs, which makes available multiple power-split layouts to select according to the current driving condition so as to pursue high-efficiency performance.

However, any HEV can achieve an actual reduction in fuel consumption and emissions in comparison with a conventional vehicle only if an effective energy management strategy (EMS) is implemented onboard. Hence, the demanded power should be instantaneously split between the engine and the battery so as to keep the ICE operating as efficiently as possible, minimise the powertrain power losses, and maintain the battery state of charge (SOC) around a desired value.

Due to the different nature of the main components of a hybrid electric powertrain, its design and analysis often require expertise in several fields, e.g., mechanics, electrics, and control systems. Thus, owing to the two kinematic degrees of freedom of PS-CVTs, the high

constructive complexity, the wide variety of the feasible solutions, and the possibility of switching the operating mode, the power-split powertrain requires dedicated mathematical tools that must be accessible to scholars and engineers from different scientific areas.

The most common approaches of the relevant literature use an equivalent representation of the PSU based on the lever analogy or the graph theory. The lever analogy is mainly adopted for analysis purposes, but it is not suitable to address more complex PS-CVTs with ordinary gearing and multiple modes. On the other hand, the graph theory is mainly adopted in the design stage, but the enabled design procedure relies on a merely explorative approach achievable only by the aid of extensive computation, which hinders the designer's awareness towards the optimal solution. Moreover, both approaches are not suitable for a rapid assessment of the PSU power losses, which, thus, are often neglected.

On the contrary, this dissertation aims to study and extend a unified parametric model for PS-CVTs that enables a universal formulation suitable for both analysis and design purposes. The mathematical treatment relies on physically-consistent functional parameters that univocally characterise any PSU. The resulting equations of speed, torque, and power ratios do not depend on the PSU constructive arrangement, which, instead, only affects the numerical value of the functional parameters. Moreover, a modular, hierarchical design procedure is enabled, as well as a rapid assessment of the PSU meshing losses. As a result, the model provides all the crucial features that a mathematical tool for PS-CVTs requires within a comprehensive formulation.

The main advancements of this research are the extension of three previous contributions already available in the literature, where the fundamentals of the modular parametric design and the analysis of single-mode PS-CVTs with up to two PGs were addressed, as well as the PSU meshing losses. Firstly, the analysis procedure has been extended also to multi-mode PS-CVTs with any number of PGs, not only in power-split operation, but also in the full-electric mode. This enabled a comprehensive assessment of the powertrain response, considering also the PSU meshing losses. Moreover, the modular design procedure has been used for the global design of a power-split powertrain. Thanks to the utmost generality of the approach, it has been applied to propose the first power-split hybridisation of an oil drilling rig to recover braking energy during the gravity-driven work phases. Nonetheless, the analysed case study has revealed that the integration of an energy management strategy is essential to pursue the optimal sizing of the thermal and electric unit.

Therefore, the research has been focused also on the implementation of effective EMSs relying on the parametric model to assess the optimal operations of power-split hybrid electric powertrains. In this regard, two different approaches have been developed to

optimise the operation of the power-split hybrid electric powertrain. The first method deals with the offline assessment of the optimal operating maps resulting in the maximisation of the powertrain global efficiency. The second contribution integrates the unified parametric model within an EMS based on the model predictive control. The universal mathematical formulation of the parametric model and the possibility of a rapid evaluation of the PSU meshing losses have allowed proposing a universal model predictive controller with integrated mode switch and assessing how the consideration of PSU meshing losses and electric machines efficiency affects the controller performance, by comparing internal models with different complexity.

The contents of the dissertation are organised as follows.

Chapter 1 introduces the main features and classification of hybrid electric vehicles, focusing on the power-split layout. It includes several examples of commercial PS-CVTs and a literature review on the most common models and EMSs for the power-split powertrain, to highlight the literature gaps and the novelty of this research.

Chapter 2 describes the unified parametric model that is the core of the research work presented in this dissertation: the universal schematisation of any power-split unit and the functional parameters underpinning the mathematical treatment are introduced, along with the equations of the speed, torque, and power ratios. The procedure assessing the PSU meshing losses is described. Lastly, the rearrangement for the model to be extended to the pure electric operation is presented.

Chapter 3 shows how to use the model described in Chapter 2 in the analysis stage. The procedure for identifying the functional parameters for any exiting PSU is presented. An example of application on the multi-mode PSU deployed on the Cadillac CT6 has been proposed.

Chapter 4 describes the hierarchical and modular design procedure enabled by the unified parametric model and reports the considered case study of the oil drilling rig.

Chapter 5 and Chapter 6 deal with the problem of the energy management of power-split HEVs and present the offline optimisation strategy and the model predictive control framework, respectively.

The Conclusions section summarises the main findings of the research activity and paves the path for future development in a broad perspective.

CHAPTER 1
INTRODUCTION TO POWER-SPLIT HYBRID ELECTRIC CVTS

According to the data released by the European Union (EU) updated to 2019[1] [1], the greenhouse gases (GHG) emitted by the transport sector have increased over the last decades, in contrast with the decreasing trend of other sectors. Fig. 1.1 shows the GHG emitted by sector in EU-27 expressed as CO_2 equivalent normalised to 1990. The CO_2 equivalent is a metric measure indicating the number of metric tons of CO_2 emissions with the same global warming potential as one metric ton of another greenhouse gas. However, despite the increase of the GHG emitted by the transport sector, a global emissions reduction has been recorded. Indeed, as shown in Fig. 1.2, the CO_2 emissions caused by transportation accounted for the 25.8% of the total emissions in the EU in 2019, with the largest share of 71.6% coming from the road transportation. In this respect, the highest contribution is from cars (60.7%), followed by heavy-duty vehicles (27.0%) and light-duty trucks (11.1%).

Therefore, with the 'Fit for 55' package under the European Green Deal [2], the EU has adopted a series of policies to achieve the climate neutrality by 2050, pursuing a 55% reduction in transport-related greenhouse gas emissions by 2030. Some of these initiatives foster the uptake of zero- and low-emission vehicles, namely, vehicles emitting up to 50 g CO_2/km, including battery electric vehicles, fuel cell electric vehicles using hydrogen, and

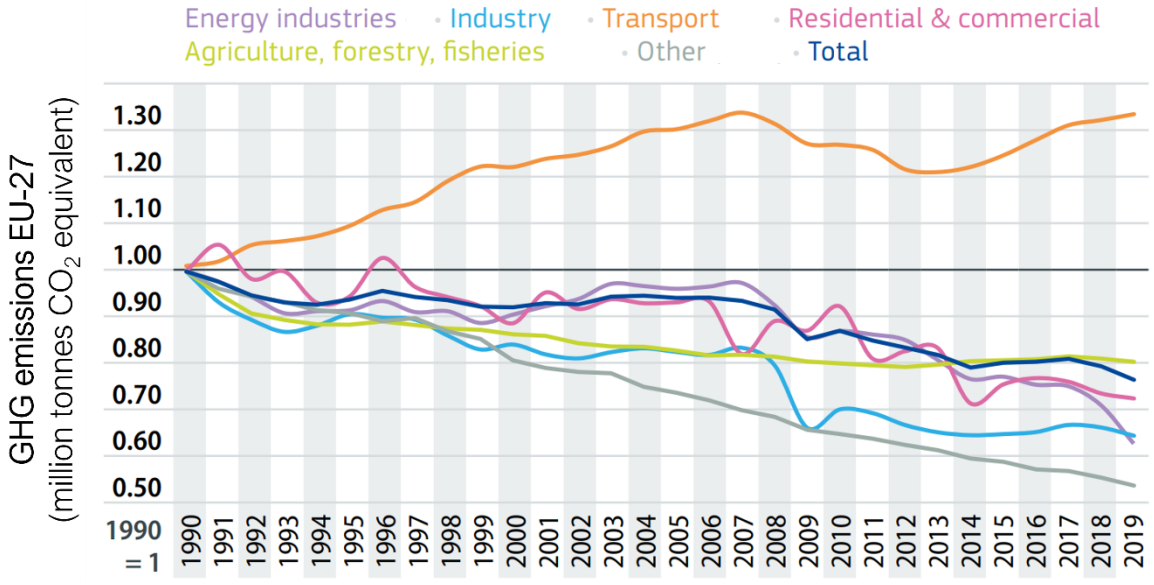

Fig. 1.1. Trend of greenhouse gases emitted by sector in EU-27 from 1990 to 2019 [1].

[1] Although latest data referring to 2020 and 2021 are also available, they have not be considered here since they reflect the implications of the Covid-19 pandemic.

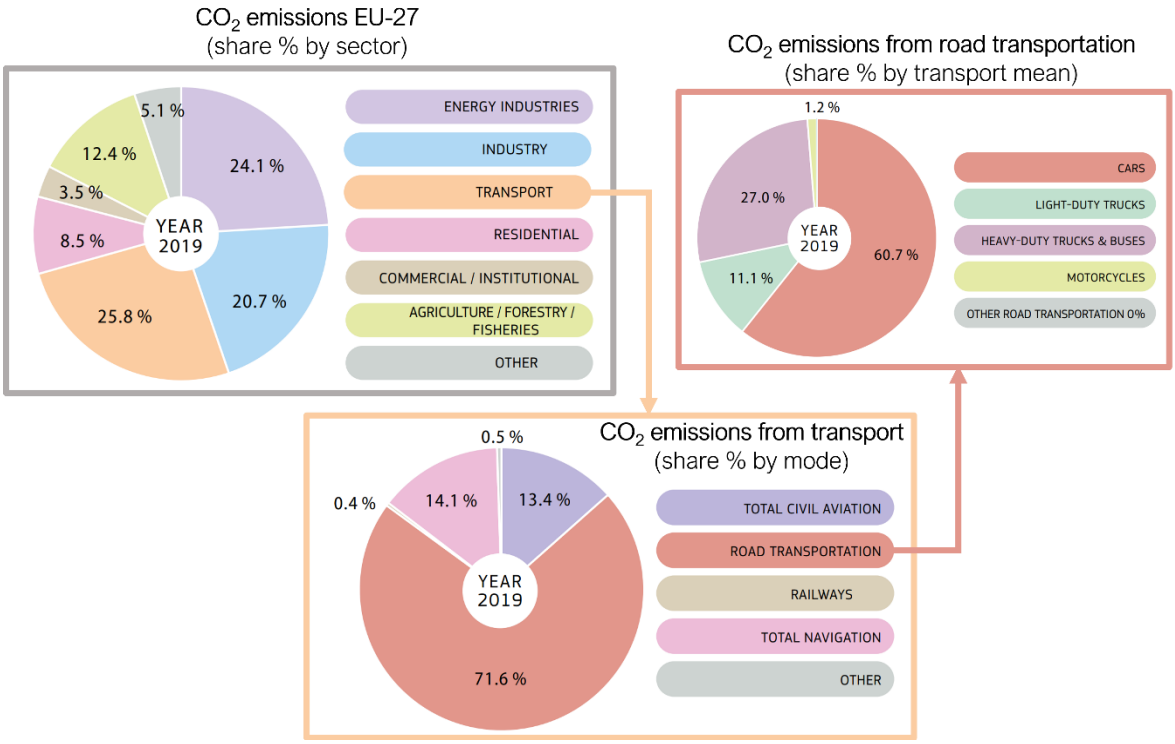

Fig. 1.2. CO_2 emissions in EU-27 in 2019: percentage share of the global emissions by sector, percentage share of the transport emissions by mode, and percentage share of the road transportation emissions by mean of transport [1].

plug-in hybrid electric vehicles. However, it is foreseen that new cars will be only zero-emission starting from 2035, thus gradually moving away not only from the traditional internal combustion engine (ICE), but also from the hybrid electric powertrain.

Nonetheless, the milestone of phasing out hybrid electric vehicles (HEVs) in favour of battery or fuel-cell electric vehicles within the next decade appears rather ambitious. As shown in Fig. 1.3, the car market share in 2019-2022 was still dominated by petrol and diesel engines, but alternatively-powered vehicles account for 47.1%. However, 32.0% of new cars were hybrid electric and only 12.1% were powered by battery or fuel cell [3]. This may indicate a certain customers' reluctance to adopt electric vehicles, which, although they succeed in reducing onboard tank-to-wheel emissions, are still affected by some major issues including range anxiety, high cost, and battery lifetime. Furthermore, the current electric supply appears inadequate to bear the significantly higher demand that the widespread adoption of battery electric vehicles would imply, in terms of charging infrastructure [4] and power generation [5,6]. Indeed, carbon neutrality in the transport sector cannot be achieved without a full transition to renewable energy for electricity generation. Moreover, the low specific energy of a pure electric powertrain hinders its adoption in transportation modes with demanding energy requirements, such as heavy-duty vehicles, agricultural machinery, vessels, and aircraft.

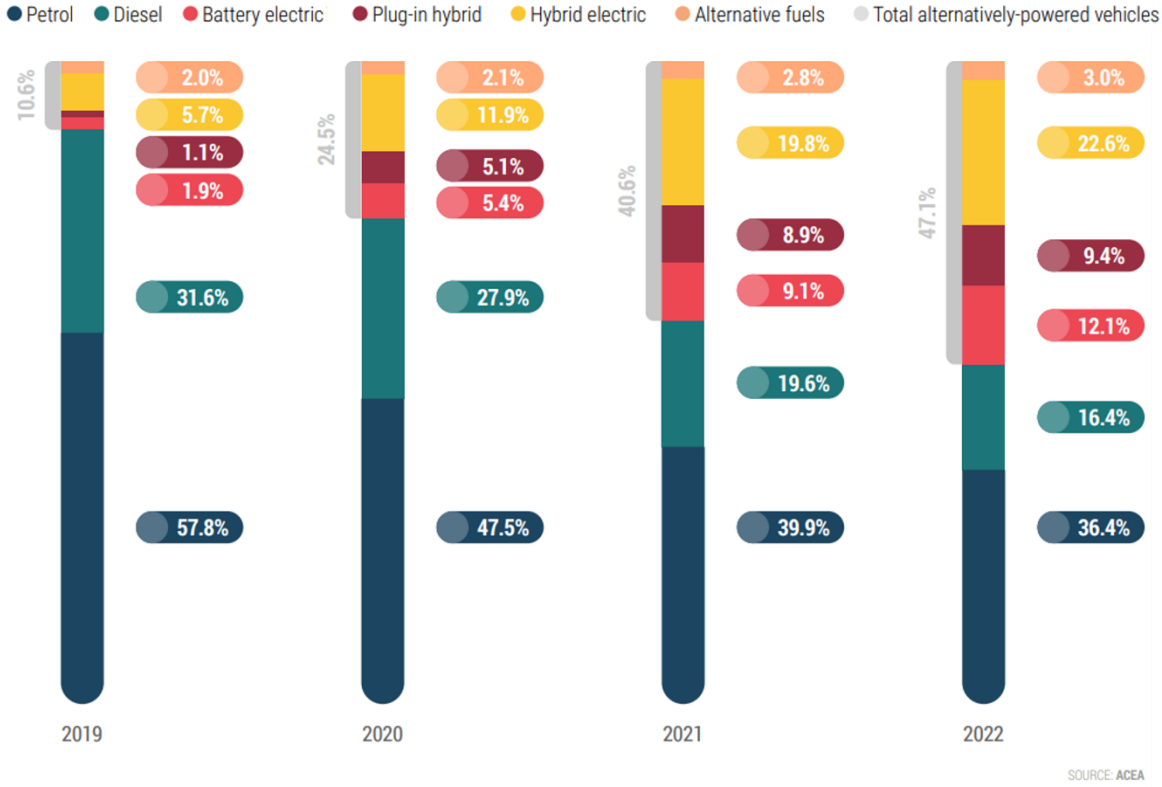

Fig. 1.3. New EU car sales from 2019-2022 by power source [3].

On the contrary, the synergy between the internal combustion engine and the electric unit in the hybrid electric powertrain overcomes the main downsides of pure electric vehicles, appearing suitable for rapid extensive uptake until the ultimate establishment of pure electric propulsion.

1.1 Hybrid electric vehicles

Hybrid electric vehicles take advantage of technologies from both electric and ICE-powered vehicles and overcome their drawbacks thanks to the synergy between two different power sources, namely, the thermal engine and the electric unit. The electric unit includes the battery pack, one or two electric machines, and the power converters. The efficiency of the ICE is enhanced by the electrical system, which allows the engine to work within its most efficient functioning range by gathering surplus power for battery recharge or by providing a power boost during acceleration. Furthermore, regenerative braking and full-electric driving options are also available.

Typically, low noise, fuel saving, and reduction of CO_2 emissions make the full-electric mode ideal for urban driving, while the involvement of the engine provides better performance in extra-urban driving. Nevertheless, several hybrid electric powertrains are available, differing in the functional architectures, depending on how the thermal and electric unit interact, or in the degree of electrification, related to the power size of the electric unit.

1.1.1 HEVs functional architectures

The most common differentiation of hybrid electric powertrain is series, parallel, and combined hybrid, depending on the connections between the engine, one or more electric motors, and the final drive [7,8,17,18,9–16]. The combined hybrid configuration includes the series-parallel and the power-split architectures. Each layout determines different power flows and specific ways of functioning. In the following, each HEV functional set-up is described in terms of the functional arrangement, functioning modes, and pros and cons.

- SERIES HYBRID

The series hybrid architecture has been conceptualised as a full-electric vehicle provided with an additional energy source, namely, the ICE, to recharge the battery and extend the range. A series hybrid powertrain consists of the ICE and two electric machines (Fig. 1.4). The ICE output is connected to the first electric machine, which converts the mechanical power supplied by the engine into electrical energy that can be transmitted to the battery pack or the second electric machine. The latter acts mainly as an electric motor to propel the vehicle. Still, its functioning mode can be reversed into electrical generation during regenerative breaking to transform the mechanical power of the wheels into electrical energy to be stored in the batteries. Thus, the electric storage system is a bidirectional energy source connected to a DC power bus. An AC/DC rectifier is needed at the generator output, while a reversible converter is deployed to control the electric traction motor.

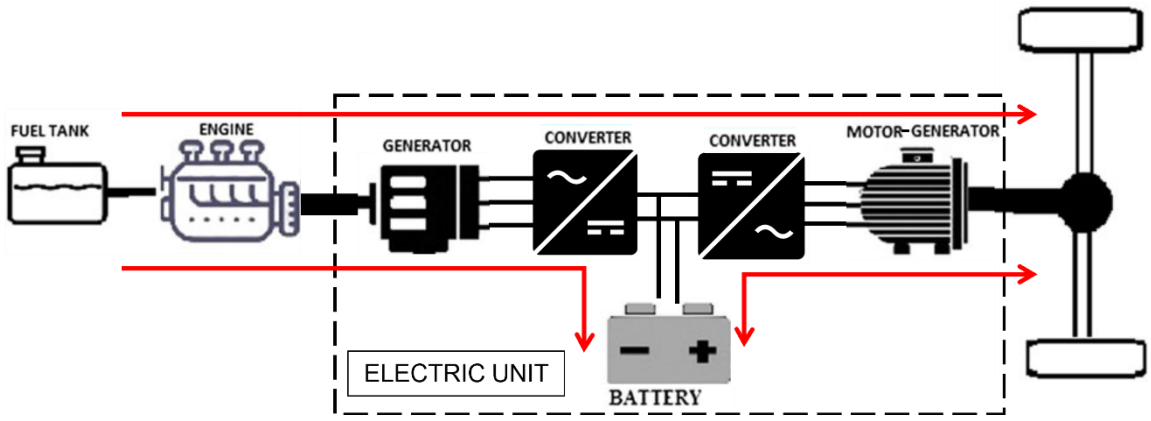

Fig. 1.4. Series hybrid powertrain. The arrows show the possible direction of the power flows.

The main advantage of the series hybrid powertrain is that the engine is kinematically decoupled from the wheels. As a result, the driveline does not strictly require any clutch or gearbox, in contrast to the conventional ICE-powered vehicles. Moreover, the engine can continuously operate within its most efficient range since the electric unit can compensate for any lack or surplus of power through the regulation of the torque and the speed of the

electric motor. Also, control strategies for series HEVs are relatively simple and aim to keep the battery state of charge (SOC) between 40% and 80%.

Nevertheless, only one out of the three actuators onboard contributes to the vehicle traction, namely, the traction motor, which is sized to satisfy the total power demand. As a result, the powertrain encumbrance and weight are significant. Moreover, all the power provided by the engine must undergo multiple energy conversions from the mechanical form to the electrical one and vice-versa, causing considerable losses and reducing the overall transmission efficiency. Hence, the series hybrid is potentially more successful in urban driving, since the engine can operate at the most efficient point despite transient driving, whereas it is less efficient in extra-urban steady-state driving. For these reasons, this solution is mainly deployed in urban vehicles, but is less successful in touring vehicles.

- PARALLEL HYBRID

The parallel hybrid configuration has been conceived as a traditional ICE-powered vehicle with an additional electric power source for the high-load functioning mode, the regenerative braking, and the full-electric operations. Unlike the series hybrid, only one electric machine is needed. The ICE and the electric machine are attached to a designated transmission so that they can power the vehicle either individually or by summing up their power in parallel (Fig. 1.5). Both the ICE and the electric machine are mechanically coupled to the wheels. The electric machine can be used as a motor when the battery provides traction power or as a generator when batteries are recharged by the power supplied by the ICE or recovered during braking. A single reversible DC/AC converter is needed.

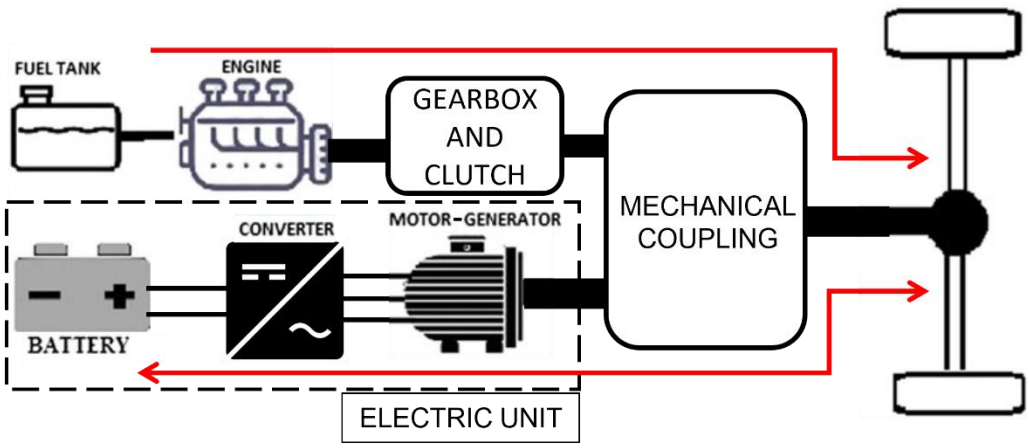

Fig. 1.5. Parallel hybrid powertrain. The arrows show the possible direction of the power flows.

The engine and the electric machine can be mechanically coupled in a multi-shaft configuration by ordinary gearing or pulley and chain assembly, or in a single-shaft arrangement where the rotor of the electric motor is directly connected with the ICE output shaft. In these types of coupling, the ICE speed is univocally dependent on the wheels speed. Hence, a conventional transmission with clutch, gearbox, and differential gear is always required in the parallel powertrain. The location of the electric motor differentiates the parallel hybrid architecture into five subcategories, shown in Fig. 1.6 [16,19]. The P0 and P1 layouts are typically deployed when the electric power is small; the electric machine is connected to the ICE by a belt or directly mounted on the ICE crankshaft, respectively. P2 and P3 layouts are suitable for a larger electric unit; the electric machine is located on the input transmission shaft or on the output transmission shaft, respectively. Therefore, the transmission system does not affect the torque provided by the electric motor in the P3 layout. Moreover, in neither P2 nor P3 the engine can recharge the battery at a standstill because the motor is rigidly connected to the driven wheels. Furthermore, in the P2 layout, the energy recovered through regenerative braking must pass through the transmission. Lastly, in the P4 layout, also known as the "through-the-road" parallel hybrid, the ICE handles the traction of the forward wheels, whereas the electric motor propels the rear wheels. Hence, the mechanical connection between the engine and the electric machine is realised only through the road, indeed. The P4 configuration allows a four-wheel drive.

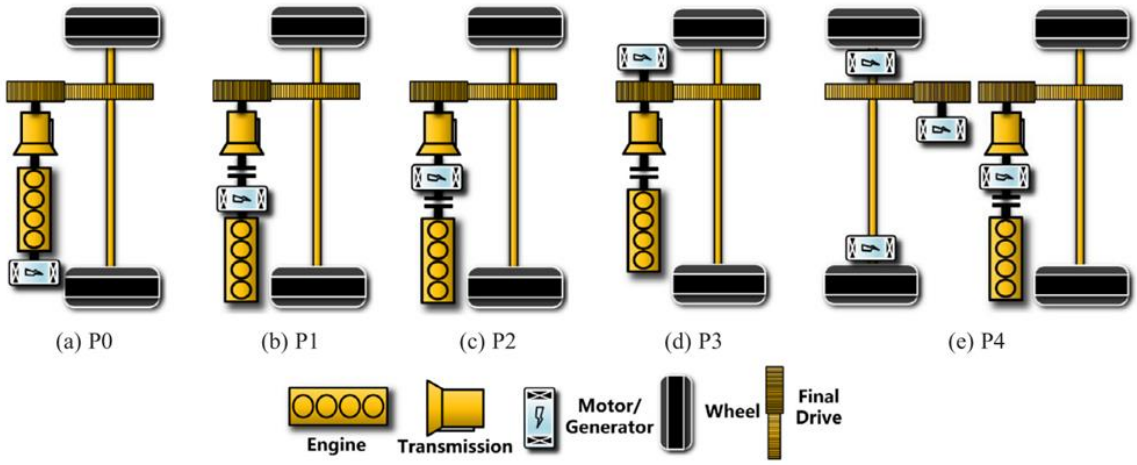

Fig. 1.6. Parallel hybrid sub-categories depending on the position of the electric machine(s) [16].

The advantage of parallel hybrid, if compared to the series configuration, is that the only electric machine needed can be sized for a portion of the maximum power requirement of the vehicle. Furthermore, the lack of multiple energy conversion enhances overall efficiency.

Nonetheless, the ICE is kinematically coupled to the wheels; therefore, a traditional

transmission with a clutch and a gearbox is required. Moreover, the ICE cannot be operated stationarily at its most efficient functioning point. Also, it is not possible to exploit the electric unit without depleting or increasing the battery SOC.

- COMBINED HYBRID: SERIES-PARALLEL

After the full development of the series and parallel architectures, new hybrid powertrains merging the main features of both were implemented. The simplest combined hybrid is the series-parallel configuration, which consists of a parallel hybrid layout with an additional electric machine, used as a generator, kinematically coupled to the ICE (Fig. 1.7). The other electric machine is used primarily as a motor to propel the vehicle or as a generator during regenerative braking. A clutch is deployed between the ICE and the final drive linked to the wheels and the second motor/generator. If the clutch is disengaged, the powertrain operates in the series hybrid mode; if the clutch is engaged, the powertrain operates in the parallel hybrid mode.

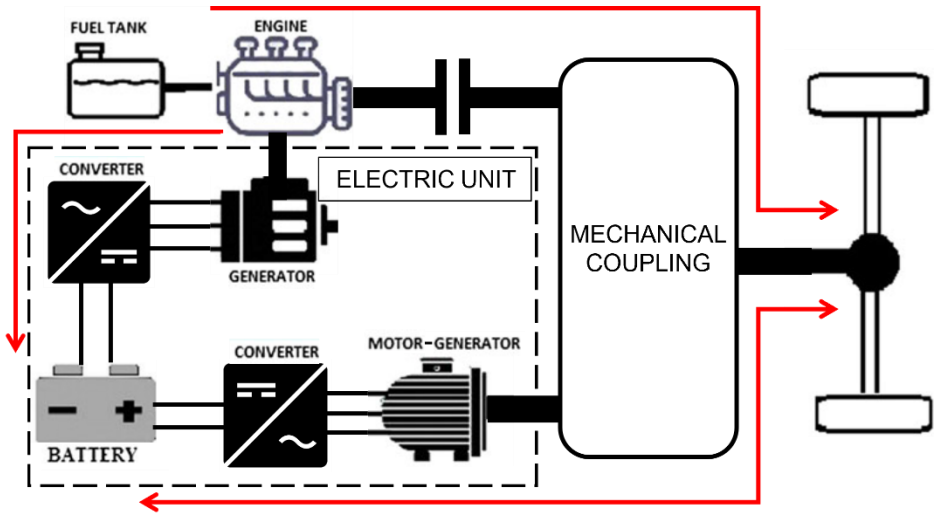

Fig. 1.7. Series-parallel hybrid powertrain. The arrows show the possible direction of the power flows.

- COMBINED HYBRID: POWER-SPLIT

A more complex and promising solution is the power-split hybrid architecture. The core of this layout is the power-split continuously variable transmission (PS-CVT) that couples the internal combustion engine and the final drive replacing the traditional transmission system made up of a gearbox and a clutch (Fig. 1.8).

A PS-CVT involves two kinematic degrees of freedom. Hence, the ICE speed is decoupled from the vehicle speed and a continuous variation of the transmission ratio is achieved by adjusting the speed of two reversible electric machines. As a result, the engine

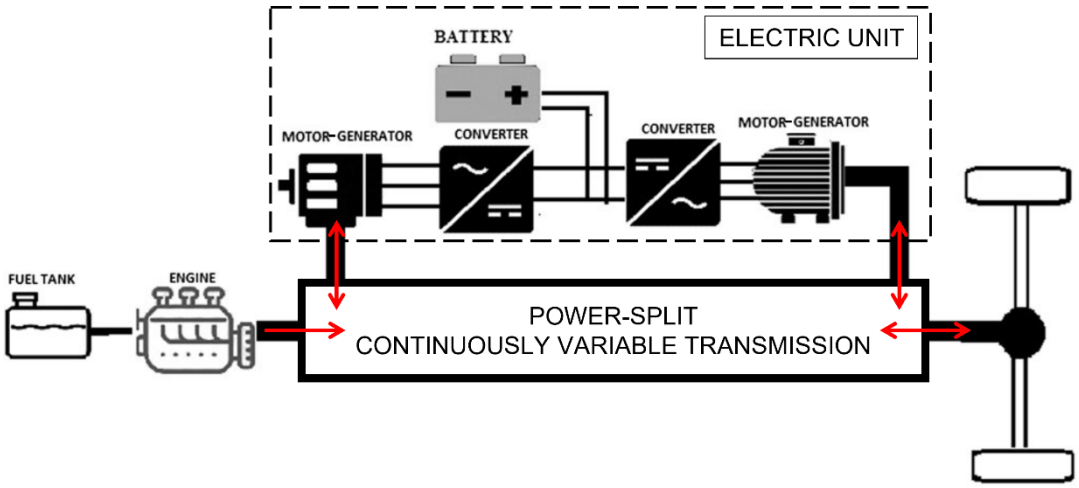

Fig. 1.8. Power-split hybrid powertrain. The arrows show the possible direction of the power flows.

can operate at its best efficiency condition, as in series hybrid configurations. Moreover, the engine power can be transferred to the electric unit for battery recharging but also to the final drive for traction, as in parallel hybrid set-ups. The driving in full-electric mode and the regenerative braking are also available.

Power-split CVTs are described in more detail in Section 1.2.

1.1.2 HEVs degree of electrification

The degree of electrification of a HEV is defined as the ratio between the peak electrical power and the total peak power available on the vehicle. A higher level of electrification can potentially increase fuel savings and reduce emissions. However, in general, the price of the vehicles increases for a higher degree of electrification. The most common classification includes the four types of hybrid electric vehicles [9,10,14–18,20–22] differing in the size of the electric unit. These are briefly described in the following, along with a few examples of vehicles currently available in the European and American markets.

- MICRO HYBRID

Micro-HEVs have a degree of hybridisation lower than 10%. A small starter/generator operated at 12 or 48 V provides the start-and-stop system with the vehicle stationary, as well as mild regenerative braking. It is also used as an alternator for the additional electrical loads on the vehicle. Although the electric machine is not directly involved in vehicle propulsion, the fuel efficiency can improve around 5 to 10% in city driving. Examples of micro-HEVs are the Citroen C3 e-HDi, Fiat 500 Hybrid, Fiat Panda Hybrid, Suzuki Ignis, and Suzuki Swift.

- MILD HYBRID

Mild-HEVs have a higher degree of hybridisation, up to 25%. A larger electric machine, operating at 48 V or 90 V, provides start-and-stop, more effective regenerative braking, and

power assist when an acceleration boost is required. Fuel-saving can be improved by up to 25%. Examples of mild-HEVs have been manufactured by BMW, Ford, Hyundai, Jaguar, Land Rover, Mazda, Mercedes-Benz, Suzuki, and Volkswagen. Micro- and mild-HEVs usually deploy parallel hybrid architecture in the P0 or P1 layout.

- FULL HYBRID

Full hybrid electric vehicles (FHEVs) have a degree of hybridisation ranging from 25% to 50%, thus requiring larger batteries and electric motors, as well as high-voltage systems (200–300 V) and complex electronics. FHEVs enable pure electric driving for a short-medium range. Batteries can be recharged only by the surplus power provided by the engine or by regenerative braking. Fuel saving can be improved by 30–50% by implementing proper energy management strategies to enhance performance, energy efficiency, or emission reduction. Examples of FHEVs are available in the series hybrid configuration from Nissan, in the parallel hybrid configuration from Hyundai, in the series-parallel configuration from Honda, Hyundai, and Renault, and in the power-split configuration from Chevrolet, Ford, Lexus, Suzuki, and Toyota.

- PLUG-IN HYBRID

Plug-in hybrid electric vehicles differ from FHEVs in the degree of hybridisation, which is higher than 50% in PHEVs, and the recharge method, since PHEVs can be plugged into the power grid to recharge the battery. As a result, PHEVs can drive in a charge-depleting mode, during which the battery SOC on average decreases, and in a charge-sustaining mode, which is the only available in FHEVs, during which the battery SOC slightly fluctuates around a certain SOC. Moreover, PHEVs use larger batteries that provide a more extended range in pure-electric driving (30–60 km). The plug-in hybrid setup is mainly available in the parallel configuration, such as in the hybrid technologies developed by Audi, BMW, Citroen, Jaguar, Jeep, Honda, Hyundai, Land Rover, Mercedes-Benz, Opel, Peugeot, Porsche, Renault, and Volkswagen; Honda and Renault have been proposed series-parallel PHEVs, while power-split PHEVs have been developed by Cadillac, Ford, Lexus, Suzuki, and Toyota. Among the PHEVs, are the extended-range electric vehicles (E-REVs), having a larger electric unit. The vehicle is mainly driven in full-electric operation and the engine is turned on only when the battery SOC falls below a minimum level [9,10,23,24]. A Plug-in HEV may still rely on the ICE to reach its maximum vehicle power, whereas an E-REV has full power capability in electric-only operation. One example of an E-REV with a series powertrain is the BMW i3 RE, while the second generation of the Chevrolet Volt is a power-split E-REV.

A summary of the HEVs classification based on the size of the electric unit is shown in Fig. 1.9 [9].

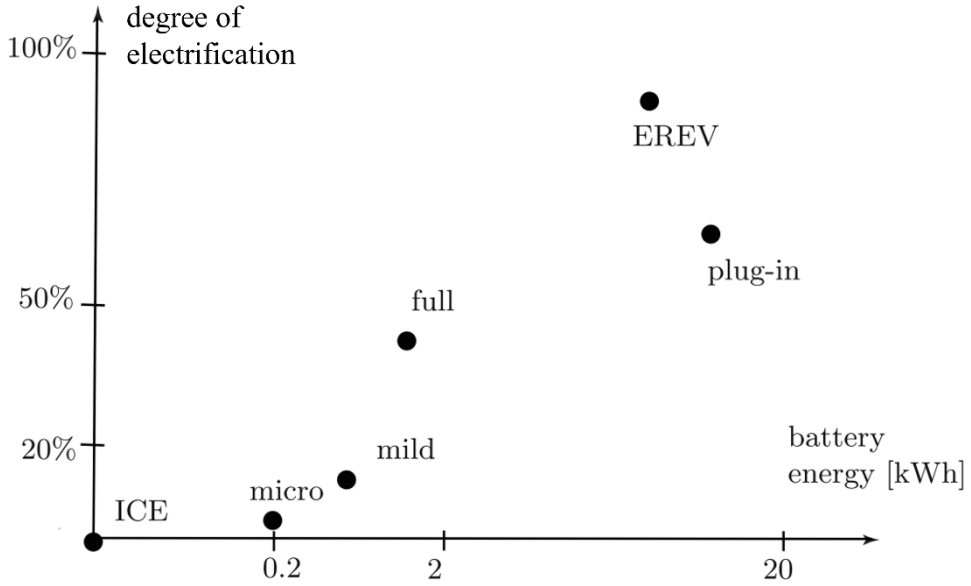

Fig. 1.9. Classification of HEVs in terms of degree of electrification: typical values of the battery energy [9].

1.2 Power-split continuously variable transmissions

Unlike the series-parallel concept specifically developed after vehicles hybridisation, the power-split transmission system had been already deployed in ICE-powered vehicles to improve the efficiency and the ratio spread of conventional continuously variable transmissions [19,25,26].

Any PS-CVT consists of a power-split unit (PSU) and a continuously variable unit (CVU). The PSU is a four-port mechanism that comprises at least one planetary gear train (PG) and, optionally, one or more ordinary gear trains (OGs). The adoption of planetary gearing involves two degrees of freedom, in general, for both speeds and torques established on the PSU ports, that can be connected to the ICE, the wheels, and the two shafts of the CVU. The PSU delivers a portion of the engine power to the electric unit, as in series hybrid, whereas the remaining fraction is mechanically transmitted to the wheels, being involved in the vehicle traction as in parallel hybrid.

Before the development of power electronics, the CVU consisted in a mechanical or hydraulic speed variator [27]. In HEVs, the electric unit itself is deployed as CVU, whereby the continuous variation of the transmission ratio is achieved by the combined use of two electric machines at a variable speed. Moreover, in contrast to the traditional belt variator, the electric unit is an active CVU, providing additional power for vehicle propulsion or gathering the ICE surplus power for battery recharging.

The simplest PSU arrangement includes only one planetary gear train. It is generally known as shunt PS-CVT, which can furtherly be classified into input-split (or output-coupled) or output-split CVT (or input-coupled). The utmost constructive simplicity of shunt PS-CVTs makes them one of the most successful hybrid systems in the automotive market. Nonetheless, a single planetary gearing either enhances the efficiency by reducing the power size of the variator or, alternatively, expands the overall speed ratio range.

A more complex mechanical layout with two or more planetary gear trains leads to compound PS-CVTs. Compound PS-CVTs often embed a clutches system which makes available several constructive arrangements to select according to the current demanded torque and speed. Multi-mode PS-CVTs enhance the minimisation of the power size of the electric machines and increase the overall ratio spread. Nevertheless, the constructive arrangement of the transmission is more complex, along with the management of the power flow.

1.2.1 Input-split hybrid electric powertrains

In the input-split CVT, the engine is connected to the power-split device. At the same time, the speed of one motor/generator speed is directly proportional to the vehicle speed, since the final drive and one electric machine are connected by an ordinary gear train.

The most popular input-split hybrid transmission was implemented on the first and second generation of Toyota Prius, the first power-split hybrid electric vehicle put on the market in 1997 [7,10,16,17,28,29]. The first generation of the Toyota hybrid system, shown in Fig. 1.10, includes two electric machines attached to the sun gear and the ring gear of the planetary gear train, whereas the internal combustion engine is connected to the carrier. The output shaft is linked with the MG2 by an ordinary gear train.

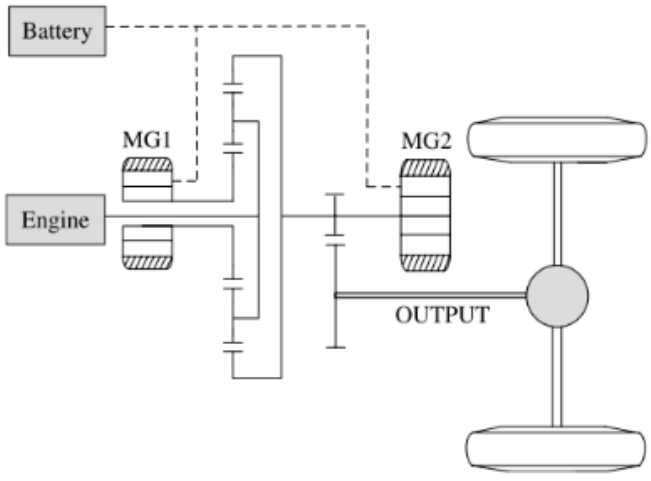

Fig. 1.10. Toyota hybrid system input-split drivetrain (1st and 2nd Gen. Toyota Prius) [7].

Ford developed a very similar input-split concept, the so-called Ford Hybrid System, on Ford Focus, Kuga, Mondeo, Galaxy, and S-Max [7,29]. The only difference between Ford and Toyota hybrid systems concerns the fixed-ratio gear between MG2 and the output shaft (Fig. 1.11).

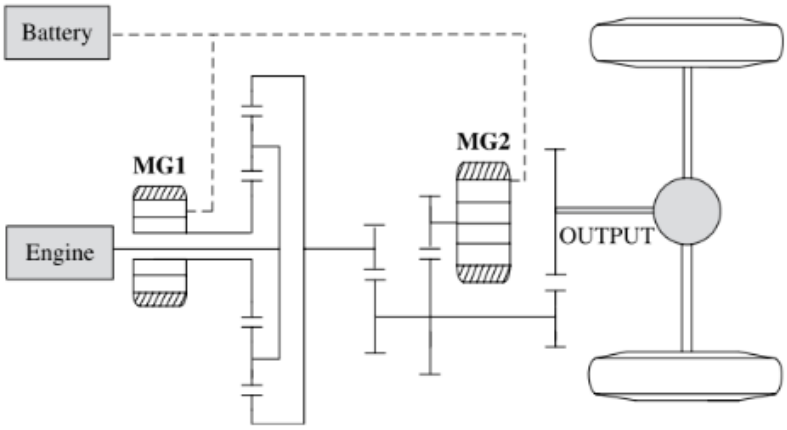

Fig. 1.11. Ford Hybrid System input-split powertrain [7].

The third generation of the Toyota Prius PS-CVT includes a second planetary gear train operating as a fixed gear ratio (Fig. 1.12(a)). It was also implemented on the Toyota Camry. Toyota Highlander, Lexus RX400h, and Lexus RX450h are based on the same power-split arrangement with a third motor on the rear axle to further improve performance [1,5,11,13]. The fourth generation of the Toyota Prius shares the same power-split device arrangement as the previous generations, but it has a different arrangement of the fixed-ratio gear, as shown in Fig. 1.12(b) [30].

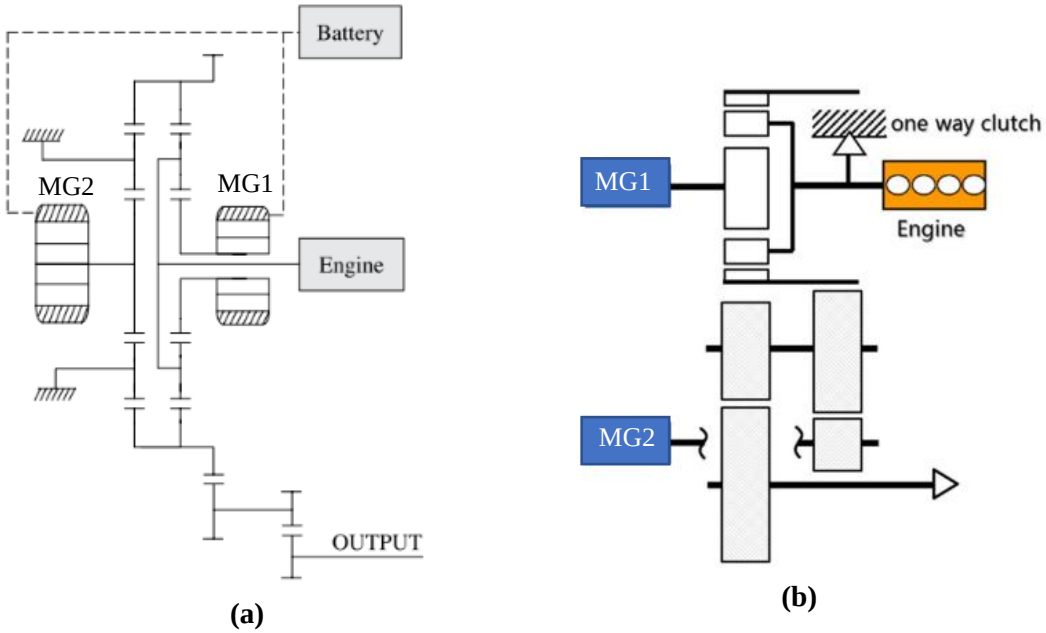

Fig. 1.12. Toyota Hybrid System input-split powertrain: (a) 3rd Gen. Toyota Prius [7]; (b) 4th Gen. Toyota Prius [30].

In addition, Toyota launched further advancements in its input-split technology, mainly adopted in Lexus cars, where a system of clutches and brakes can modify the final fixed ratio [10,16,29].

1.2.2 Output-split hybrid electric powertrains

In an output-split transmission, the output shaft is connected to the power-split device, whereas the ICE speed is kinematically coupled to the speed of one electric machine. The most popular output-split drivetrain is implemented on the first generation of Chevrolet Volt, shown in Fig. 1.13 [7,10,29,31].

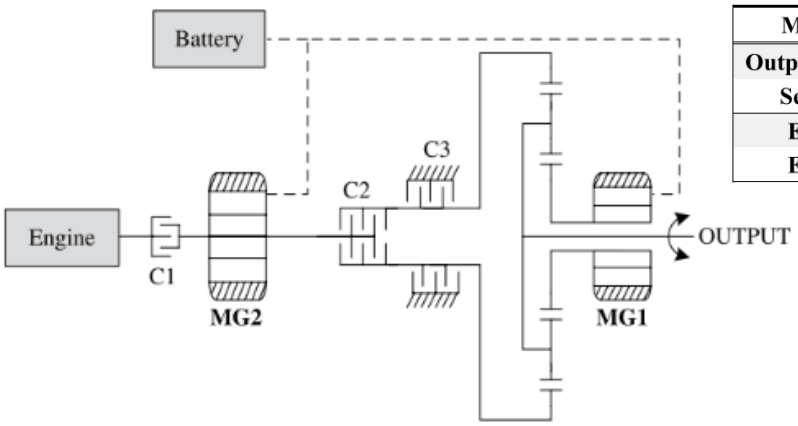

Mode	C3	C2	C1
Output-Split		X	X
Series	X		X
EV1	X		
EV2		X	

Fig. 1.13. Chevrolet Volt powertrain (1st Gen.) and operating modes [7].

Embedding the one-way clutch C1, the rotating multi-plate clutch C2, and the brake C3 makes the Chevrolet Volt drivetrain a multi-mode transmission. The output-split operation is achieved by engaging C1 and C2. By disengaging C2, the ICE is decoupled from the wheels to achieve series hybrid or full-electric vehicle (EV) operations. In EV1, only MG1 propels the vehicles, whereas, in EV2, both electric motors can provide traction power. The first generation of Chevrolet Volt drivetrain is the simplest example of multi-mode PS-CVTs, addressed in more details in the next subsection.

1.2.3 Multi-mode compound-split hybrid electric powertrains

As seen in the first generation of Chevrolet Volt, exploiting a system of clutches and brakes results in multi-mode power-split transmission. By adequately engaging or disengaging one or more clutches, it is possible to enable different constructive layouts.

Several studies claim that the multi-mode power-split CVTs significantly improve efficiency and driving performance compared with single-mode powertrains [32–34]. Deploying two or three PGs in a multi-mode arrangement can improve acceleration performance, especially in SUVs, trucks, or buses [32]. On the other hand, using more than

three PGs can be unnecessary, even counter-productive [33], because of the excessive mechanical complexity and encumbrance. As a matter of fact, the additional degrees of freedom available in the design phase allow the designer to adapt better the PSU power flows to the power demand of different driving conditions by minimising the fraction of converted power and maximising overall efficiency among an extended speed ratio range. On the other hand, if the mechanical complexity increases, encumbrance, weight, and costs may increase as well, thus reducing fuel-saving and mechanical efficiency.

General Motors stands out in the market of multi-mode PS-CVTs. As well as the first and second generation of Chevrolet Volt PS-CVT, General Motors developed the multi-mode PS-CVT of the Cadillac CT6 PHEV.

The second generation of the Chevrolet Volt transmission is a multi-mode PS-CVT including two planetary gearing (Fig. 1.14) [7,16,28,35,36]. A third planetary gear train combined with a chain drive (not shown in Fig. 1.14) acts as a fixed-ratio gear in the final drive. The clutches C1, C2, and C3 enable the shift between different modes.

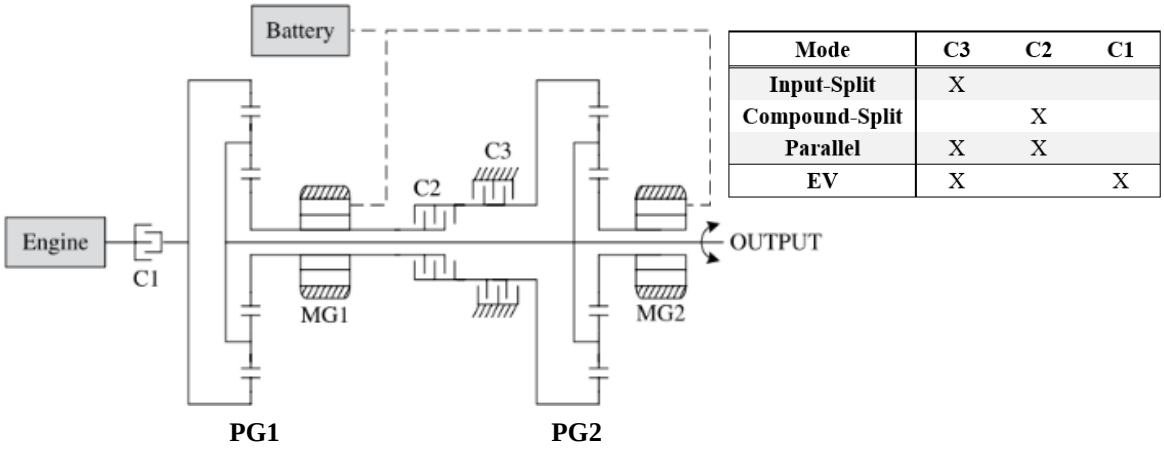

Mode	C3	C2	C1
Input-Split	X		
Compound-Split		X	
Parallel	X	X	
EV	X		X

Fig. 1.14. Chevrolet Volt powertrain (2nd Gen.) and operating modes [7].

By engaging only the clutch C3, the ring gear of planetary-gearing 2 (PG2) is braked to the frame; thus, only PG1 acts as an epicyclic gear unit with non-proportional speeds of its branches. This realises an input-split mode, mainly exploited for lower vehicle speeds. A compound-split mode is achieved at higher speeds by engaging only the clutch C2, which connects the PG2 ring gear to the MG1 and the PG1 sun gear. The simultaneous engagement of C2 and C3 realises a fixed-ratio parallel mode, where only MG2 can operate, and the ICE speed is univocally coupled to the vehicle speed. Moreover, two EV modes can be performed by additionally engaging the one-way clutch C1, which locks the ICE and the PG1 ring gear to the frame. However, as shown in Fig. 1.14, General Motors exploits only the EV operation derived from the input-split arrangement.

The multi-mode power-split CVT of the Cadillac CT6 is significantly more complex [16,28,37]. As shown in Fig. 1.15, it comprises three planetary gear trains and five clutches, resulting in eleven different operating modes.

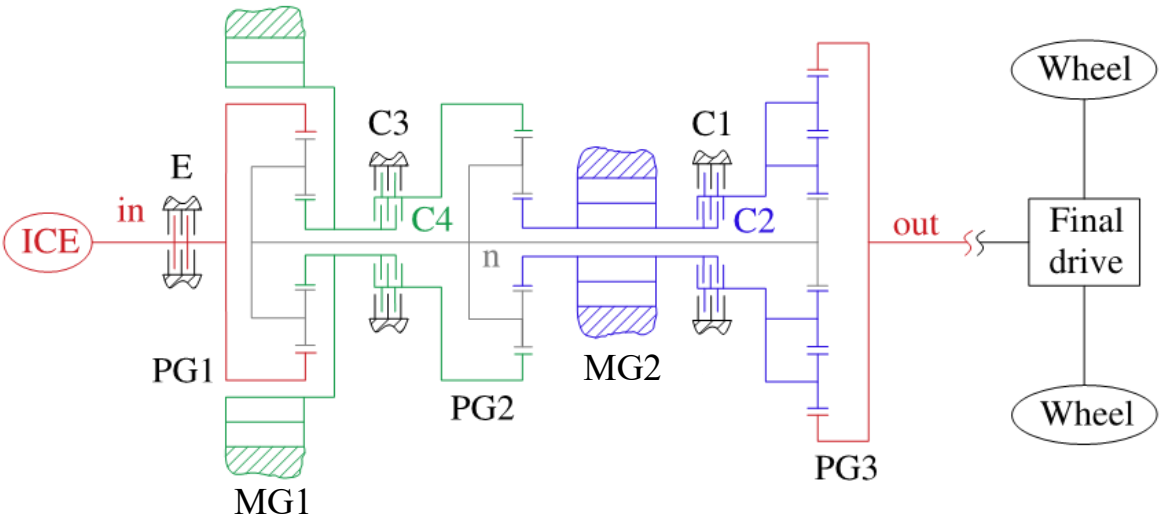

Mode	C1	C2	C3	C4	E
Input-spit 1	X		X		
Parallel 1	X		X	X	
Compound 1	X			X	
Parallel 2	X	X		X	
Compound 2		X		X	
Parallel 3		X	X	X	
Input-spit 2		X	X		
EV1	X		X		X
EV2	X			X	X
EV3			X	X	X
EV4		X	X		X

Fig. 1.15. Cadillac CT6 PHEV powertrain and operating modes.

If clutches C1 and C3 are engaged, a shunt input-split mode is achieved, since PG2 and PG3 are kinematically equivalent to an ordinary gear train and the output speed is proportional to the speed of MG2. Another input-split mode is realised when C2 and C3 are simultaneously engaged because all the three PG3 branches rotate at proportional speed to MG2. By engaging the clutches C1 and C4, PG1 and PG2 operate in a two-PG compound-split mode, while PG3 acts as a fixed-ratio gear. Lastly, all the three PGs are fully active in a second compound-split mode, where C2 and C4 are engaged.

Each power-split mode has a corresponding EV operation, achievable by activating the E clutch that provides the reaction torque on the input shaft while the ICE is off. In all the EV modes, speed ratios between the various PSU branches are univocally defined.

The parallel modes imply a high efficiency because the motors do not convert engine power. In Parallel 1, MG1 can be switched off, while MG2 can produce electric power to charge the batteries or convert it into mechanical form and provide an acceleration boost. The operation in Parallel 3 is very similar, except for the functioning of PG3, whose all branches are rotating, but still, it acts as a fixed-ratio gear. Parallel 2 is not significantly exploited during the drive but is only used to shift between Compound 1 and Compound 2. Indeed, in several multi-mode PS-CVTs, the shift between two contiguous modes is realised when the relative speed of the shafts attached to the involved clutches is null to prevent clutches from slipping. As a result, all the parallel modes assure a synchronous shift.

The power-split architecture, especially in the multi-mode arrangement, offers a high level of flexibility both in the design stage and in the powertrain operation during the drive. Thus, significant enhancements in fuel saving and performance are potentially achievable. Nevertheless, the high constructive complexity requires dedicated mathematical models to design and analyse a power-split powertrain. Moreover, these models have to be suitable for the integration within the energy management strategy (EMS) and powertrain control system, which pursue the most efficient performance by relying on more complex algorithms than the other hybrid architecture. In this regard, Section 1.3 presents a literature review of the models for PS-CVTs commonly adopted in the relevant literature, while the most common EMSs for power-split HEVs are outlined in Section 1.4.

1.3 Models for power-split CVTs

Despite the apparent advantages of power-split transmissions, the wide variety of existing and non-existing PS-CVTs requires universal formulations for analysis purpose for their integration within an EMS. Similarly, the considerable number of feasible solutions available in the design stage complicates their synthesis [25,38].

The graph theory [39] is the most common method adopted to carry out an automated synthesis of power-split transmissions. The powertrain structure is converted into abstract entities and numerical combinations to be introduced in optimization algorithms to search for all potential constructive arrangements [40–47]. However, a merely explorative approach is pursued, which enables the automatic generation of a broad design space. Indeed, this procedure often results in hundreds of billions of potential solutions [38], without any indication on the selection of the best transmission layout. Thus, it is apparent that the screening and selection of the best constructive layout cannot be effectively fulfilled by the designer alone, who instead should rely on computer-aided design techniques [48,49]. The graph theory is sometimes used along with a matrix approach to address the synthesis of

multi-mode transmissions [50] or deployed for analysis purposes [51,52].

An alternative approach for power-split transmissions design is based on the optimization of the most promising mature technologies available on the market [30,53–56]. However, this procedure is unsuitable to meet specific functional requirements, especially outside the automotive field, given the limited number of already implemented solutions.

Alternative design approaches based on the lever analogy have been proposed in [54,57,58]. The lever analogy is a representation of the rotating parts for the planetary gear by a single vertical lever [59]. Torques are represented by horizontal forces on the lever and the lever motion represents the rotational velocities. Thanks to the straightforward reduction of any single or compound PGs to the corresponding lever, the lever analogy is more practical than the graph theory for analysis purpose [60–65]. However, it is less efficient in the design stage, because of the lack of a generalised formulation. Moreover, the lever analogy becomes excessively convoluted in modelling complex PS-CVTs and it is not suitable to consider the deployment of any ordinary gear trains in the PSU.

In addition to these, models based on a matrix approach have been proposed in [66,67] to address the synthesis and the analysis of multi-mode PS-CVTs, although some arbitrary restrictive assumptions limit the design space, resulting in a sub-optimal exploration of the feasible layouts. Other approaches are based on the investigation of the power flows established in the PSU to synthesise the best power-split solution leading to the absence of power recirculation in the electric unit [68–72]. In [73] an efficiency- and performance-oriented design procedure has been proposed, but the considered design space is limited. All these methods often lack generality.

Besides the difficulty in the design stage due to the large number of available solutions, the increased complexity of PS-CVTs hinders an adequate consideration of the transmission power losses. This is due to the intrinsic difficulty in evaluating PG power losses, which can be divided into load-dependent and load-independent losses [74,75]. Load-dependent or mechanical losses are due to the relative motion of the loaded components, i.e., gear meshes and bearings, that produces friction losses due to sliding and rolling. On the contrary, load-independent or spin losses are caused by the interaction of the gear train components with the surrounding medium, which can be oil (churning losses), or air or air/oil mixture (windage losses). Spin losses occur also when the gear train does not transmit power and are mainly due to the drag losses of the spinning components, the viscous losses in bearings, and the pocketing of the fluid at the gear mesh interface. PG power losses has been the subject of extensive studies, resulting in three main approaches: experimental investigation [74,76], elastohydrodynamic lubrication formulation of the contacting surfaces [77], and models

using a constant or empirically estimated friction coefficient [78–83]. Due to the simplified formulation, the last approach is the most practical. Only the power losses due to sliding friction in meshing pairs are often considered, as they are the most significant ones [74,76]. Nonetheless, even under this simplifying assumption, including an accurate assessment of the PSU meshing power losses during the design stage or within an EMS is still challenging because it often involves case-specific formulations necessary to consider the actual power flow into each PG branch. For instance, [84–89] propose an analytical model to assess power flows and efficiency of PS-CVTs, but these contributions deal with only one specific constructive arrangement and relies on case-specific equations, which need a preliminary evaluation of the power flows. Other case-related formulations have been proposed in [80,90–94].

Among the several approach proposed in literature, a unified parametric model, addressed in [83,95,96], stands out as a universal and straightforward tool for both analysis and design phase. The mathematical treatment relies on physically-consistent functional parameters that univocally characterise any PSU. The resulting equations of speed, torque, and power ratios do not depend on the PSU constructive arrangement, which, instead, only affects the numerical value of the functional parameters. Moreover, a modular, hierarchical design procedure for PS-CVTs is enabled, as well as a rapid assessment of the PSU meshing losses. The model was proposed for the first time in [95], where a hierarchical and modular procedure for the functional design of a single-mode PS-CVT was described. Then, a method for deriving the functional parameters underpinning the model for PS-CVTs with up to two PGs was presented in [96]. The model was further extended in [83], where a rapid procedure to assess the PSU meshing losses without any case-specific formulation was addressed. In [83,95,96] the mathematical treatment is dimensionless, i.e., PSU speed, torque, and power are expressed as fractions of the ICE speed, torque, and power, respectively. Moreover, the sizing and operations of the ICE and MGs were not considered in the numerical example on the design of a PS-CVT provided in [95]. Thus, the main focus on the contributions [83,95,96] consists in the driveline itself, with a limited emphasis on the operation of the other components of the powertrain, i.e., the ICE and the electric unit, for a given vehicle speed and demanded torque determined by the driving conditions.

1.4 Energy management strategies for power-split HEVs

Implementing an effective EMS is vital to achieve the full benefits of HEVs. An actual reduction in fuel consumption and emissions can be obtained only if the demanded power is instantaneously split between the engine and the battery so as to keep the ICE operating as

efficiently as possible, minimise the powertrain power losses, and maintain the battery state of charge (SOC) around a desired value.

Besides the minimisation of the fuel consumption, the objectives of the EMS can include the reduction of CO_2 and pollutant emissions, improvement of drivability and comfort, and preserve the battery life [12]. Moreover, different control strategies should be adopted for FHEVs and PHEVs since battery recharge from the grid available in PHEVs enables driving in a charge-depleting mode, in contrast to FHEVs that only allow a charge-sustaining drive [97–99]. Thus, the cost function minimised by the EMS should be defined accordingly to the powertrain characteristics to enhance fuel saving while maintaining the battery SOC within the desired range. Nonetheless, different cost functions deeply affect the resulting optimised operation of the powertrain [100].

Several EMSs for HEVs have been developed [12,18,106–109,98–105]. They are commonly divided into rule-based and optimisation-based EMSs. The former determine the control actions by relying on a set of rules derived from heuristics or from the prior knowledge of the optimal solution obtained by optimisation-based algorithms. Consequently, rule-based EMSs are suitable for real-time implementation but often lead to a suboptimal solution. On the other hand, optimisation-based EMSs consist of establishing and solving a constrained optimisation problem based on the minimisation of a cost function. Some optimisation-based EMSs, such as dynamic programming, Pontryagin's minimum principle, simulated annealing, genetic algorithm, and game theory, are able to find a global optimum, but can be implemented only offline because of the high computational time and the need for prior knowledge of the driving cycle. On the contrary, other optimisation-based EMSs, such as the equivalent consumption minimisation strategy, model predictive control (MPC), and reinforcement learning, are based on algorithms that can solve an instantaneous optimisation problem, potentially in real-time. Nonetheless, they result in a local optimum and require a simplified vehicle model that balances accuracy and computational effort. Moreover, the results of a preliminary offline optimisation may be used as look-up tables to speed up the online optimisation.

Among the EMSs outlined above, this research has been focused on MPC because of its capability to deal with complex multivariable constrained problems on the basis of the prediction of the system future state in a receding horizon framework [110–112]. Although the quality of the optimisation outcome is strongly dependent on the quality of the prediction and information on the road/traffic conditions ahead, MPC does not require knowing the full driving cycle in advance, as in global optimisation-based EMSs. Instead, such information on the route can be instantaneously acquired by the vehicle sensors, global positioning

systems, and intelligent transportation systems. As a result, the implementation of predictive controllers for automotive applications, benefitting from different typologies of preview information, is a clear trend in recent research, not only for EMS development [113–116]. In this regard, a case study on a power-split HEV presented in [117], proved that a 4% gain in fuel saving can be obtained if MPC is adopted in place of the EMS developed by the vehicle manufacturer. Nonetheless, also the accuracy of the vehicle model on which the optimisation algorithm is based may affect the controller performance in terms of both fuel saving and computational time. Thus, the internal model implemented within the control strategy should be complex enough to guarantee optimal powertrain operation in real time, while also involving a low running time.

The latest contributions available in the literature on MPC strategies applied to power-split HEVs mainly focus on more reliable predictions of future driving conditions [118,119,128–130,120–127] and more efficient optimisation algorithms [27,28,31–39]. Some of these contributions deal with multi-mode PS-CVTs [120,121,123,126,127,130,133–135], but only Oncken et al. [126] and Wang et al. [135] address in detail the mode shift strategy. The major challenge of a multi-mode PS-CVT is that, besides the continuous optimisation to allocate power among the thermal and electric units, additional discrete optimisation is required for mode selection. To overcome this issue, a two-level real-time-capable controller consisting of a discrete mode path planning and a continuous MPC is proposed in [126]. The solution presented in [135] is the only one that integrates the mode shift strategy into the MPC framework through a novel receding horizon algorithm combining MPC with dynamic programming. Its real-time implementation has not been tested. In the other cases, the mode shift strategy has relied on precalculated mode shift maps, often obtained through offline optimisation, which provide the optimal operating mode on the basis of the current driving conditions, e.g., the actual vehicle speed and driver demanded torque. Then, the optimal mode is provided as an external input to the MPC EMS, which involves as many internal models as the number of available modes.

Moreover, the analysis of the literature reveals that, while considering the conversion power losses in the ICE, MGs, and the battery within the MPC internal model is well-established, the vast majority of the published research works neglect any power losses in the PGs of the PSU, while there are some attempts [124,129,137] to consider a global efficiency of the PSU. Still, they fail to consider the possibility of power flow reversal during regenerative braking or when an MG switches from motoring to generating operations and vice versa. The analysis of how the inclusion of the PSU power losses in the internal model affects the MPC performance is not available in the literature.

1.5 Literature gaps and research novelty

The literature analysis on the models for PS-CVTs reveals that the most common approaches are affected by: 1) the lack of generality due to case-specific formulations, or alternatively, 2) the loss of physical consistency for more general treatments. Moreover, a general mathematical treatment for the adequate consideration of the PSU power losses is often missing.

In this framework, the unified parametric model for PS-CVTs described in [83,95,96] stands out as a novel alternative for offering within a comprehensive formulation all the crucial features that a mathematical tool for PS-CVTs requires. Hence, the aim of the research work described in this dissertation has been to study the potentialities of this model and expand it to provide a unique general formulation for all the existing and non-existing PSU, including the assessment of the PSU meshing losses. This enables: 1) a hierarchical and modular design procedure for the power-split powertrain, and 2) a rapid analysis of any power-split powertrain, also in the multi-mode arrangement, suitable to be embedded in the EMS.

To this purpose, the outputs of the research subject of this dissertation, which have been presented in [139–144], concern:

1) the rearrangement of the mathematical formulation of [95] to align it with the formulation adopted in [83] and to extend the model validity to the full-electric operation (Chapter 2, adapted from [139]);
2) the extension of the analysis procedure to multi-mode transmissions with any number of PGs and modes (Chapter 3, adapted from [139]);
3) the application of the modular design procedure for the global design of a power-split powertrain (Chapter 4, adapted from [140]);
4) the adoption of the parametric model to assess the optimal operations of the power-split hybrid electric powertrain so as to implement an efficient energy management strategy (Chapter 5 and Chapter 6).

Regarding the last point, two different approaches have been developed to optimise the operation of the power-split hybrid electric powertrain. The first method deals with the offline assessment of the optimal operating maps resulting in the maximisation of an index related to the powertrain global efficiency (Chapter 5, adapted from [141–143]). The second contribution integrates the unified parametric model within an EMS based on the model predictive control (Chapter 6, adapted from [144]). Two main gaps have emerged from the literature analysis on MPC for the EMS of power-split hybrid electric vehicles:

1) the lack of integration of the discrete mode shift strategy within the MPC framework

using a continuous formulation in a single and universal internal model, which is essential to find the optimal profile of all the control inputs over the prediction horizon, including the mode selection, through a single optimal control problem;

2) the lack of a comparative analysis of MPC internal models with different levels of complexity to assess how the accuracy of the internal model affects the controller performance.

The accuracy and complexity of the vehicle internal model implemented within the MPC formulation might affect the EMS performance in terms of fuel saving and running time. Thus, a comparison of different internal models is proposed to assess the influence of the following factors:

1. PSU meshing losses;
2. MGs efficiency;
3. the inertial load of the actuators.

Although the PSU meshing losses are usually far lower than the power lost in the electro-mechanical conversion in the MGs and chemical-mechanical conversion in the ICE, they may become significant for considerable relative speed of PGs branches and high transmitted power. Moreover, their evaluation may help to select the optimal PSU constructive arrangement among those functionally equivalent in the design stage. Thus, evaluating their influence on the MPC performance may be interesting. Regarding the MGs efficiency, polynomial fitting is rather common in the literature to include the efficiency maps within a continuous formulation. Nonetheless, it may be useful to assess the effects of a constant efficiency to be considered during the design stage, when the optimal functional parameters are not selected and the MGs are not sized yet. Lastly, the inertia of the actuators is nearly always neglected within the MPC formulation because its consideration would involve an additional state that complicates the problem and increases the computational effort.

The universal mathematical formulation of the parametric model and the possibility of a rapid evaluation of the PSU meshing losses have allowed 1) proposing a universal model predictive controller with integrated mode switch and 2) assessing how the consideration of PSU meshing losses and electric machines efficiency affects the controller performance, by comparing internal models with different complexity.

CHAPTER 2
A UNIFIED PARAMETRIC MODEL FOR PS-CVTs

This chapter describes in detail the unified parametric model for PS-CVTs underpinning the research. The mathematical treatment presented in [95] is aligned with the formulation adopted in [83]. Indeed, the independent variables and functional parameters adopted in [95] are suitable for a passive mechanical CVU with one kinematic degree of freedom (DOF); on the contrary, the formulation used in [83] and described in this chapter uses basic parameters that are better suited for modelling the behaviour of an electric CVU with two DOFs. Moreover, the formulation is rearranged for modelling also the full-electric operation of the vehicle.

The basics of PSU kinematics and the definition of the functional parameters governing the model are defined in Section 2.1; Section 2.2 addresses the PSU ideal kinetostatics. Section 2.3 deals with the characterisation of the PSU by the generalised characteristic function, a tool crucial for both analysis and design purposes. Section 2.4 outlines the assessment of the PSU meshing losses as presented in [83] introducing some minor simplifications. In Section 2.5, the model is adapted to model the full-electric operation.

The speed of each of the three branches of a PG, i.e., the sun gear (S), the ring gear (R), and the carrier (C), is linearly dependent on the speed of the other two according to the Willis equation:

$$\Psi = \frac{\omega_R - \omega_C}{\omega_S - \omega_C} = \left.\frac{\omega_R}{\omega_S}\right|_{\omega_C=0} \tag{2.1}$$

where ω_R, ω_S, and ω_C are the speed of the ring gear, the sun gear, and the carrier, respectively, whereas Ψ is the PG Willis ratio, defined as the ratio between the ring and the sun gear when the carrier is stationary. Instead, the ratio between the torque developed in ideal conditions on two PG branches is a function of the Willis ratio only:

$$\frac{T_S}{T_C} = \frac{\Psi}{1-\Psi}; \qquad \frac{T_R}{T_C} = \frac{1}{\Psi - 1}; \qquad \frac{T_S}{T_R} = -\Psi \tag{2.2}$$

where T_R, T_S, and T_C are the ideal torques on the ring gear, sun gear, and carrier, respectively.

As addressed in Section 1.3, several power-split architectures are available, which can vary for the number and arrangement of PGs, OGs, and clutches and brakes in the case of multi-mode PS-CVTs. The speed, torque, and power ratios between any two PSU shafts depend on how the PGs branches are connected, as well as on the PGs constructive ratio.

Moreover, any OGs and the connections between the PSU internal shafts with the actuators and the wheels must also be considered to model the whole power-split driveline. As a result, modelling any power-split powertrain by using Eqs. (2.1)-(2.2) involves equations suitable only for the analysed PS-CVT; whenever the PSU constructive arrangement changes, even just in terms of the connections between shafts as in a multi-mode layout, a different set of equations must be considered.

On the contrary, under the unified formulation of the considered parametric model, any PSU is modelled as a four-port device that a set of functional parameters can comprehensively characterise. The PSU external ports are connected to the ICE, the wheels, and the two electric MGs. They are indicated as the port *in*, *out*, *i*, and *o*, respectively (Fig. 2.1). The equations of PSU speed, torque and power ratios, resulting from this general parametric approach and presented in the next sections, are universal and do not change from one PSU to another. The only difference is the numerical value of the functional parameters.

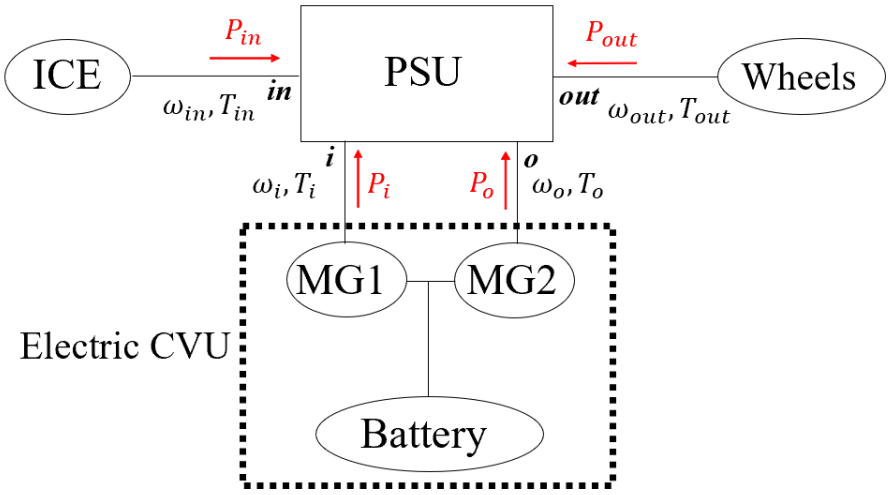

Fig. 2.1. General representation for any PS-CVT. The arrows show the positive power flows.

2.1 Kinematics of PS-CVTs

Any PSU is a combination of planetary gear trains, whose branches rotate at linearly dependent speeds, ordinary gear trains, whose shafts have proportional speeds, and isokinetic joints, consisting of two or more shafts rotating at the same speed. Consequently, for some PSU shafts their rotational speed is proportional to the engine speed (ω_{in}), for others to the output speed (ω_{out}), for others it is a linear combination of both. In order to treat a two-DOF problem as a single-DOF one, any rotational speed is normalised to the engine speed. For the generic *j*th shaft in the PSU, the *j*th speed ratio τ_j is defined as follows:

$$\tau_j = \frac{\omega_j}{\omega_{in}} = A_j + B_j\,\tau \tag{2.3}$$

where τ is the overall speed ratio between the PSU output and input shaft:

$$\tau = \frac{\omega_{out}}{\omega_{in}} \tag{2.4}$$

A_j and B_j are two constant coefficients that depend on the PSU constructive parameters and can be derived as in Section 2.1.1.

2.1.1 Nodal ratios and corresponding speed ratios

The overall transmission ratio τ achieved when a generic *k*th shaft is stationary is called nodal ratio:

$$\tau_{\#k} = \left.\frac{\omega_{out}}{\omega_{in}}\right|_{\omega_k=0} \tag{2.5}$$

In the remainder of this section, we refer to a finite and non-zero nodal ratio as a proper nodal ratio. Hence, the nodal ratios associated with the output and input shafts are not proper, since $\tau_{\#out} = 0$ and $\tau_{\#in} = \infty$ from Eq. (2.5). Similarly, the nodal ratios associated with the shafts having a rotational speed proportional to ω_{out} or ω_{in} are not proper, because they equal zero or ∞, respectively.

The value of the speed ratios τ_j achieved in correspondence of a nodal ratio $\tau_{\#k}$ is the corresponding speed ratio:

$$\tau_{j\#k} = \left.\frac{\omega_j}{\omega_{in}}\right|_{\omega_k=0} \tag{2.6}$$

If $j = k$, $\tau_{j\#k}$ equals zero.

A_j and B_j can be assessed by writing Eq. (2.3) in two operating conditions, i.e., when the *j*th shaft is stationary and when the *k*th shaft is stationary, with $k \neq j$. Indeed, the consideration of these two conditions results in a two-variable linear system (Eqs. (2.7)-(2.8)), whose resolution leads to A_j and B_j (Eqs. (2.9)-(2.10)):

$$\tau_{j\#j} = \left.\frac{\omega_j}{\omega_{in}}\right|_{\omega_j=0} = A_j + B_j\,\tau_{\#j} = 0 \tag{2.7}$$

$$\tau_{j\#k} = \left.\frac{\omega_j}{\omega_{in}}\right|_{\omega_k=0} = A_j + B_j\,\tau_{\#k} \tag{2.8}$$

$$A_j = \frac{\tau_{\#j}\cdot\tau_{j\#k}}{\tau_{\#j} - \tau_{\#k}} \tag{2.9}$$

$$B_j = \frac{\tau_{j\#k}}{\tau_{\#k} - \tau_{\#j}} \tag{2.10}$$

Thus, Eq. (2.3) can be rewritten as follows:

$$\tau_j = \tau_{j\#k}\frac{\tau - \tau_{\#j}}{\tau_{\#k} - \tau_{\#j}} \tag{2.11}$$

Hence, the PSU speed ratios depend on the overall transmission ratio τ and the functional

parameters consisting of speed ratios assessed when a PSU shaft is stationary.

2.1.2 Mechanical points and CVU speed ratios

Rereferring Eq. (2.11) to the shaft *i* and *o* leads to the definition of the CVU kinematics, i.e., the MGs speed in a hybrid electric powertrain:

$$\tau_i = \frac{\omega_i}{\omega_{in}} = \tau_{i\#o} \frac{\tau - \tau_{\#i}}{\tau_{\#o} - \tau_{\#i}} \tag{2.12}$$

$$\tau_o = \frac{\omega_o}{\omega_{in}} = \tau_{o\#i} \frac{\tau - \tau_{\#o}}{\tau_{\#i} - \tau_{\#o}} \tag{2.13}$$

The nodal ratios $\tau_{\#i}$ and $\tau_{\#o}$ referred to the shafts *i* and *o*, connected to the CVU, are called mechanical points. The mechanical points and the corresponding CVU speed ratios $\tau_{o\#i}$ and $\tau_{i\#o}$ are sufficient to comprehensively address the kinematics of the CVU, whichever the PSU layout is. Fig. 2.2 is a visual example representing the linear trend of τ_i and τ_o and the physical meaning of the basic functional parameters. The slope and the axis intercepts of the two lines change with the specific power-split transmission.

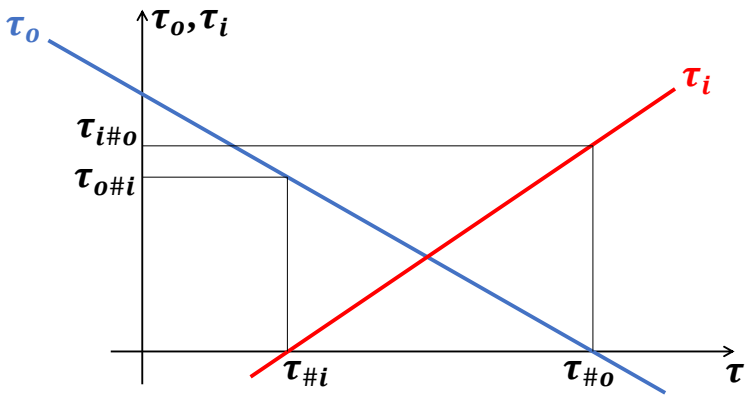

Fig. 2.2. Example of linear CVU speed ratios and meaning of mechanical points and CVU corresponding speed ratios.

In a power-split HEV, τ_o and τ_i are the electric machines speeds normalised to the ICE speed; therefore, a mechanical point is the overall transmission ratio realised when one electric machine is stationary. As a result, no power is flowing through the motionless MG, hence no electric losses due to power conversion occur. Furthermore, in a multi-mode PS-CVT, the mode switch is often performed in correspondence with a mechanical point, since the stationarity of one or more shafts prevents clutches plates from slipping.

Moreover, one mechanical point is zero in an input-split CVT because a fixed-ratio connection is realised between the output shaft and one of the CVU shafts. For instance, if the output shaft is attached to the shaft *i*, then $\tau_{\#i} = 0$. Instead, if the output speed is proportional to the speed of the shaft *o*, then $\tau_{\#o} = 0$. On the contrary, in an output-split

CVT, where the input shaft is directly connected to the shaft *i* or *o*, one mechanical point tends to infinity ($\tau_{\#i} \to \infty$ or $\tau_{\#o} \to \infty$, respectively).

2.2 Ideal PSU kinetostatics

Assuming that the power flowing through the PSU main shafts is positive if entering the PSU (see Fig. 2.1), the power balance of the PSU in ideal conditions, i.e., when any power loss is neglected, is:

$$P_{in} + P_{out} + P_i + P_o = 0 \tag{2.14}$$

Normalising to the input power, i.e., the power supplied by the ICE, the power balance becomes:

$$1 + p_{out} + p_i + p_o = 0 \tag{2.15}$$

where:

$$p_{out} = \frac{P_{out}}{P_{in}}; \qquad p_i = \frac{P_i}{P_{in}}; \qquad p_o = \frac{P_o}{P_{in}} \tag{2.16}$$

The same normalised approach can be considered also to define torques developed in the main shafts:

$$\Theta = \frac{T_{out}}{T_{in}}; \qquad \theta_i = \frac{T_i}{T_{in}}; \qquad \theta_o = \frac{T_o}{T_{in}} \tag{2.17}$$

Thus, Eq. (2.15) can be written as:

$$1 + \Theta\, \tau + \theta_i\, \tau_i + \theta_o\, \tau_o = 0 \tag{2.18}$$

2.2.1 Ideal CVU torques

Since the devices included in the PSU involve speed-independent torque ratios in ideal conditions (see Eqs. (2.2)), Eq. (2.18) can be assessed in the condition whereby one CVU shaft is stationary to obtain the normalised torque on the other CVU shaft. For instance, by assuming $\omega_o = 0$, Eq. (2.18) becomes:

$$1 + \Theta\, \tau_{\#o} + \theta_i\, \tau_{i\#o} = 0 \tag{2.19}$$

from which θ_i is:

$$\theta_i = -\frac{1 + \Theta\, \tau_{\#o}}{\tau_{i\#o}} \tag{2.20}$$

Similarly, assuming that $\omega_i = 0$ leads to the definition of θ_o:

$$\theta_o = -\frac{1 + \Theta\, \tau_{\#i}}{\tau_{o\#i}} \tag{2.21}$$

Thus, the CVU torque ratios are ruled by the overall torque ratio Θ.

2.2.2 Mechanical points and ideal CVU power flows

From the combination of Eqs. (2.12), (2.13), (2.20), and (2.21), the normalised power that flows in the CVU shafts in ideal conditions can be calculated:

$$p_i = \frac{P_i}{P_{in}} = \frac{\omega_i}{\omega_{in}} \cdot \frac{T_i}{T_{in}} = \tau_i \cdot \theta_i = \frac{(\tau - \tau_{\#i})(1 + \Theta\ \tau_{\#o})}{\tau_{\#i} - \tau_{\#o}} \tag{2.22}$$

$$p_o = \frac{P_o}{P_{in}} = \frac{\omega_o}{\omega_{in}} \cdot \frac{T_o}{T_{in}} = \tau_o \cdot \theta_o = \frac{(\tau - \tau_{\#o})(1 + \Theta\ \tau_{\#i})}{\tau_{\#o} - \tau_{\#i}} \tag{2.23}$$

p_i and p_o are null respectively for $\tau = \tau_{\#i}$ or $\Theta = -1/\tau_{\#o}$ and $\tau = \tau_{\#o}$ or $\Theta = -1/\tau_{\#i}$. It means that the occurrence of one of these circumstances causes a reversal of the CVU power flows.

By defining as overall apparent efficiency η the opposite of the output power normalised to the input power, Eqs. (2.22)-(2.23) can be expressed as functions of η:

$$\eta = -p_{out} = -\frac{P_{out}}{P_{in}} = -\frac{\omega_{out}}{\omega_{in}} \cdot \frac{T_{out}}{T_{in}} = -\tau\ \Theta \tag{2.24}$$

$$p_i = \frac{(\tau - \tau_{\#i})(\tau - \eta\ \tau_{\#o})}{\tau(\tau_{\#i} - \tau_{\#o})}; \qquad p_o = \frac{(\tau - \tau_{\#o})(\tau - \eta\ \tau_{\#i})}{\tau(\tau_{\#o} - \tau_{\#i})} \tag{2.25}$$

η is "apparent" because it is not only related to the transmission power losses, but also depends on the energy stored or provided by the CVU. If the CVU is a traditional V-belt variator, η can vary from 0 to 1. Conversely, if the CVU is the electric unit of a HEV, it is $\eta > 1$ when the electric unit provides surplus power for the traction, discharging the battery, or if $\eta < 1$ during the battery recharging phases, even though any power loss is neglected. Moreover, a reversal of the output power flow results in $\eta < 0$, e.g., during engine-on regenerative breaking.

Eqs. (2.22), (2.23), and (2.25) show that the ideal power flows of the electric unit are fully defined by the mechanical points. Thus, selecting mechanical points means establishing the power flowing into the electric machines as a function of the overall transmission ratio τ and the normalised output power (i.e. η) or, alternatively, as function of τ and the overall torque ratio Θ. Once fixed the mechanical points, the definition of the corresponding CVU speed ratios rules the CVU torque ratios by Eqs. (2.20)-(2.21). This enables the designer to prioritise the characterisation of the electric motors during the design and only then to select the constructive PSU layout since each constructive layout is characterised by univocal functional parameters, but different constructive layouts can be arranged by the same functional parameters. Moreover, the knowledge of mechanical points and corresponding CVU speed ratios allows a rapid analysis of the PS-CVT without the need for further enquiring about the constructive layout of the transmission. Thus, the relationships of this section, despite neglecting any power loss, are a very powerful tool for comparing the several

feasible configurations at the early stage of the functional design. The procedure for identifying the functional parameters from any PSU constructive arrangement is described in Section 3.1.

2.3 PSU characterisation: TPMs and characteristic functions

Any PSU can be modelled as a combination of three-port mechanisms (TPMs). Fig. 2.3 shows a generic TPM, enclosed in a dashed-line rectangle. It consists of one planetary gear train whose shafts rotate at non-proportional speeds, represented by a rounded-corner square and defined by its Willis ratio Ψ, and up to three fixed-ratio gears, indicated by rhombi and defined by the related speed ratio k. The power is assumed positive if entering the TPM. Furthermore, Fig. 2.3 clarifies the nomenclature used for TPMs: using the capital letters *X*, *Y*, and *Z* is a general way to refer to the internal TPM shafts linked to the PG ring gear, sun gear, or carrier (*R*, *S*, and *C*), while the lowercase letter *x*, *y*, and *z* are referred to the external TPM shafts linked to the PSU main ports (*in*, *out*, *o*, *i*, …).

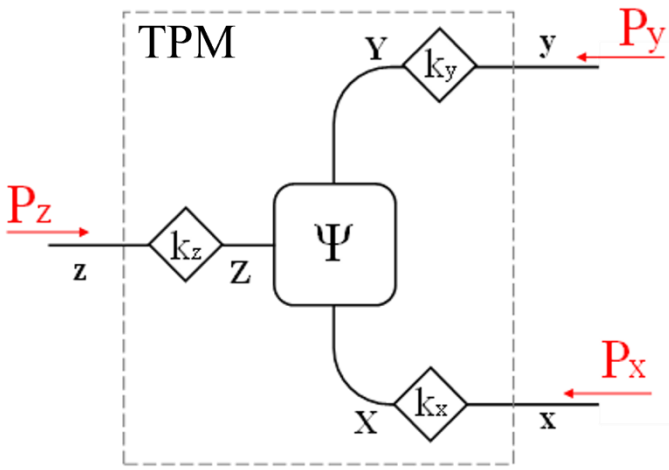

Fig. 2.3. General scheme for a three-port mechanism (TPM). PG is represented by a rounded-corner square, OGs are represented by rhombi. The arrows show the positive power flows.

A shunt PSU comprises one TPM, which has available only three external connections to be associated with the four PSU main ports. Thus, two out of the PSU main ports must be kinematically connected through a fixed speed ratio. Excluding the trivial solution whereby the input and the output port are directly connected, one of the two CVU shafts must be coupled with the input shaft or with the output shaft, resulting in the output-split or input-split layout shown in Fig. 2.4, respectively. Hence, in a shunt PSU, only one external shaft has a rotational speed that is not proportional either to ω_{in} or to ω_{out}, but it is a linear combination of both. As a result, there is only one proper nodal ratio (see Sections 2.1.1 and 2.1.2).

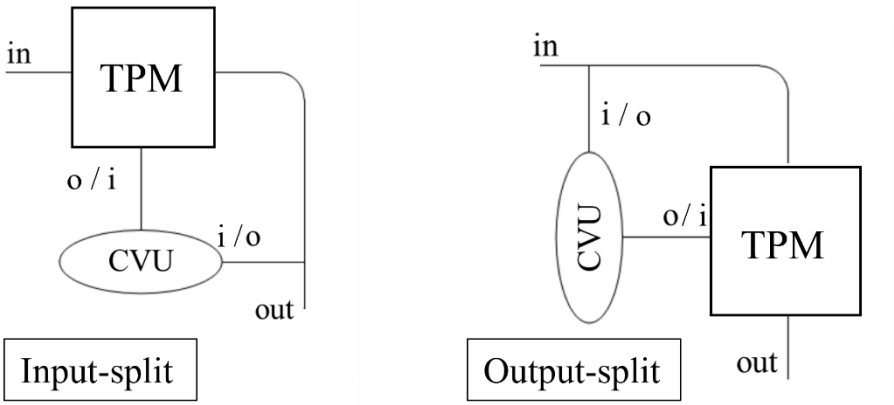

Fig. 2.4. Schematization of the input-split and output-split layouts. Shafts *i* and *o* can be assigned arbitrarily.

A compound PSU with two TPMs, shown in Fig. 2.5, has four ports available to be connected with the four PSU external ports. Thus, two PSU shafts have a rotational speed not proportional either to ω_{in} or to ω_{out}, implying two proper nodal ratios, i.e., the two mechanical points (see Section 2.1.2).

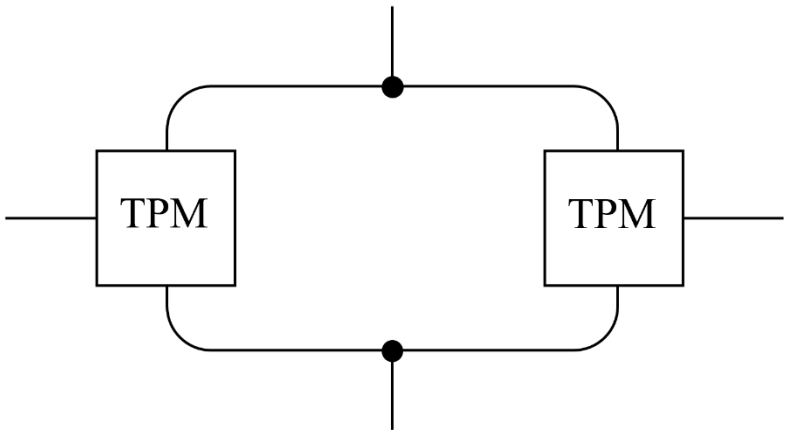

Fig. 2.5. Schematization of a compound-split PSU with two TPMs.

The two mechanical points are sufficient to totally define the CVU power flows, as addressed in Section 2.2.2. Therefore, any further TPM over two affects neither the CVU ideal power flows nor kinematics. Nonetheless, it can be useful to use more than two TPMs to arrange multi-mode transmission. Using three, four, or more TPMs implies that three, four, or more shafts have a rotational speed not proportional either to ω_{in} or to ω_{out}, implying three, four, or more proper nodal ratios. Moreover, five, six, or more shafts are potentially available for external connections, but the core structure of the PSU requires only four main shafts to be linked with the ICE, the CVU and the wheels. As a result, one, two, or more available ports must be unloaded. Nonetheless, an unloaded port must be an

isokinetic joint made up of two or more shafts rotating at the same speed, while a TPM branch not connected with any other TPM must be assigned to one PSU external port. An isokinetic joint externally unloaded is called a neutral node and is indicated by the subscript n. Hence, a neutral node consists of an isokinetic joint that merges two or more branches linked neither with the CVU nor with the input/output of the driveline. Therefore, a neutral node is a fictitious PSU port since it does not have any external connection.

To facilitate understanding, Fig. 2.6 shows the different core structures of a three-TPM PS-CVT. Starting from the two-TPM configuration of Fig. 2.5, the third TPM can be attached to two isokinetic joints (layout I), to two free shafts (layout II) or to one isokinetic joint and one free shaft (layout III). As a result, from Fig. 2.6 it is apparent that in layout I there are only two ports that can be potentially associated with a neutral node, while in layouts II and III there are four and three potential neutral nodes, respectively.

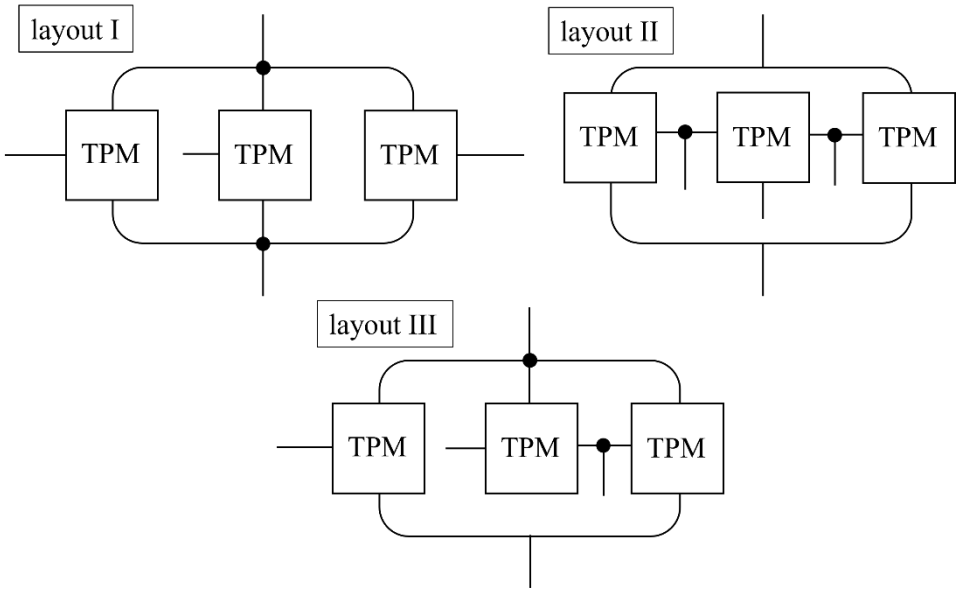

Fig. 2.6. Available layouts for a three-TPM PS-CVTs.

In general, the number of TPMs, indicated as N_{TPM}, included in the PSU equals the number of shafts whose rotational speed is proportional neither to ω_{in} nor to ω_{out}, but which is a linear combination of both. Thus, each TPM ensures the existence of a proper nodal ratio, i.e., a finite and non-zero nodal ratio, which can be freely selected during the design. Moreover, in a PSU, there are $N_{TPM} + 2$ ports potentially available for external connection with the four PSU main ports linked with the ICE, the CVU, and the wheels. Hence, there are as many neutral nodes as the additional TPMs over two, recalling that a neutral node is an isokinetic joint that merge two or more branches linked neither with the CVU nor with the input/output of the driveline.

Nodal ratios rule a set of characteristic functions, defined as the speed ratio between two generic TPM branches when the third one is stationary, divided by the same speed ratio when the third shaft is moving:

$$\phi^{z}_{x/y} = \frac{\tau_x/\tau_y\big|_{\tau_{z=0}}}{\tau_x/\tau_y} = \frac{\tau_{\#z} - \tau_{\#x}}{\tau_{\#z} - \tau_{\#y}} \cdot \frac{\tau - \tau_{\#y}}{\tau - \tau_{\#x}} \tag{2.26}$$

The subscripts x, y and z depend on the considered PSU main shafts. Eq. (2.26) can be derived from Eq. (2.11) considering $k = z$ and $j = x$ or $j = y$.

Characteristic functions are a crucial tool for this model because they play an important role in both the design and analysis stage.

2.3.1 Characteristic functions and PSU functional design

The introduction of the characteristic functions to model the PSU kinematics enables the designer to pursue the optimal operation of PGs, which occurs when the three PGs branches rotate synchronously at the same speed. In this way, the meshing losses of the PG are null, and thus the power losses in the PSU are minimised. To ensure that all the PGs included in the PSU can reach their synchronism within the desired working range, the design procedure proposed in [95] relates the overall transmission ratio whereby a PG works synchronously (τ_*) to the PG constructive arrangement through the logical steps described in the following.

Firstly, the fixed-ratio of every OG is defined as the ratio between the speed of the TPM external shaft and the speed of the shaft linked to the PG:

$$k_x = \frac{\omega_x}{\omega_X}; \qquad k_y = \frac{\omega_y}{\omega_Y}; \qquad k_z = \frac{\omega_z}{\omega_Z} \tag{2.27}$$

Now, let us define as fixed-Z speed ratio $\psi^{Z}_{X/Y}$ the ratio between ω_X and ω_Y of the PG achieved when $\omega_Z = 0$:

$$\psi^{Z}_{X/Y} = \frac{\omega_X - \omega_Z}{\omega_Y - \omega_Z} = \frac{\omega_X}{\omega_Y}\bigg|_{\omega_{Z=0}} \tag{2.28}$$

Thus, $\psi^{C}_{R/S}$ equals the Willis ratio Ψ by definition (see Eq. (2.1)).

Since $\omega_x/\omega_y = \tau_x/\tau_y$, from Eq. (2.26) and Eq. (2.27), it is:

$$\phi^{z}_{x/y} = \frac{\omega_x/\omega_y\big|_{\omega_z=0}}{\omega_x/\omega_y} = \frac{k_x}{k_y}\frac{\omega_X}{\omega_Y}\bigg|_{\omega_Z=0} \cdot \frac{k_y}{k_x}\frac{\omega_Y}{\omega_X} = \frac{\omega_X}{\omega_Y}\bigg|_{\omega_Z=0} \cdot \frac{\omega_Y}{\omega_X} \tag{2.29}$$

At the PG synchronism, namely, for $\tau = \tau_*$, it is $\omega_Y/\omega_X = 1$. Hence, Eq. (2.29) results in:

$$\phi^{z}_{x/y}(\tau_*) = \frac{\tau_x/\tau_y\big|_{\tau_{z=0}}}{\tau_x/\tau_y\big|_{\tau_*}} = \psi^{Z}_{X/Y} \tag{2.30}$$

Eq. (2.30) correlates the speed of the TPM external ports with the speed of the PG branches bypassing the possible presence of OGs. Owing to Eq. (2.30), once the nodal ratios

are selected, there is a univocal relation between the synchronous condition τ_* of a PG and its Willis ratio, depending on how the PG branches (*R*, *S*, and *C*) are connected to the PSU main ports (*in*, *out*, *i*, *o*, n_1, …) and not on the OGs.

In a preliminary design stage, Eq. (2.30) enables the exploitation of the design chart [95], which allows a quick comparison between the main features of different feasible solutions. The design chart is a graphical representation of all the PSU characteristic functions that take on values comprised within the desired range of the Willis ratio (preferably from $-2/3$ to $-1/3$ [83]). Choosing one, two, or *N* curves of the design chart implies the definition of a feasible layout with one, two, or *N* TPMs — and thus *N* proper nodal ratios. Selecting a point from a specific curve implies the definition of the PG Willis ratio and the position of the carrier (linked to the main port *z*), the ring gear (linked to *x*) and the sun gear (linked to *y*), as well as the synchronous point τ_* of a PG. The use of the design chart is explained in detail in Section 4.1.2.

The number of characteristic functions grows factorially with the number of TPMs — and thus of neutral nodes. Indeed, each TPM can be associated with three main ports out of the available ones, which are as many as $\mathrm{N_{TPM}}$+2, as stated above. Furthermore, for each triad of main ports attached to the TPM, there are $\mathbf{P}_3^3 = 6$ possible ways to arrange the position of carrier, ring gear, and sun gear. As a result, the number of all characteristic functions as a function of $\mathrm{N_{TPM}}$ is:

$$\binom{\mathrm{N_{TPM}}+2}{3}\cdot \mathrm{P}_3^3 = \mathrm{N_{TPM}}\cdot(\mathrm{N_{TPM}}+1)\cdot(\mathrm{N_{TPM}}+2) \tag{2.31}$$

In [96] the authors listed explicitly all the 24 characteristic functions for the design of PS-CVTs with up to two active planetary gear trains. However, the only Eq. (2.26) is sufficient to assess any characteristic function independently from the PSU layout if the computational process is automated by exploiting a permutation of the nodal ratios.

Lastly, imposing a certain synchronous point for the involved PGs results in constraining the constructive ratio of the OGs in the TPM:

$$\frac{k_x}{k_y} = \frac{\tau_x}{\tau_y}\bigg|_{\tau_*} = -\frac{\tau_{x_{\#y}}}{\tau_{y_{\#x}}}\cdot\frac{\tau_* - \tau_{\#x}}{\tau_* - \tau_{\#y}}; \qquad \frac{k_x}{k_z} = \frac{\tau_x}{\tau_z}\bigg|_{\tau_*} = -\frac{\tau_{x_{\#z}}}{\tau_{z_{\#x}}}\cdot\frac{\tau_* - \tau_{\#x}}{\tau_* - \tau_{\#z}} \tag{2.32}$$

since at the PG synchronism $\omega_X = \omega_Y = \omega_Z$ in Eqs. (2.27). Using two equations like Eq. (2.32) for each TPM is sufficient to completely arrange the ordinary gear trains.

An example of the application of the parametric model for the design of a power-split hybrid electric powertrain is reported in Chapter 4.

2.3.2 Characteristic functions and PSU analysis

In the analysis stage, the PGs Willis ratios of the PGs are known parameters as well as

the connections between their shafts and the PSU ports. Thus, Eqs. (2.26) and (2.30) can be used to compute the overall transmission ratio corresponding to the PG synchronism as follows:

$$\tau_* = \frac{\Psi\left(\frac{\tau_{\#z} - \tau_{\#y}}{\tau_{\#z} - \tau_{\#x}}\right)\tau_{\#x} - \tau_{\#y}}{\Psi\left(\frac{\tau_{\#z} - \tau_{\#y}}{\tau_{\#z} - \tau_{\#x}}\right) - 1} \tag{2.33}$$

where $\tau_{\#x}$ is the nodal ratio referred to the main port linked with the ring gear, $\tau_{\#y}$ is referred to the main port linked with the sun gear, and $\tau_{\#z}$ is related to the main port linked with the carrier.

Furthermore, characteristic functions represent the opposite of the ratio between the ideal power transmitted by two shafts of a TPM:

$$\phi^z_{x/y} = -\frac{P_y}{P_x} = -\frac{p_y}{p_x} \tag{2.34}$$

Eq. (2.34) can be easily proved using the ideal power balance of the TPM (Eq. (2.35)), considered when $\omega_z = 0$ (Eq. (2.36)).

$$P_x + P_y + P_z = 0 \tag{2.35}$$

$$\omega_x T_x + \omega_y T_y = 0 \tag{2.36}$$

This leads to the identification of the ideal torque ratio between the shafts *y* and *x* when the shaft *z* is stationary as the opposite of the speed ratio assessed in the same condition:

$$\frac{T_y}{T_x} = -\frac{\omega_x}{\omega_y}\bigg|_{\omega_z=0} = -\frac{\tau_x}{\tau_y}\bigg|_{\tau_z=0} \tag{2.37}$$

Thus:

$$\frac{P_y}{P_x} = \frac{T_y}{T_x}\cdot\frac{\omega_y}{\omega_x} = -\frac{\tau_x}{\tau_y}\bigg|_{\tau_z=0}\cdot\frac{\tau_y}{\tau_x} = -\phi^z_{x/y} \tag{2.38}$$

Eq. (2.34) is a powerful tool for assessing the ideal power flow distribution in the PSU, as it is addressed in the next Section 2.4. Furthermore, there is no difference in considering the characteristic functions referring to the external TPM shafts (x, y, z) or to the PG branches (X, Y, Z), as in ideal conditions the presence of the OGs does not alter power flows, thus neither their ratios.

2.4 PSU power losses

Sections 2.2 and 2.3.2 neglect any power loss in the PSU. The assumption of ideal conditions does not significantly affect PS-CVTs analysis, as the mechanical losses are negligible if the transmission is well designed, i.e., the PGs always operate close to their synchronism. However, considering the PSU power losses is essential to implement an

effective energy management strategy to obtain the best energy efficiency. Furthermore, the assessment of the power losses in the driveline can aid the designer in detecting the best solution among several available constructive layouts.

The parametric model under consideration provides a rapid approximated procedure to consider the PSU meshing losses. The formulation was presented in [83] and depends on the PSU nodal ratios without relying on case-specific equations. This section summarises the main features of the method, introducing some minor simplifications to the treatment proposed in [83]. In the following, power losses are normalised to the input power; overlining a power flow or a torque indicates that they refer to the condition whereby the PSU meshing losses are considered.

The total PSU meshing losses are the sum of the losses occurring in every PG and OG. As was demonstrated in [83], the mechanical power losses occurring in an OG linking the branch *x* of the TPM to the shaft *X* of the PG are:

$$\bar{p}_L|_{OG} = \frac{\bar{P}_L|_{OG}}{P_{in}} \approx -\left|\left(1-\eta_{X/x}\right) p_x\right| \tag{2.39}$$

where $\eta_{X/x}$ is the OG efficiency and $p_x = P_x/P_{in}$ is the ideal normalised power flowing through the shaft *x* external to the TPM that, in ideal conditions, equals the power flowing through the shaft *X* connected to the PG. When possible, it is more convenient to choose shaft *x* among the four PSU external shafts; in this way, $p_x = 1$ if *x* = *in*, $p_x = -\eta$ if *x* = *out*, or p_x is given by Eqs. (2.22), (2.23), and (2.25) if *x* = *i* or *x* = *o*. Otherwise, p_x can be calculated by combining Eq. (2.34) with power conservation in an isokinetic joint.

The mechanical power losses occurring in a PG are:

$$\bar{p}_L|_{PG} = \frac{\bar{P}_L|_{PG}}{P_{in}} \approx -\left|\left(1-\eta^Z_{Y/X}\right)\left(\frac{\phi^Z_{x/y}-\psi^Z_{X/Y}}{1-\psi^Z_{X/Y}}\right)p_x\right| \tag{2.40}$$

where p_x is that defined above, $\psi^Z_{X/Y} = \left(\psi^Z_{Y/X}\right)^{-1}$ is the fixed-*Z* speed ratio of the PG (Eq. (2.28)) and $\eta^Z_{Y/X} = \left(\eta^Z_{X/Y}\right)^{-1}$ is its fixed-*Z* efficiency:

$$\eta^Z_{Y/X} = -\frac{\bar{P}_Y}{\bar{P}_X}\bigg|_{\omega_Z=0} = -\frac{\bar{T}_Y}{\bar{T}_X}\frac{\omega_Y}{\omega_X}\bigg|_{\omega_S=0} \tag{2.41}$$

In correspondence with the PG synchronism ($\tau = \tau_*$), Eq. (2.40) correctly implies that the PG meshing losses are null owing to Eq. (2.30).

Usually, the PG fixed-*Z* speed ratio and efficiency are known in the fixed-carrier condition, because they are the PG Willis ratio $\Psi = \psi^C_{R/S}$ and the basic efficiency $\eta_0^{\pm 1} = \eta^C_{R/S}$, respectively. Nevertheless, in some cases, it is more convenient to match a different permutation of *X, Y,* and *Z*, depending on which p_x TPM power flow is known or more

directly computable. In these cases, $\psi_{X/Y}^{Z}$ can be calculated by the relationships of Table 2.1 as functions of Willis ratio Ψ [83], while a more straightforward formulation than the one described in [83] has been proposed in [139] to assess $\eta_{Y/X}^{Z}$. Indeed, it is:

$$\eta_{Y/X}^{Z} = \psi_{Y/X}^{Z} / \bar{\psi}_{Y/X}^{Z} \tag{2.42}$$

where $\bar{\psi}_{X/Y}^{Z}$ is an adjusted fixed-Z speed ratio which can be obtained from Table 2.1 by replacing Ψ with $\Psi/\eta_0^{\pm 1}$.

Table 2.1. Fixed-Z speed ratio of a PG as a function of the Willis ratio.

$\boldsymbol{\psi_{R/S}^{C}}$	$\boldsymbol{\psi_{S/R}^{C}}$	$\boldsymbol{\psi_{S/C}^{R}}$	$\boldsymbol{\psi_{C/S}^{R}}$	$\boldsymbol{\psi_{C/R}^{S}}$	$\boldsymbol{\psi_{R/C}^{S}}$
Ψ	$\frac{1}{\Psi}$	$\frac{\Psi-1}{\Psi}$	$\frac{\Psi}{\Psi-1}$	$\frac{1}{1-\Psi}$	$1-\Psi$

Eq. (2.42) can be obtained from the resolution of the linear system of the equations related to the external torques equilibrium, the kinematic equation, and the definition of the basic efficiency of a PG. For example, supposing that the fixed-Z apparent efficiency of our interest is $\eta_{R/C}^{S}$, we have:

$$\begin{cases} \bar{T}_C + \bar{T}_R + \bar{T}_S = 0 \\ \Psi = \dfrac{\omega_R - \omega_C}{\omega_S - \omega_C} \\ \eta_0^{\pm 1} = -\dfrac{\bar{T}_R}{\bar{T}_S}\dfrac{\omega_R}{\omega_S}\Big|_{\omega_C=0} \end{cases} \Rightarrow \frac{\bar{T}_R}{\bar{T}_C} = -\frac{1}{1-\Psi/\eta_0^{\pm 1}};\ \frac{\omega_R}{\omega_C}\Big|_{\omega_S=0} = 1-\Psi = \psi_{R/C}^{S} \tag{2.43}$$

hence:

$$\eta_{R/C}^{S} = -\frac{\bar{T}_R}{\bar{T}_C}\frac{\omega_R}{\omega_C}\Big|_{\omega_S=0} = \frac{1-\Psi}{1-\Psi/\eta_0^{\pm 1}} = \psi_{R/C}^{S} / \bar{\psi}_{R/C}^{S} \tag{2.44}$$

and similarly for the other cases.

Eq. (2.40) was derived in [83] by expressing the PG torque ratios in real conditions as functions of the fixed-Z speed ratio $\psi_{Y/X}^{Z}$ and fixed-Z efficiency $\eta_{Y/X}^{Z}$. Then, these torque ratios and the PG speed ratios are introduced in the PG power balance considering the meshing losses, which is:

$$\omega_X \bar{T}_X + \omega_Y \bar{T}_Y + \omega_Z \bar{T}_Z + \bar{P}_{loss}|_{PG} = 0 \tag{2.45}$$

The resulting formulation would have implied an iterative formulation to assess the correct assumption on the power flow direction in calculating PG basic efficiency η_0, to prevent any switch in the sign of the PG meshing losses since it must always be $\bar{P}_{loss}|_{PG} \leq 0$. In other words, when calculating $\eta_{Y/X}^{Z}$ as function of η_0, we must discern between η_0 and ${\eta_0}^{-1}$ by verifying whether the power actually enters the equivalent fixed-carrier PG through the sun

gear or if, conversely, the driver is the ring gear. This switch may happen in correspondence with the PG synchronism or when the sign of the torque on a PSU shaft switches. Nonetheless, in [83] it is proved that $\eta^Z_{Y/X}$ is usually high for the common values of η_0 if it is $\Psi < 0.5$ or $\Psi > 2$. Moreover, if $\eta^Z_{Y/X} \to 1$ then $\eta^Z_{X/Y} = \left(\eta^Z_{Y/X}\right)^{-1} \cong 2 - \eta^Z_{Y/X}$. This implies that $\eta^Z_{Y/X}$ and its reciprocal $\eta^Z_{X/Y}$ can be used interchangeably in Eq. (2.40). Hence, the definition of only *Z* is sufficient to assess the fixed-*Z* apparent efficiency, defined simply as η^Z. Similar considerations are valid for the assessment of the meshing losses in the OGs: Eq. (2.39) is valid if the OG efficiency is sufficiently high and $\eta_{X/x}$ and $\eta_{x/X}$ can be used indifferently.

2.4.1 Real CVU power flows

In the considered model, for a given input and output power, the PSU mechanical losses are supposed to be compensated only by the electric machines; thus, $P_{in} = \bar{P}_{in}$ and $P_{out} = \bar{P}_{out}$. The resulting power flowing through the shafts *i* and *o* were obtained in [83] through the procedure described in the following.

The sum of the CVU power flows in real conditions can be obtained from the normalised real power balance of the PSU:

$$\bar{p}_{in} + \bar{p}_{out} + \bar{p}_i + \bar{p}_o + \bar{p}_L = 0 \tag{2.46}$$

$$\bar{p}_i + \bar{p}_o = \bar{\theta}_i \tau_i + \bar{\theta}_o \tau_o = -(1 - \eta + \bar{p}_L) \tag{2.47}$$

where $\bar{p}_L$ indicates the total meshing power losses in the PSU $\bar{P}_L$ normalised to the input power. $\bar{P}_L$ are assessed by summing the losses in PGs and OGs:

$$\bar{P}_L = \sum \bar{P}_L|_{PG} + \sum \bar{P}_L|_{OG} \tag{2.48}$$

The real torque ratios $\bar{\theta}_o$ and $\bar{\theta}_i$ are still speed-independent, thus they linearly depend on the overall torque ratio $\Theta = -\eta/\tau$, as in ideal conditions (Section 2.2.1). Consequently, $\bar{\theta}_o$ and $\bar{\theta}_i$ remain constant if Θ is constant; this means that the directional derivative of Eq. (2.47) along the vector $\begin{bmatrix}\tau \\ \eta\end{bmatrix} = \sqrt{\tau^2 + \eta^2}\begin{bmatrix}\hat{\tau} \\ \hat{\eta}\end{bmatrix}$ is:

$$\bar{\theta}_i \frac{d\tau_i}{d\tau}\hat{\tau} + \bar{\theta}_o \frac{d\tau_o}{d\tau}\hat{\tau} = \hat{\eta} - \nabla\bar{p}_L \begin{bmatrix}\hat{\tau} \\ \hat{\eta}\end{bmatrix} \tag{2.49}$$

where $\nabla\bar{p}_L = \begin{bmatrix}\frac{\partial\bar{p}_L}{\partial\tau} & \frac{\partial\bar{p}_L}{\partial\eta}\end{bmatrix}$ is the gradient of $\bar{p}_L$. By combining Eqs. (2.47) and (2.49), the real CVU power flows $\bar{p}_o$ and $\bar{p}_i$ are obtained after extensive math:

$$\bar{p}_i = \frac{\bar{P}_i}{P_{in}} = p_i - \frac{\tau_i}{\tau_{i_{\#o}}}\left[\bar{p}_L + \left(\frac{\partial \bar{p}_L}{\partial \tau} + \frac{\partial \bar{p}_L}{\partial \eta}\frac{\eta}{\tau}\right)(\tau_{\#o} - \tau)\right] \tag{2.50}$$

$$\bar{p}_o = \frac{\bar{P}_o}{P_{in}} = p_o - \frac{\tau_o}{\tau_{o_{\#i}}}\left[\bar{p}_L + \left(\frac{\partial \bar{p}_L}{\partial \tau} + \frac{\partial \bar{p}_L}{\partial \eta}\frac{\eta}{\tau}\right)(\tau_{\#i} - \tau)\right] \tag{2.51}$$

Moreover, recalling that Eqs. (2.50)-(2.51) were derived considering the directional derivative along the vector whereby Θ is constant, only the variation with τ has to be considered if the independent variables used to define $\bar{p}_L$ are τ and Θ. Hence, Eqs. (2.50)-(2.51) reduce to:

$$\bar{p}_i = p_i - \frac{\tau_i}{\tau_{i_{\#o}}}\left[\bar{p}_L + \frac{d\bar{p}_L}{d\tau}(\tau_{\#o} - \tau)\right] \tag{2.52}$$

$$\bar{p}_o = p_o - \frac{\tau_o}{\tau_{o_{\#i}}}\left[\bar{p}_L + \frac{d\bar{p}_L}{d\tau}(\tau_{\#i} - \tau)\right] \tag{2.53}$$

Once the real CVU power flows are assessed, the real torque ratios $\bar{\theta}_i$ and $\bar{\theta}_o$ can be swiftly evaluated by dividing $\bar{p}_i$ and $\bar{p}_o$ by τ_i and τ_o, respectively:

$$\bar{\theta}_i = \theta_i - \frac{1}{\tau_{i_{\#o}}}\left[\bar{p}_L + \frac{d\bar{p}_L}{d\tau}(\tau_{\#o} - \tau)\right] \tag{2.54}$$

$$\bar{\theta}_o = \theta_o - \frac{1}{\tau_{o_{\#i}}}\left[\bar{p}_L + \frac{d\bar{p}_L}{d\tau}(\tau_{\#i} - \tau)\right] \tag{2.55}$$

2.4.2 Conversion power losses in the ICE and electric unit

The dimensionless approach described above in this section leads to the complete characterisation of the speed, torque, and power of the CVU shafts *i* and *o* expressed as a fraction of the input speed, torque, and power. The independent variables of the model are the overall speed ratio τ and the overall torque ratio Θ or the opposite of the overall power ratio η. Moreover, the consideration of the meshing power losses in the PSU is also included. Nonetheless, the described dimensionless approach is not suitable to assess the conversion power losses occurring in the ICE and in the electric unit, because the efficiency of these actuators varies as a function of their speed and torque. Thus, the knowledge of their actual operating point is required to evaluate their conversion losses, along with the knowledge of their efficiency maps.

Due to the two DOFs of the power-split powertrain, the ICE operating point for given vehicle speed and demanded torque is not univocally defined, but it is the result of the adopted EMS. Therefore, the benefit of using the dimensionless approach outlined in this section is that the PS-CVT behaviour can be comprehensively analysed starting from the only knowledge of the functional parameters, without requiring any information on the actual operating points of the engine and electric machines and on the EMS. In this regard,

an example of the application of the parametric model for PS-CVTs analysis is presented in Chapter 3. Instead, the integration of the model with an EMS that allows the assessment of the actual operating point of the actuators and the respective power losses is addressed in Chapter 5 and Chapter 6.

2.5 Full-electric operations

The parametric model described in the previous sections is suitable for comprehensively analysing any PS-CVT with two DOFs for both speed (Eqs. (2.12)-(2.13)) and torque (Eqs. (2.20)-(2.21)) or power (Eqs. (2.22)-(2.23), (2.25)).

In this section, the mathematical formulation is rearranged to assess the meshing power losses in the PSU and the resulting power flowing through the electric machines when the full-electric operation is achieved, whereby the ICE is turned off and the vehicle is propelled only by the electric unit. Indeed, if for the power-split operation it is convenient to refer the variables to the input shaft, the normalization to T_{in} and P_{in} is not advisable in full-electric modes, as T_{in} is a reaction torque and P_{in} is null.

In the full-electric operation, the shaft *in* directly connected to the ICE is braked to the frame; thus, only one kinematic DOF is available. Therefore, the speed ratio between any two PSU branches is fixed and PGs are used only for torque multiplication from the electric machines to the output. As a result, the kinematic relationships computed for $\omega_{in} = 0$ ($\tau \rightarrow \infty$) can be normalised to the output speed and are constant:

$$\left.\frac{\omega_o}{\omega_{out}}\right|_{\omega_{in}=0} = \frac{\tau_{o_{\#i}}}{\tau_{\#i} - \tau_{\#o}}; \quad \left.\frac{\omega_i}{\omega_{out}}\right|_{\omega_{in}=0} = \frac{\tau_{i_{\#o}}}{\tau_{\#o} - \tau_{\#i}}; \quad \left.\frac{\omega_o}{\omega_i}\right|_{\omega_{in}=0} = -\frac{\tau_{o_{\#i}}}{\tau_{i_{\#o}}} \tag{2.56}$$

The torque distribution can be derived from the power balance of the PSU in ideal conditions (Eq. (2.14)) computed for $P_{in} = 0$:

$$T_{out}\omega_{out} + T_o\omega_o + T_i\omega_i = 0 \tag{2.57}$$

By dividing Eq. (2.57) to ω_{out} and introducing Eqs. (2.56), the contribution of both electric motors to the output torque is:

$$T_{out} = \frac{\tau_{o_{\#i}}}{\tau_{\#o} - \tau_{\#i}} T_o + \frac{\tau_{i_{\#o}}}{\tau_{\#i} - \tau_{\#o}} T_i \tag{2.58}$$

In other words, given a certain P_{out} requested for vehicle propulsion, the power flowing in one electric motor can be freely selected, as opposed to the power-split operation where it would be more convenient to constrain the electric unit behaviour to the input (ICE) and output powers (Eqs. (2.22)-(2.23), (2.25)).

Furthermore, the same method proposed in Section 2.4 enables the assessment of the PSU meshing losses occurring in full-electric operation if the power losses normalisation is not

performed for P_{in} as in Eqs. (2.39)-(2.40). However, $\eta_{X/x}$, η^Z and $\psi^Z_{X/Y}$ are not affected by the variation of the normalising power and neither is the characteristic function $\phi^z_{x/y}$, being a powers ratio (Eq. (2.34)). Consequently, for full-electric operation, $\phi^z_{x/y}$ can be easily computed by Eq. (2.26) for $\tau \to \infty$, by avoiding to refer the shaft *x* to a branch involving an infinite nodal ratio (such as the shaft *in*) to prevent numerical errors in $\phi^z_{x/y}$ computation. As a result, the meshing losses can be normalised to any PSU power flow, if also P_x is normalized to the same power. For convenience, we choose $-P_{out} = -\bar{P}_{out}$ as reference power. The minus sign is due to the actual negative sign of P_{out}, because coming out from the PSU (see Fig. 2.1). Hence, Eqs. (2.39)-(2.40) become:

$$\bar{p}'_L|_{OG} \approx -\left|\left(1-\eta_{X/x}\right) p'_x\right| \tag{2.59}$$

$$\bar{p}'_L|_{PG} \approx -\left|\left(1-\eta^Z_{Y/X}\right)\left(\frac{\phi^z_{x/y}-\psi^Z_{X/Y}}{1-\psi^Z_{X/Y}}\right) p'_x\right| \tag{2.60}$$

where $\bar{p}'_L = -\bar{P}_L/P_{out}$ and $p'_x = -P_x/P_{out}$.

After the normalisation for $-P_{out}$, the ideal power balance of Eq. (2.57) becomes $p'_o + p'_i = 1$, from which $p'_o = 1 - p'_i$ and $p'_i = 1 - p'_o$. Instead, when PSU meshing losses are considered, it is:

$$\bar{p}'_o + \bar{p}'_i + \bar{p}'_L = 1 \tag{2.61}$$

from which we can derive the real power flowing through one MG after that the real power flowing through the other MG is fixed and the PSU meshing losses are assessed. However, neither $\bar{p}'_o$ nor $\bar{p}'_i$ should take on negative values, thereby avoiding unnecessary CVU power recirculation. After assessing the real power ratios of the electric motors, the real torque ratios can be swiftly evaluated by dividing them by the speed ratios (2.56).

In the case study proposed in Chapter 3, the full-electric operation is also assessed by using the formulation presented in this section.

CHAPTER 3
ANALYSIS OF POWER-SPLIT CVTS

The parametric model described in Chapter 2 allows a comprehensive analysis of any PS-CVT thanks to the universal and generalised formulation based on the functional parameters. Hence, provided that the functional parameters characterising the PSU under consideration are known, the PSU kinematics (Section 2.1), kinetostatics (Section 2.2), and meshing losses (Section 2.4) can be assessed, also in the full-electric operation (Section 2.5).

In general, for an existing power-split transmission, the functional parameters in terms of nodal ratios and corresponding speed ratios are not explicitly disclosed; however, these functional parameters can be derived from the constructive arrangement of the PSU. To this purpose, a procedure for identifying the functional parameters from the constructive layout was presented in [96], but it only befits a power-split transmission with up to two TPMs and is based on a case-specific formulation hardly automatable.

Section 3.1 describes a novel pocedure, presented in [139], for identifying the functional parameters. It is based on a generalised matrix approach suitable for any PSU, with any number of TPMs and operating modes. Moreover, the mathematical treatment does not require any case-specific formulas, thus the computing process is easily automatable by numerical software. Then, Section 3.2 addresses a case study on the application of the unified parametric model for analysing the multi-mode PS-CVT of the Cadillac CT6 PHEV, as proposed in [139]: starting from the known constructive arrangement of the PSU for each of the available eleven modes, the procedure of Section 3.1 is applied to identify the functional parameters for each mode; then, the dimensionless approach described Chapter 2 is applied to comprehensively assess the PS-CVT kinematics, kinetostatics, and PSU meshing losses for each operating mode, including the full-electric ones.

3.1 Procedure of identification of the functional parameters

To perform the identification of the functional parameters from a PS-CVT, it needs to be known:

- the constructive parameters of the involved gear trains, i.e., the PGs and OGs teeth ratios;
- the PSU arrangement and the mutual connections between the devices.

The aim is to evaluate:

- the nodal ratios, i.e., the mechanical points $\tau_{\#i}$ and $\tau_{\#o}$ and the nodal ratios referred to as the neutral nodes ($\tau_{\#n1}$, $\tau_{\#n2}$, …);
- the corresponding speed ratios for each nodal ratio.

As addressed in Section 2.3, the number of non-zero and finite nodal ratios equals the number of the TPM included in the PSU; each nodal ratio implies as many corresponding ratios as the number of TPMs minus one.

The functional parameters are obtained by performing some matrix operations derived from the linear system describing the kinematic constraints of the PSU:

$$[\mathbf{K}]\{\boldsymbol{\omega}\} = \{0\} \tag{3.1}$$

where $[\mathbf{K}]$ is the constraints matrix and $\{\boldsymbol{\omega}\}$ is a vector containing the angular speeds of the PSU shafts. To accelerate the computational process, it is advised to sort the rotational speeds included in $\{\boldsymbol{\omega}\}$ so that the elements of the first rows are the speeds of the main shafts, starting from ω_{out} and ω_{in} and then ω_i and ω_o, immediately followed by the ones referred to the neutral nodes and then all the others. Thus, $\{\boldsymbol{\omega}\}$ is defined as follows:

$$\{\boldsymbol{\omega}\} = [\omega_{out} \quad \omega_{in} \quad \omega_i \quad \omega_o \quad \omega_{n1} \quad \omega_{n2} \quad \cdots]' \tag{3.2}$$

Each row of the matrix $[\mathbf{K}]$ reflects the kinematic constraints due to each mechanical device, hence $[\mathbf{K}]$ is a sparse matrix. In particular, owing to Eq. (2.1), for the *j*th PG it is:

$$\omega_{Cj}\left(1 - \Psi_j\right) + \omega_{Sj}\left(\Psi_j\right) + \omega_{Rj}(-1) = 0 \tag{3.3}$$

where Ψ_j is the PG Willis ratio. For the *x*th OG it is:

$$\omega_x(-1) + \omega_X(k_x) = 0 \tag{3.4}$$

An isokinetic joint linking two shafts is a particular OG with $k = 1$.

Eq. (3.1) is valid also for modelling multi-mode PS-CVTs, where the PSU includes brakes and clutches that modify the connections among the PSU branches (see Section 1.2.3). Indeed, the working principle of a clutch connecting the *X*th PSU shaft to the frame ($\omega_x = 0$) can be mathematically modelled by a fixed-ratio gear having a constructive ratio tending to ∞; similarly, an engaged clutch connecting two rotating PSU branches acts as an isokinetic joint, and thus $k = 1$. Shifting from one mode to another results in a variation of the constraint matrix $[\mathbf{K}]$; as a result, the numerical values of the functional parameters related to two power-split modes differ. However, the mathematical treatment for the analysis of the PS-CVT does not change and it is the one described in Chapter 2.

The $[\mathbf{K}]$ matrix has N_C rows, which is the number of the mechanical constraints in the PSU given by the number of PGs plus the further constraints realised by OGs, isokinetic joints, or clutches. The number of columns of $[\mathbf{K}]$ equals the number of rows of the $\{\boldsymbol{\omega}\}$ vector, which is $N_C + 2$ since the PSU has two degrees of freedom. Therefore, Eq. (3.1) is

a linear system in N_C equations and $N_C + 2$ variables. By supposing that two of the variables are known, for instance ω_{out} and ω_{in}, the remaining rotational speeds can be written as functions of ω_{out} and ω_{in}. For this purpose, it is necessary to perform a partition of the [**K**] matrix in order to obtain a two-column matrix [**W**] that relates the rotational speeds of the PSU output and input to the other speeds included in {**ω**}:

$$[\mathbf{K}]\{\boldsymbol{\omega}\} = \underbrace{\begin{bmatrix} k_{1,1} & k_{1,2} & k_{1,3} & \cdots & k_{1,N_C+2} \\ k_{2,1} & k_{2,2} & k_{2,3} & \cdots & k_{1,N_C+2} \\ k_{2,1} & k_{2,2} & k_{2,3} & \cdots & k_{1,N_C+2} \\ \vdots & \vdots & \vdots & \ddots & \vdots \\ k_{N_C,1} & k_{N_C,2} & k_{N_C,3} & \cdots & k_{N_C,N_C+2} \end{bmatrix}}_{[\mathbf{K}_{(1,2)}]\quad [\mathbf{K}_{1,2}]} \begin{matrix} \omega_{out} \\ \omega_{in} \\ \hline \omega_i \\ \omega_o \\ \vdots \\ \omega_{N_C+2} \end{matrix} \begin{matrix} \} \{\boldsymbol{\omega}_{known}\} \\ \\ = \{0\} \\ \} \{\boldsymbol{\omega}_{unknown}\} \end{matrix} \tag{3.5}$$

$[\mathbf{K}_{(1,2)}]$ is a submatrix of [**K**] that includes only the first two columns of [**K**], while $[\mathbf{K}_{1,2}]$ is a submatrix of [**K**] obtained by removing the first two columns of [**K**]. Hence, the previous equation can be rewritten as follows:

$$[\mathbf{K}]\{\boldsymbol{\omega}\} = [\mathbf{K}_{(1,2)}]\{\boldsymbol{\omega}_{known}\} + [\mathbf{K}_{1,2}]\{\boldsymbol{\omega}_{unknown}\} = \{0\} \tag{3.6}$$

from which we can calculate the column vector of the unknown rotational speeds:

$$\{\boldsymbol{\omega}_{unknown}\} = -[\mathbf{K}_{1,2}]^{-1} \cdot [\mathbf{K}_{(1,2)}]\{\boldsymbol{\omega}_{known}\} \tag{3.7}$$

In other terms:

$$\begin{pmatrix} \omega_i \\ \omega_o \\ \omega_{n1} \\ \vdots \end{pmatrix}_{\mathrm{N_C x 1}} = [\mathbf{W}] \begin{pmatrix} \omega_{out} \\ \omega_{in} \end{pmatrix} \tag{3.8}$$

where

$$[\mathbf{W}] = -[\mathbf{K}_{1,2}]^{-1} \cdot [\mathbf{K}_{(1,2)}] \tag{3.9}$$

Note that in Eq. (3.8) the vector of the unknown rotational speeds has N_C elements. By using the MATLAB notation that can appear more familiar, Eq. (3.9) can be considered as follows:

$$[\mathbf{W}] = -[\mathbf{K}(:, 3{:}\,\mathrm{end})]^{-1}\,[\mathbf{K}(:, 1{:}\,2)] \tag{3.10}$$

At this point, the calculation of the functional parameters from the matrix [**W**] is straightforward. After normalising the Eq. (3.8) to ω_{in} we get:

$$\begin{pmatrix} \tau_i \\ \tau_o \\ \tau_{n1} \\ \vdots \end{pmatrix}_{N_C \mathrm{x} 1} = \begin{bmatrix} w_{1,1} & w_{1,2} \\ w_{2,1} & w_{2,2} \\ \vdots & \vdots \\ w_{N_C,1} & w_{N_C,2} \end{bmatrix} \begin{pmatrix} \tau \\ 1 \end{pmatrix} \tag{3.11}$$

The first row of the system is:

$$\tau_i = w_{1,1}\tau + w_{1,2} \tag{3.12}$$

The previous equation computed for $\tau_i = 0$ leads to the calculation of the nodal ratio $\tau_{\#i}$:

$$0 = w_{1,1}\tau_{\#i} + w_{1,2} \qquad \Rightarrow \qquad \tau_{\#i} = -\frac{w_{1,2}}{w_{1,1}} \tag{3.13}$$

Similarly, by calculating the second row for $\tau_o = 0$, we can obtain the nodal ratio $\tau_{\#o}$ as $-w_{2,2}/w_{2,1}$, and so on for the other nodal ratios. As a result, the nodal ratios are the opposite of the ratio between each element of the second column of $[\mathbf{W}]$ and the corresponding element in the first column. This ratio can be calculated with the aid of numerical software, e.g., MATLAB, by using the element-wise division to obtain a vector containing all the nodal ratios:

$$\begin{pmatrix} \tau_{\#i} \\ \tau_{\#o} \\ \tau_{\#n1} \\ \vdots \end{pmatrix}_{N_C \mathrm{x} 1} = -\left[\mathbf{W}(:,2)\right] ./ \left[\mathbf{W}(:,1)\right] \tag{3.14}$$

If the vector $\{\boldsymbol{\omega}\}$ is sorted properly (see Eq. (3.2)), we can replace $[\mathbf{W}]$ with its submatrix $[\mathbf{W}^{(1,\dots,N_{TPM})}]$, which consists of the first N_{TPM} rows of $[\mathbf{W}]$, if N_{TPM} is the number of TPMs included in the PSU and of non-zero and finite nodal ratios. In this way, the unnecessary calculation of the nodal ratios related to the shafts rotating proportionally to one PSU main shaft is avoided. Thus, Eq. (3.14) returns a vector that does not contain any redundant nodal ratio.

The same matrix $[\mathbf{W}^{(1,\dots,N_{TPM})}]$ also allows the identification of the corresponding speed ratios. Indeed, when for example Eq. (3.11) is computed for $\tau = \tau_{\#i}$, it gives the corresponding speed ratios of the mechanical point related to the shaft i. The same is for the other nodal ratios. By properly assembling all the corresponding speed ratios we get a N_{TPM} by N_{TPM} square matrix whose diagonal elements are all equal to zero, while the other elements are the corresponding speed ratios:

$$\begin{bmatrix} 0 & \tau_{i_{\#o}} & \tau_{i_{\#n1}} & \cdots \\ \tau_{o_{\#i}} & 0 & \tau_{o_{\#n1}} & \cdots \\ \tau_{n1_{\#i}} & \tau_{n1_{\#o}} & 0 & \cdots \\ \vdots & \vdots & \vdots & \ddots \end{bmatrix}_{N_{TPM} \mathrm{x} N_{TPM}} = \left[\mathbf{W}^{(1,\dots,N_{TPM})}\right] \begin{bmatrix} \tau_{\#i} & \tau_{\#o} & \tau_{\#n1} & \dots \\ 1 & 1 & 1 & \dots \end{bmatrix}_{2 \mathrm{x} N_{TPM}} \tag{3.15}$$

The submatrix of $[\mathbf{W}]$ that comprises its first and second row, defined as the kinematic matrix $[\boldsymbol{\Omega}]$, can be exploited for a rapid assessment of τ_i and τ_o:

$$[\boldsymbol{\Omega}] = \left[\mathbf{W}^{(1,2)}\right] = [\mathbf{W}(1{:}\,2,:)] = \frac{1}{\tau_{\#i} - \tau_{\#o}} \begin{bmatrix} -\tau_{i\#o} & \tau_{\#i}\tau_{i\#o} \\ \tau_{o\#i} & -\tau_{\#o}\tau_{o\#i} \end{bmatrix} \tag{3.16}$$

$$\begin{pmatrix} \tau_i \\ \tau_o \end{pmatrix} = [\boldsymbol{\Omega}] \begin{pmatrix} \tau \\ 1 \end{pmatrix} \tag{3.17}$$

Eq. (3.17) is equivalent to the Eqs. (2.12)-(2.13). Furthermore, a similar matrix relation can be obtained for the ideal torque ratios of Eqs. (2.20)-(2.21):

$$\begin{pmatrix} \theta_i \\ \theta_o \end{pmatrix} = -[\boldsymbol{\Omega}^{-1}]' \begin{pmatrix} \Theta \\ 1 \end{pmatrix} = - \begin{bmatrix} \tau_{\#o}/\tau_{i\#o} & 1/\tau_{i\#o} \\ \tau_{\#i}/\tau_{o\#i} & 1/\tau_{o\#i} \end{bmatrix} \begin{pmatrix} \Theta \\ 1 \end{pmatrix} \tag{3.18}$$

This matrix approach is best suited for carrying out a quick and straightforward ideal analysis, but the relationships addressed in Sections 2.1 and 2.2 remain crucial for analysing the mechanical power losses and for design purposes.

3.2 Case study on the Cadillac CT6 multi-mode PS-CVT

The usability of the novel procedure of identification of the functional parameters is tested through a case study on the multi-mode transmission of the Cadillac CT6 PHEV, whose constructive arrangement and available operating modes are derived from [37,145], shown in Fig. 1.15, and described in Section 3.2.1. Then, a comprehensive analysis of the considered PS-CVT is performed by using the dimensionless approach described in Chapter 2, according to the flow chart shown in Fig. 3.1. Once the functional parameters for each power-split mode are identified in Section 3.2.2 by the matrix approach of Section 3.1, enclosed in the red box of Fig. 3.1, these are used in Section 3.2.3 to deduce the range of utilisation of each mode by analysing the rotational speed of the electric machines. Section 3.2.4 addresses the ideal CVU kinetostatics. Section 3.2.5 calculates the mechanical power losses and the resulting power and torque on the CVU shafts. The complete study of kinematics and real power flows shown in the flow chart is carried out also for full-electric operation in Section 3.2.6. Some of the results of this section have been presented in [139].

3.2.1 Constructive layout of the multi-mode PS-CVT of the Cadillac CT6

The Cadillac CT6 propulsion system includes a 2.0L 4-cylinder gasoline engine with turbocharging, direct injection and continuously variable valve timing acting on 4 valves per cylinder. The electric unit is provided with an 18.4 kWh battery pack, located in the rear, which offers more than 70 km of pure electric range and interacts with the two electric machines, which are identical in size, through a power inverter module that manages the electric power flows. The electric MGs were optimised to pursue the best balance among performance, cost, and efficiency [146,147]. MG1 is an induction electric machine mainly

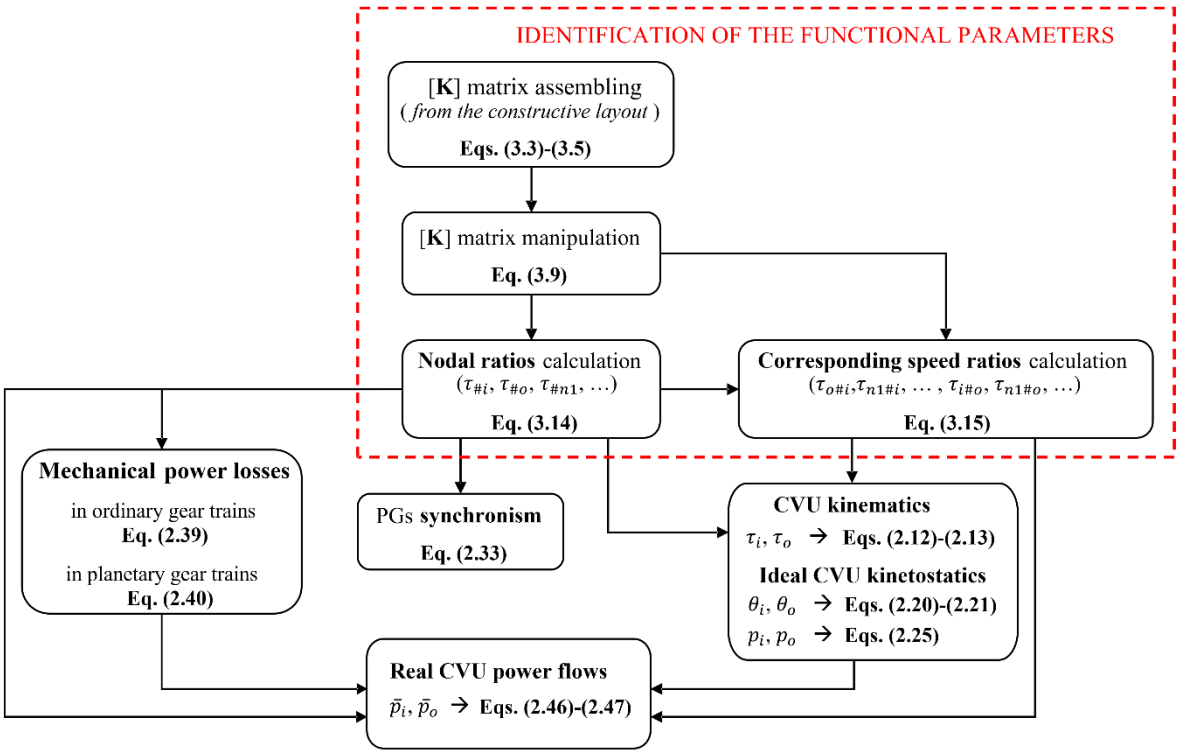

Fig. 3.1. Flow chart of the procedure for PS-CVTs analysis [139].

used as a generator during hybrid propulsion or for supporting MG2 during the full-electric drive. MG2 is an interior permanent magnet motor and is the main electric actuator.

The equivalent functional layout of the multi-mode power-split hybrid electric powertrain of the Cadillac CT6 is represented in Fig. 3.2 according to the symbology introduced in Chapter 2.

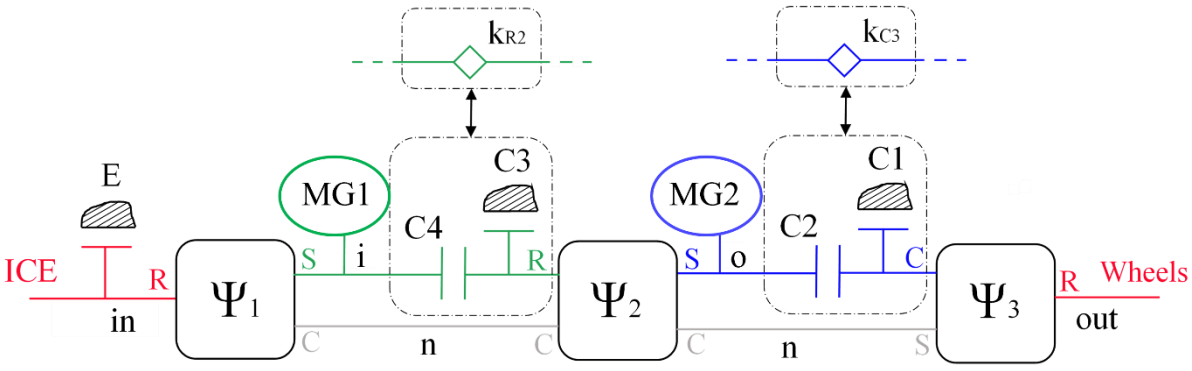

Fig. 3.2. Functional layout of Cadillac CT6 power-split hybrid electric powertrain [139].

The transmission under consideration consists of three planetary gear trains: PG1 and PG2 are identical, and their Willis ratio is $\Psi_1 = \Psi_2 = -0.505$; PG3 includes two sets of

planet gears and its Willis ratio is $\Psi_3 = 0.44$. The ICE (shaft in) is connected to the PG1 ring gear. The PG3 ring gear is the transmission output, which is linked to a final drive (shaft out) to deliver traction power to the wheels. In the following, the final drive is ignored because it does not affect the PSU behaviour. Also, the PG1 carrier, the PG2 carrier, and the PG3 sun gear are constrained to rotate together by a common shaft that is a neutral node (shaft n). The two electric machines can act as motors or generators: MG1 (shaft i) is directly linked with the PG1 sun gear, while MG2 (shaft o) is directly linked with the PG2 sun gear. Lastly, five multi-plate clutches enable several possible modes of operation. The half-stationary clutches C1 and C3 can act as a brake on the PG3 carrier and the PG2 ring gear, respectively. The fully-rotating clutch C2 can connect the PG2 sun gear – and thus MG2 – to the PG3 carrier, while the fully-rotating clutch C4 can connect the PG1 sun gear – and thus MG1 – to the PG2 ring gear. The brake E- can prevent the ICE from moving and provides the reaction torque on the input shaft during full-electric operation.

Clutches could be engaged in $2^5 = 32$ different arrangements, among which 16 can enable the full-electric drive (EV modes) when the clutch E is engaged, while the remaining 16 result in power-split hybrid operations [63]. However, not all these alternatives are suitable for vehicle propulsion since some of them cannot provide power on the output shaft. Indeed, if all the clutches are disengaged, four available kinematic DOFs are available, namely, two for each PG (six in total) minus two DOFs owing to the common shaft. Since each engaged clutch subtracts a further DOF, two clutches – not more and not less than two – among C1, C2, C3 and C4 must be engaged to achieve the power-split hybrid propulsion. However, C1 and C2, or C3 and C4 cannot be engaged at the same time otherwise the transmission is unable to transmit power to the final drive.

As a result, the viable power-split modes are only the four reported in Table 3.1. In particular, if clutches C1 and C3 are engaged, a shunt input-split mode is achieved, since PG2 and PG3 are kinematically equivalent to an ordinary gear train and the output speed is proportional to the speed of MG2. Another input-split mode is realised when C2 and C3 are both engaged because all three PG3 branches rotate with a speed that is proportional to the one of MG2. By engaging the clutches C1 and C4, PG1 and PG2 operate in a compound split mode, while PG3 acts as an OG. Finally, all three PGs are active in a second compound split mode, where C2 and C4 are engaged.

Table 3.1. Cadillac CT6 PS-CVT clutches operations for each of the eleven modes. Engaged clutches are marked with an X.

MODE	C1	C2	C3	C4	E
INPUT-SPLIT 1	X		X		
PARALLEL 1	X		X	X	
COMPOUND 1	X			X	
PARALLEL 2	X	X		X	
COMPOUND 2		X		X	
PARALLEL 3		X	X	X	
INPUT-SPLIT 2		X	X		
EV 1	X		X		X
EV 2	X			X	X
EV 3			X	X	X
EV 4		X	X		X

If three clutches are engaged, the transmission has only one DOF and the overall speed ratio is fixed. This situation is useful when a MG is stationary at its mechanical point. Indeed, by closing a third clutch the reaction torque on the shaft that connects the MG to the PSU can be provided by the frame, rather than by the MG itself, which therefore is unloaded. This condition determines a fixed-ratio parallel hybrid mode, whereby a MG is switched off while the other electric machine can provide additional power for boosting the vehicle propulsion or can recharge the battery, but at a fixed speed ratio. However, since operating in a fixed-ratio parallel hybrid mode means operating in correspondence with a mechanical point of a power-split mode, it does not need to be addressed separately. Table 3.1 also shows that for each power-split mode there is a corresponding EV mode, achieved by engaging the clutch E.

3.2.2 Identification of the functional parameters

In this section, the functional parameters are derived by applying the new method explained in section 3.1. The first step is to determine the constraints matrix from the constructive arrangement of the PSU in each of the four power-split modes. The constraints matrix [**K**] has as many rows as the number of constraints. Ignoring the simple isokinetic joints, which would cause redundant equations, the constructive constraints are related to the three PGs and the clutches system. In particular, the action of the clutch E is not considered now because it only affects the full-electric modes. Also, since the activation of C3 and C4 is mutually exclusive in the power-split operation (see Table 3.1), they impose a single constraint on the shaft linked to the PG2 ring gear, which can be modelled by a fictitious fixed-ratio gear k_{R2} (see Fig. 3.2) that switches from 1 to ∞ depending on the engaged clutch.

The clutches C1 and C2, likewise, constrain the PG3 carrier acting like a fictitious fixed-ratio gear k_{C3}. Hence, there are 3+2 constraints: the [**K**] matrix dimension is 5x7 (i.e., $N_C \cdot (N_C + 2)$), while the rotational speed vector $\{\boldsymbol{\omega}\}$ contains 7 elements $(N_C + 2)$.

The rotational speed vector chosen to properly assemble [**K**] is:

$$\{\boldsymbol{\omega}\} = [\omega_{out} \quad \omega_{in} \quad \omega_i \quad \omega_o \quad \omega_n \quad \omega_{R2} \quad \omega_{C3}]'$$

The general constraint matrix related to the power-split modes is:

$$[\mathbf{K}] = \begin{bmatrix} 0 & -1 & \Psi_1 & 0 & 1-\Psi_1 & 0 & 0 \\ 0 & 0 & 0 & \Psi_2 & 1-\Psi_2 & -1 & 0 \\ -1 & 0 & 0 & 0 & \Psi_3 & 0 & 1-\Psi_3 \\ 0 & 0 & -1 & 0 & 0 & k_{R2} & 0 \\ 0 & 0 & 0 & -1 & 0 & 0 & k_{C3} \end{bmatrix}$$

where $k_{R2} = \omega_i/\omega_{R2}$ and $k_{C3} = \omega_o/\omega_{C3}$. According to Table 3.1 and Fig. 3.2, k_{R2} is equal to 1 when the clutch C4 is engaged (in COMPOUND 1 and COMPOUND 2 operating modes) or to ∞ when the clutch C3 is engaged (in INPUT-SPLIT 1 and INPUT-SPLIT 2). Similarly, k_{C3} is equal to 1 when the clutch C2 is active (in COMPOUND 2 and INPUT-SPLIT 2) or to ∞ when the clutch C1 is active (in INPUT-SPLIT 1 and COMPOUND 1).

After determining [**K**], the matrix approach was implemented in MATLAB, where the matrix [**W**] was calculated through Eq. (3.10). The implementation of a for-loop speeds up the replication of the same calculations for each mode. Hence, the model is highly automatable. In the numerical computing environment, ∞ was replaced by a value sufficiently high (e.g., 10^5). Since there are three TPMs, only the first, second and third row of [**W**] are necessary to evaluate the nodal ratios and the corresponding speed ratios of the shafts *i*, *o*, and *n* by Eqs. (3.14)-(3.15). The results are reported in Table 3.2.

Table 3.2. Nodal ratios and corresponding speed ratios for *i*, *o*, and *n* for the power-split modes.

MODE	$\boldsymbol{\tau_{\#i}}$	$\boldsymbol{\tau_{\#o}}$	$\boldsymbol{\tau_{\#n}}$	$\boldsymbol{\tau_{i_{\#o}}}$	$\boldsymbol{\tau_{i_{\#n}}}$	$\boldsymbol{\tau_{o_{\#i}}}$	$\boldsymbol{\tau_{o_{\#n}}}$	$\boldsymbol{\tau_{n_{\#i}}}$	$\boldsymbol{\tau_{n_{\#o}}}$
INPUT-SPLIT 1	0.29	0	0	-2.0	-2.0	2.0	0	0.66	0
COMPOUND 1	0.29	0.59	0	2.0	-2.0	2.0	3.9	0.66	1.3
COMPOUND 2	1.4	0.59	2.2	2.0	-2.0	2.0	3.9	0.66	1.3
INPUT-SPLIT 2	1.4	0	0	-2.0	-2.0	2.0	0	0.66	0

3.2.3 Kinematic analysis and mode shift strategy

The mechanical points and the corresponding speed ratios of Table 3.2 characterise the CVU kinematic through Eqs. (2.12)-(2.13) or, equivalently, Eq. (3.17). The speed ratios of MG1 (τ_i) and MG2 (τ_o) are shown in Fig. 3.3 as functions of the overall speed ratio τ.

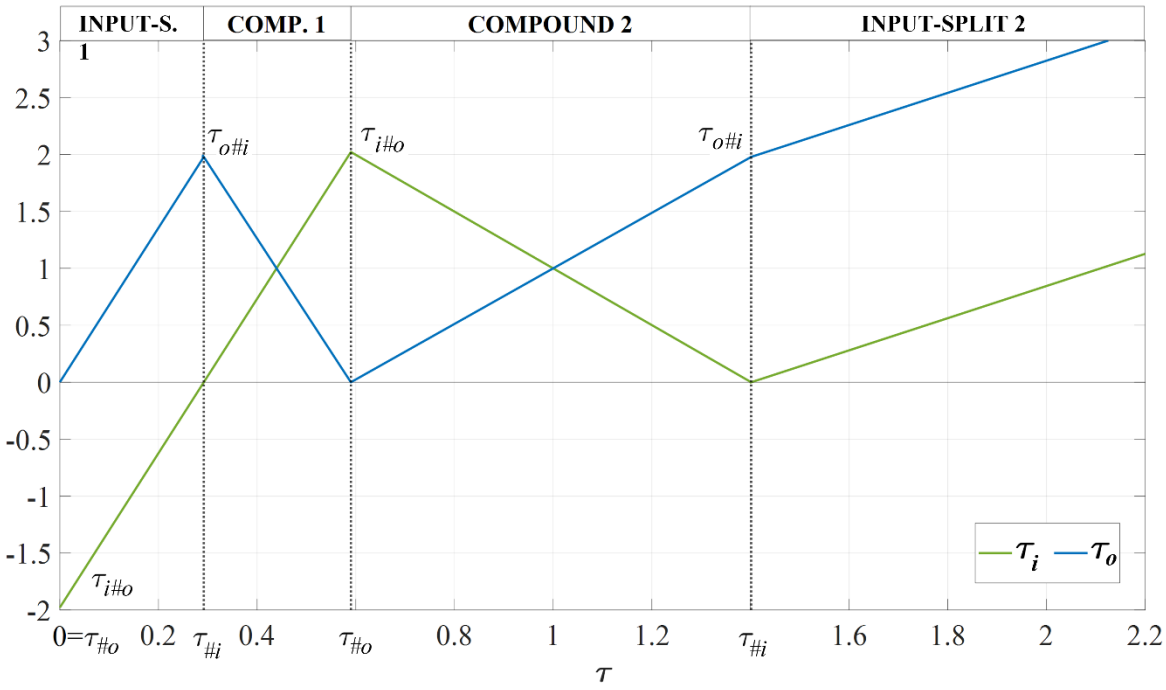

Fig. 3.3. Speed ratios of MG1 (τ_i) and MG2 (τ_o) as functions of the overall speed ratio τ.

Potentially, each power-split mode could be used for any overall transmission ratio τ, but the MGs maximum speed is limited by constructive and technological constraints. Therefore, multi-mode transmissions are arranged to modify the PSU internal connections, implying different functional parameters (Table 3.2) that involve different speed ratios (Fig. 3.3). However, it is advisable to perform the shift from one mode to another when the shafts involved in clutches operation have a null relative speed to prevent clutches from slipping. Hence, a synchronous switch can be realised in correspondence with the mechanical points, whereby one MG is stationary, along with the PSU shaft connected to that MG. Thus, Table 3.2 suggests that the shift between INPUT-SPLIT 1 and COMPOUND 1 should be performed in the common mechanical point $\tau_{\#i} = 0.29$, the shift between COMPOUND 1 and COMPOUND 2 should be performed in $\tau_{\#o} = 0.59$, and the shift between COMPOUND 2 and INPUT-SPLIT 2 should be performed in $\tau_{\#i} = 1.4$.

Moreover, as stated above, fixed-ratio parallel hybrid modes can be achieved in correspondence with the mechanical points. Thus, if the clutches C1 and C2 are engaged along with C4, MG2 is unloaded and $\tau = \tau_{\#o} = 0.59$,. Instead, if the clutches C3 and C4 are engaged along with C1 or C2, MG1 is unloaded and $\tau = \tau_{\#i} = 0.29$ or $\tau = \tau_{\#i} = 1.4$, respectively.

To conclude the kinematic analysis of the transmission, the overall speed ratio whereby PGs operate synchronously was calculated for each power-split mode through Eq. (2.33) and

listed in Table 3.3. The missing values are due to the fact that the PG acts as an OG within that mode, thus it cannot reach the synchronism. Moreover, all the active PGs reach synchronism at the same τ_* in compound-split modes because of the lack of intermediate OGs.

Table 3.3. Overall transmission ratio τ_* whereby the PGs are synchronous.

	INPUT-SPLIT 1	COMPOUND 1	COMPOUND 2	INPUT-SPLIT 2
PG1	0.44	0.44	1.0	2.1
PG2	-	0.44	1.0	-
PG3	-	-	1.0	-

3.2.4 Ideal CVU kinetostatics

The ideal CVU torque ratios were assessed by Eqs. (2.20)-(2.21), equivalent to Eq. (3.18), and plotted as functions of the overall speed ratios τ and the overall apparent efficiency $\eta = -\tau\,\Theta$ in Fig. 3.4 and Fig. 3.5. The contour spacing is 5% for θ_i and 10% for θ_o. The torque on the shaft *i* linked to MG1 expressed as a fraction of the input power is constant for the two input-split modes and equals $-1/\tau_{i_{\#o}} = 0.5$ (Eq. (2.20)). Instead, the absolute value of the normalised torque on the shaft *o* connected to MG2 increases asymptotically in the nearby of the stall condition ($\tau = 0$), even though in Fig. 3.5 it is graphically limited to 2.

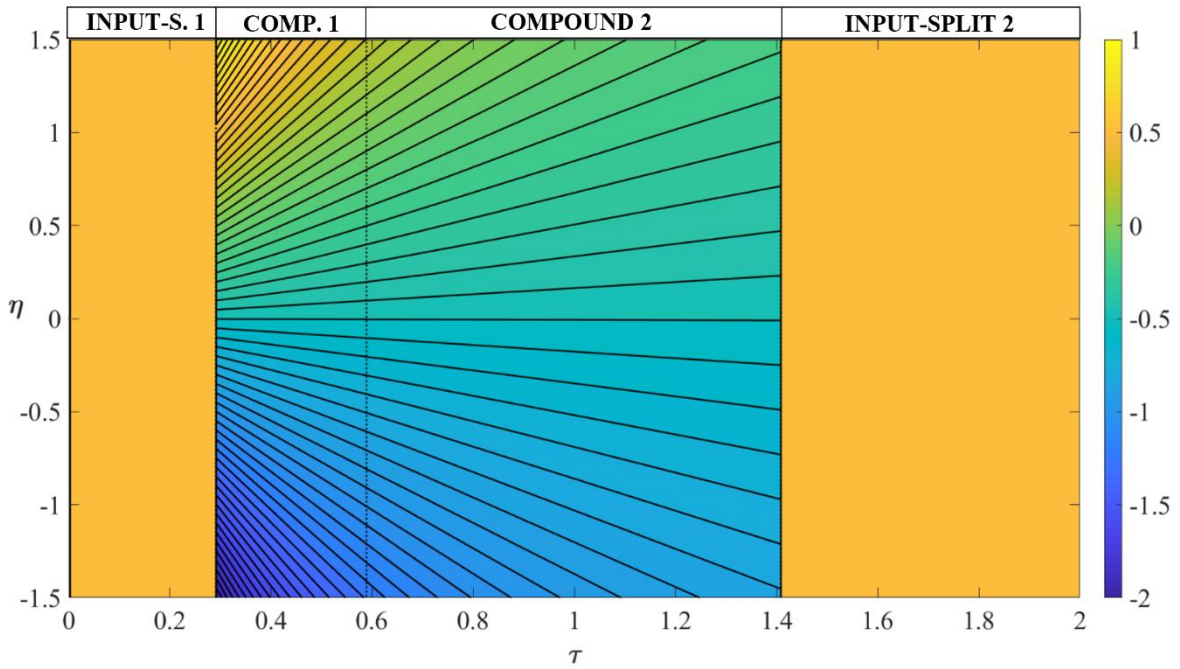

Fig. 3.4. Ideal torque on the shaft *i* as a fraction of the input torque (θ_i).

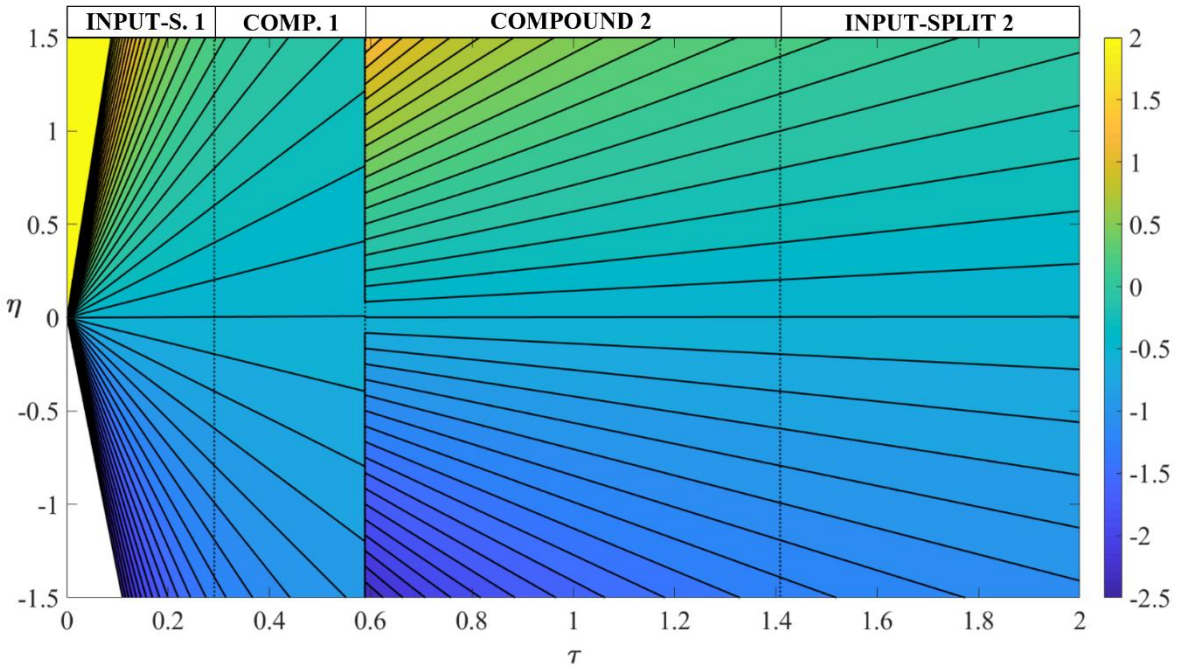

Fig. 3.5. Ideal torque on the shaft *o* as a fraction of the input torque (θ_o).

Then, the ideal power flowing through the CVU shafts was assessed by Eqs. (2.25). In Fig. 3.6 and Fig. 3.7, p_i and p_o are represented as functions of τ and η. In both figures, the contour spacing is 10%. Moreover, according to Eqs. (2.25) and Table 3.2, $p_i = 0$ for $\tau = \tau_{\#i}$ and for $\eta = \tau/\tau_{\#o}$, while $p_o = 0$ for $\tau = \tau_{\#o}$ and for $\eta = \tau/\tau_{\#i}$. Also, the normalised power flowing through the shaft *i* does not depend on the overall apparent efficiency η in the input-split modes whereby $\tau_{\#o} = 0$.

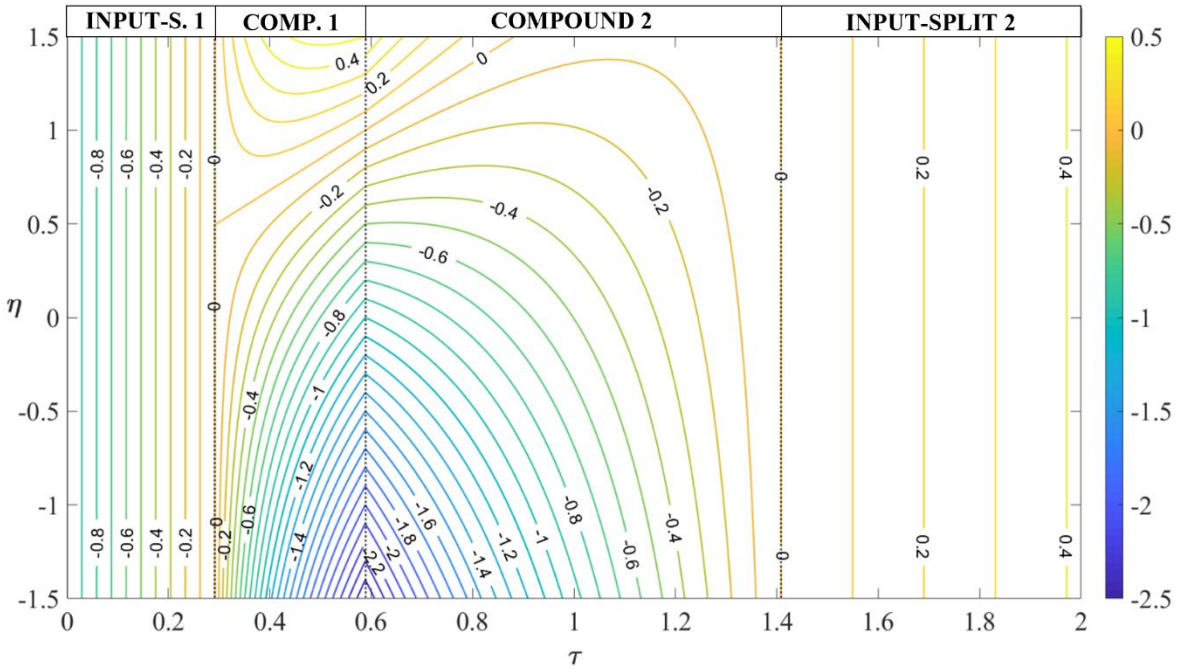

Fig. 3.6. Ideal power flowing through the shaft *i* as a fraction of the input power (p_i).

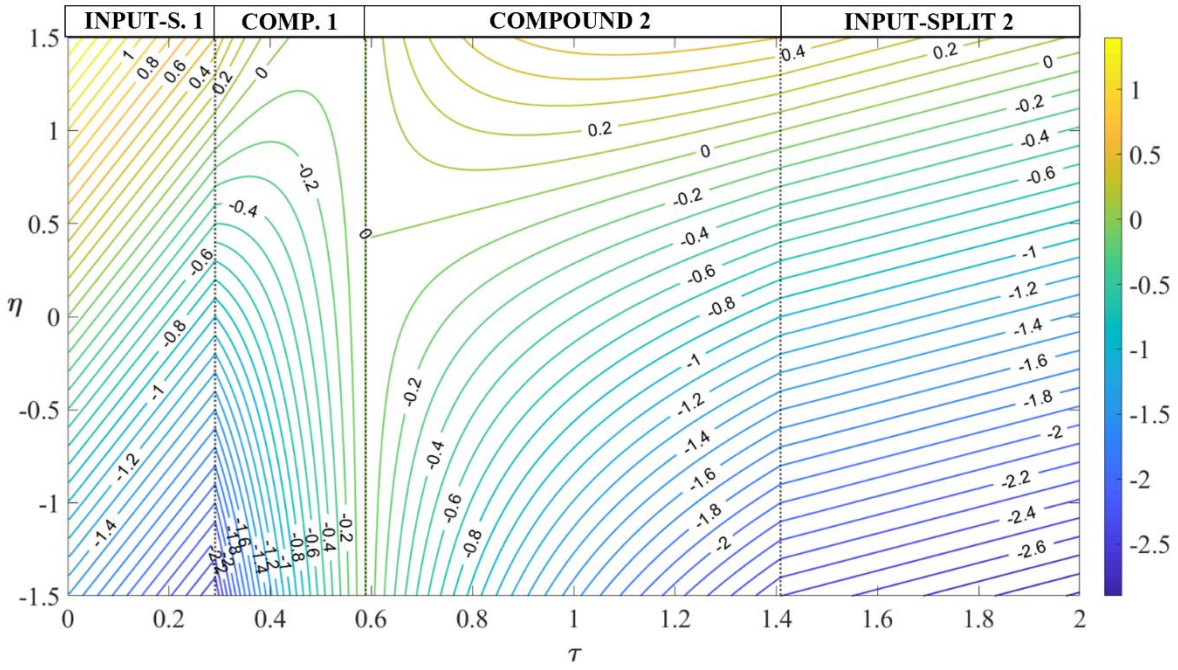

Fig. 3.7. Ideal power flowing through the shaft *o* as a fraction of the input power (p_o).

3.2.5 PSU meshing losses

According to Section 2.4, the total meshing power losses result from the sum of the meshing losses occurring in each PG. Any loss in the clutches is neglected. Thus, the total meshing losses are:

$$\bar{p}_L = \bar{p}_L|_{PG1} + \bar{p}_L|_{PG2} + \bar{p}_L|_{PG3}$$

which were calculated by Eq. (2.40), after labelling each branch of the TPMs as reported in Table 3.4. Nonetheless, any other reference notation could have been chosen for applying Eq. (2.40), since the meshing losses occurring in a PG depend only on the relative speed between two of its branches and on the torques.

Table 3.4. Reference notation of the TPMs shafts for the calculation of meshing losses in power-split modes.

	x	***X***	***y***	***Y***	***z***	***Z***
PG1	*in*	ring	*i*	sun	*n*	carrier
PG2	*n*	carrier	*o*	sun	*i*	ring
PG3	*out*	ring	*n*	sun	*o*	carrier

Therefore:

$$\bar{p}_L|_{PG1} = -\left|(1-\eta^C)\left(\frac{\phi^n_{in/i} - \psi^C_{R/S}}{1-\psi^C_{R/S}}\right)p_{in}\right|$$

$$\bar{p}_L|_{PG2} = -\left|(1-\eta^R)\left(\frac{\phi^i_{n/o}-\psi^R_{C/S}}{1-\psi^R_{C/S}}\right)p_n\right|$$

$$\bar{p}_L|_{PG3} = -\left|(1-\eta^C)\left(\frac{\phi^o_{out/n}-\psi^C_{R/S}}{1-\psi^C_{R/S}}\right)p_{out}\right|$$

The most convenient PSU main port was chosen as *x* for each PG. Indeed, $p_{in} = \bar{p}_{in} = 1$ and $p_{out} = \bar{p}_{out} = -\eta$ by definition. Furthermore, the real power transmitted by the PG1 ring gear equals p_{in} and the real power transmitted by the PG3 ring gear equals p_{out}, owing to the lack of OGs on the involved shafts. On the other hand, the power transmitted by the PG2 carrier can be calculated only in ideal conditions, by the principle of power conservation in the neutral node *n* and Eq. (2.34):

$$p_n|_{PG2} = -\,p_n|_{PG1} - p_n|_{PG3} = p_{in}\cdot\phi^i_{in/n} + p_{out}\cdot\phi^o_{out/n}$$

Table 3.5 summarises the fixed-*Z* apparent efficiencies η^Z and the fixed-*Z* speed ratios $\psi^Z_{X/Y}$ for each PG, based on the functional and constructive layout of the transmission. The basic efficiency was supposed to be slightly lower for PG3 because it has one more gear meshing between the two sets of planet gears.

Table 3.5. Fixed-*Z* apparent efficiencies and fixed-*Z* speed ratios as functions of the basic efficiency η_0 and the Willis ratio Ψ.

	$\boldsymbol{\Psi}$	$\boldsymbol{\eta_0}$	$\boldsymbol{\psi^Z_{X/Y}}$	$\boldsymbol{\eta^Z = \psi^Z_{X/Y}/\bar{\psi}^Z_{X/Y}}$
PG1	-0.505	0.97	Ψ	η_0
PG2	-0.505	0.97	$\dfrac{\Psi}{\Psi-1}$	$\dfrac{\Psi/(\Psi-1)}{\Psi/\eta_0/(\Psi/\eta_0-1)}$
PG3	0.44	0.96	Ψ	η_0

The involved characteristic functions were obtained by Eq. (2.26) using the proper nodal ratios from Table 3.2, as well as $\tau_{\#in} = 10^5$ and $\tau_{\#out} = 0$. The calculation of the power losses led to the power losses map of Fig. 3.8, where the PSU meshing losses are shown as a function of the overall transmission ratio τ and the overall apparent efficiency η. These losses are expressed as a fraction of the input power and the contour spacing is 0.005. In both the compound-split modes, the power losses are minimum for τ = 0.44 and τ = 1, which correspond to the PGs synchronism (see Table 3.3). Nonetheless, for τ = 1 the meshing power losses are null, because all the three PGs operate at synchronism. Instead, for τ = 0.44 the meshing power losses are minimum but not null since only PG1 and PG2 are synchronous, while PG3 operates as an OG.

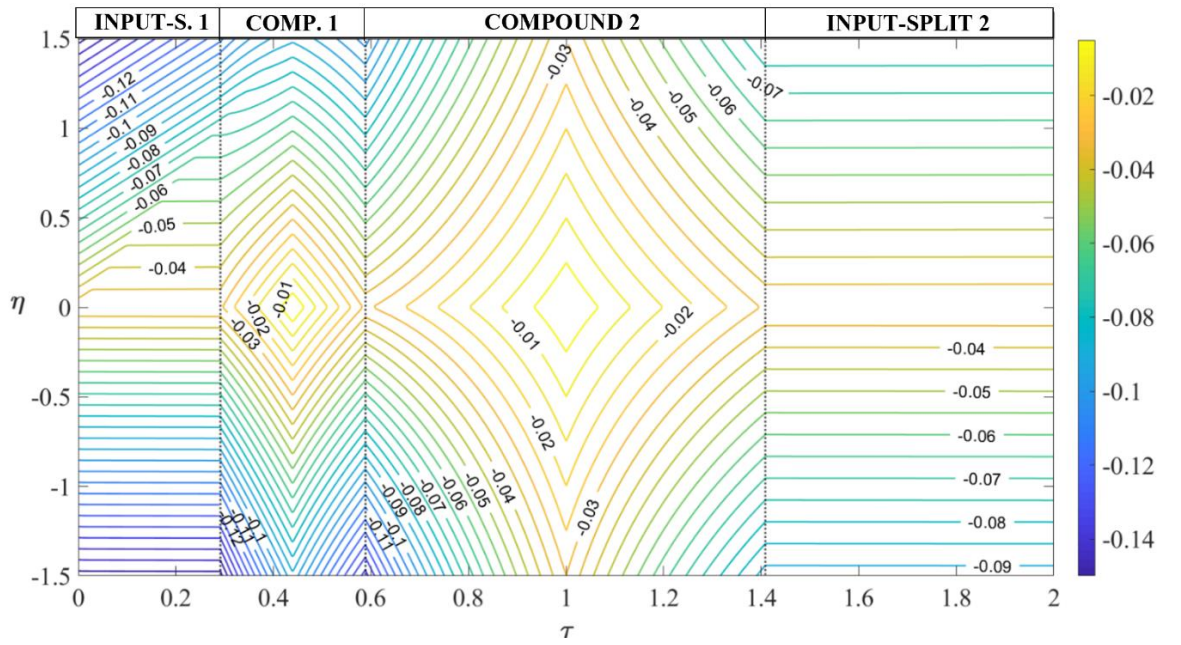

Fig. 3.8. PSU meshing losses in power-split modes as a fraction of the input power ($\bar{p}_L$).

After computing the PSU meshing losses, the resulting power flowing in the CVU shafts was obtained by Eqs. (2.50)-(2.51) and shown in Fig. 3.9 and Fig. 3.10. The contour spacing is 0.1. Although the power losses do not show any discontinuities, their gradient does, owing to a torque or speed reversal in the PSU that would imply a switch in the PGs basic efficiency η_0. Although any a priori prediction of the power flow direction is not required by the adopted approximated method to address the switch of η_0, the physical consistence of the model is confirmed by the results of Fig. 3.9 and Fig. 3.10 and it is mathematically ensured by the absolute value in Eqs. (2.40). The gradient discontinuity is reflected in the real CVU power flows in correspondence with the synchronism or the mode shift.

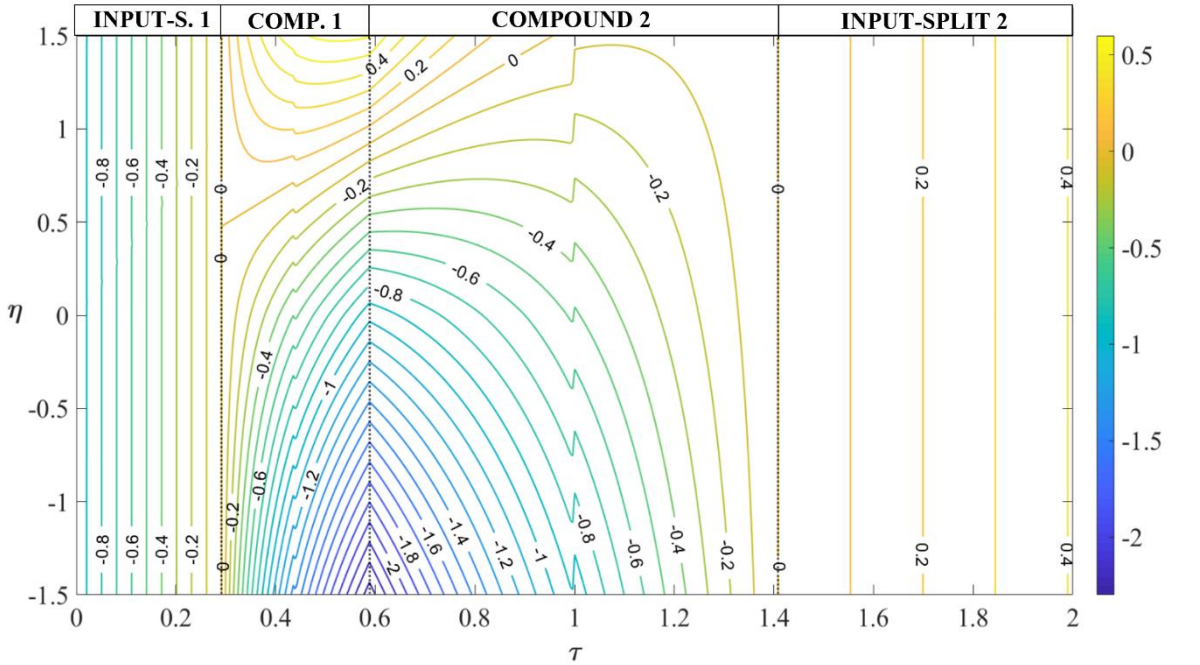

Fig. 3.9. Real power flowing through the shaft *i* as a fraction of the input power ($\bar{p}_i$).

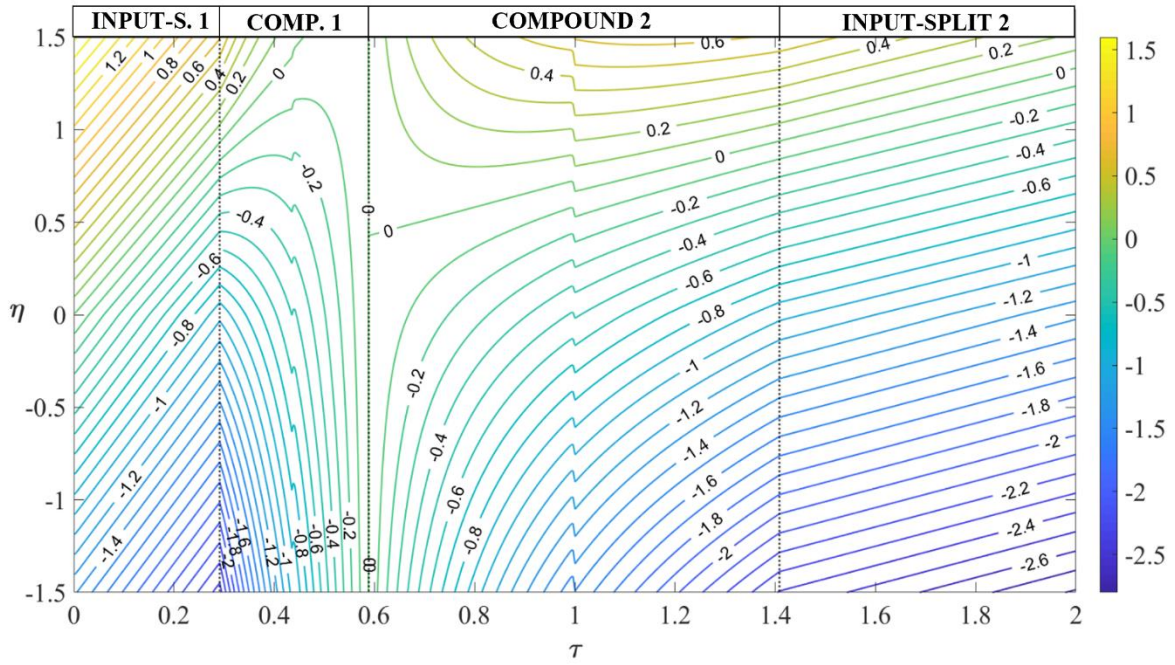

Fig. 3.10. Real power flowing through the shaft *o* as a fraction of the input power ($\bar{p}_o$).

The same discontinuities are detected in the resulting CVU torques, which were calculated by dividing $\bar{p}_i$ by τ_i and $\bar{p}_o$ by τ_o. In Fig. 3.11 and Fig. 3.12, the real CVU normalised torques are represented with a contour spacing of 5% for $\bar{\theta}_i$ and 10% for $\bar{\theta}_o$.

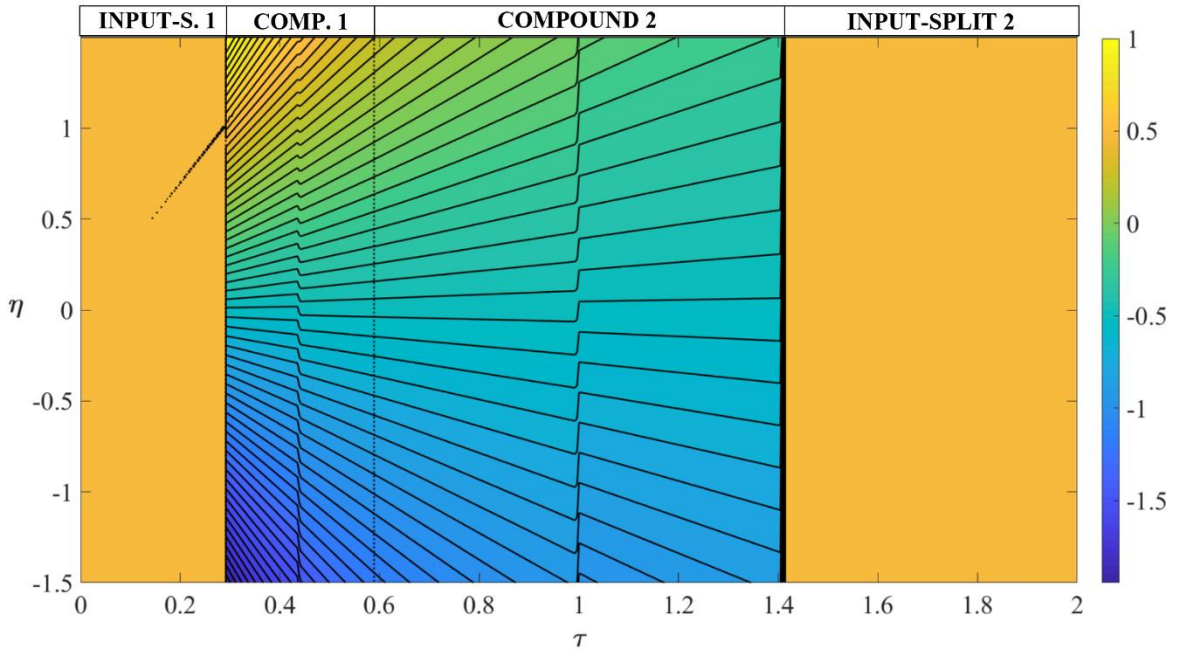

Fig. 3.11. Real torque on the shaft *i* as a fraction of the input torque ($\bar{\theta}_i$).

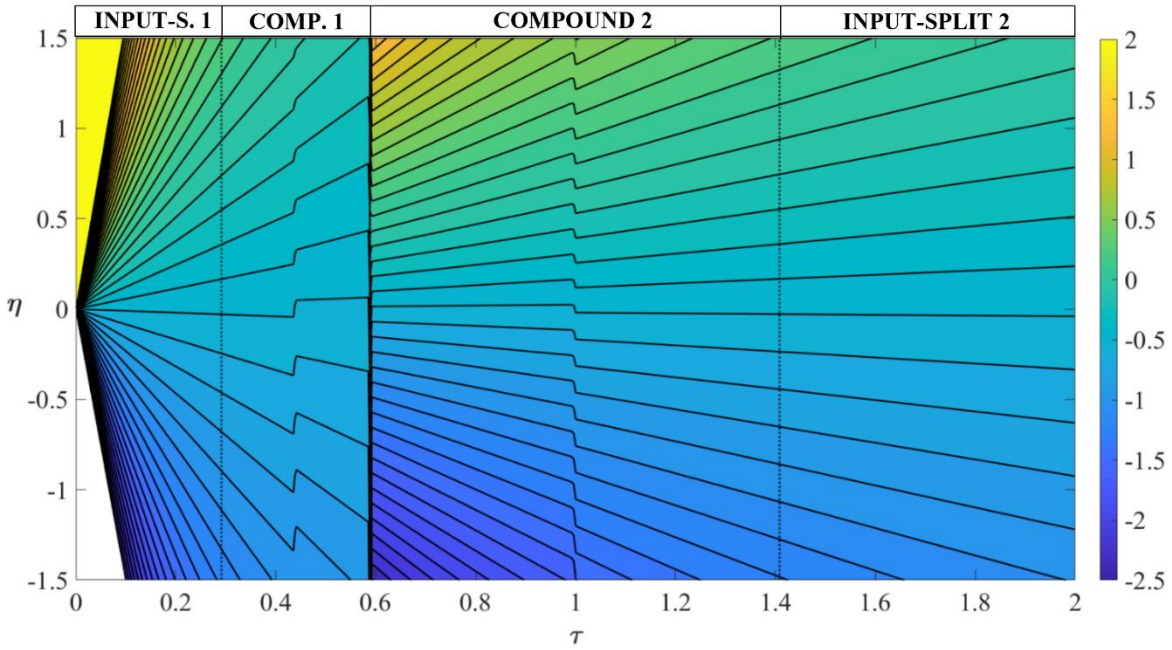

Fig. 3.12. Real torque on the shaft *o* as a fraction of the input torque ($\bar{\theta}_o$).

3.2.6 Analysis in full-electric operation

According to Section 2.5, the same functional parameters related to each power-split mode can be used to evaluate the transmission behaviour in the respective full-electric mode. Hence, this section analyses the four EV modes indicated in Table 3.1 by using the nodal ratios and the corresponding speed ratios of Table 3.2.

The ratios between the speed of electric machines and the output shaft were computed by Eqs. (2.56) and listed in Table 3.6. These speed ratios are constant, thus, imposing ω_{out} implies univocal rotational speeds for both MG1 and MG2. Furthermore, EV 1 and EV 2 achieve the highest speed ratios available among the EV modes, which are very similar to the speed ratio between the MG2 and the output shaft realised during the parallel hybrid operation for $\tau = \tau_{\#i} = 0.29$. Therefore, both EV 1 and EV 2 might be used for providing acceleration at low vehicle speed to comply with the MGs maximum speed. Owing to their kinematics similarity, the choice between EV 1 and EV 2 may depend on the respective PSU meshing losses. On the other hand, the speed ratios of EV 3 and EV 4 are lower, therefore they can be used at higher vehicle speeds. Nonetheless, the speed ratio of EV 4 is the same speed ratio between the MG2 and the output shaft realised during the parallel hybrid operation for $\tau = \tau_{\#i} = 1.4$. Since this fixed-ratio functioning point is exploited for overdrive, EV 4 might not be suitable for full-electric drive whereby the vehicle usually achieves a lower maximum speed, because the MGs would work at an inconveniently low speed. Moreover, MG1 and MG2 rotate at a very similar speed in all EV modes, but in a reverse direction in EV 2 and EV 3.

Table 3.6. Speed ratios in EV modes.

MODE	ω_o/ω_{out}	ω_i/ω_{out}	ω_o/ω_i
EV 1	6.8	6.8	1.0
EV 2	6.8	-6.6	-1.0
EV 3	-2.5	2.4	-1.0
EV 4	1.4	1.4	1.0

The mechanical power losses in EV modes were assessed by the same equations used in Section 3.2.5 computed for $\tau = \tau_{\#in} = 10^5$ and normalised to the opposite of the output power. Moreover, it is advisable to change the reference notation for PG1 according to Table 3.7 to avoid that $x = in$ (see Section 2.5).

Table 3.7. Reference notation of the TPMs shafts for the calculation of meshing losses in EV modes.

	x	***X***	***y***	***Y***	***z***	***Z***
PG1	*i*	sun	*in*	ring	*n*	carrier
PG2	*n*	carrier	*o*	sun	*i*	ring
PG3	*out*	ring	*n*	sun	*o*	carrier

The equations used for calculating power losses are:

$$\bar{p}'_L\big|_{PG1} = -\left|(1-\eta^C)\left(\frac{\phi^n_{i/in} - \psi^C_{S/R}}{1-\psi^C_{S/R}}\right)p'_i\right|$$

$$\bar{p}'_L\big|_{PG2} = -\left|(1-\eta^R)\left(\frac{\phi^i_{n/o} - \psi^R_{C/S}}{1-\psi^R_{C/S}}\right)p'_n\right|$$

$$\bar{p}'_L\big|_{PG3} = -\left|(1-\eta^C)\left(\frac{\phi^o_{out/n} - \psi^C_{R/S}}{1-\psi^C_{R/S}}\right)p'_{out}\right|$$

where $p'_{out} = \bar{p}'_{out} = -1$, while $p'_i\big|_{PG1}$ and $p'_n|_{PG2}$ must be assessed by combining Eq. (2.34) with the principle of power conservation:

$$p'_i\big|_{PG1} = p'_i - p'_i\big|_{PG2} = p'_i + \phi^n_{o/i}\cdot p'_o\big|_{PG2} = p'_i + \phi^n_{o/i}\cdot\left(p'_o - p'_o\big|_{PG3}\right) = \\ = p'_i + \phi^n_{o/i}\cdot\left(p'_o + \phi^n_{out/o}\cdot p'_{out}\right)$$

$$p'_n|_{PG2} = -p'_n|_{PG1} - p'_n|_{PG3} = p'_i\big|_{PG1}\cdot\phi^{in}_{i/n} + p'_{out}\cdot\phi^o_{out/n}$$

Fig. 3.13 shows the power losses as a function of $p'_o = -P_o/P_{out} = \bar{p}'_o$; Fig. 3.14 shows the resulting CVU power flows, whereby $\bar{p}'_i = 1 - \bar{p}'_L - \bar{p}'_o$. Fig. 3.13 suggests that EV 1 should be preferred to EV 2 for lower vehicle speeds because of the lower power losses. Furthermore, the power losses occurring in EV 1 are constant, therefore the PSU mechanical efficiency is not affected by the power rates provided by each motor. EV 4 is the most

efficient mode, thus, where possible, it should be preferred to EV 3, which, on the contrary, is the least efficient. However, as stated before, EV 4 might be unsuitable for the full-electric drive, thus the exploitation of EV 3 for the highest vehicle speeds may be unavoidable.

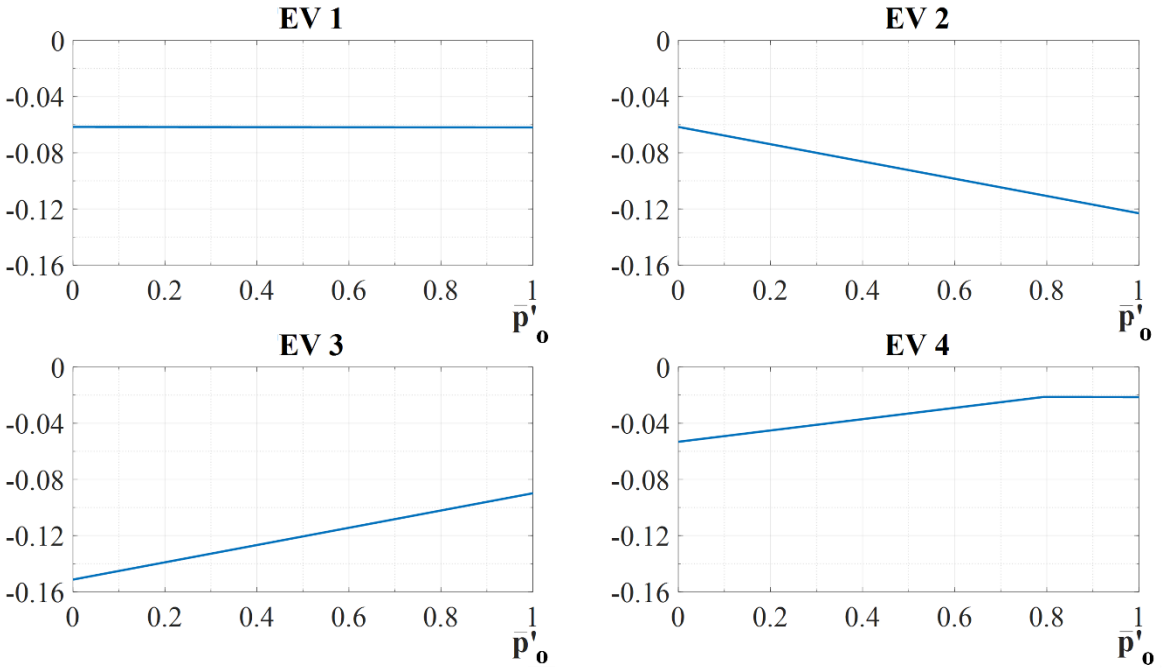

Fig. 3.13. PSU meshing losses in EV modes as a fraction of the output power ($\bar{p}'_L$).

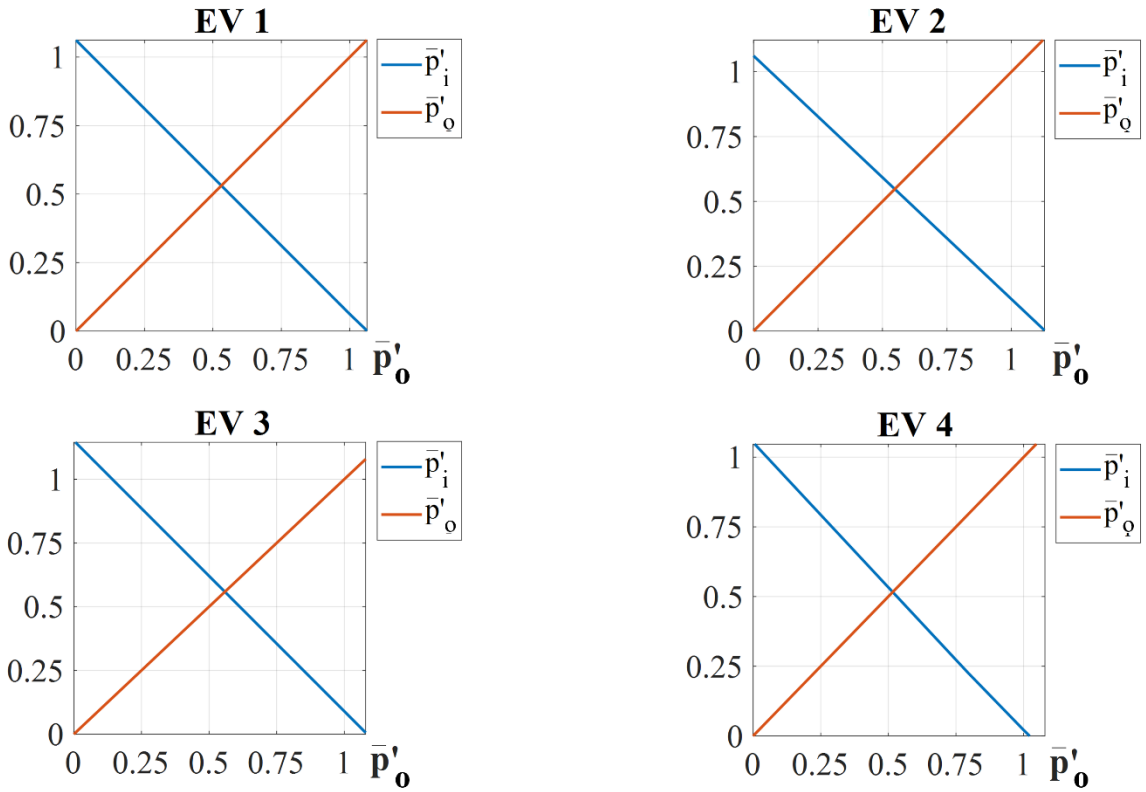

Fig. 3.14. Real CVU power flows in EV modes as a fraction of the output power.

CHAPTER 4
FUNCTIONAL DESIGN OF PS-CVTS

The generality of the parametric model described in Chapter 2 enables a hierarchical and modular procedure for the design of the power-split powertrain.

As addressed in Section 3.1, the functional parameters of an existing PSU are univocally defined; however, the same set of functional parameters can be achieved by several constructive arrangements. The variation of the PS-CVT constructive layout results in a variation of the numerical value of the functional parameters underpinning the model described in Chapter 2, and not in the form of the basic equations, which are universal. Indeed, modelling the PSU as a four-port mechanism whose kinematics and kinetostatics are univocally defined by the only functional parameters enables the assessment of the speed, torque and power ratios among the PSU external ports before the PSU constructive arrangement has been defined. Similarly, the consideration of the three-port mechanisms as core units of the PSU and the use of their characteristic functions allows the designer to model the global PSU kinematics before the synthesis of the PGs and OGs included in the PSU.

As a result, the enabled design procedure consists of subsequent phases which are decoupled one from another so as to optimize the ICE, the electric machines, and the gear trains without any mutual interference. Moreover, in contrast to the mere explorative approach usually adopted in the literature, the designer oversees the physical consistency of their decisions through the whole design process. Indeed, the proposed approach allows the prioritisation of the selection of the mechanical points to minimise the size of the electric unit, which is usually the most expensive equipment. This is possible because the only mechanical points are sufficient to fully define the power flows of the electric unit (see Eqs. (2.22), (2.23), (2.25)). Hence, the electric MGs can be selected. The same mechanical points lead to the definition of the PSU kinematics and to the exploitation of a PSU design chart, by which the PGs Willis ratio can be chosen to achieve the PGs synchronism within the desired PSU working range. In this way, since the meshing losses in a PG are null at its synchronism, they are minimised within the whole working range. Lastly, selecting the corresponding speed ratios leads to the sizing of the OGs necessary to comply with the maximum speed and torque of the electric MGs.

A design procedure for PS-CVTs based on the parametric model was introduced in [95],

where a numerical example of a PSU design was provided. The proposed design procedure is suitable for the functional design of a single-mode shunt and compound PSU with up to two TPMs. However, sizing and operations of the ICE and electric machines were not considered. Furthermore, the terminology and the mathematical treatment used in [95] were not aligned with the unified formulation presented in Chapter 2. In [148], the parametric model was used to design an automotive power-split transmission. Within the research described in this dissertation, the modular and hierarchical design procedure presented in [95] has been applied to hybridise an oil drilling rig and recover energy braking during the gravity-driven lowering phases.

Soil drilling is a very energy-consuming process [149], where the energy efficiency can be enhanced in several ways, including the improvement of the drill bit material [150], the implementation of a proper control strategy to increase the engine efficiency [151], and the embedding of an energy storage system to modulate the peak power requested to the engine [152–154]. In addition, the release of gravitational energy during the lowering phases of drilling, tripping in, and casing can be exploited by avoiding completely dissipative braking but recovering part of the braking power hydraulically [155], mechanically [156], or electrically [157,158]. Nonetheless, the literature analysis has revealed that this is the first power-split electric hybridisation of a drilling rig for this purpose.

The results reported in this chapter were presented in [140]. The modular and hierarchical procedure for the design of PS-CVTs is reported in Section 4.1. The design requirements of the addressed case study are presented in Section 4.2, where the oil drilling rig to hybridise is described. The results of the research are presented in Section 4.3; two solutions differing in the ICE size are proposed and discussed.

4.1 A modular parametric design for PS-CVTs

The design procedure addressed in this chapter aims to synthesise the best power-split powertrain to fulfil some functional and constructive requirements, which determine the desired range of variation for the overall speed ratio τ and the overall power ratio $-\eta$. The operating range of the power-split powertrain depends on the desired operations of the system to hybridise and on the characteristics of thermal and electric actuators. Nevertheless, these design requirements are usually identifiable before the transmission design process. After this preliminary analysis, a hierarchical and modular approach for the design of the power-split powertrain can be achieved through the following steps:

1) selection of the mechanical points and electric machines power size;
2) synthesis of planetary gearing through a PSU design chart;

3) selection of the corresponding speed ratios;
4) synthesis of ordinary gearing.

4.1.1 Selection of the mechanical points

From Eqs. (2.25), which can be rearranged as in Eqs. (4.1)-(4.2), the power flows of the electric machines (P_i and P_o) are ruled only by the mechanical points:

$$P_i = \frac{(\tau - \tau_{\#i})(\tau - \eta\,\tau_{\#o})}{\tau(\tau_{\#i} - \tau_{\#o})} P_{in} \tag{4.1}$$

$$P_o = \frac{(\tau - \tau_{\#o})(\tau - \eta\,\tau_{\#i})}{\tau(\tau_{\#o} - \tau_{\#i})} P_{in} \tag{4.2}$$

As a result, within the desired range of variation of τ and η, selecting the mechanical points involves a univocal range of variation of the power flowing through the electric unit. Therefore, selecting the combination of mechanical points that minimises the power of the electric MGs could be particularly cost-effective given the high prices of electric equipment.

Nevertheless, as addressed in [148], selecting a proper control strategy is crucial to carry out an optimisation process aimed at assessing the best mechanical points to pursue a downsizing of the involved actuators while complying with the desired performance. In particular, during the selection of the optimal mechanical points, two different assumptions can be considered in order to minimise the power size of the electric unit:

- $P_o = -P_i$, whereby the ICE only supplies the total power required in output;
- $P_o = P_i$, whereby the ICE power is higher or lower than the required one, resulting in battery recharging or discharging, respectively.

Moreover, given that in correspondence with a mechanical point the power flowing in one electric machine is null, it would be advisable to narrow the operating range as close as possible to the mechanical points. In this way, the electromechanical conversions and the related power losses would be reduced and the overall efficiency improved. However, this would result in a limited working range; thus, only implementing a multi-mode transmission enables the achievement of both lower CVU size (and thus lower conversion losses) and an extended range of the overall transmission ratio.

In this regard, as addressed in Section 2.3, the number of nodal ratios available in the design stage equals the number of TPMs in the PSU. Thus, for a two-PG compound PSU, both mechanical points can be freely selected, while for a shunt PSU, only one. Indeed, in an input-split transmission where the MG1 speed (or MG2) is proportional to the output speed, only $\tau_{\#o}$ (or $\tau_{\#i}$) can be freely chosen since $\tau_{\#i} = 0$ (or $\tau_{\#o} = 0$). Similarly, in an output-split transmission where the MG1 speed (or MG2) is proportional to the input speed, only $\tau_{\#o}$ (or $\tau_{\#i}$) can be freely chosen since $\tau_{\#i} = \infty$ (or $\tau_{\#o} = \infty$). If the PSU includes more

than two TPMs, further nodal ratios than the two mechanical points should be defined; however, since the electric CVU has two degrees of freedom, only two nodal ratios, i.e., the two mechanical points, are sufficient to completely define the CVU power flows (Eqs. (4.1)-(4.2)). Therefore, deploying more than two TPMs does not affect the ideal power flows, but it is useful to realise multi-mode transmissions to extend the optimal operating range of the PS-CVT. However, the design problem of multi-mode PS-CVTs has not been included within the scope of this research and the design procedure described in this section is suitable only for single-mode PS-CVTs with up to two TPMs.

4.1.2 Synthesis of planetary gearing: the PSU design chart

According to Eq. (2.30), the characteristic function $\phi^{z}_{x/y}$, defined in Eq. (2.26), computed for the transmission ratio τ_* corresponding to the synchronous condition of a PG, equals the PG Willis ratio if the PG carrier is connected to the main port z, the ring gear to the main port x, and the sun gear to the main port y. This property enables a straightforward procedure to select the constructive parameters of the PGs and their synchronous point through a PSU design chart.

After establishing the nodal ratios in a proper number depending on the number of the involved PGs, it is possible to compute the totality of the characteristic functions related to all the available TPM configurations (see Eq. (2.31)), which differ one from each other for the involved PSU main ports and for the linkage among the PSU main ports and the PG branches. Hence, all the characteristic functions can be plotted in a PSU design chart, as functions of the overall transmission ratio τ.

The PSU design chart is an intelligible tool that enables the designer to synthesise the PGs by selecting their Willis ratio within a desired range and imposing their synchronism for whichever τ. To this purpose, it is sufficient to select one point from one or more characteristic functions plotted on the design chart, depending on the number of TPMs; the abscissa of the selected point represents the transmission ratio τ_* corresponding with the PG synchronism, while the ordinate is the PG Willis ratio. The subscripts of the selected characteristic function determine the connection of the PG carrier (linked to *z*), ring gear (linked to *x*), and sun gear (linked to *y*) with the PSU main ports. Two PGs having the same carrier position but swapped positions for the sun and the ring gears are constructively the same PG, even though their Willis ratios are one the reciprocal of the other one.

The constructive layout of the PS-CVT is determined by the combination of the subscripts of the selected curves on the PSU design chart. In particular, a shunt PS-CVT involves only one PG, therefore one point must be selected from one curve out of the 24 available

obtainable by considering all the four PSU eternal shafts — some of which are overlapped because two speeds are proportional. For a compound PS-CVT, the number of points to be chosen is the same as the number of TPMs involved in the transmission. The subscripts common to two or more selected characteristic functions indicate the label of the shafts attached to the same isokinetic joint. For a PS-CVT including three or more TPMs, the design procedure is more complicated. Firstly, the number of the available characteristic functions grows factorially — e.g., there are 60 characteristic functions for three-TPM compound-split CVT, according to Eq. (2.31). Secondly, the label of each PSU main shaft must appear at least once among the chosen characteristic functions, instead, the label of each neutral node must appear at least twice. Lastly, each label cannot appear more times than the number of TPMs, since the latter establishes the maximum number of shafts converging in an isokinetic joint.

The advantages of the graphical procedure enabled by the PSU design chart are various. First, the PGs synthesis is performed without directly involving the OGs, which do not need to be synthesised beforehand. Furthermore, plotting only the characteristic functions comprised within the desired Willis ratio range (usually $-2/3 \div -1/3$) enables to automatically discard less efficient or not feasible constructive solutions (see [83,95]). Also, selecting the PGs synchronism within the actual working range increases the transmission mechanical efficiency (see Section 2.4). Lastly, selecting two or more points corresponding to the intersection of two or more curves allows the deployment of PGs with the same Willis ratio and synchronous point, reducing the transmission complexity and cost. In this regard, the paper [96] has proved that the adoption of the PSU design chart could have led to a more cost-effective arrangement of the PSU of the Chevrolet Volt; indeed, it would have been possible to include two identical PGs instead of the two different PGs deployed by the manufacturer while maintaining the same PGs synchronous ratio.

4.1.3 Selection of the corresponding speed ratios

The corresponding speed ratios rule the speed and torque ratios at the PSU ports along with the nodal ratios. Indeed, according to Eqs. (2.12)-(2.13), the MG1 and MG2 speeds are:

$$\omega_i = \tau_{i\#o} \frac{\tau - \tau_{\#i}}{\tau_{\#o} - \tau_{\#i}} \omega_{in} \tag{4.3}$$

$$\omega_o = \tau_{o\#i} \frac{\tau - \tau_{\#o}}{\tau_{\#i} - \tau_{\#o}} \omega_{in} \tag{4.4}$$

While, according to Eqs. (2.20)-(2.21), the torques on the shaft connected to the electric unit are:

$$T_i = \frac{\eta\,\tau_{\#o} - \tau}{\tau \cdot \tau_{i\#o}} T_{in} \tag{4.5}$$

$$T_o = \frac{\eta\,\tau_{\#i} - \tau}{\tau \cdot \tau_{o\#i}} T_{in} \tag{4.6}$$

Consequently, the corresponding speed ratios should be selected to comply with the speed and torque constraints imposed by the operating range of the ICE and electric machines. As shown in Eqs. (4.3)-(4.6), the speed and torque on the shaft i are ruled by the corresponding speed ratio $\tau_{i\#o}$, while $\tau_{o\#i}$ affects the speed and torque on the shaft o.

In a shunt PS-CVT, where only one mechanical point is proper (see Section 2.1.1), Eqs. (4.3)-(4.6) can be simplified. Recalling that $\tau = \omega_{out}/\omega_{in}$ and $\eta = -(\omega_{out}T_{out})/(\omega_{in}T_{in})$, in an input-split layout (see Fig. 2.4), supposing that the shaft o is directly coupled with the shaft out, it is $\tau_{\#o} = 0$; then:

$$\omega_i = -\frac{\tau_{i\#o}}{\tau_{\#i}}(\omega_{out} - \tau_{\#i}\omega_{in}) \tag{4.7}$$

$$\omega_o = \frac{\tau_{o\#i}}{\tau_{\#i}}\omega_{out} \tag{4.8}$$

$$T_i = -\frac{1}{\tau_{i\#o}} T_{in} \tag{4.9}$$

$$T_o = -\frac{\tau_{\#i}T_{out} + T_{in}}{\tau_{o\#i}} \tag{4.10}$$

In an output-split layout (see Fig. 2.4), supposing that the shaft o is directly coupled with the shaft in, it is $\tau_{\#o} = \infty$ and $\tau_{i\#o} = \infty$; then, by performing the limit of Eqs. (4.3)-(4.6), it is:

$$\omega_i = \frac{\tau_{i\#o}}{\tau_{\#o}}(\omega_{out} - \tau_{\#i}\omega_{in}) \tag{4.11}$$

$$\omega_o = \tau_{o\#i}\omega_{in} \tag{4.12}$$

$$T_i = -\frac{\tau_{\#o}}{\tau_{i\#o}} T_{out} \tag{4.13}$$

$$T_o = -\frac{\tau_{\#i}T_{out} + T_{in}}{\tau_{o\#i}} \tag{4.14}$$

Note that the ratio $\tau_{i\#o}/\tau_{\#o}$ in Eqs. (4.11) and (4.13) is finite; physically, it depends on the PG Willis ratio and the OGs constructive ratio; mathematically, it is the result of the limit of the ratio between two infinite quantities. During the selection of the corresponding speed ratios in the design of an output-split transmission, the ratio $\tau_{i\#o}/\tau_{\#o}$ is the free parameter to comply with the constraints on MG1 speed and torque (see Section 4.3.1.3).

From Eqs. (4.7)-(4.10) related to the input-split layout, it is apparent that the speed ω_o of the CVU shaft directly coupled with the shaft out is directly proportional to the PSU output speed ω_{out} depending on the corresponding speed ratio $\tau_{o\#i}$, while the speed ω_i of the other

CVU shaft is a linear combination of ω_{out} and ω_{in}; on the contrary, T_o is a linear combination of T_{out} and T_{in}, while T_i is directly proportional to the PSU input torque T_{in} depending on the corresponding speed ratio $\tau_{i\#o}$. Thus, an input-split layout is an output-coupled PS-CVT kinematically, but an input-coupled PS-CVT kinetostatically.

Similarly, in the output-split arrangement (Eqs. (4.11)-(4.14)), the speed ω_o of the CVU shaft directly coupled with the shaft in is directly proportional to the PSU input speed ω_{in} depending on the corresponding speed ratio $\tau_{o\#i}$, while the speed ω_i of the other CVU shaft is a linear combination of ω_{out} and ω_{in}; on the contrary, T_o is a linear combination of T_{out} and T_{in}, while, T_i is directly proportional to the PSU output torque T_{out} depending on the ratio $\tau_{i\#o}/\tau_{\#o}$. Thus, an output-split layout is an input-coupled PS-CVT kinematically, but an output-coupled PS-CVT kinetostatically.

4.1.4 Synthesis of ordinary gearing

After selecting the nodal ratios and the corresponding speed ratios, the PSU kinematics is fully characterised. The OGs on each TPM branch must be synthesised to ensure that the kinematic constraints are satisfied during PG synchronism, as demonstrated in [95]. Therefore, the fixed ratios of the OGs belonging to the same TPM are ruled by the following equations, equivalent to Eqs. (2.32):

$$\frac{k_x}{k_y} = \left.\frac{\omega_x}{\omega_y}\right|_{\tau_*} ; \qquad \frac{k_x}{k_z} = \left.\frac{\omega_x}{\omega_z}\right|_{\tau_*} \tag{4.15}$$

After calculating the ratios of Eqs. (4.15), one OG can be chosen arbitrarily, e.g., equal to 1 to simplify the constructive arrangement, while the others are assessed subsequently. Further strategies for pursuing constructive simplicity, especially in a compound-split layout, are suggested in [95]. For instance, two or more OGs linked to the same main shaft but belonging to different TPMs can be merged into a unique one. Moreover, selecting two PGs with the same synchronous point leads to a further constructive simplification, since Eqs. (4.15) return the same ratio if the two TPMs share two isokinetic joints.

In a shunt PS-CVT, which is constructively made up of a single TPM, the consideration of the simultaneous existence of two TPMs having the same PG (and thus mechanical points) but different corresponding speed ratios is useful to ensure two degrees of freedom in the selection of the corresponding speed ratios to comply with the MGs constraints of speed and torque. In this way, three equations as those in Eq. (4.15), taken so as to include each of the four OGs on the PSU main ports at least once, are sufficient to define the PSU OGs. By way of example, in an input-split transmission where the shaft o is directly coupled to the shaft out, the two TPMs to be considered are those connected to the shafts in, i, and out, and

those connected to the shafts in, i, and o.

4.2 Case study on an oil drilling rig: description and operations

The oil drilling rig considered as a case study in this research is the Drillmec MR-8000 [159]: a mobile self-propelled rig with a maximum static hook load of 200 tons and a maximum drilling depth of 3000 m. Since this research aims to hybridise the drilling rig to recover braking energy, only the hoisting system is described in more detail in this section. Other subsystems are deployed in the plant, such as the mud pumping system, the hydraulic top drive providing the rotative drilling torque, and auxiliary equipment for lubrication, drill pipe handling, and casing pipe cementation; however, these subsystems are powered by different powertrains than the one that feeds the hoisting system.

The hoisting mechanism under analysis, shown in Fig. 4.1, relies on a drawworks, namely, a large winch that reels out and in the drilling line in a controlled fashion. The drilling line is winded on the crown block and the travelling block. The latter carries a block made up of the top drive and the hook, which raises or lowers the drilling stem. The raising phases are powered by two diesel engines with 403 kW rated power each. The power flows of the prime movers combine together in an engine coupler and then in a chain box connected to the winch. The lowering phases are gravity-driven, and a brake system ensures the adequate descending speed of the drill stem. However, introducing an electric unit upstream of the drawworks would enable regenerative braking instead of dissipative friction braking to recover energy while the drill stem is lowered into the wellbore. Thus, this research aims to replace the diesel prime movers and the compound block with a hybrid electric power-split powertrain (see Fig. 4.1) to recover braking energy and reduce the thermal power needed thanks to the addition of the battery as a further power source. Therefore, a design requirement of this work is to keep only one diesel ICE in the hybridised rig. Moreover, the power-split unit decouples the ICE speed from the winch speed; hence, the ICE is potentially capable of continuously operating within the most efficient range.

To design the power-split transmission, it is essential to know the speed, torque, and power required on the output shaft. For this purpose, a 3000 m deep drilling was simulated, with intermediate casing at 500, 1500, and 2500 m. The series of operations required to perform and complete an intermediate casing are the following:

1) DRILLING: the drill string is slowly lowered into the wellbore while the top drive provides the drill bit with the torque to drill. When the drilling depth equals the drill

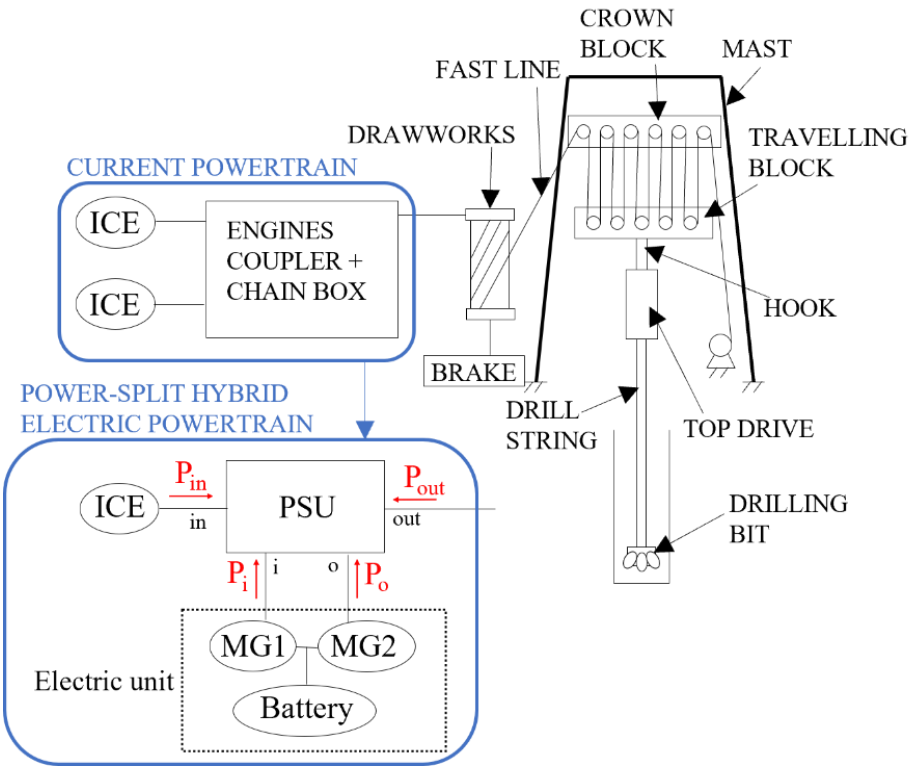

Fig. 4.1. Drillmec MR-8000 hoisting system and drawworks prime movers before and after hybridisation. The arrows show the positive power flows.

string length, the drill string is blocked into the wellbore while the top drive and hook block alone is raised to attach two more drill pipes and resume drilling.

2) TRIP-OUT: when the desired casing depth is reached, the top drive and hook block is raised to pull out of the hole the drill string. When a double stand of drill pipes comes out of the wellbore, it is removed from the top drive and hook block, which is lowered to lift the remaining drill string.
3) CASING: a joint of two casing pipes is lowered into the wellbore; then, the top drive and hook block is raised to pick up another joint and repeat the operation. When the casing pipes into the wellbore reach the bottom of the wellbore, they are cemented.
4) TRIP-IN: the drill string is run into the hole, starting from the drill collars, which are thicker than the drill pipes to provide the weight on the bit. When a double stand of drill collars or drill pipes is completely lowered into the wellbore, the top drive and hook block is raised to pick up another double stand and repeat the operation until the drill string occupies the whole wellbore length. Then, the drilling phase can restart.

To simplify the analysis, a realistic constant speed is assumed for the top drive and hook block in each phase, shown in Table 4.1 and derived from [149].

Table 4.1. Speed of the top drive and hook block in each phase.

Phase	Hook speed [m/s]
Drilling	0.002
Trip-out/-in	−0.2/0.2
Casing	0.1
Unladed lowering/raising	0.8/−0.8

The hook load was simulated by considering the weight of the hook, the top drive, the casing pipes during the casing phase, and the drill collars and drill pipes during the tripping phases, reduced by the weight on the bit and the buoyancy factor due to the immersion in drilling fluid during the drilling phase. The constructive parameters used in this analysis are reported in Table 4.2 and derived from [149]. Any inertial effects or other disturbances were neglected.

Table 4.2. Constructive parameters of the drill string.

Weight of top drive and hook block	16.5 t
Weight on the bit	5 t
Buoyancy factor	0.8
Drill collar and drill pipe length	9.5 m
Drill collars specific weight	225 kg/m
Drill pipes specific weight	33 kg/m
Casing pipe length	7.5 m
Casing pipe specific weight (up to 500 m)	160 kg/m
Casing pipe specific weight (up to 1500 m)	90 kg/m
Casing pipe specific weight (up to 2500 m)	60 kg/m
Casing pipe specific weight (up to 3000 m)	40 kg/m

From data in Table 4.1 and Table 4.2, the linear speed, force, and power on the hook can be assessed and then reduced in terms of rotational speed, torque, and power on the PSU output shaft. The results shown in Figs 4.2–4.4 were obtained by considering the overall transmission ratio of 0.008 m between the hook and the PSU output shaft and the overall efficiency of 0.845, assessed from the actual constructive characteristics of the hoisting system upstream of the hook. From a simplified perspective, we omitted any bit trip for inspection and replacement of a worn or underperforming drill bit; nevertheless, it would have implied additional pull-out-of-the-hole and run-into-the-hole phases during drilling.

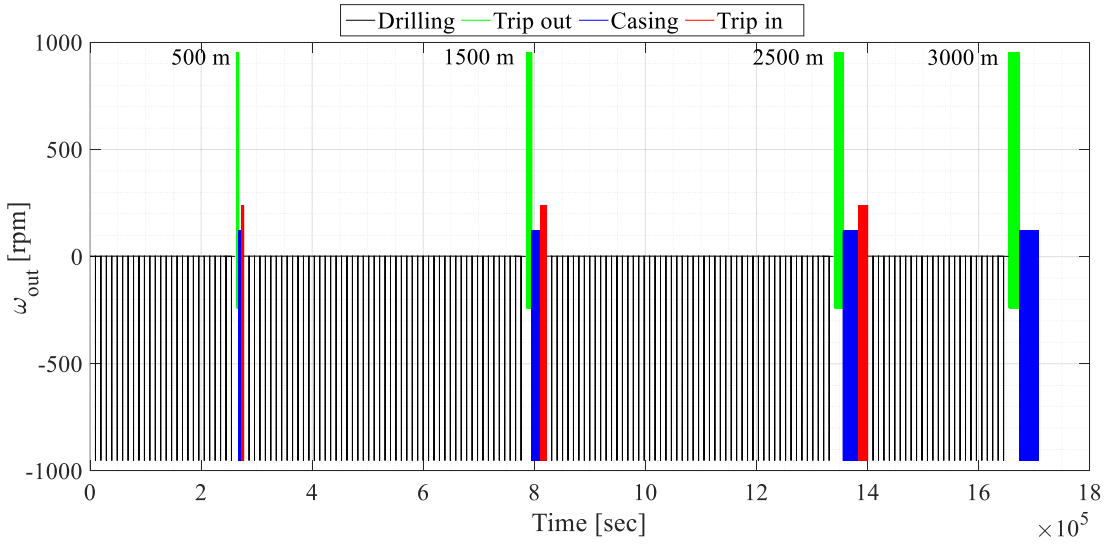

Fig. 4.2. Speed of the PSU output shaft.

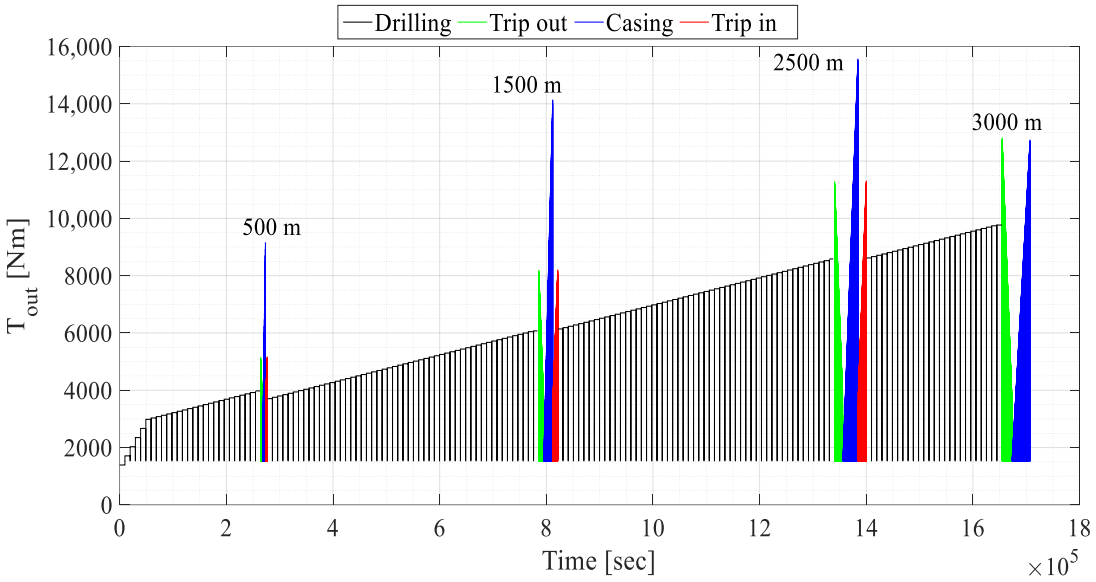

Fig. 4.3. Torque on the PSU output shaft.

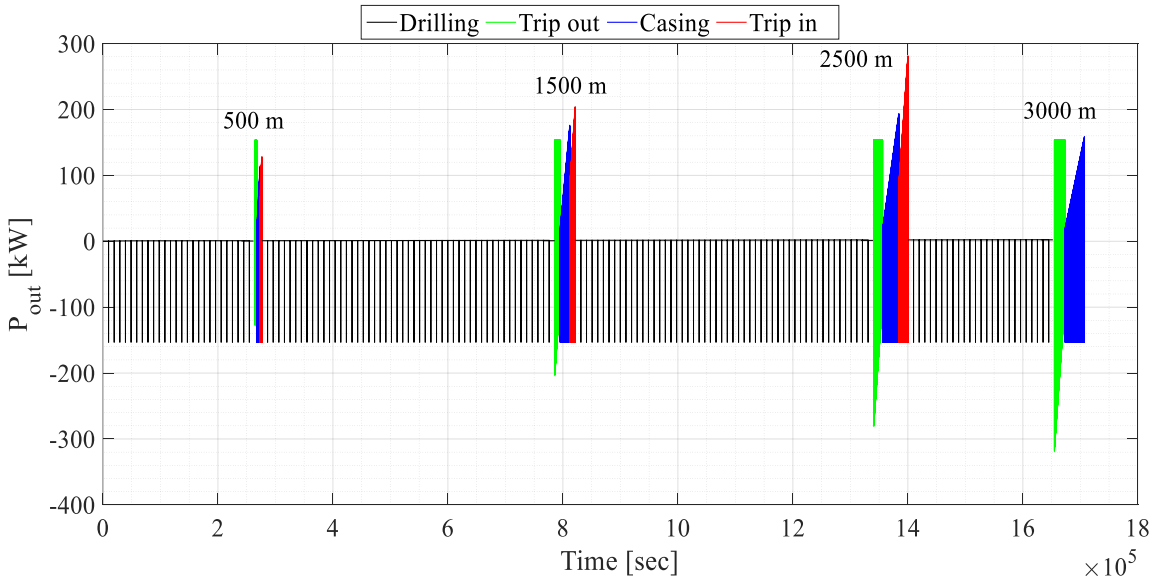

Fig. 4.4. Power through the PSU output shaft.

On the basis of the red arrows in Fig. 4.1 showing that a power flow is positive if entering the PSU, from Fig. 4.4, it is easy to identify the raising phases ($P_{out} < 0$), during which the PSU provides power, and the lowering phases ($P_{out} > 0$), when energy recovery can be realised.

4.3 Application of the design procedure and proposed solutions

The design procedure described in Section 4.1 is applied to synthesise the power-split transmission for the oil drilling rig shown in Fig. 4.1. The overall speed and power ratios are evaluated starting from the output speed (Fig. 4.2) and power (Fig. 4.4), and assuming that ICE works at its best-efficiency operating point. Then, the mechanical points are selected to minimise the power of the electric machines, and the PSU design chart is obtained to synthesise the PGs. Lastly, the corresponding speed ratios are selected according to the speed and torque operating range of each electric machine, and the OGs are synthesised.

Two possible solutions are proposed in the following, differing in the ICE power size. In this regard, an energy management strategy would have been essential to select the optimal ICE power size. Nonetheless, more accurate knowledge of the system operations would have been necessary to pursue the global energetic optimisation of the oil drilling rig chosen as a case study. Therefore, in the following, we firstly explore the solution—preferred by the manufacturer—where one of the two 403-kW ICEs of the current configuration is suppressed and only one of them is maintained. Then, a solution deploying a downsized engine is investigated to prove how it affects the electric unit power size. In both cases, once the ICE operating point is selected upstream of the design process, the designer has complete control

over the following stages to select the power size of the electric MGs and synthesise the PSU.

4.3.1 First solution with the existing ICE

In this scenario, the thermal unit consists of one of the two 403-kW ICEs deployed in the original configuration. This solution may be preferable for the manufacturer wanting to deploy the current engine fleet in the hybrid powertrain.

The overall speed and power ratios can be easily assessed from their definition (see Eqs. (2.4), (2.24)). The PSU output speed ω_{out} and output power P_{out} are those shown in Fig. 4.2 and Fig. 4.4, respectively. As for the ICE operating point, it is assumed that $\omega_{in} = 1400$ rpm, $P_{in} = 305$ kW, and $T_{in} = 2080$ Nm to let it continuously work at its most efficient operations. The resulting τ and η for the simulated drilling are shown in Fig. 4.5.

Table 4.3 reports the resulting τ for each drilling subphase described in Section 4.2.

Table 4.3. PSU overall speed ratio for each drilling process phase.

Phase	τ
Drilling	0.0017
Trip-out	−0.17
Casing	0.085
Trip-in	0.17
Hook + Top drive up	−0.68
Hook + Top drive down	0.68

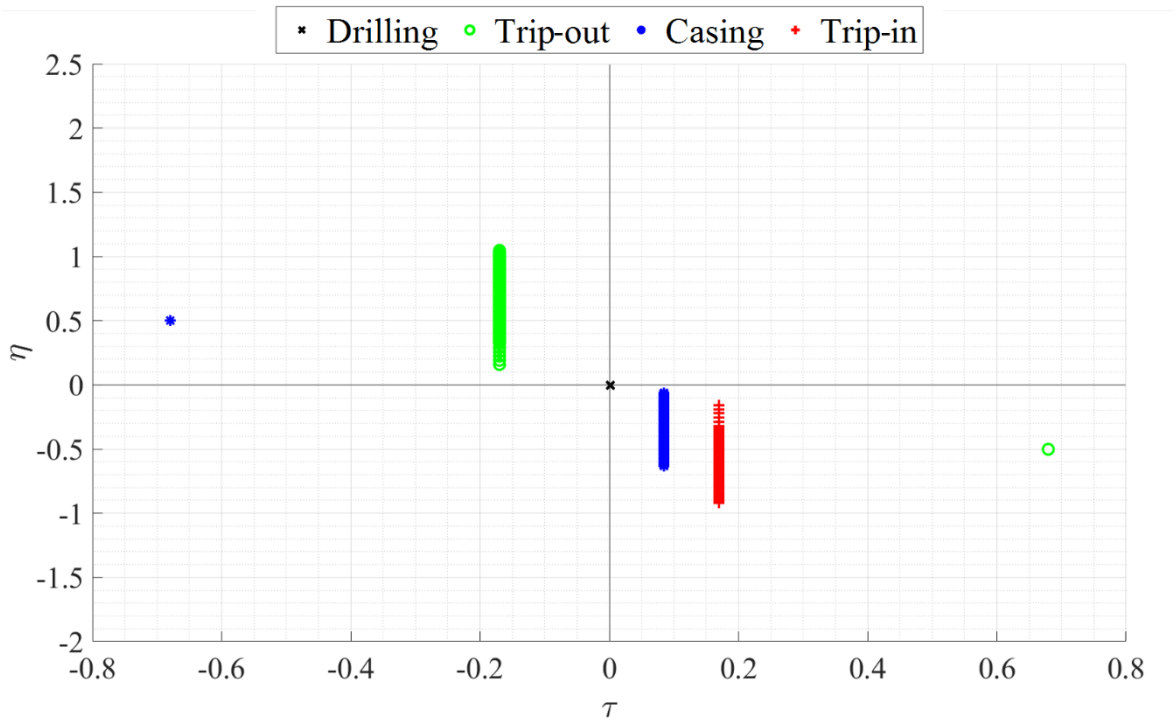

Fig. 4.5. PSU overall speed and power ratios for the simulated drilling with ICE working at 1400 rpm and 2080 Nm.

4.3.1.1 Selection of the mechanical points and electric machines power size

The procedure to select the mechanical points is performed by implementing an optimisation algorithm to choose the combination of mechanical points leading to the lowest power size of the electric machines. Several compound-split, input-split, and output-split layouts were simulated by imposing that at least one long-lasting phase is performed at the mechanical point to reduce the power in the electrical path. Thus, the free mechanical points (two for compound solutions, one for shunt ones) are chosen among the values of the overall speed ratios reported in Table 4.3. Then, the mechanical power demand of each electric machine was computed by Eqs. (4.1)-(4.2) in each operating point. Lastly, the couple of mechanical points resulting in the lowest maximum power for each electric machine were selected as the best solution.

The power-split functional layout resulting in the lowest electric machines rated power is an output-split solution with $\tau_{\#o} = \infty$ and $\tau_{\#i} = 0.085$. Thus, the power flowing through MG1 during casing operation is null and the power-split transmission operates as a parallel hybrid layout. The power flowing through MG1 and MG2 during the drilling phases for the selected mechanical points is reported in Table 4.4. The maximum power demand is 479 kW for MG1 and 499 kW for MG2. Thus, we select two electric machines with 500 kW rated power, which is the nearest power size commonly available on the market. The selected MGs have a base speed of 1000 rpm, a maximum speed of 4000 rpm, and a maximum torque of 4775 Nm.

Table 4.4. MGs extreme power for each drilling subphase for $\tau_{\#o} = \infty$ and $\tau_{\#i} = 0.085$. MG1 and MG2 maximum power are indicated in bold.

Drilling Subphase	τ	η	P_{MG1} [kW]	P_{MG2} [kW]
Drilling	0.0017	−0.0078	120	−427
Drilling	0.0017	−0.0011	17.0	−322
Casing	0.085	−0.64	0	**−499**
Casing	0.085	−0.065	0	−325
Trip-out	−0.17	0.16	72.4	−329
Trip-out	−0.17	1.05	**479**	−465
Trip-in	0.17	−0.92	−141	−446
Trip-in	0.17	−0.16	−24.1	−329
Hook + top drive up	−0.68	0.503	172	−324
Hook + top drive down	0.68	−0.503	−134	−324

4.3.1.2 PSU design chart and planetary gearing synthesis

All the characteristic functions obtainable from the permutation of $\tau_{\#out} = 0$, $\tau_{\#in} = \infty$, $\tau_{\#i} = 0.085$, and $\tau_{\#o} = \infty$ taken three at a time are evaluated by Eqs. (2.26). Then, the

design chart shown in Fig. 4.6 is realised by plotting the resulting characteristic functions within the τ range comprised from −0.68 to 0.68. The Y-axis, corresponding to the Willis ratio of the eligible PG, ranges from −2/3 to −1/3. Because of the coincidence of $\tau_{\#o}$ with $\tau_{\#in}$, some curves appear overlapped. Since the output-split layout consists of a single PG, only one point should be selected from the design chart. Selecting a point of intersection between one characteristic curve and one of the τ at which the system operates (Table 4.3) implies that the PG works at its synchronism in a long-lasting operating point, avoiding any meshing power loss. Therefore, it is rather intuitive to select the intersection between the $\phi^{i}_{out/o}$ curve (coincident with $\phi^{i}_{out/in}$) and $\tau = -0.17$. This choice leads to the synthesis of a PG with a Willis ratio equal to −0.5, which is synchronous during the trip-out operations at $\tau_* = -0.17$. The PG carrier is connected to MG1, the ring gear to the PSU output shaft, and the sun gear to MG2, whose rotational speed is proportional to the ICE speed.

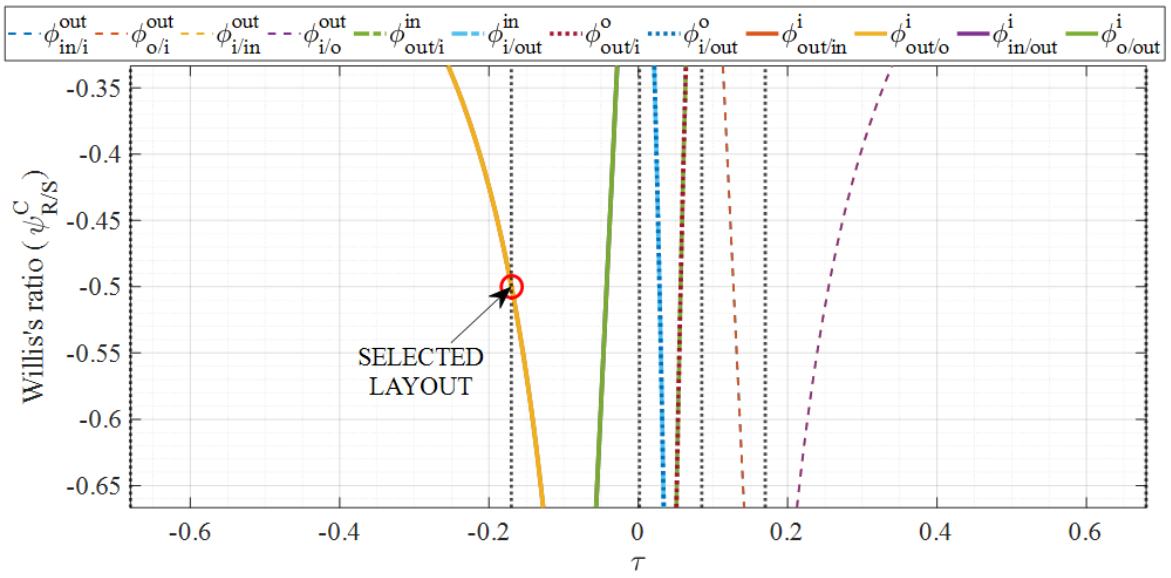

Fig. 4.6. PSU design chart for PG synthesis and selected layout with ICE working at 1400 rpm and 2080 Nm.

4.3.1.3 Selection of the corresponding speed ratios

As shown in Eqs. (4.3)-(4.6), the MG1 speed and torque are ruled by the corresponding speed ratio $\tau_{i\#o}$, while $\tau_{o\#i}$ affects the MG2 speed and torque.

The selection of $\tau_{o\#i}$ is performed by ensuring compliance with MG2 maximum speed and torque constraints for $\tau = \tau_{\#i} = 0.085$, which is also the most demanding scenario (Table 4.4). Since, from Eq. (4.4), $\omega_o = \tau_{o\#i} \cdot \omega_{in}$ for $\tau_{\#o} = \infty$, $\tau_{o\#i}$ can be selected to let MG2 work at the speed resulting in its highest efficiency. Supposing that the best-efficiency operations of MG2 are realized at 3500 rpm, it is:

$$\tau_{o\#i} = \frac{\omega_{o\,opt}}{\omega_{in}} = \frac{3500}{1400} = 2.5$$

The corresponding speed ratio $\tau_{i\#o}$ is ∞ by definition; however, by considering the limit for $\tau_{\#o} \to \infty$ and $\tau_{i\#o} \to \infty$ of Eq. (4.5), the MG1 torque in an output-split configuration results in:

$$T_i = -\frac{\tau_{\#o}}{\tau_{i\#o}} T_{out}$$

where $\tau_{\#o}/\tau_{i\#o}$ is a finite ratio depending on the constructive parameters of the selected PG and the eventual OGs. This ratio is selected so as to comply with MG1 maximum torque for any value of T_{out}, which can be defined accordingly to Eq. (2.24) as:

$$T_{out} = -\frac{\eta}{\tau} T_{in}$$

Thus, the constraint on MG1 maximum torque is ensured by imposing that MG1 reaches its maximum torque when the maximum output torque is required:

$$\frac{\tau_{\#o}}{\tau_{i\#o}} = -\frac{T_{MG1_{max}}}{T_{out_{max}}} = -\frac{4775}{15554} = -0.307$$

At this point, the operations of the electric machines are defined for any operating point. Table 4.5 shows MG1 and MG2 speed and torque for the extreme values of η for each drilling process phase. The constraints on the maximum speed and torque are always fulfilled.

Table 4.5. MG1 and MG2 extreme operations for each drilling subphase with ICE working at 1400 rpm and 2080 Nm.

Drilling Subphase	τ	η	ω_i [rpm]	T_i [Nm]	ω_o [rpm]	T_o [Nm]
Drilling	0.0017	−0.0078	380	3000	3500	−1170
Drilling	0.0017	−0.0011	380	427	3500	−880
Casing	0.085	−0.64	0	4775	3500	−1360
Casing	0.085	−0.065	0	490	3500	−886
Trip-out	−0.17	0.16	1160	595	3500	−898
Trip-out	−0.17	1.05	1160	3930	3500	−1270
Trip-in	0.17	−0.92	−387	3470	3500	−1210
Trip-in	0.17	−0.16	−387	595	3500	−898
Hook + top drive up	−0.68	0.503	3490	472	3500	−884
Hook + top drive down	0.68	−0.503	−2710	472	3500	−884

4.3.1.4 Ordinary gearing synthesis

The last design step involves the synthesis of the ordinary gear trains included in the PSU. At this point, the nodal and corresponding speed ratios are defined, as well as the PG synchronous ratio τ_*. Thus, Eqs. (4.15) can be evaluated involving each TPM shaft at least once:

$$\frac{k_o}{k_{out}} = \frac{\omega_o}{\omega_{out}}\bigg|_{\tau_*} = \frac{\tau_{o\#i}}{\tau_*} = -14.7$$

$$\frac{k_i}{k_{out}} = \frac{\omega_i}{\omega_{out}}\bigg|_{\tau_*} = \frac{\frac{\tau_{i\#o}}{\tau_{\#o}}(\tau_* - \tau_{\#i})}{\tau_*} = -0.489$$

$$\frac{k_{in}}{k_{out}} = \frac{\omega_{in}}{\omega_{out}}\bigg|_{\tau_*} = \frac{1}{\tau_*} = -5.89$$

Where ω_o and ω_i speeds were those in Eqs. (4.11)-(4.12); $\tau_{\#o}/\tau_{i\#o} = -0.307$ as defined in Section 4.3.1.3.

Table 4.6 shows the possible OG combinations obtained by assuming that at least one OG has a fixed ratio equal to 1, thus, it can be omitted. The combination in the fourth row seems preferable because the fixed ratios are averagely more easily achievable by single-stage gearing.

Table 4.6. Possible combinations for OGs with ICE working at 1400 rpm and 2080 Nm.

k_{in}	k_{out}	k_o	k_i
1	−0.170	2.50	0.830
−5.88	1	−14.7	−4.89
0.400	−0.0680	1	0.332
1.20	−0.205	3.01	1

Fig. 4.7 summarises the functional layout of the output-split transmission designed for the first analysed case, where one of the ICEs currently deployed on the drilling rig is kept working at 1400 rpm and 2080 Nm.

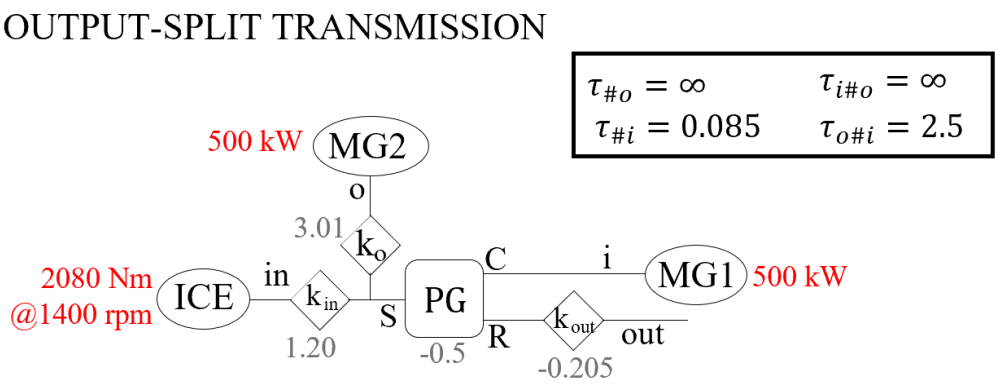

Fig. 4.7. Functional layout of the output-split transmission designed for ICE working at 1400 rpm and 2080 Nm.

4.3.2 Second solution with a new downsized ICE

In the previous scenario, Fig. 4.5 shows that, in the majority of drilling rig operating points, the overall power ratio η is far lower than one. This means that the ICE power almost

always significantly overcomes the output power demand for drill string motion. Consequently, the ICE surplus energy is transferred to the electric unit, and two electric machines with 500 kW of rated power each are required for this purpose. However, a more balanced solution can be found by downsizing the ICE size. For instance, a smaller ICE reaching its most efficient operations at $\omega_{in} = 1400$ rpm, $T_{in} = 1045$ Nm, and $P_{in} = 153$ kW would provide an intermediate power that equals the power required for raising the top drive and hook block, which is the most frequent drilling process subphase since it is performed during drilling, casing, and trip-in. In the following, the design process described in Section 4.1 and applied in Section 4.3.1 is carried out to design the power-split transmission considering the new downsized ICE.

The overall speed and power ratios are assessed from Eqs. (2.4), (2.24), by considering the PSU output speed ω_{out} and output power P_{out} reported in Fig. 4.2 and Fig. 4.4, $\omega_{in} = 1400$ rpm, $P_{in} = 153$ kW, and $T_{in} = 1045$ Nm. The resulting τ and η for the simulated drilling are shown in Fig. 4.8.

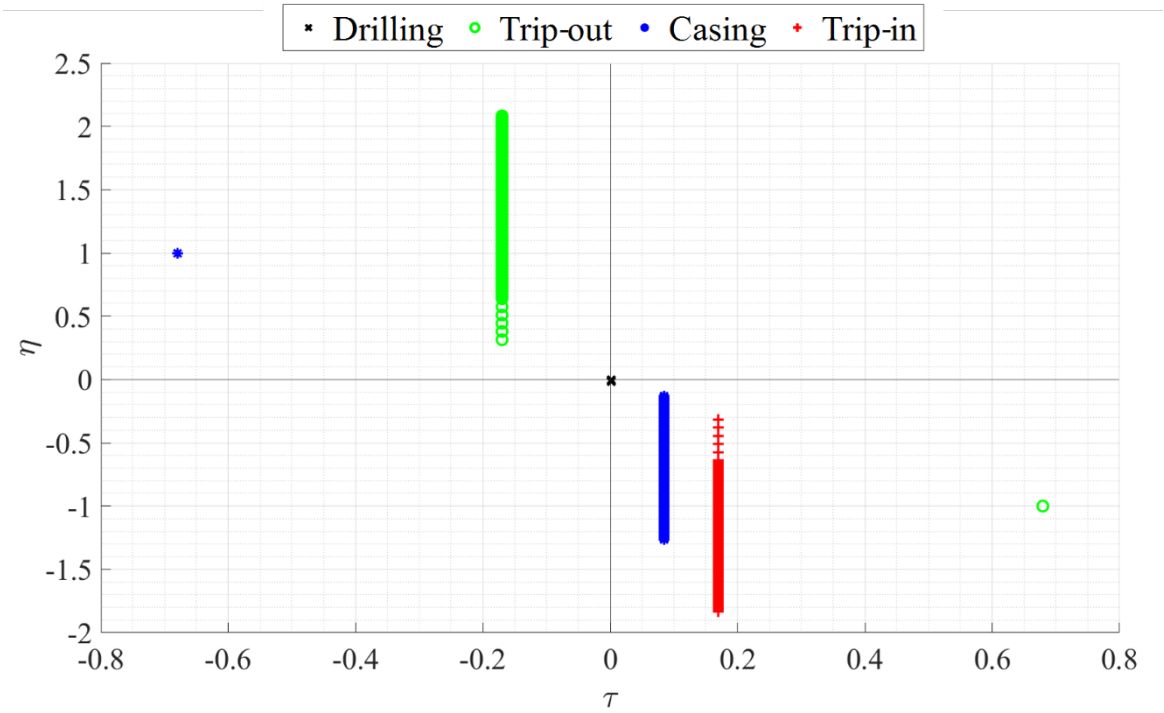

Fig. 4.8. PSU overall speed and power ratios for the simulated drilling with ICE working at 1400 rpm and 1045 Nm.

4.3.2.1 Selection of the mechanical points and electric machines power size

The same procedure proposed in Section 4.3.1.1 is carried out. In this case, the power-split functional layout resulting in the lowest rated power for the electric MGs is an input-split solution with $\tau_{\#o} = 0$ and $\tau_{\#i} = -0.68$. The power flowing through MG1 and MG2 for the selected mechanical points is reported in Table 4.7. The power flowing through MG1

is null when the top drive and hook block alone are raised. Moreover, MG2 power is zero when the top drive and hook block is lowered or raised. Consequently, when the top drive and hook block is raised, the electric unit is not involved in the operations, since the ICE power equals the power needed for raising operations. Instead, when the block is lowered, the powertrain operates in a parallel hybrid mode to recover the braking energy through MG1. The maximum power demand for MG1 is 307 kW, while for MG2, it is 281 kW. Thus, we select two electric motors with 315 kW rated power, which is the nearest power size commonly available on the market. This value is significantly lower than the 500-kW rated power required in the first solution. The selected motor-generators have a base speed of 1000 rpm, a maximum speed of 4000 rpm, and a maximum torque of 3008 Nm.

Table 4.7. MGs extreme power for each drilling subphase for $\tau_{\#o} = 0$ and $\tau_{\#i} = -0.68$. MG1 and MG2 maximum power are indicated in bold.

Drilling Subphase	τ	η	P_{MG1} [kW]	P_{MG2} [kW]
Drilling	0.0017	−0.0155	−154	−2.00
Drilling	0.0017	−0.0022	−154	0.0357
Casing	0.085	−1.27	−172	−175
Casing	0.085	−0.130	−172	−0.700
Trip-out	−0.17	0.315	−115	9.93
Trip-out	−0.17	2.09	−115	**281**
Trip-in	0.17	−1.84	−192	−243
Trip-in	0.17	−0.315	−192	−9.93
Hook + top drive up	−0.68	1.00	0	0
Hook + top drive down	0.68	−1.00	**−307**	0

4.3.2.2 PSU design chart and planetary gearing synthesis

The PSU design chart obtained from $\tau_{\#out} = 0$, $\tau_{\#in} = \infty$, $\tau_{\#i} = -0.68$, and $\tau_{\#o} = 0$ is shown in Fig. 4.9. Given the coincidence of $\tau_{\#o}$ with $\tau_{\#out}$, some curves appear overlapped. The selected PG has a Willis ratio equal to −1/3, and it is synchronous during the trip-out operations at $\tau_* = -0.17$. Since the chosen layout belongs to the $\phi_{i/o}^{in}$ curve (coincident with $\phi_{i/out}^{in}$), the PG carrier is connected to the ICE, the ring gear to MG1, and the sun gear to MG2, whose rotational speed is proportional to the PSU output speed.

4.3.2.3 Selection of the corresponding speed ratios

For the selected input-split layout, both $\tau_{i\#o}$ and $\tau_{o\#i}$ can be freely assigned. From Eqs. (4.4), (4.6), $\tau_{o\#i}$ rules the MG2 speed and torque; in particular, it is the ratio between ω_o and ω_{in} when $\tau = \tau_{\#i}$, which is also the maximum speed ratio in absolute terms. Thus, $\tau_{o\#i}$ can be evaluated by the following expression to fulfill the MG2 maximum speed constraint:

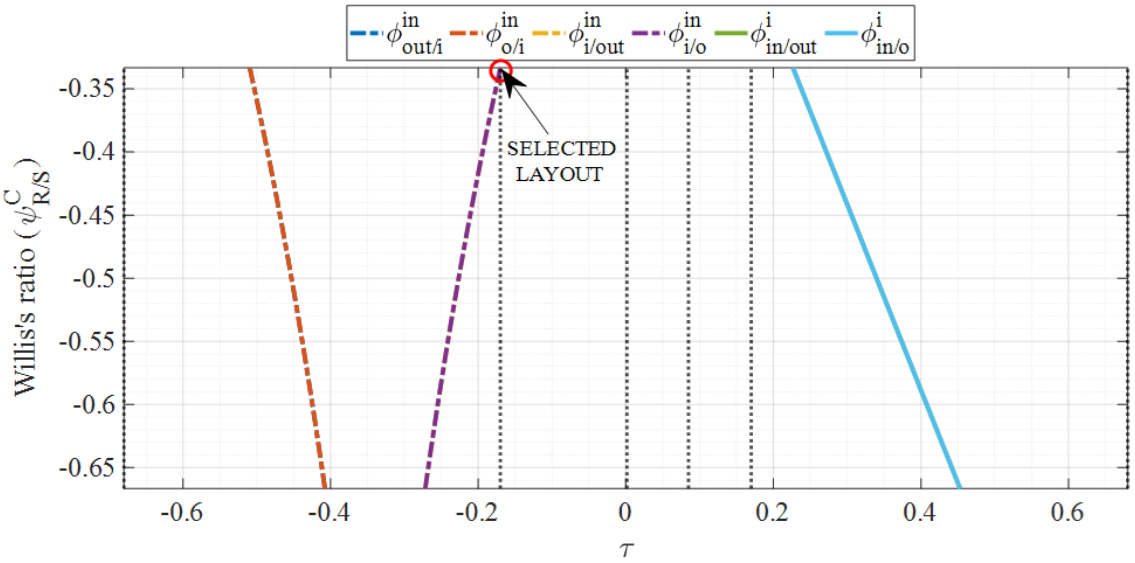

Fig. 4.9. PSU design chart for PG synthesis and selected layout with ICE working at 1400 rpm and 1045 Nm.

$$\tau_{o\#i} = \frac{\omega_{o\,max}}{\omega_{in}} = \frac{4000}{1400} = 2.86$$

Similarly, $\tau_{i\#o}$ rules the MG1 speed and torque (Eqs. (4.3), (4.5)). However, the same approach is not suited for $\tau_{i\#o}$ selection, since $\tau_{\#o}$ is not the extreme value of the operating τ range. Nonetheless, Eq. (4.5) shows that $T_{in} = -\tau_{i\#o} \cdot T_i$ for $\tau_{\#o} = 0$. As a result, $\tau_{i\#o}$ can be selected to let MG1 work at the torque resulting in its highest efficiency, namely, around the torque provided for the MG1 maximum speed:

$$\tau_{i\#o} = -\frac{T_{in}}{T_{i_{max\ speed}}} = -\frac{1045}{752} = -1.39$$

The resulting MG1 and MG2 speed and torque are reported in Table 4.8.

Table 4.8. MG1 and MG2 extreme operations for each drilling subphase with ICE working at 1400 rpm and 1045 Nm. MG2 torque values exceeding the maximum torque of 3008 Nm are in bold.

Drilling Subphase	τ	η	ω_i [rpm]	T_i [Nm]	ω_o [rpm]	T_o [Nm]
Drilling	0.0017	−0.0155	−1951	752	−9.72	1962
Drilling	0.0017	−0.0022	−1951	752	−9.72	−35.04
Casing	0.085	−1.27	−2190	752	−500.0	**3333**
Casing	0.085	−0.130	−2190	752	−500.0	13.31
Trip-out	−0.17	0.315	−1460	752	1000	94.81
Trip-out	−0.17	2.09	−1460	752	1000	2682
Trip-in	0.17	−1.84	−2433	752	−1000	2321
Trip-in	0.17	−0.315	−2433	752	−1000	94.81
Hook + top drive up	−0.68	1.00	0	752	4000	0
Hook + top drive down	0.68	−1.00	−1951	752	−9.72	1962

These results show that the constraint on MG2 maximum torque does not allow the full braking energy recovery when the casing is performed at a higher depth (lower η). To overcome the problem, it is not advisable to deploy ordinary gearing outside the PSU to decrease the MG2 required torque because this would violate the constraint on MG2 maximum speed. However, the constraint on the MG2 maximum torque can be overcome in several ways, for instance: by modifying ICE operations under critical casing conditions; introducing dissipative braking to lower P_{out} and increase the PSU overall power ratio η; increasing the MG2 power size.

4.3.2.4 Ordinary gearing synthesis

Eqs. (4.15) for synthesising the ordinary gear trains in the adopted input-split layout result in:

$$\frac{k_o}{k_{in}} = \frac{\omega_o}{\omega_{in}}\bigg|_{\tau_*} = \frac{\tau_{o\#i}}{\tau_{\#i}}\tau_* = 0.714$$

$$\frac{k_i}{k_{in}} = \frac{\omega_i}{\omega_{in}}\bigg|_{\tau_*} = -\frac{\tau_{i\#o}}{\tau_{\#i}}(\tau_* - \tau_{\#i}) = -1.04$$

$$\frac{k_{out}}{k_{in}} = \frac{\omega_{out}}{\omega_{in}}\bigg|_{\tau_*} = \tau_* = -0.170$$

Table 4.9 shows the possible OG combinations obtained by assuming that at least one OG has a fixed ratio equal to 1, thus, it can be omitted. The combination in the first row seems preferable.

Table 4.9. Possible combinations for OGs with ICE working at 1400 rpm and 1045 Nm.

k_{in}	k_{out}	k_i	k_o
1	−0.170	−1.04	0.714
−5.89	1	6.14	−4.20
−0.959	0.163	1	−0.685
1.40	−0.238	−1.46	1

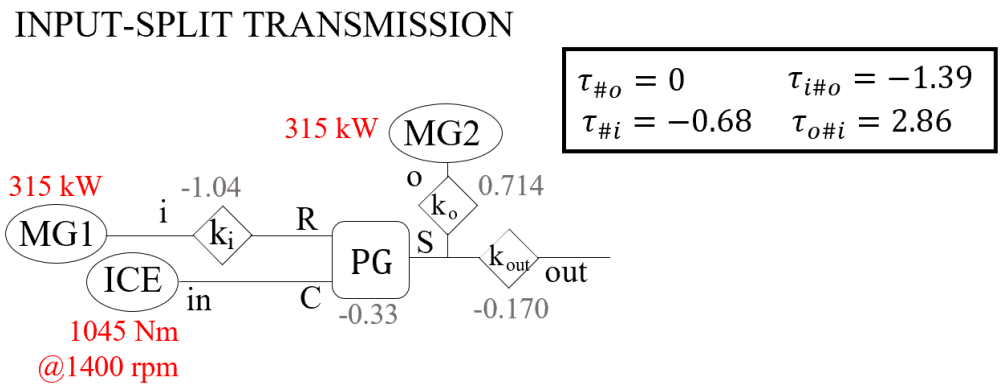

Fig. 4.10. Functional layout of the input-split transmission designed for ICE working at 1400 rpm and 1045 Nm.

Fig. 4.10 summarises the functional layout of the input-split transmission designed for the second analysed case where a downsized ICE working at 1400 rpm and 1045 Nm is deployed.

The selected layout includes an ordinary gear train, k_i, with a constructive ratio very close to −1. The transmission constructive complexity may be reduced by imposing $k_i = 1$, by slightly varying the numerical value of $\tau_{i\#o}$ and inverting its sign, by keeping unchanged the remaining functional parameters. Alternatively, $k_i = 1$ may be realised by keeping unchanged all the functional parameters and inverting the sign of the fixed ratio of any other OG; this would imply also a different Willis ratio and a different synchronous ratio of the PG, according to the PSU design chart of Fig. 4.9. Consequently, the trip-out operations would be performed for an overall transmission ratio very close to the PG synchronism, still ensuring high PG efficiency (see Section 2.4).

4.3.3 Solutions comparison and discussion

This research aimed to apply the modular and parametric design procedure to propose a novel hybridisation of the oil drilling rig. Although a realistic but simplified working cycle is simulated for the drilling rig operations—for instance, any dynamic aspect is neglected, likewise any interaction between the drill string or the casing with the wellbore walls—the design procedure validity is not compromised. Indeed, it would be sufficient to retrieve data from a real similar drilling rig to identify the actual overall speed and power ratios on which the design process should be based.

Two scenarios differing in engine power size are investigated to probe how the engine selection affects the electric machines power size. In the first one, only one of the two engines deployed in the original drilling rig plant is kept in the hybrid layout. We supposed that the engine always operates at its most efficient point, providing 305 kW. An output-split transmission results in the lowest electric machines power size, equal to 500 kW each. However, the power required in the transmission output for hoisting operations is widely lower than 305 kW for most drilling rig functioning. This implies that such a high engine power is almost always unnecessary and causes an oversizing of the electric unit, which has to store the energy recovered during the lowering phases and the ICE surplus power.

Therefore, a second scenario with a downsized engine was considered. In this case, the ICE provides 153 kW, and two electric machines with 315 kW of rated power each are required. The transmission synthesis results in an input-split layout. The second scenario seems preferable given the smaller electric unit resulting in lower costs, proving that the initial ICE sizing is crucial to optimise the hybridised powertrain in both energetical and

cost-effective terms. Therefore, further research is needed to minimise the overall energy consumption as well as the thermal and electric unit power size by introducing proper engine control strategies. For instance, in both scenarios, the engine is kept on during regenerative braking, which would not be necessary to sustain only the drawworks operations. Including an on-off control strategy for the engine would further reduce the power unit size. Nonetheless, the proposed solutions enable significant fuel savings compared to the current non-hybrid plant, thanks to thermal unit downsizing and the possibility of exploiting the braking energy recovered and stored in the battery to supply other auxiliary loads of the drilling rig plant.

To conclude, the proposed case study has revealed that integrating the design procedure with the development of an effective energy management strategy is essential to select the optimal power size of the ICE which, consequently, would lead to the synthesis of the optimal PS-CVT through the procedure described in this chapter. Hence, Chapter 5 and Chapter 6 deal with the integration of the parametric model within an EMS to assess the optimal operations of any power-split powertrain.

CHAPTER 5
OPTIMAL OPERATING MAPS FOR POWER-SPLIT HEVS

The analysis procedure presented in Chapter 3 enables a rapid assessment of any power-split powertrain, being based on dimensionless independent and dependent variables expressed as speed, torque, and power ratios that result in utmost generality. Nonetheless, the determination of the actual operating point of the ICE and electric MGs for a given vehicle speed and demanded torque has not been considered.

The knowledge of the functioning point of the actuators is essential for the assessment of the fuel consumption and the battery power, as well as the conversion power losses occurring in the ICE and electric unit. This information is crucial for the implementation of the energy management strategy, aimed at reducing fuel consumption and emissions by instantaneously splitting the demanded power between the engine and the battery so as to keep the ICE operating as efficiently as possible, minimise the powertrain power losses, and maintain the battery state of charge around a desired value (see Section 1.4).

To move from the dimensionless approach of Chapter 3 to a dimensional approach that returns the operating points of the actuators, it is necessary to define the dimensionless independent variables of the mathematical treatment, i.e., the overall speed ratio, the overall torque ratio, and, thus, the overall power ratio. Hence, for a given vehicle speed and demanded torque, defining the ICE operation is necessary to determine the operating points of the electric MGs. The ICE speed and torque are instantaneously defined during the drive through an online EMS; for offline optimisations, the ICE operation can be explored by assuming an adequate value of speed and torque within the available working range. The conversion power losses in the engine and the fuel consumption are assessed according to the brake specific fuel consumption map; similarly, the efficiency maps of the electric machines are required to assess their power losses and the resulting battery power.

The integration of the internal model with an EMS based on the model predictive control, which is potentially capable of online implementation, is addressed in Chapter 6. Instead, the present chapter is focused on an offline optimisation aimed at the assessment of the powertrain best operations resulting in the maximisation of a global performance index. By considering different combinations of input and output speed and torque, the powertrain response has been explored in terms of the functioning point and power losses of the ICE and electric MGs, net battery power, and powertrain global efficiency. The results are

collected in some optimal operating maps collecting all data of interest, which can be used as look-up tables to reduce the computational effort during the implementation of an online EMS. Indeed, thanks to the generality of the parametric model, the proposed approach is the ideal basis for the development of new energy management strategies, as it applies to any hybrid electric powertrain without requiring an in-deep knowledge of the behaviour of each component of the powertrain; therefore, it offers a neutral environment for engineers with different expertise.

The procedure to assess the optimal operating maps of any power-split HEV by using the unified parametric model is described in Section 5.1. Section 5.2 proposes an example of application on the Chevrolet Volt, equipped with a multi-mode PS-CVT, in steady-state power-split and full-electric drive. In Section 5.3, the same approach is adopted to propose a comparison between two performance indices to consider the different working principles of the thermal and electric units.

5.1 Offline assessment of the optimal operation

This section describes the procedure adopted for the offline assessment of the optimal operation of any power-split hybrid electric powertrain for a given vehicle speed and demanded torque. It includes the following steps:

1) identification of the functional parameters of the considered PSU;
2) comprehensive dimensionless analysis of the PSU behaviour in terms of speed, torque, and power ratios, including the consideration of PSU meshing losses;
3) identification of the range of interest of the overall transmission ratio τ and power ratio η;
4) introduction of ICE and MGs efficiency maps and evaluation of the global response of the powertrain in terms of ICE operations and fuel power, MGs operations and battery power;
5) definition and assessment of the performance index to optimise and extraction of the optimal operation complying with the constructive and instantaneous constraints.

After carrying out the dimensionless analysis of the PSU based on the parametric model (steps 1 and 2) as described in the example of application in Section 3.2, the shift to dimensional variables is realised by introducing the characteristic curves of the power source attached to the port *in* and the load attached to the port *out*. In other words, for addressing the power-split drive, the independent variables τ and η need to be defined, which implies that ω_{out}, ω_{in}, P_{out}, and P_{in} need to be defined. Instead, for considering a full-electric drive, it is necessary to assume P_{out} and the power of one electric machine, while the MGs speeds

are univocally defined for a given ω_{out}.

The output speed ω_{out} is directly related to the vehicle speed, while the output power delivered to the wheels depends on the vehicle speed (V_{veh}) and acceleration (a_{veh}), as follows:

$$P_{out}(V_{veh}, a_{veh}) = -(mg\sin\gamma + f_r mg\cos\gamma + \frac{1}{2}c_d A_f \rho_a V_{veh}^2 + \delta m a_{veh})V_{veh} \quad (5.1)$$

P_{out} is negative because when delivered by the PSU (see Fig. 2.1). In Eq. (5.1), m is the vehicle mass, $g = 9.81$ m/s^2 is the gravitational acceleration, γ is the road slope expressed in radians, f_r is the rolling resistance coefficient, c_d is the drag coefficient, A_f is the vehicle frontal area, ρ_a is the air density, and δ is a coefficient to consider the rotational inertia.

For each feasible combination of V_{veh} and a_{veh}, the functioning point of the ICE has to be selected in terms of speed (ω_{in}) and torque (T_{in}) to determine the overall speed and power ratios:

$$\tau(V_{veh}, \omega_{in}) = \frac{V_{veh}}{R_w \cdot \omega_{in}} \quad (5.2)$$

$$\eta(V_{veh}, T_{out}, \omega_{in}, T_{in}) = -\frac{P_{out}}{\omega_{in} T_{in}} \quad (5.3)$$

where R_w is the wheels radius. In the considered offline framework, the whole ICE working range must be explored to investigate all the possible powertrain functioning points for a given vehicle speed and acceleration. Thus, ICE operations can be freely selected from the ICE efficiency maps.

Each engine operating point involves a certain engine efficiency. As a result, the power supplied by the fuel can be easily calculated as well:

$$P_{fuel}(\omega_{in}, T_{in}) = \frac{\omega_{in} T_{in}}{\eta_{ICE}} \quad (5.4)$$

Thus, once the vehicle speed and engine operating point are fixed, the overall speed and power ratios are univocally defined and are used to interpolate the speed and power ratios obtained from the dimensionless analysis. Then, these ratios can be multiplied by the corresponding ω_{in} and $P_{in} = \omega_{in} T_{in}$ to assess the rotational speed of the electric machines (ω_i, ω_o) and their actual mechanical power ($\bar{P}_i$, $\bar{P}_o$). In this way, the operating point of both electric machines is determined, leading to the assessment of their efficiency from their efficiency map. Lastly, the net electric power flowing to or from the battery is computed as:

$$P_{batt}(V_{veh}, P_{out}, \omega_{in}, T_{in}) = \bar{p}_i P_{in} \eta_{MG1}^{-sign(\bar{p}_i)} + \bar{p}_o P_{in} \eta_{MG2}^{-sign(\bar{p}_o)} \quad (5.5)$$

The described procedure outputs a set of matrices containing all the possible powertrain operations for each combination of vehicle speed and acceleration.

In full-electric drive, for a given vehicle speed, the rotational speeds of the electric

machines are univocally determined by Eqs. (2.56). Therefore, after the assessment of P_{out} through Eq. (5.1), the torque of one electric machine has to be defined, which can range from its minimum to maximum value related to the MG rotational speed, according to the MG efficiency map. Thus, an array with different values of $p'_i = -(\omega_i \cdot T_i)/P_{out}$ or $p'_o = -(\omega_o \cdot T_o)/P_{out}$ is used to interpolate the results of the dimensionless analysis.

Then, the performance index to optimise is defined and assessed for any combination of V_{veh}, P_{out}, ω_{in}, and T_{in}. The present research has been focused on the optimisation of the powertrain global efficiency, as it is addressed in Sections 5.2.3 and 5.3.2.

At the end of the computational process, the resulting arrays contain all the data of the powertrain operations in terms of MGs speed and torque, battery power, and performance index for any combination of V_{veh}, P_{out}, ω_{in}, and T_{in}. Thus, the results are filtered by eliminating those operations that do not comply with the constructive constraints, such as ICE and MGs maximum and minimum speed and torque, and the boundary on the battery power depending on the battery state of charge. The constructive constraints of the actuators are defined as:

$$\begin{gathered}
\omega_{ICE,min} \leq \omega_{in} \leq \omega_{ICE,max} \\
T_{ICE,min}(\omega_{in}) \leq T_{in}(\omega_{in}) \leq T_{ICE,max}(\omega_{in}) \\
\omega_{MG1,min} \leq \omega_i \leq \omega_{MG1,max} \\
T_{MG1,min}(\omega_i) \leq T_i(\omega_i) \leq T_{MG1,max}(\omega_i) \\
\omega_{MG2,min} \leq \omega_o \leq \omega_{MG2,max} \\
T_{MG2,min}(\omega_o) \leq T_o(\omega_o) \leq T_{MG2,max}(\omega_{in})
\end{gathered} \tag{5.6}$$

The boundary values of the battery power depend on the instantaneous SOC, but the proposed static analysis cannot include such considerations. Therefore, four different scenarios for the battery SOC are simulated. In the first one ($\mathrm{SOC} = \mathrm{FREE}$), the battery can always provide or gather any power comprised between the lower and the higher values:

$$P_{max,charge} \leq P_{batt} \leq P_{max,discharge} \tag{5.7}$$

The condition whereby the battery is completely charged and thus prevented from receiving further power is indicated as $\mathrm{SOC} = 1$ and implies $P_{max,charge} = 0$. On the contrary, if the battery is fully discharged ($\mathrm{SOC} = 0$), it cannot supply power and hence $P_{max,discharge} = 0$. Lastly, the SOC can be maintained constant if $P_{batt} = 0$ ($\mathrm{SOC} = \mathrm{CONSTANT}$).

5.2 Case study on the multi-mode Voltec II

This section is adapted from [142], where the procedure described in Section 5.1 was applied to assess the optimal operation of the second generation of the Chevrolet Volt. The

steady-state drive in power-split and full-electric operation was considered. Section 5.2.1 describes the multi-mode PS-CVT of the Chevrolet Volt; Section 5.2.2 shows the results derived from the dimensionless analysis in power-split and in full-electric operation; Section 5.2.3 describes the procedure for assessing the operating maps and defines the optimisation problem; Section 5.2.4 presents the results of the offline optimisation in power-split and in full-electric drive.

5.2.1 Chevrolet Volt: vehicle and transmission specifications

The second generation of the Chevrolet Volt deploys a multi-mode PS-CVT referred to as Voltec II, whose constructive arrangement is outlined in Section 1.2.3. Fig. 5.1 shows the powertrain power-split layout derived from [35].

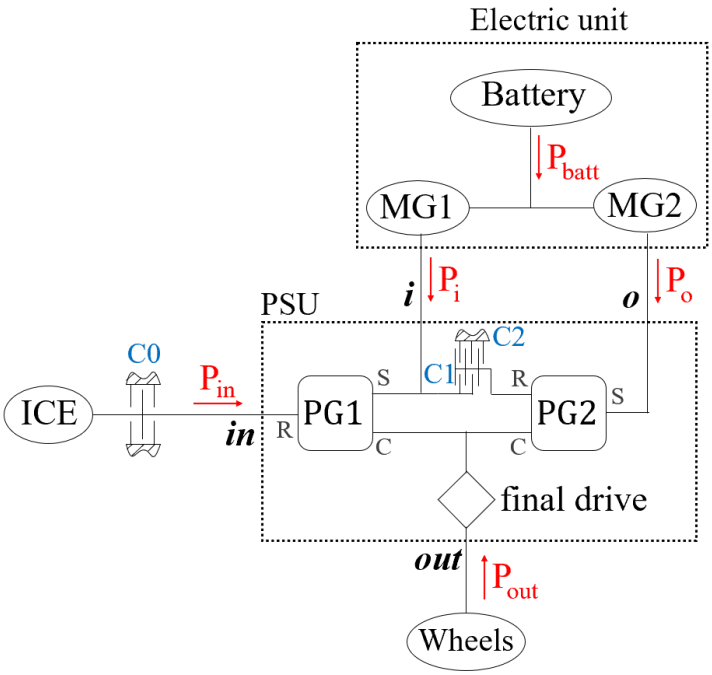

Fig. 5.1. Functional layout for Chevrolet Volt II power-split hybrid electric powertrain [35]. The arrows show the positive power flows.

The power-split transmission system of the Chevrolet Volt includes two PGs and a final drive. The final drive consists of a third PG with stationary ring gear and a chain drive; thus, it can be modelled as a fixed-ratio OG. The Willis ratios of the two PGs are $\Psi_1 = -0.535$ and $\Psi_2 = -0.481$, the fixed ratio of the final drive is $k_{fd} = 0.379$.

The ring gear of PG1 is connected to the ICE, the sun gear to the electric machine MG1, and the carrier to the final drive, as the carrier of PG2. The sun gear of PG2 is connected to the electric machine MG2, while the ring gear can be connected to the PG1 sun gear and MG1 by the clutch C1 or braked to the frame by the brake C2. Thus, the state of C1 and C2 determines which transmission mode is engaged, as indicated in Table 5.1. When only C2 is

engaged, PG2 realises a fixed speed ratio between the final drive and MG2, while only PG1 has three branches with non-proportional speeds; therefore, the PSU operates in input-split mode. When only C1 is engaged, the MG1 torque is allocated on both PGs and a compound-split mode is achieved.

Simultaneously engaging C1 and C2 results in a fixed-ratio parallel mode with the shaft *i* stationary, whereby MG1 is turned off and only MG2 can operate for traction or regenerative braking. However, since operating in a fixed-ratio parallel hybrid mode means operating in correspondence with a mechanical point of a power-split mode, it does not need to be addressed separately.

Moreover, by additionally engaging the one-way clutch C0, which locks to the frame of the ICE and the PG1 ring gear, two full-electric modes can be performed. However, as shown in Table 5.1, General Motors considers only the full-electric operation derived from the input-split arrangement.

Table 5.1. Clutches operations for mode shifts. X indicates engaged clutches.

Mode	C0	C1	C2
INPUT-SPLIT			X
PARALLEL		X	X
COMPOUND-SPLIT		X	
EV	X		X

5.2.2 Dimensionless speeds, torques, and meshing power losses

The functional parameters of the Voltec II in input-split and compound-split operations are assessed by the matrix approach presented in Section 3.1 and listed in Table 5.2. The obtained values agree with those considered in [83,96], where the dimensionless parametric analysis was applied to the Chevrolet Volt for the first time.

Table 5.2. Functional parameters of Voltec II.

Mode	$\tau_{\#i}$	$\tau_{\#o}$	$\tau_{o\#i}$	$\tau_{i\#o}$
INPUT-SPLIT	0.247	0	2.00	-1.87
COMPOUND-SPLIT	0.247	0.510	2.00	2.00

Once the functional parameters are known, the dimensionless approach addressed in Chapter 2 is applied to analyse both the power-split and full-electric operation in terms of speed, torque, and power ratios, including the evaluation of the meshing power losses in the PSU. Since the procedure is analogous to the one described in Section 3.2, only the results are discussed here for brevity.

The dimensionless results obtained for the power-split operation are shown in Fig. 5.2. Starting from the functional parameters of Table 5.2, the speed ratio $\tau_i = \omega_i/\omega_{in}$ between MG1 and the ICE was computed as a function of the overall speed ratio τ, as well as the speed ratio $\tau_o = \omega_o/\omega_{in}$ between MG2 and the ICE. These are shown in Fig. 5.2(a) for both input- and compound-split modes. The shift between one mode to the other occurs at the mechanical point $\tau = \tau_{\#i} = 0.247$. For $\tau = \tau_* = 0.379$ both electric machines rotate at the same speed, therefore both PGs work at their synchronous condition. At the PGs synchronism, the PSU meshing losses (Fig. 5.2(b)) show a minimum, because the absence of relative motion between the PGs branches prevents any friction meshing loss. The meshing losses of Fig. 5.2(b) were calculated as a fraction of the input power as a function of the overall speed ratio τ and the opposite of the overall power ratio $\eta = -P_{out}/P_{in}$ by adding the meshing losses in the final drive and in the PGs:

$$\bar{p}_L = \bar{p}_L|_{PG1} + \bar{p}_L|_{PG2} + \bar{p}_L|_{fd} \tag{5.8}$$

where:

$$\bar{p}_L|_{fd} = -\left|\left(1 - \eta_{fd}\right)p_{out}\right| \tag{5.9}$$

with $\eta_{fd} = 0.953$ and $p_{out} = -\eta$. The notation of Table 5.3 was considered to assess the meshing losses in the PGs.

Table 5.3. Reference notation of the TPMs shafts for the calculation of meshing losses in power-split modes.

	x	***X***	***y***	***Y***	***z***	***Z***
PG1	*in*	ring	*i*	sun	*out*	carrier
PG2	*out*	carrier	*i*	ring	*o*	sun

Therefore:

$$\bar{p}_L|_{PG1} = -\left|(1 - \eta^C)\left(\frac{\phi^{out}_{in/i} - \psi^C_{R/S}}{1 - \psi^C_{R/S}}\right)p_{in}\right| \tag{5.10}$$

$$\bar{p}_L|_{PG2} = -\left|(1 - \eta^S)\left(\frac{\phi^{o}_{out/i} - \psi^S_{R/C}}{1 - \psi^S_{R/C}}\right)p_{out}\right| \tag{5.11}$$

where $p_{in} = 1$ by definition. On the other hand, the power transmitted by the PG2 carrier can be calculated only in ideal conditions, by the principle of power conservation in the neutral node *out* and Eq. (2.34):

$$p_{out}|_{PG2} = p_{out} - p_{out}|_{PG1} = p_{out} + p_{in} \cdot \phi^{i}_{in/out} \tag{5.12}$$

Table 5.4 summarises the fixed-*Z* apparent efficiencies η^Z and the fixed-*Z* speed ratios $\psi^Z_{X/Y}$ for each PG, based on the functional and constructive layout of the transmission.

Table 5.4. Fixed-Z apparent efficiencies and fixed-Z speed ratios as functions of the basic efficiency η_0 and the Willis ratio Ψ.

	$\boldsymbol{\Psi}$	$\boldsymbol{\eta_0}$	$\boldsymbol{\psi^Z_{X/Y}}$	$\boldsymbol{\eta^Z = \psi^Z_{X/Y}/\bar{\psi}^Z_{X/Y}}$
PG1	$\Psi_1 = -0.535$	$\eta_{0_1} = 0.96$	$\psi_1 = \Psi_1 = -0.535$	$\eta_1 = \eta_{0_1} = 0.96$
PG2	$\Psi_2 = -0.481$	$\eta_{0_2} = 0.96$	$\psi_2 = \dfrac{1}{1-\Psi_2} = 0.675$	$\eta_2 = \dfrac{1-\Psi_2}{1-\Psi_2/\eta_{0_2}} = 0.987$

The PSU meshing losses enabled the calculation of the real power that the electric machines should provide to or collect from the PSU as a fraction of the input power (Fig. 5.22(c) and Fig. 5.2(d)).

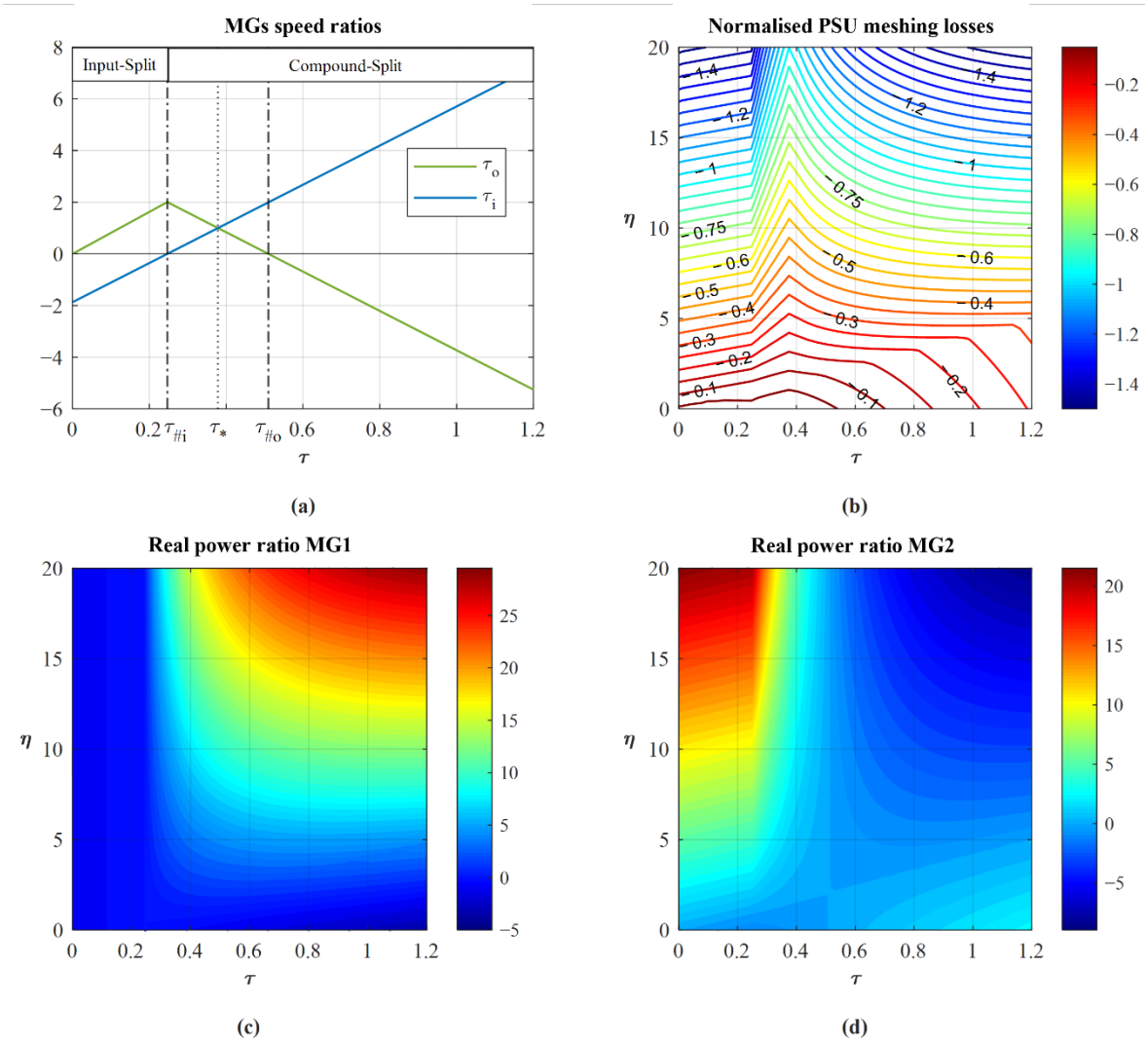

Fig. 5.2. Dimensionless results of Voltec analysis in power-split operation. (**a**) MGs speed ratios; (**b**) PSU meshing losses as a fraction of the input power; (**c**) MG1 real power as a fraction of the input power; (**d**) MG2 real power as a fraction of the input power.

The full-electric operations are assessed according to Section 2.5. As the engine is inactive in the full-electric drive (clutch C0 is engaged), speeds and power can be more conveniently normalised to the output ones. Since the shaft *in* is motionless, the speed ratio between the electric MGs and the shaft *out* is univocally defined as:

$$\begin{aligned} \left.\frac{\omega_i}{\omega_{out}}\right|_{\omega_{in}=0} &= \frac{\tau_{i_{\#o}}}{\tau_{\#o} - \tau_{\#i}} = 7.58 \\ \left.\frac{\omega_o}{\omega_{out}}\right|_{\omega_{in}=0} &= \frac{\tau_{o_{\#i}}}{\tau_{\#i} - \tau_{\#o}} = 8.12 \end{aligned} \tag{5.13}$$

The functional parameters used in Eq. (5.13) are those related to the input-split mode since it is the only mode exploited by General Motors to perform the EV operation. The global PSU meshing losses normalised to the opposite of the output power are the sum of the losses in the final drive, calculated as:

$$\bar{p}'_L|_{OG} = -\frac{\bar{P}_{Loss}|_{OG}}{P_{out}} \approx -\left|\left(1-\eta_{fd}\right) p'_{out}\right| \tag{5.14}$$

and those occurring in the PGs:

$$\bar{p}'_L|_{PG1} = -\frac{\bar{P}_{Loss}|_{PG1}}{P_{out}} \approx -\left|(1-\eta^R)\left(\frac{\phi^{in}_{out/i} - \psi^R_{C/S}}{1-\psi^R_{C/S}}\right) p'_{out}\right| \tag{5.15}$$

$$\bar{p}'_L|_{PG2} = -\frac{\bar{P}_{Loss}|_{PG2}}{P_{out}} \approx -\left|(1-\eta^C)\left(\frac{\phi^{out}_{o/i} - \psi^C_{S/R}}{1-\psi^C_{S/R}}\right) p'_o\right| \tag{5.16}$$

The parameters used in Eqs. (5.15)-(5.16) are indicated in Table 5.5, while in Eq. (5.15) $p'_{out}|_{PG1}$ is the portion of p'_{out} flowing in PG1, which can be computed as the difference between the power flowing into the final drive and its portion flowing in PG2 as follows:

$$p'_{out}|_{PG1} = p'_{out} - p'_{out}|_{PG2} = p'_{out} + p'_o \phi^i_{o/out} \tag{5.17}$$

Table 5.5. PGs reference notation, fixed-*Z* speed ratios, and fixed-*Z* efficiency.

	x* - *X	***y* - *Y***	***z* - *Z***	$\psi^Z_{X/Y}$	η^Z
PG1	*out* – Carrier	*i* – Sun	*in* – Ring	$\psi^R_{C/S} = \frac{\Psi_1}{\Psi_1 - 1}$	$\eta^R = \frac{1-\Psi_1}{\eta_0 - \Psi_1}$
PG2	*o* – Sun	*i* – Ring	*out* – Carrier	$\psi^C_{S/R} = \frac{1}{\Psi_2}$	$\eta^C = \eta_0$

Considering $\bar{p}'_o = p'_o = -P_o/P_{out}$ as the independent variable, the dimensionless power flowing in the other electric machine can be calculated from the PSU real power balance of Eq. (2.61). The results of the dimensionless analysis of full-electric operation are shown in Fig. 5.3.

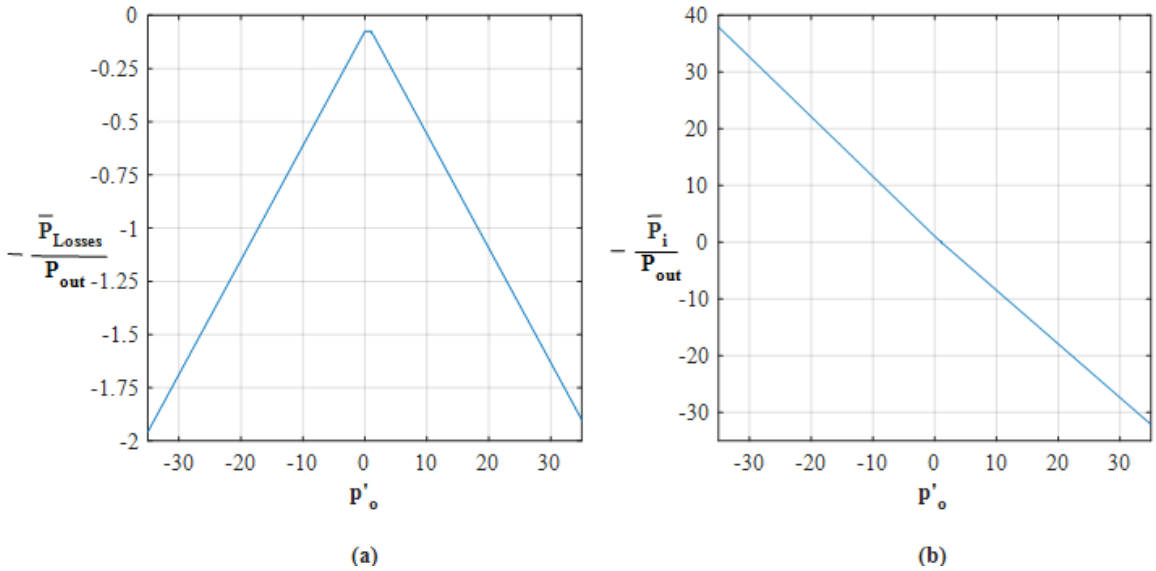

Fig. 5.3. Dimensionless results of Voltec analysis in full-electric operation. (**a**) Mechanical power losses in the PSU as a fraction of $-P_{out}$; (**b**) MG1 real power as a fraction of $-P_{out}$.

5.2.3 Identification of the optimal operating maps

To assess the optimal operating maps according to Section 5.1, the dimensionless results of Section 5.2.2 can be interpolated for the values of interest of τ and η in power-split operations and p'_o in full-electric drive.

The demanded power is assessed according to Eq. (5.1) considering the vehicle parameters of Table 5.6. The steady-state drive was considered.

Table 5.6. Chevrolet Volt parameters.

Unladen mass m_0 **[kg]**	**Rolling resistance** f_r **[-]**	**Drag coefficient** C_d **[-]**	**Frontal area** A_f **[m²]**	**Wheel radius** R_w **[m]**
1607	0.011	0.28	2.20	0.32

When the power-split operation is analysed, the possible values of τ and η are obtained by dividing each ω_{out} and P_{out} for all the available ω_{in} and P_{in} (Eqs. (5.2)-(5.3)) according to the ICE operating map shown in Fig. 5.4. The power supplied by the fuel is assessed on the basis of the ICE efficiency in the considered operating point, according to Eq. (5.4). Then, the results of Fig. 5.2 are interpolated for any combination of τ and η to assess the MGs speed and power necessary to obtain the resulting battery power, according to Eq. (5.5) and the MGs efficiency dependant on their operating point (Fig. 5.5).

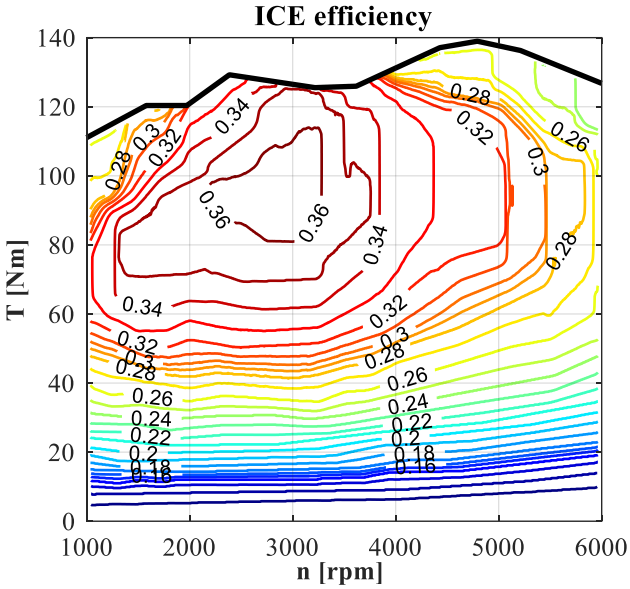

Fig. 5.4. Efficiency map of the Chevrolet Volt ICE derived from [35].

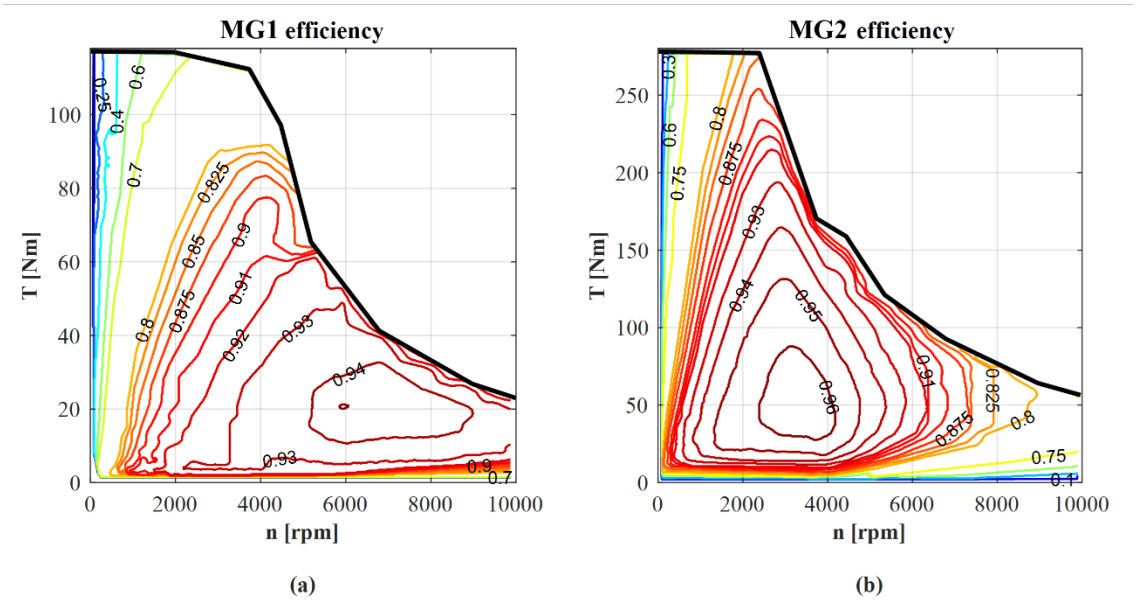

Fig. 5.5. Efficiency maps of Chevrolet Volt electric machines derived from [162] exploited for motoring and generating operation.

By the procedure addressed herein, a set of matrices containing data describing all the possible powertrain power-split operations in the steady-state drive are obtained. A cost function to minimise or an objective function to maximise can be associated with each powertrain operation to select the best functioning points of the actuators for a given vehicle speed. In the proposed example, the maximum global efficiency is pursued. According to the direction of the battery power, P_{batt} can be an output or input power in the powertrain (see Fig. 5.1). Therefore, if $P_{batt} > 0$ the battery supports the ICE in the vehicle propulsion, and the global efficiency ε is:

$$\varepsilon(V_{veh}, \omega_{in}, T_{in}) = -\frac{P_{out}}{P_{fuel} + P_{batt}} \tag{5.18}$$

If $P_{batt} < 0$ the ICE delivers power in surplus which can be used to recharge the battery, and the global efficiency is:

$$\varepsilon(V_{veh}, \omega_{in}, T_{in}) = -\frac{P_{out} + P_{batt}}{P_{fuel}} \tag{5.19}$$

Eventually, it is possible to extract the maximum value from the matrix ε for a given vehicle speed and find the related ICE and electric machines operation resulting in the most efficient driving.

Nevertheless, the working points that violate a constructive constraint of actuators (Eqs. (5.6)) or batteries (Eq. (5.7)) should not be included among the potential optimal ones. Therefore, the final operating maps do not include the functioning points whereby the ICE or electric machines operation is not included within the maps of Fig. 5.4 and Fig. 5.5, or the battery power overcomes the maximum limit according to the considered SOC condition, as indicated in Table 5.7.

Table 5.7. Constraints on battery power according to the SOC condition.

SOC	$\boldsymbol{P_{max,charge}}$ **[kW]**	$\boldsymbol{P_{max,discharge}}$ **[kW]**
FREE	−120	120
0	−120	0
1	0	120
CONSTANT	0	0

In full-electric drive, the ICE is off and the MGs speed is univocally defined by Eqs. (5.13) for a given vehicle speed. Therefore, the only degree of freedom is the torque of one electric machine. The independent variable is p'_o, obtained by dividing the P_o available for any ω_o (from Fig. 5.5(b)) established for the considered vehicle speed. The results of Fig. 5.3 are interpolated for any p'_o to assess the operation of MG1 and compute the resulting battery power, according to Eq. (5.5). After excluding the results that violate the MGs constraints (Eqs. (5.6)), the global efficiency to maximise in full-electric operations is evaluated as:

$$\varepsilon(V_{veh}, T_o) = -\frac{P_{out}}{P_{batt}} \tag{5.20}$$

In full-electric operation, the battery SOC is supposed to be always sufficient to provide the demanded power.

5.2.4 Resulting optimal operating maps

The procedure described in Section 5.2.3 for calculating the optimal operating maps was implemented in MATLAB on the basis of the dimensionless results of Section 5.2.2. The results reported in this section were computed by considering a total vehicle mass equal to $m = 1750$ kg in plain ($\gamma = 0°$). The analysed vehicle speed ranges from 5 to 200 km/h.

For analysing the power-split drive, the mesh grid used in input to the MATLAB script to explore the ICE operation was obtained by the arrays $\omega_{in} = 1000{:}\,10{:}\,6000$ rpm and $T_{in} = 10{:}\,1{:}\,140$ Nm. The results of Fig. 5.6, Fig. 5.7, Fig. 5.8, Fig. 5.9, Fig. 5.10, and Fig. 5.11 show the optimal operating points resulting from the optimisation procedure aimed at maximising the global efficiency.

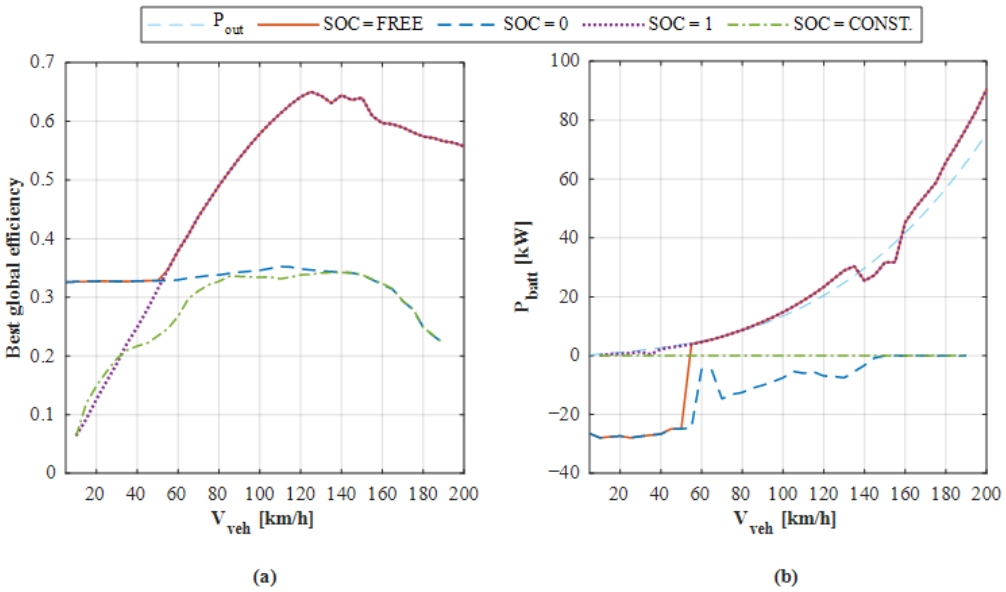

Fig. 5.6. (a) Best global efficiency in power-split operation; **(b)** battery power in the optimal power-split operating points.

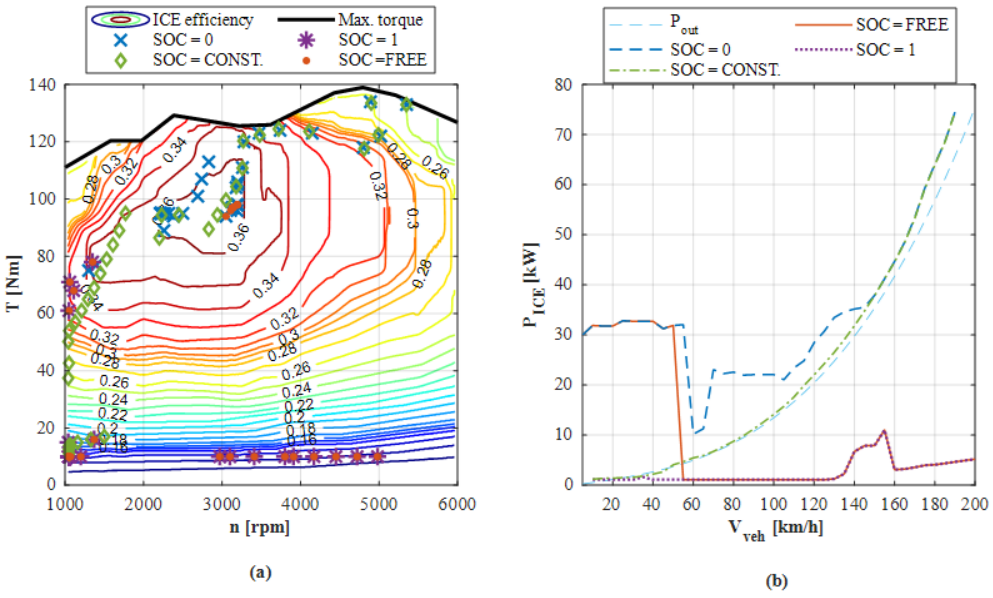

Fig. 5.7. ICE optimal power-split operation: **(a)** ICE functioning points; **(b)** ICE power.

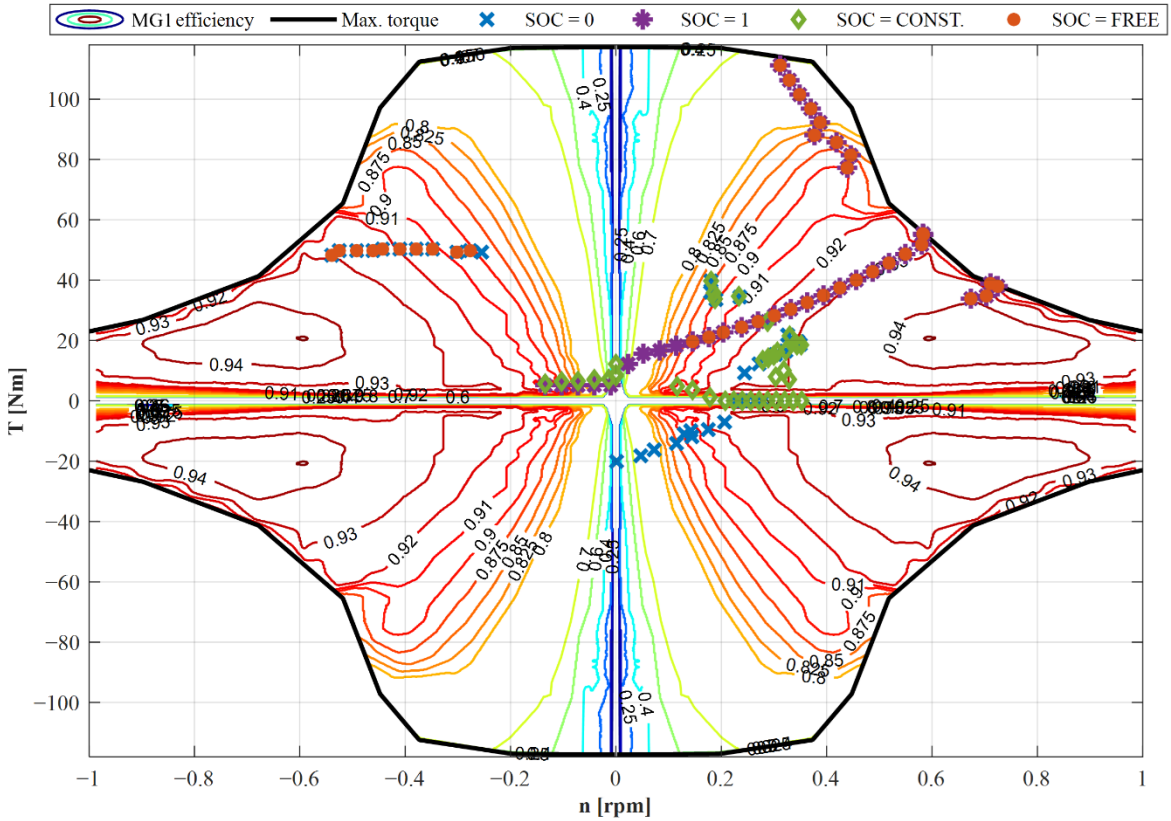

Fig. 5.8. MG1 optimal functioning points in power-split operation.

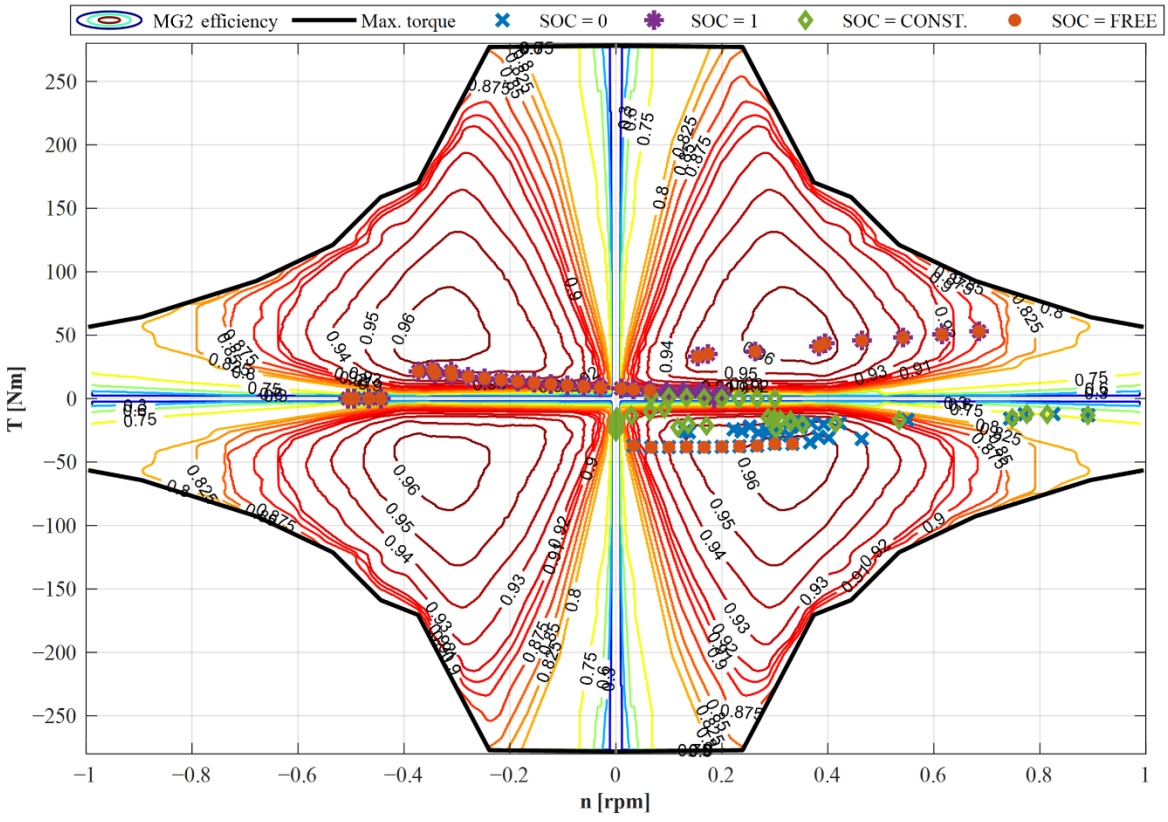

Fig. 5.9. MG2 optimal functioning points in power-split operation.

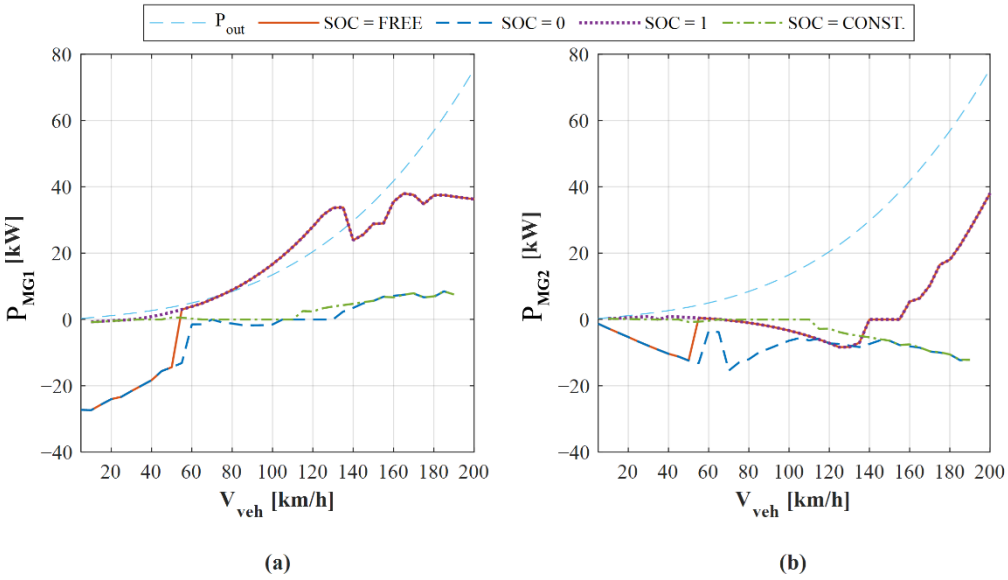

Fig. 5.10. Electric machines optimal power in power-split operation: **(a)** MG1 power; **(b)** MG2 power.

Fig. 5.6(a) shows that the best results are achieved for SOC = FREE since the availability of the battery both as a power source and power storage enables the most efficient power flows (Fig. 5.10). Nevertheless, the maximum global efficiency is lower than 0.33 up to 50 km/h, therefore it would be more advisable to turn off the engine and drive in full-electric operation. The only reason to let the ICE work at lower speeds is to recharge the battery if possible (SOC = FREE or SOC = 0). In this case, the ICE should operate in the maximum efficiency region, otherwise, it should be turned off also for higher speeds if the battery can supply power for propulsion (SOC = FREE or SOC = 1) (Fig. 5.7). In this way, the global efficiency is significantly enhanced (Fig. 5.6(a)), since the demanded output power would be provided by the electric unit (Fig. 5.6(b)), which is more efficient than the ICE.

Nevertheless, a more robust control strategy should regulate the battery power according to the instantaneous SOC to ensure sufficient range. Indeed, for speeds higher than 100 km/h, the optimal powertrain operation would be achieved at the expense of the driving range. Therefore, over 100 km/h would be even more advisable to limit the power supplied by the battery and increase that provided by the ICE, even though this would reduce the global efficiency.

On the other hand, if the battery is completely discharged (SOC = 0) or a sustaining-charge driving is desired (SOC = CONSTANT), the demanded output power should be provided mainly by the engine (Fig. 5.7(b)). In this case, the battery charging is recommended between 50 and 145 km/h, while over 145 km/h keeping the SOC constant would result in greater efficiency. Nonetheless, since the ICE maximum power is 75 kW [35], the vehicle speed cannot exceed 190 km/h with SOC = 0 or SOC = CONSTANT.

Fig. 5.8, Fig. 5.9, and Fig. 5.10 show the optimal utilisation of the electric machines in

power-split operation. They suggest using both MG1 and MG2 as generators for battery recharging up to 50 km/h. It is the same from 50 to 130 km/h if SOC = 0, while MG1 should be used as a motor and MG2 as a generator if the battery can provide power (SOC = FREE or SOC = 1). In the latter case, the mechanical energy converted to electric energy by MG2 is reconverted to the mechanical form by MG1. Over 155 km/h, both MG1 and MG2 should be used as motors for SOC = FREE or SOC = 1.

The optimal mode selection can be obtained from the optimal overall transmission ratio of Fig. 5.11. Recalling that the input-split mode is engaged for $\tau < \tau_{\#i}$ and the compound-split mode for $\tau > \tau_{\#i}$ (see Fig.5.2(a)), Fig. 5.11 shows that for lower speeds the input-split mode should be preferred, while the compound-split mode is advisable at higher speeds. Moreover, it is worth noting that for SOC = 0 and SOC = CONSTANT (i.e., if the battery cannot provide power for propulsion) the optimal overall speed ratio at medium-high speed is the one that realises the PGs synchronism, whereby the mechanical power losses are minimised (Fig. 5.2(b)).

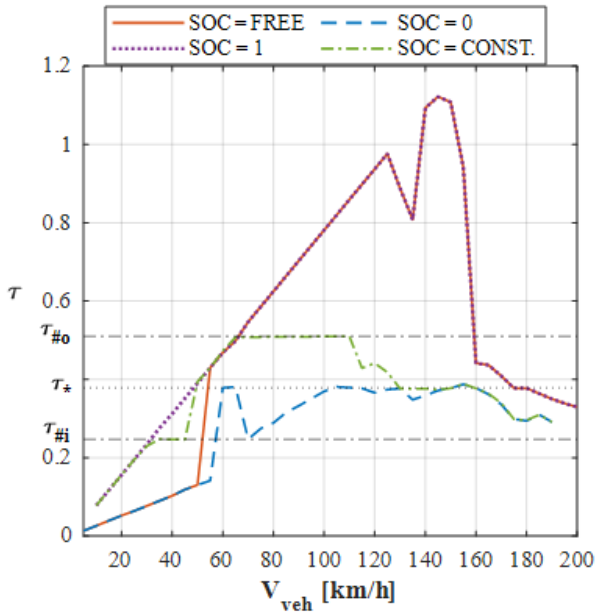

Fig. 5.11. Optimal overall transmission ratio and mode selection in power-split operation.

For analysing the full-electric drive, the array used in input to the MATLAB script was $T_o = -280{:}\,1{:}\,280$ Nm. The results of Fig. 5.12 and Fig. 5.13 are related to the best operating points of the electric MGs resulting in the highest global efficiency for each vehicle speed.

Fig. 5.12(a) shows that the global efficiency in EV mode is averagely higher than the one achievable in power-split operation. However, the full-electric drive is suggested only for low–medium speed because exploiting the only battery power for propelling the vehicle in steady-state drive at higher speeds would imply a reduced range. Over 145 km/h, full-electric

driving cannot be achieved because the required rotational speed of MG2 would overcome its maximum value. Fig. 5.13 shows that the optimal EV operation in steady-state drive involves the exploitation of MG1 except for two limited vehicle ranges from 5 to 15 km/h and from 50 to 60 km/h. From 135 to 145 it is advisable to operate with both electric machines acting as motors.

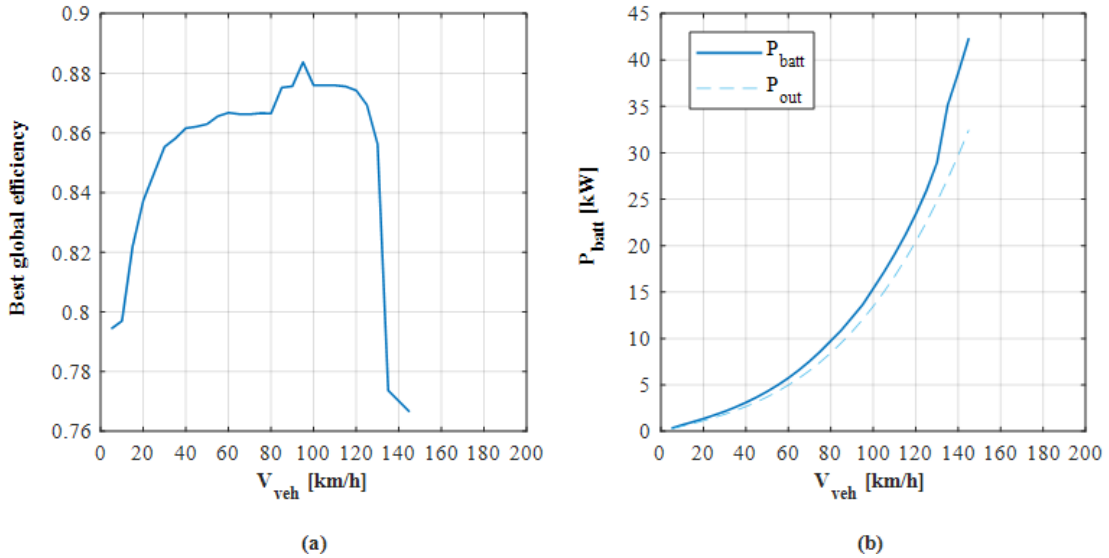

Fig. 5.12. (a) Best global efficiency in EV operation; **(b)** battery power in the optimal EV operating points.

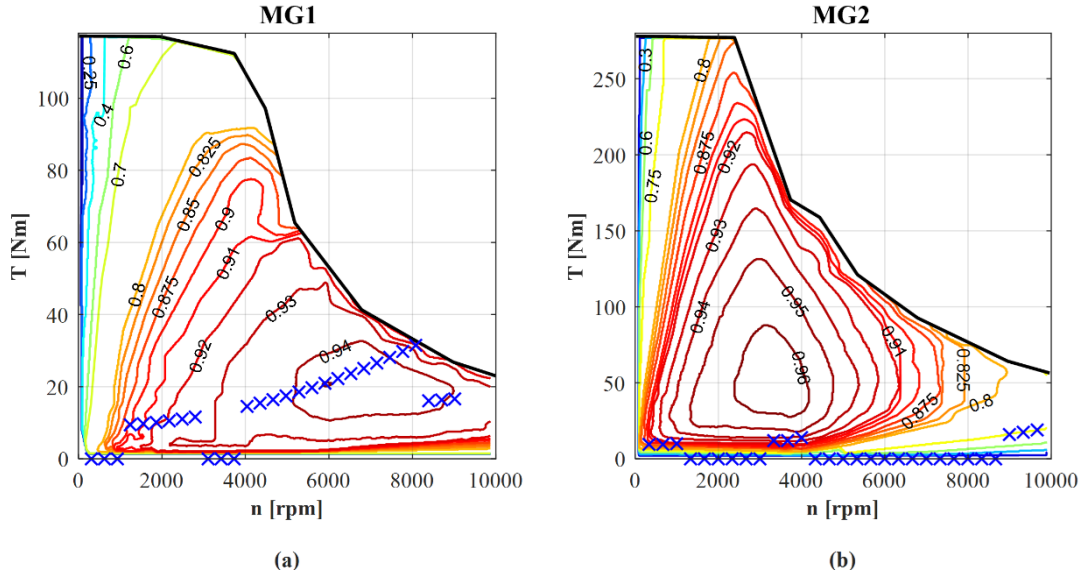

Fig. 5.13. Electric machines optimal EV operation: **(a)** MG1 functioning points; **(b)** MG2 functioning points.

5.3 Case study on the comparison between two performance indices

Assuming as objective function the powertrain global efficiency as defined in Eqs. (5.18)-(5.19) could lead to the underuse of the ICE and overuse of the battery power for vehicle traction, given the lower efficiency of the thermal unit in comparison with the efficiency of

the electric equipment. The worse performance of the ICE is due to the fact that it converts low-quality energy of fossil fuel into mechanical energy; instead, the electric motors generate mechanical energy from high-quality electric energy, which, however, is usually obtained from the ICE operation, especially in FHEVs. To consider the profoundly different working principles and performance of ICE and electric MGs, a power-weighted efficiency approach was proposed in [67,69,160,161]. The underpinning idea is that the actual efficiency of each actuator should be normalised to its maximum efficiency to fairly compare the performance of ICE and electric unit. However, the approach proposed in this paper differs from the power-weighted efficiency approach of [67,69,160,161] mainly because of the inclusion of mechanical power losses evaluation, which are neglected in [67,69,160,161].

This section, adapted from [143], proposes a comparison between the real powertrain efficiency and an equivalent efficiency that includes the normalised efficiency of the actuators. A single-mode output-split transmission is considered as a case-study; it is described in Section 5.3.1, which also reports the results of the dimensionless analysis. Section 5.3.2 introduces the new performance index definition and calculation; Section 5.3.3 reports and discusses the results of the comparison.

The first performance index taken into account is the real global efficiency of the powertrain ε, already described in Section 5.2.3 and indicated as the ratio between the output power delivered to the wheels (P_{out}) and the input power provided by the fuel combustion (P_{fuel}), corrected by the potential battery power flow (P_{batt}) according to its direction:

$$\varepsilon(V_{veh}, a_{veh}, \omega_{in}, T_{in}) = -\frac{P_{out} + \left(\frac{1-\alpha}{2}\right) P_{batt}}{P_{fuel} + \left(\frac{1+\alpha}{2}\right) P_{batt}} \tag{5.21}$$

where $\alpha = sign(P_{batt})$. According to the conventional positive sign of power flows $\alpha = 1$ for battery discharge ($P_{batt} > 0$, in input to the powertrain), while $\alpha = -1$ for battery recharge ($P_{batt} < 0$, in output). Thus, Eq. (5.21) is equivalent to Eqs. (5.18)-(5.19).

The second performance index is defined as equivalent efficiency, which is formally defined as the powertrain global efficiency of Eq. (5.21), but includes fictitious fuel and battery power flows derived from the normalisation of the actuators efficiency to their maximum efficiency detected from their efficiency maps of Fig. 5.16. Thus, the fuel power of Eq. (5.4) and the battery power of Eq. (5.5) are rearranged as follows:

$$P_{fuel}^{eq}(\omega_{in}, T_{in}) = \frac{\omega_{in} T_{in}}{\left(\frac{\eta_{ICE}}{\eta_{ICE,max}}\right)} \tag{5.22}$$

$$P_{batt}^{eq}(V_{veh}, a_{veh}, \omega_{in}, T_{in}) = \bar{p}_i P_{in}\left(\frac{\eta_{MG1}}{\eta_{MG1,max}}\right)^{-sign(\bar{p}_i)} + \bar{p}_o P_{in}\left(\frac{\eta_{MG2}}{\eta_{MG2,max}}\right)^{-sign(\bar{p}_o)} \quad (5.23)$$

Thus, the equivalent efficiency ε_{eq} is:

$$\varepsilon_{eq}(V_{veh}, a_{veh}, \omega_{in}, T_{in}) = -\frac{P_{out} + \left(\frac{1-\alpha_{eq}}{2}\right)P_{batt}^{eq}}{P_{fuel}^{eq} + \left(\frac{1+\alpha_{eq}}{2}\right)P_{batt}^{eq}} \quad (5.24)$$

where $\alpha_{eq} = sign\left(P_{batt}^{eq}\right)$. It should be noted that ε_{eq} does not have any physical meaning, in contrast to ε.

5.3.1 *Output-split transmission under analysis and dimensionless results*

The PS-CVT under analysis is an output-split transmission designed in [148] through the modular parametric procedure adopted in Chapter 3. The constructive layout of the transmission is shown in Fig. 5.14. The PG Willis ratio is $\Psi = -0.4$, while the OGs fixed ratios are $k_{in} = \omega_{in}/\omega_R = 0.82$ and $k_{out} = \omega_{out}/\omega_C = 0.25$.

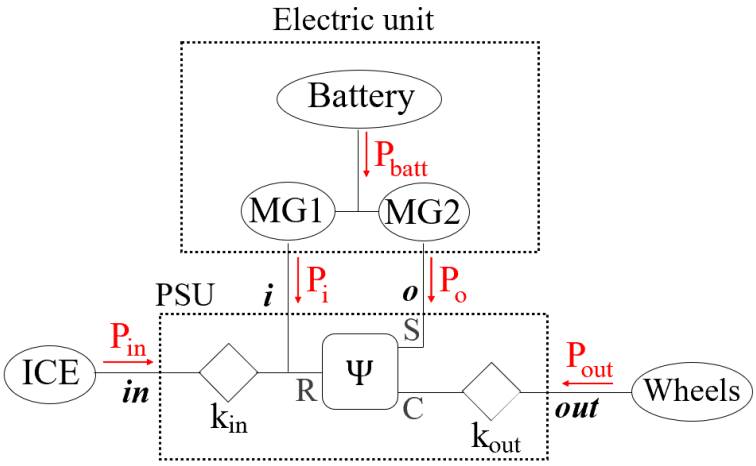

Fig. 5.14. Output-split transmission under analysis. The arrows show the positive power flows.

The PSU functional parameters are $\tau_{\#o} = 0.218$, $\tau_{\#i} = \tau_{o\#i} = -\infty$, and $\tau_{i\#o} = 1.22$. The application of the analysis procedure of Chapter 2 leads to the calculation of the dimensionless results shown in Fig. 5.15, where the MGs speed ratios, the normalised PSU meshing losses, and the normalised real mechanical power required to/supplied by the electric MGs are reported.

The meshing losses of Fig. 5.15(b) were calculated as a fraction of the input power as a function of the overall speed ratio τ and the opposite of the overall power ratio $\eta = -P_{out}/P_{in}$ by adding the meshing losses in the final drive and in the PGs:

$$\bar{p}_L = \bar{p}_L|_{OG_{in}} + \bar{p}_L|_{OG_{out}} + \bar{p}_L|_{PG} \quad (5.25)$$

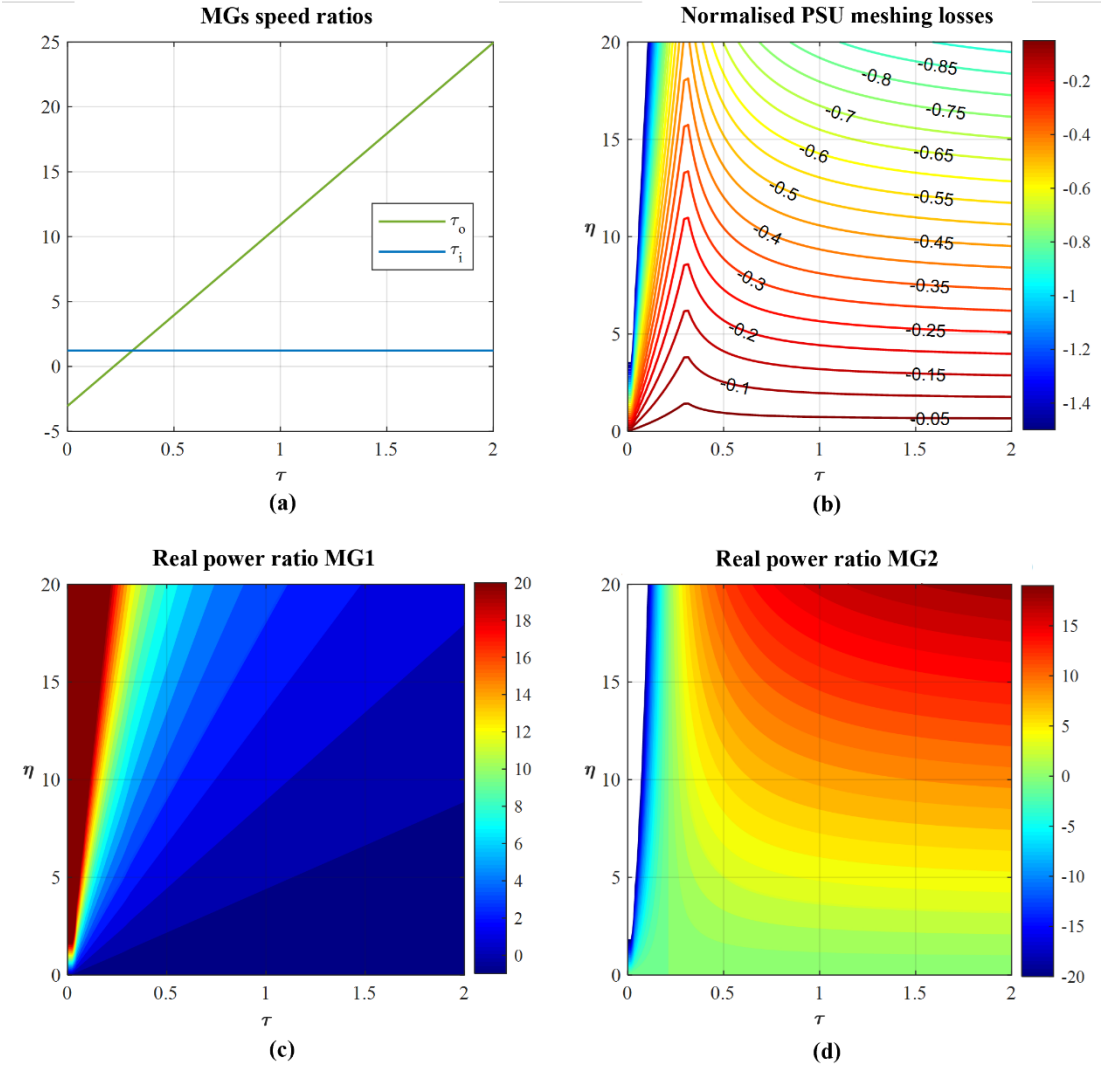

Fig. 5.15 Results of the dimensionless analysis: **(a)** MGs speed ratios; **(b)** PSU meshing losses as a fraction of the input power; **(c)** MG1 real power as a fraction of the input power; **(d)** MG2 real power as a fraction of the input power.

where:

$$\begin{aligned} \bar{p}_L|_{OG_{in}} &= -\left|\left(1-\eta_{OG_{in}}\right)p_{in}\right| \\ \bar{p}_L|_{OG_{out}} &= -\left|\left(1-\eta_{OG_{out}}\right)p_{out}\right| \\ \bar{p}_L|_{PG} &= -\left|\left(1-\eta^S\right)\left(\frac{\phi^o_{out/i}-\psi^S_{C/R}}{1-\psi^S_{C/R}}\right)p_{out}\right| \end{aligned} \tag{5.26}$$

with $p_{in}=1$ and $p_{out}=-\eta$. The OGs efficiency is $\eta_{OG_{in}}=\eta_{OG_{out}}=0.98$. The notation of Table 5.8 was considered to assess the meshing losses in the PG.

Table 5.8. PG reference notation, fixed-Z speed ratio, and fixed-Z efficiency.

x* - *X	***y* - *Y***	***z* - *Z***	η_0	$\psi^Z_{X/Y}$	η^Z
out – Carrier	*i* – Ring	*in* – Sun	0.96	$\psi^S_{C/R}=\dfrac{1}{1-\Psi}$	$\eta^S=\dfrac{1-\Psi}{1-\dfrac{\Psi}{\eta_0}}$

5.3.2 *Optimal indices assessment*

The values of interest of τ and η necessary to interpolate the dimensionless results of Fig. 5.15 are defined by establishing the desired range of vehicle speed to analyse and the resulting demanded power, computed through Eq. (5.1) considering the vehicle parameters of Table 5.9 and a coefficient of the rotational inertia $\delta = 1.10$. In contrast to Section 5.2 which focuses on the steady-state drive, vehicle acceleration is considered and simulated in a backward-facing approach to assess the optimal operating maps according to Section 5.1.

Table 5.9. Vehicle parameters.

Vehicle mass m [kg]	Rolling resistance f_r [-]	Drag coefficient C_d [-]	Frontal area A_f [m^2]	Wheel radius R_w [m]
2000	0.012	0.4	2.5	0.33

For each feasible combination of V_{veh} and a_{veh}, the whole ICE working range must be explored to investigate all the possible powertrain functioning points. Thus, ICE operations can be freely selected from the ICE efficiency map of Fig. 5.16(a). Each engine operating point involves a certain engine efficiency. As a result, the power supplied by the fuel can be easily calculated through Eq. (5.4).

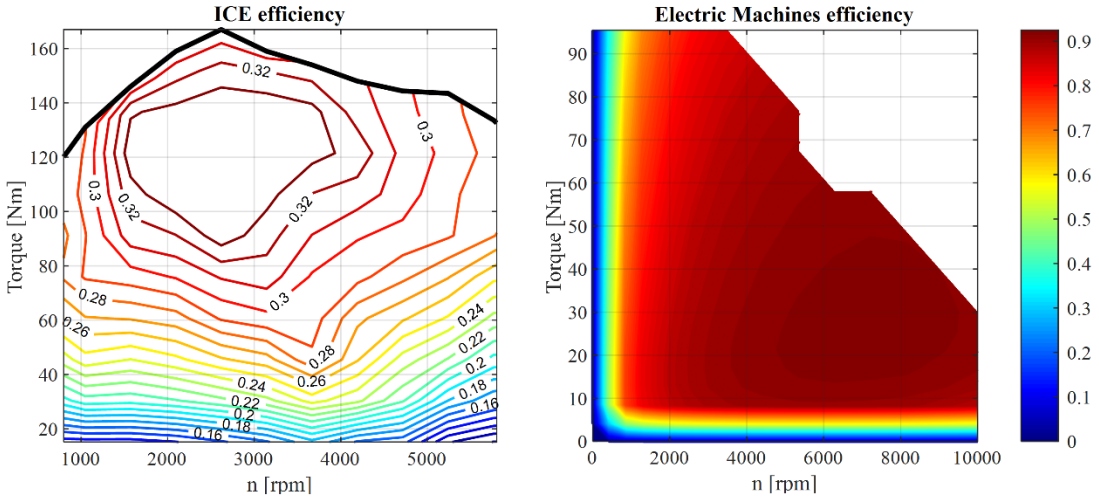

Fig. 5.16. (a) ICE efficiency map; **(b)** electric MGs efficiency map.

The results of Fig. 5.15 are interpolated for any combination of τ and η to assess the MGs speed and power necessary to obtain the resulting battery power, according to Eq. (5.5) and the MGs efficiency dependant on their operating point. In this powertrain, MG1 and MG2 are identical [148] and the efficiency map of Fig. 5.16(b) is considered for both MGs in motoring and generating operations.

The described procedure outputs a set of matrices containing all the possible powertrain

operations for each combination of vehicle speed and acceleration. For any powertrain operation, the two performance indices ε and ε_{eq} of Eqs. (5.21) and (5.24) are assessed.

After the calculation of the performance indices, only the feasible powertrain operations are eligible to become the optimal ones that maximise ε or ε_{eq}. Hence, all the solutions violating the constraints on the actuators speed and torque (Eqs. (5.6)) or the battery power (Eq. (5.7)) are excluded according to the actuators working range of Fig. 5.16 and the SOC constraints of Table 5.10.

Table 5.10. Constraints on battery power according to the SOC condition.

SOC	$P_{max,charge}$ [kW]	$P_{max,discharge}$ [kW]
FREE	−70	70
0	−70	0
1	0	70
CONSTANT	0	0

5.3.3 Results and comparison

The procedure described in Section 5.3.2 to assess the performance indices was implemented in MATLAB for a vehicle speed ranging from 0 to 200 km/h and a vehicle acceleration ranging from 0 to 2 m/s^2. A null road slope was considered ($\gamma = 0$). However, the calculation can be repeated for any desired road slope. The mesh grid used in input to the MATLAB script was derived by imposing $\omega_{in} = 800{:}\,10{:}\,5800$ rpm and $T_{in} = 20{:}\,1{:}\,167$ Nm.

For each combination of vehicle speed and acceleration, this section provides the optimal powertrain operations that maximise the real global efficiency or equivalent efficiency in terms of battery power and ICE and MGs functioning points.

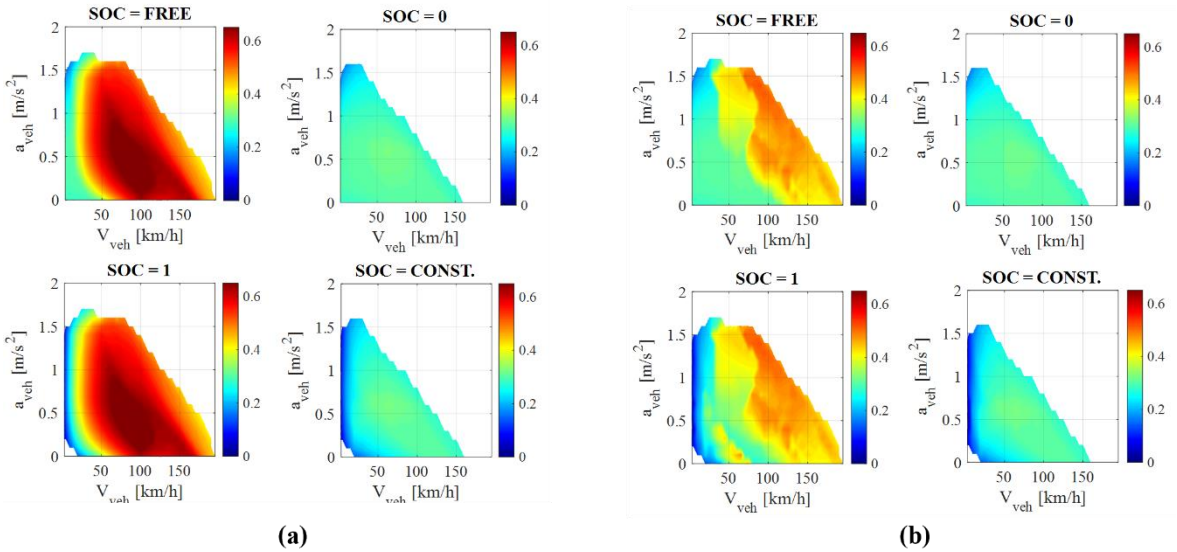

Fig. 5.17. Real global efficiency resulting from ε optimisation **(a)** and ε_{eq} optimisation **(b)**.

Fig. 5.17 shows a comparison between the optimal real global efficiency ε obtained by maximising the real global efficiency itself (Fig. 5.17(a)) or the equivalent global efficiency ε_{eq} (Fig. 5.17(b)). The optimisation of the two performance indices leads to different results. In particular, when the battery can provide electric energy, namely, for $\mathrm{SOC} = \mathrm{FREE}$ and $\mathrm{SOC} = 1$, the optimisation of the equivalent efficiency significantly differs from the optimisation of the real global efficiency. This is due to the diverse utilisation of the engine (Fig. 5.18) and battery power (Fig. 5.19). The real powertrain global efficiency is optimised by minimising the ICE contribution to the propulsion (Fig. 5.18(a)), or, in other words, by maximising the power supplied by the battery (Fig. 5.19(a)) when possible, because of the much lower efficiency of the engine in comparison to the efficiency of the electric MGs. The minimisation of the ICE operation results in higher real global efficiency (Fig. 5.17(a)). On the contrary, the equivalent efficiency is maximised when the engine operates within its most efficient region (Fig. 5.18(b)); thus, less battery power is required for the traction, but surplus engine power is used for battery recharging (Fig. 5.19(b)). However, the resulting real global efficiency is lower (Fig. 5.17(b)).

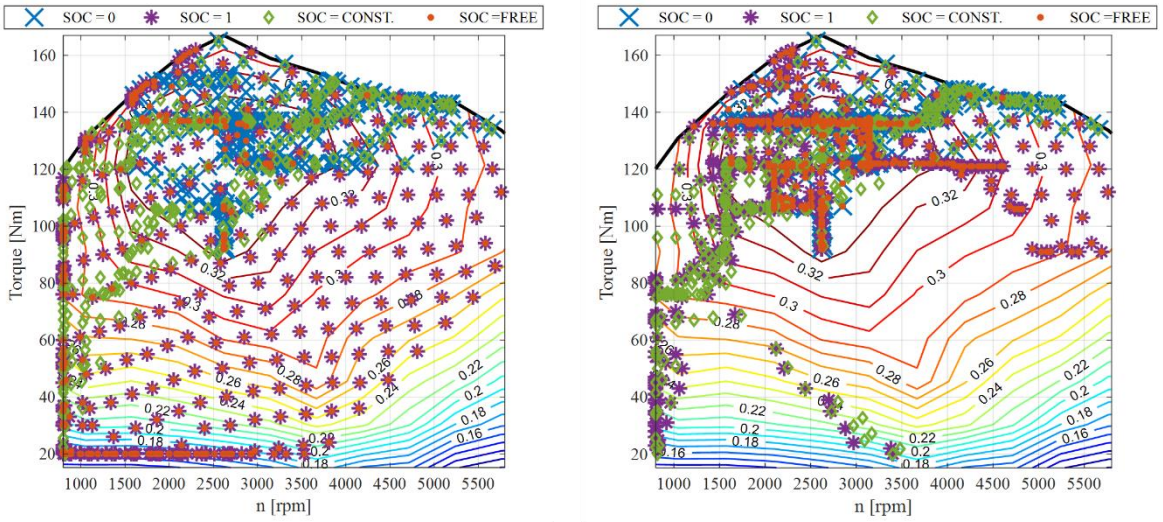

Fig. 5.18. ICE operation resulting from ε optimisation **(a)** and ε_{eq} optimisation **(b)**.

These results suggest that the optimisation of the actual powertrain efficiency would lead to a long-term charge-depleting drive, while the maximisation of the equivalent efficiency would allow a charge-sustaining drive. Hence, the first approach would be more suitable for PHEVs, while the second for FHEVs that cannot be recharged from the grid.

A deeper analysis of the results in Fig. 5.17, Fig. 5.18, and Fig. 5.19 suggests a correlation between the trend of the highest real global efficiency achievable in each optimisation scenario by varying the constraints on the battery SOC. Indeed, in general, the real global

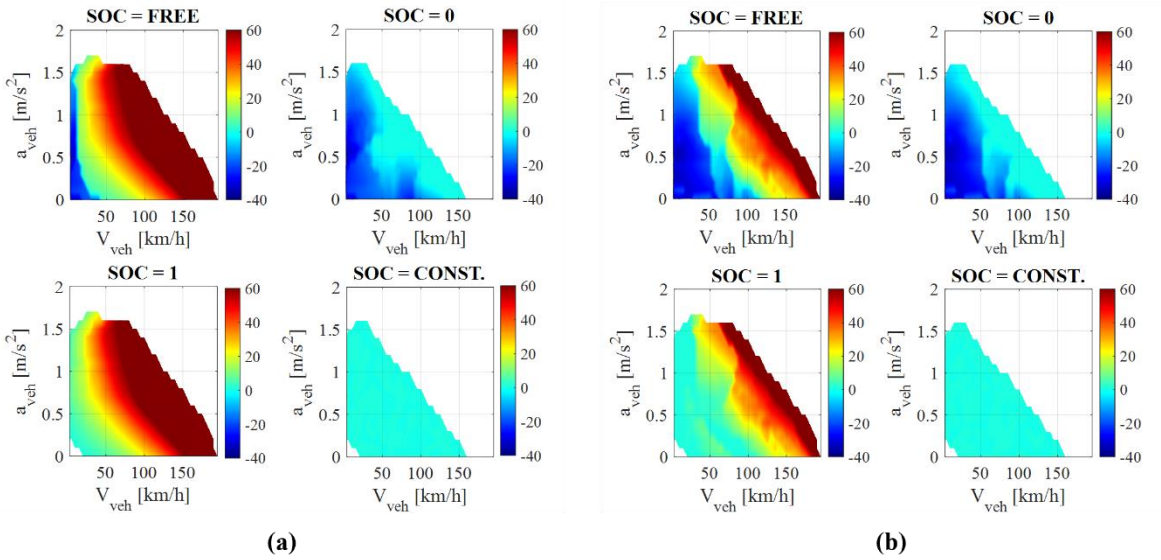

Fig. 5.19. Battery power ([kW]) resulting from ε optimisation **(a)** and ε_{eq} optimisation **(b)**.

efficiency is higher if the battery SOC is unconstrained (SOC = FREE). If this result is obvious when the optimised index is the real global efficiency itself, it cannot be taken for granted when the equivalent efficiency is optimised, precisely because they are two different objective functions. Indeed, for a speed range of 30-75 km/h and low acceleration, the best global efficiency is achieved for SOC = 1 and not for SOC = FREE when the equivalent efficiency is optimized (Fig. 5.17(b)). Moreover, both strategies output similar results when the battery is completely discharged (SOC = 0) or a constant SOC is desired (SOC = CONSTANT). In this case, lower speeds and accelerations can be reached because the battery cannot support the engine for traction. Also, the ICE power increases for both optimisation strategies for high vehicle speeds and accelerations because the battery power would not be sufficient to provide the demanded power alone. Moreover, the condition whereby the ICE is turned off was not simulated; thus, low vehicle speeds and accelerations appear unfeasible for SOC = 1 and SOC = CONSTANT because the battery cannot gather the engine surplus power.

Fig. 5.20 and Fig. 5.21 show the optimal operations of MG1 and MG2, respectively. The functioning points of each MG are similar for SOC = 0 and SOC = CONSTANT for both optimisation strategies. Instead, they differ if SOC = FREE and SOC = 1, where both MG1 and MG2 are more exploited as generators when the equivalent efficiency is maximised (Fig. 5.20(b) and Fig. 5.21(b)). On the contrary, the optimisation of the real global efficiency requires more motoring operations (Fig. 5.20(a) and Fig. 5.21(a)), accordingly to the fact that more battery power is provided for vehicle propulsion.

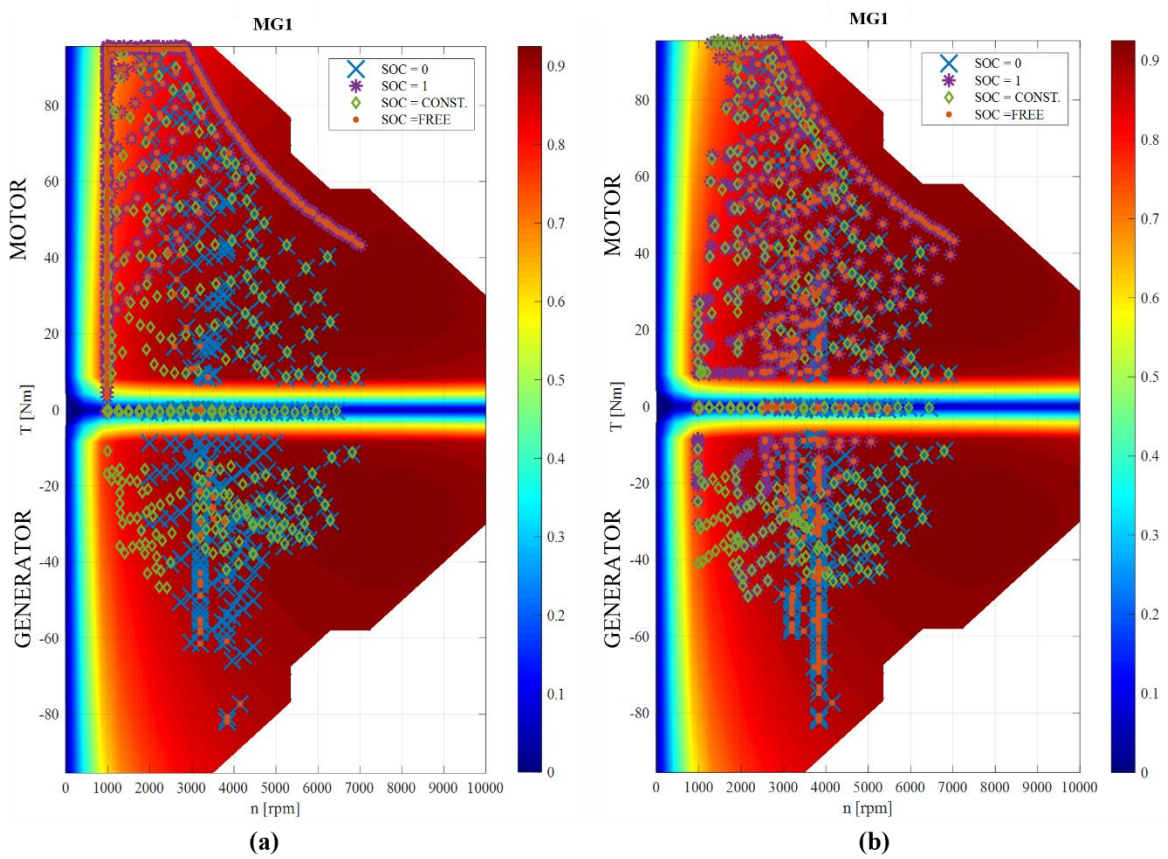

Fig. 5.20. MG1 operation resulting from ε optimisation **(a)** and ε_{eq} optimisation **(b)**.

Observing the ICE and MGs optimal speed, torque and power as functions of vehicle speed and acceleration (figures not reported here for brevity but deducible also from Fig. 5.18, Fig. 5.20, and Fig. 5.21) turns out that only MG2 is widely used at its maximum performance. In contrast, the ICE is strongly underused for low vehicle speeds and accelerations if the real global efficiency is maximised. At the same time, MG1 is rather underexploited if the equivalent efficiency is maximised. Indeed, the design of the transmission under analysis carried out in [148] aimed to potentially provide the maximum power to the wheels for any driving condition, even at low speed when high power is not required. No ICE and MGs efficiency map was considered during the design stage, nor an optimisation of any efficiency was pursued. Thus, a more efficiency-oriented design procedure could have led to different sizes of the actuators and powertrain performance.

To conclude the comparison, Fig. 5.22 shows the efficiency of ICE and MGs in each SOC scenario derived from the optimisation of the real global efficiency, while Fig. 5.23 shows their efficiency leading to the optimisation of the equivalent efficiency. These results indicate the main difference between the two performance indices. Fig. 5.23 shows that the optimisation of the equivalent efficiency leads to the maximisation of the efficiency of each power source, battery SOC notwithstanding. On the contrary, the optimisation of the real

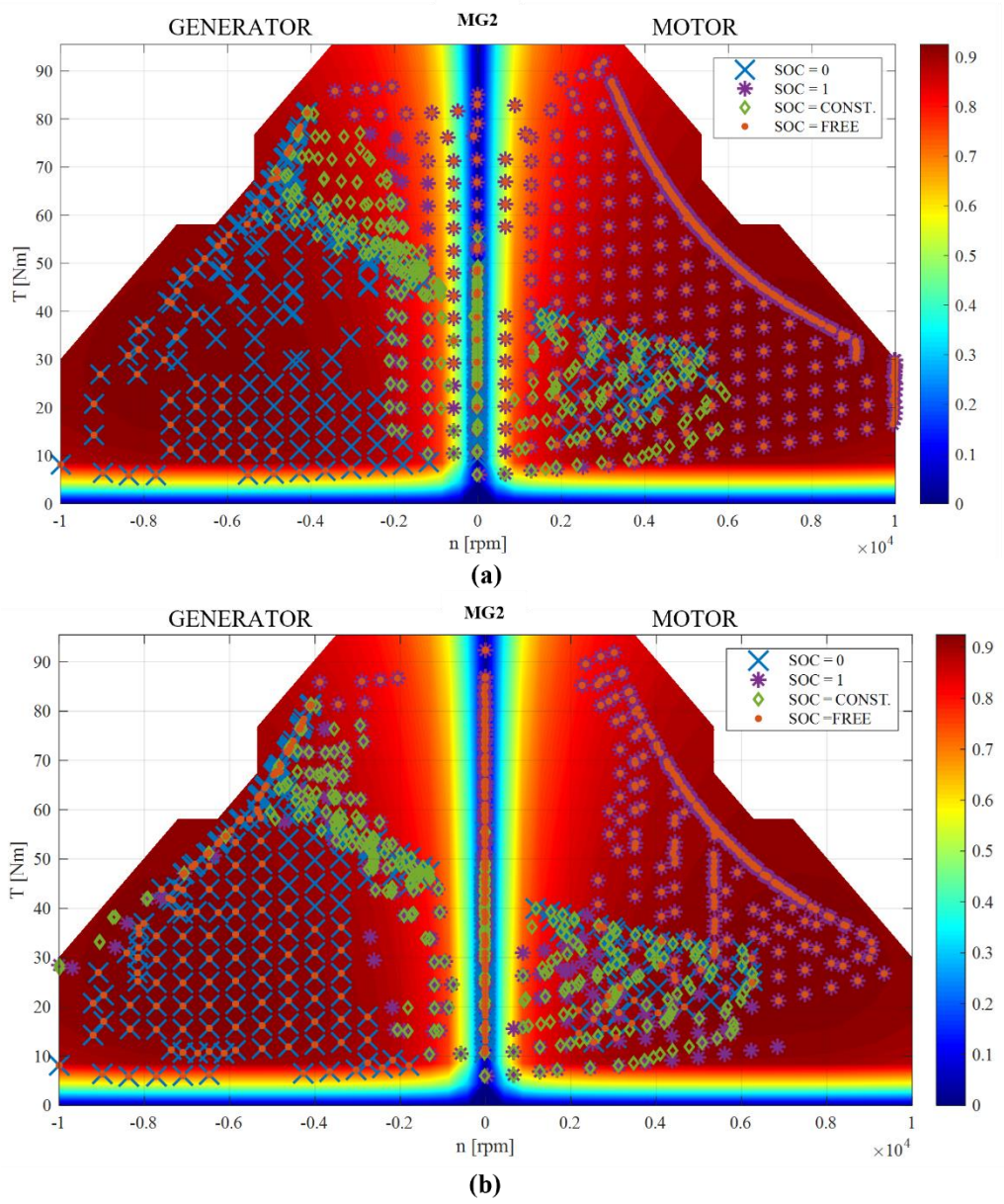

Fig. 5.21. MG2 operation resulting from ε optimisation **(a)** and ε_{eq} optimisation **(b)**.

global efficiency minimises the ICE power flows when the battery power is available, even though this implies a low-efficiency functioning point. Indeed, since the power flows provided by the engine and the battery are combined in a parallel way, the global efficiency is the average of the efficiencies of the electric and thermal paths, weighted on the basis of the power transmitted through each path. Therefore, reducing the power transmitted by the less efficient path, i.e., the ICE, improves the global efficiency. Nevertheless, for $\mathrm{SOC} = 0$ and $\mathrm{SOC} = \mathrm{CONSTANT}$, both approaches maximise the actuators efficiency. The zones where the MGs efficiency is zero in Fig. 5.22 and Fig. 5.23 are due to the fact that MG1 is running without providing any torque, while MG2 is stationary at its mechanical point.

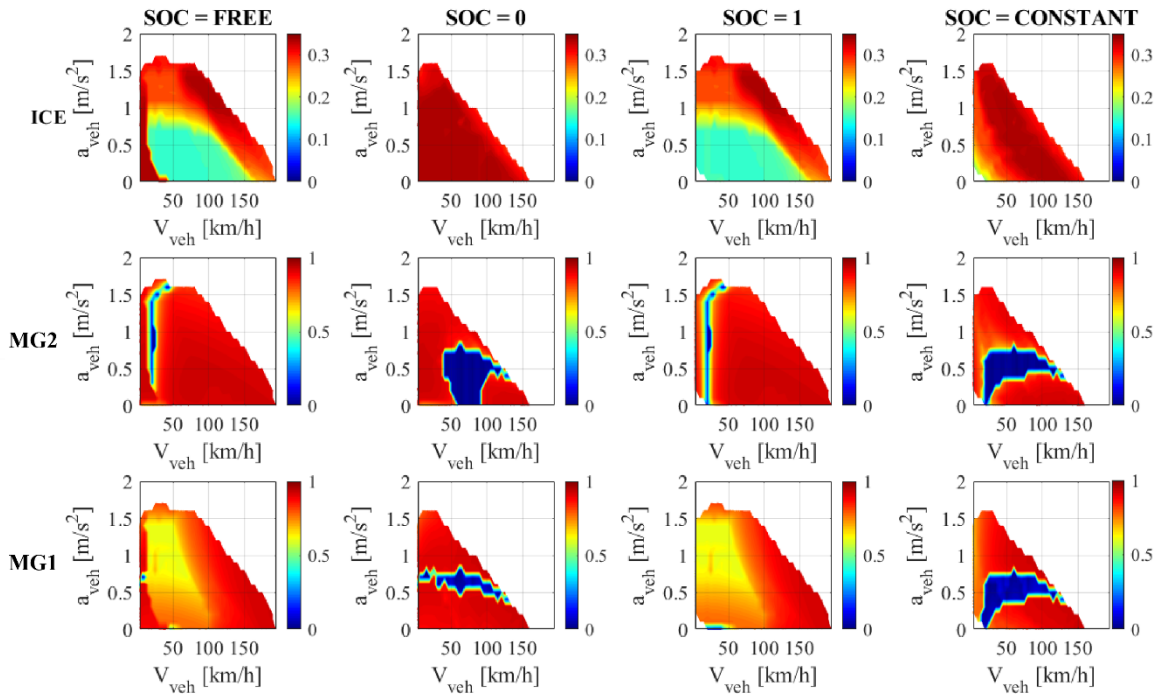

Fig. 5.22. ICE, MG2, and MG1 efficiency resulting from ε optimisation.

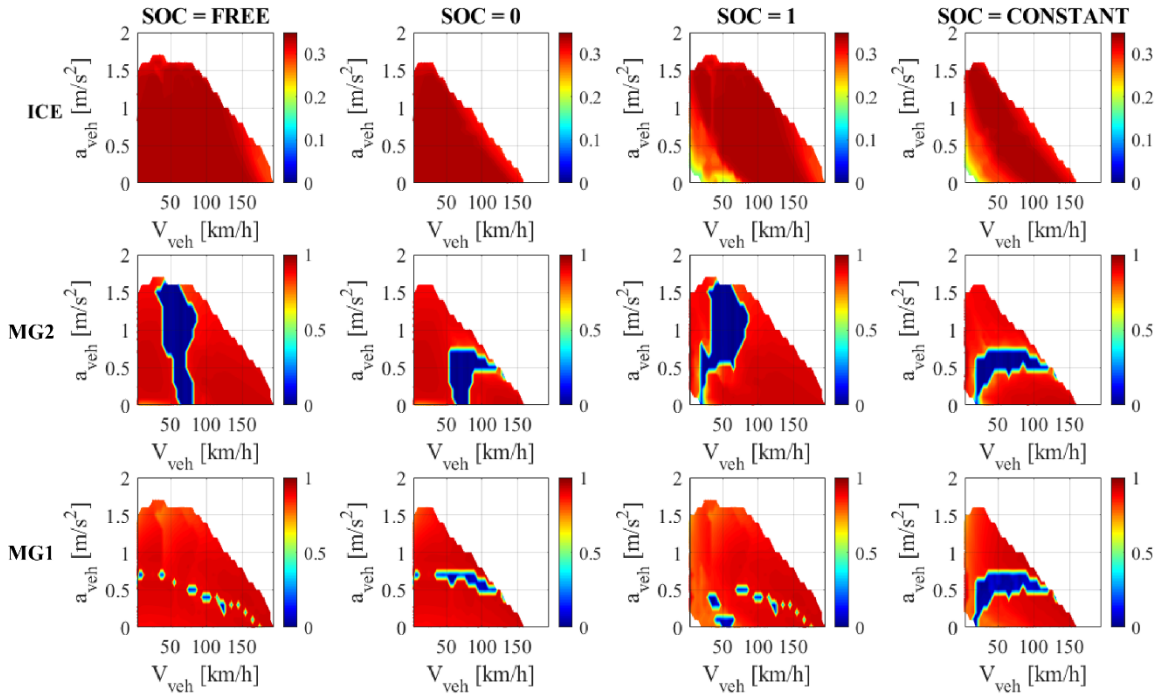

Fig. 5.23. ICE, MG2, and MG1 efficiency resulting from ε_{eq} optimisation.

CHAPTER 6
PARAMETRIC INTERNAL MODELS FOR MODEL PREDICTIVE CONTROL EMS

Model predictive control is one of the most promising energy management strategies for hybrid electric vehicles. However, owing to constructive complexity, the multi-mode power-split powertrain requires dedicated mathematical tools to model the mode switch and transmission power losses within the internal model of the controller. Thus, the transmission losses are usually neglected and the mode switch is optimised through preliminary offline simulations (see Section 1.4).

The features of the parametric model described in Chapter 2 make it suitable to integrate the discrete problem of the mode switch within a continuous MPC formulation. Indeed, changing the constructive layout, e.g., after a mode shift in a multi-mode PS-CVT, does not result in different equations, as it is for the other PS-CVT models available in the literature, but only in different functional parameters. Therefore, it is possible to model several modes within the same controller by introducing continuous switch functions to consider the functional parameters variation. As a result, any preliminary offline optimisation is unnecessary for the mode shift strategy, which, instead, can be embedded within the receding horizon framework of a single control problem.

Moreover, the same parametric model includes a fast approximated procedure to calculate the meshing losses in the PSU as a function of the PSU operating point, without requiring any case-specific formulation depending on the power flow direction (see Section 2.4). Thus, such a mathematical treatment is suitable for MPC implementation. For the first time in the field of MPC-based EMS for power-split HEVs, the influence of variable PSU power losses has been assessed by comparing internal models with different levels of complexity. The influence of actuators inertial load and MGs efficiency is also considered. The results of this comparison are useful to assess how neglecting some of these factors may affect the effectiveness of the EMS considered in the powertrain design phase when some parameters are to be defined yet.

The content of this chapter has been developed during a research period abroad at the Centre of Automotive Engineering of the University of Surrey. The procedure and the results discussed in the following have been presented in [144]. The remainder of the chapter is organised as follows: Section 6.1 presents a universal formulation, based on the parametric

model of Chapter 2, to model any power-split HEV within an MPC internal model; Section 6.2 provides an example of application to the multi-mode Voltec II, used as a case study; Section 6.3 describes the preliminary analysis that led to the definition of the internal models selected for the comparison; Section 6.4 defines the MPC problem formulation and presents a benchmarking control strategy; the results of the comparison of the MPCs embedding the different internal models and the benchmarking controller are presented and discussed in Section 6.5.

6.1 Universal parametric model for power-split HEVs

The implementation of the MPC framework requires to shift from the dimensionless mathematical treatment proposed in Chapter 2 to a dimensional model that outputs the operating point of each electric MG as a function of the vehicle speed, the driver's demand, and ICE operations resulting from the EMS, in order to assess the instantaneous fuel consumption and battery SOC. Any component in the PSU is considered as a rigid body; the inertia of ICE and MGs is included, while the inertia of shafts and gears is neglected. Fig. 6.1 shows a general representation of any power-split HEV.

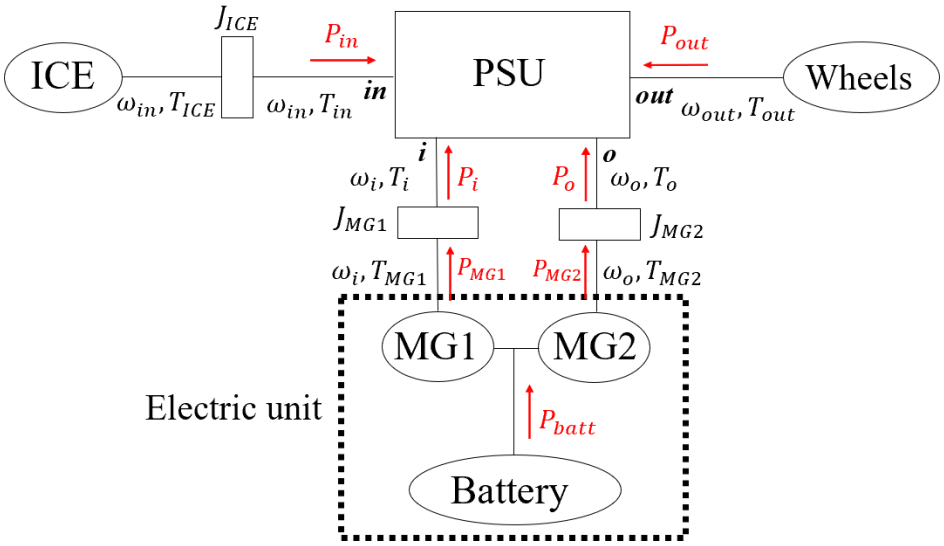

Fig. 6.1. Universal schematisation for power-split powertrain. The arrows show the positive power flows.

From Eqs. (2.12)-(2.13), the speed of the electric MGs is:

$$\begin{aligned} \omega_i &= \frac{\tau_{i\#o}}{\tau_{\#o} - \tau_{\#i}} (\omega_{out} - \tau_{\#i}\omega_{in}) \\ \omega_o &= \frac{\tau_{o\#i}}{\tau_{\#i} - \tau_{\#o}} (\omega_{out} - \tau_{\#o}\omega_{in}) \end{aligned} \tag{6.1}$$

ω_{out} is directly proportional to the vehicle speed. Equivalently, accelerations are ruled by the same relations:

$$\begin{aligned}\dot{\omega}_i &= \frac{\tau_{i\#o}}{\tau_{\#o}-\tau_{\#i}}(\dot{\omega}_{out}-\tau_{\#i}\dot{\omega}_{in})\\ \dot{\omega}_o &= \frac{\tau_{o\#i}}{\tau_{\#i}-\tau_{\#o}}(\dot{\omega}_{out}-\tau_{\#o}\dot{\omega}_{in})\end{aligned} \tag{6.2}$$

The mechanical power on the shafts i and o can be assessed by adding to the power transmitted in ideal conditions a contribution to consider the friction power losses in the PSU meshing gears:

$$\begin{aligned}\bar{P}_i &= P_i + \Delta P_{i,LOSS}\\ \bar{P}_o &= P_o + \Delta P_{o,LOSS}\end{aligned} \tag{6.3}$$

where P_i and P_o are the ideal power flows, ruled only by the mechanical points according to Eqs. (2.22),(2.23), and (2.25):

$$\begin{aligned}P_i &= \frac{1}{\tau_{\#i}-\tau_{\#o}}(\omega_{out}-\tau_{\#i}\omega_{in})(\tau_{\#o}T_{out}-T_{in})\\ P_o &= \frac{1}{\tau_{\#o}-\tau_{\#i}}(\omega_{out}-\tau_{\#o}\omega_{in})(\tau_{\#i}T_{out}-T_{in})\end{aligned} \tag{6.4}$$

The contribution due to the meshing losses is:

$$\begin{aligned}\Delta P_{i,LOSS} &= -\frac{\omega_i T_{in}}{\tau_{i\#o}}\left[\bar{p}_L + \frac{\partial \bar{p}_L}{\partial \tau}(\tau_{\#o}-\tau)\right]\\ \Delta P_{o,LOSS} &= -\frac{\omega_o T_{in}}{\tau_{o\#i}}\left[\bar{p}_L + \frac{\partial \bar{p}_L}{\partial \tau}(\tau_{\#i}-\tau)\right]\end{aligned} \tag{6.5}$$

according to Eqs. (2.52)-(2.53), where the PSU meshing losses $\bar{p}_L$ are evaluated as addressed in Section 2.4. If the PSU losses are neglected, $\Delta P_{i,LOSS} = \Delta P_{o,LOSS} = 0$. In Eqs. (6.4)-(6.5), T_{in} is the torque on the PSU input shaft, while T_{out} is the torque on the PSU output shaft, depending on the demanded torque, T_{dem}, consisting of the aerodynamic, rolling, grade and inertial resistances as follows:

$$T_{dem} = -\left(\frac{1}{2}c_d A_f \rho_a V_{veh}^2 + f_r mg\cos\gamma + mg\sin\gamma + \delta m a_{veh}\right)R_w \tag{6.6}$$

where c_d is the drag coefficient, A_f is the vehicle frontal area, ρ_a is the air density, V_{veh} is the vehicle speed, f_r is the rolling friction coefficient, m is the vehicle mass, g is the gravitational acceleration, γ is the road gradient, δ is the coefficient that accounts for the rotational inertia, a_{veh} is the vehicle acceleration, and R_w is the wheel rolling radius. For the power sign convention indicated in Fig. 6.1, whereby the power is positive if entering the PSU, T_{out} is negative during vehicle traction and positive during braking. To consider the operation of the friction brakes to avoid MGs saturation during regenerative braking, T_{out} is considered as:

$$T_{out} = T_{dem} - T_{brake} \tag{6.7}$$

where $T_{brake} > 0$ is the friction brake torque.

The torque on the shafts i and o of the PSU can be assessed by dividing Eqs. (6.3) by Eqs. (6.1), while the mechanical torque at the actuators level is affected by their moments of inertia, J_{ICE}, J_{MG1}, and J_{MG2}:

$$\begin{aligned} T_{ICE} &= T_{in} + J_{ICE}\dot{\omega}_{in} \\ T_{MG1} &= \bar{T}_i + J_{MG1}\dot{\omega}_i \\ T_{MG2} &= \bar{T}_o + J_{MG2}\dot{\omega}_o \end{aligned} \tag{6.8}$$

Once the ICE operating point is known, the fuel rate can be assessed from the ICE efficiency map, as follows:

$$\dot{m}_{fuel} = \frac{\omega_{in} T_{ICE}}{H_{LHV} \cdot \eta_{ICE}} \tag{6.9}$$

where H_{LHV} is the fuel lower heating value and η_{ICE} is the engine efficiency, which is a function of the ICE speed and torque.

The electric power of each MG depends on the mechanical power delivered or absorbed and on its efficiency η_{MG1} or η_{MG2}:

$$\begin{aligned} P_{MG1,el} &= \omega_i T_{MG1} {\eta_{MG1}}^{-sign(\omega_i T_{MG1})} \\ P_{MG2,el} &= \omega_o T_{MG2} {\eta_{MG2}}^{-sign(\omega_o T_{MG2})} \end{aligned} \tag{6.10}$$

For an ideal battery, the net power flow is:

$$P_{batt,id} = P_{MG1,el} + P_{MG2,el} \tag{6.11}$$

A simplified battery model widely adopted in the relevant literature considers an equivalent circuit with a voltage source in series with a resistor. The battery efficiency η_{batt} can be assessed as:

$$\eta_{batt} = \frac{V_{OC} + \sqrt{V_{OC}^2 - 4\left|P_{batt,id}\right| R_{batt}}}{2V_{OC}} \tag{6.12}$$

where V_{OC} is the open-circuit voltage and R_{batt} is the battery internal resistance. Then, the actual battery power is:

$$P_{batt} = P_{batt,id} {\eta_{batt}}^{-sign(P_{batt,id})} \tag{6.13}$$

The battery current can be expressed as the ratio between the battery power and the output voltage determined by Kirchhoff's voltage law. Then, the rate of the battery state of charge is the opposite of the ratio between the battery current and the battery capacity Q_{batt}:

$$\dot{SOC} = -\frac{V_{OC} - \sqrt{V_{OC}^2 - 4P_{batt}R_{batt}}}{2R_{batt}Q_{batt}} \tag{6.14}$$

6.2 Case study on the multi-mode Voltec II

For any existing power-split HEV, the parametric model described in Section 2.1 can be used as the internal model for MPC formulation, after identifying the PSU functional parameters for each transmission mode through the procedure of Section 3.1, assessing the

power losses with the method of Section 2.4, and including the ICE and MGs efficiency maps. The resulting constrained nonlinear optimisation problem must involve continuously differentiable constraints and objective functions if gradient-based optimisation methods are used to search for the optimal solution. Thus, a continuous formulation is required for the functional parameters switching, the PSU meshing losses, and the actuators maps.

This section shows an example of application to the multi-mode PS-CVT Voltec II, described in Section 1.2.3 and Section 5.2.1. The available functioning modes and the respective functional parameters are reported in Table 5.1 and Table 5.2. The second generation of the Chevrolet Volt is an extended-range hybrid electric vehicle equipped with a large battery pack to ensure a significant range in pure electric driving. However, when the battery SOC reaches the minimum value of 16%, a power-split hybrid charge-sustaining mode is activated, and the variation of the battery SOC is maintained within $\pm 1\%$ [35,162,163]. Only the charge-sustaining operation has been considered in this study. Fig. 6.2 shows the powertrain power-split layout including the actuators inertia, and Table 6.1 summarises the main vehicle parameters derived from [35,162,163].

Table 6.1. Chevrolet Volt II parameters derived from [35,162,163].

Component	Symbol	Parameter	Value
Vehicle	m_0	Unladen vehicle mass	1,607 kg
	c_d	Drag coefficient	0.28
	A_f	Frontal area	2.20 m^2
	f_r	Rolling friction	0.011
	R_w	Wheel radius	0.32 m
	δ	Coefficient of rotational inertia	1.04
ICE	P_{ICE}^{max}	Maximum power	75 kW
	T_{ICE}^{max}	Maximum torque	140 Nm
	ω_{ICE}^{max}	Maximum speed	6,000 rpm
	J_{ICE}	Moment of inertia	0.04 kgm^2
MG1 / MG2	P_{MG1}^{max} / P_{MG2}^{max}	Peak power	48 / 87 kW
	T_{MG1}^{max} / T_{MG2}^{max}	Peak torque	118 / 280 Nm
	ω_{MG1}^{max} / ω_{MG2}^{max}	Peak speed	10,000 / 10,000 rpm
	J_{MG1} / J_{MG2}	Moment of inertia	0.03 kgm^2 / 0.05 kgm^2
Battery	Q_{batt}	Battery capacity	52 Ah
	V_{OC}	Open circuit voltage	355 V
	R_{batt}	Internal resistance	0.1 Ω
	P_{batt}^{max}	Maximum battery power	120 kW
PSU	Ψ_1	PG1 Willis ratio	−0.535
	Ψ_2	PG2 Willis ratio	−0.481
	k_{fd}	Final drive ratio [-]	0.379

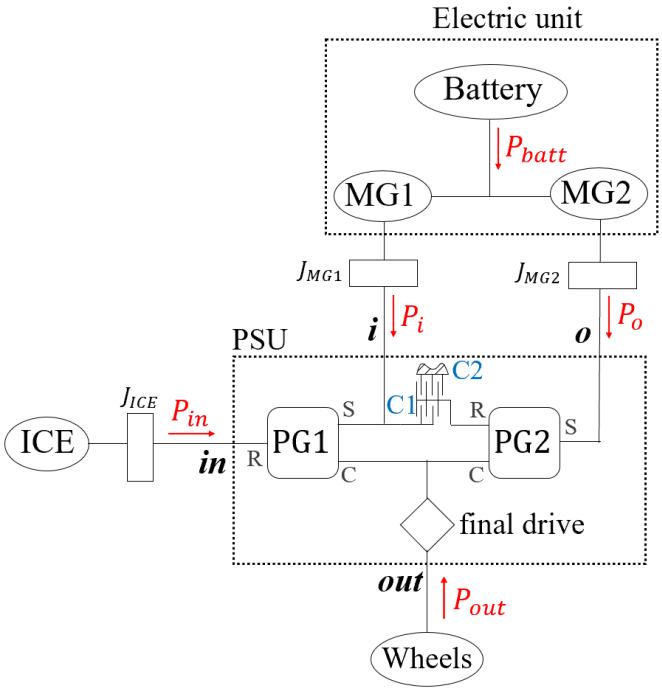

Fig. 6.2. Functional layout for Chevrolet Volt II in power-split operation.

Simultaneously engaging C1 and C2 results in a fixed-ratio parallel mode with the shaft i stationary, whereby MG1 is turned off and only MG2 can operate for traction or regenerative braking. Moreover, the ICE speed ω_{in}^{FR} in parallel mode is proportional to the wheels speed by the inverse of the mechanical point $\tau_{\#i}$, which is the overall transmission ratio when the shaft i is stationary by definition. Similarly, the corresponding speed ratio $\tau_{o\#i}$ univocally defines the speed ω_o^{FR} of the shaft o. Thus, the speed relations of Eqs. (6.1) valid for power-split operations can be replaced by the following ones in the parallel fixed-ratio mode:

$$\begin{aligned} \omega_i^{FR} &= 0 \\ \omega_{in}^{FR} &= \frac{\omega_{out}}{\tau_{\#i}} \\ \omega_o^{FR} &= \frac{\tau_{o\#i}}{\tau_{\#i}}\omega_{out} \end{aligned} \tag{6.15}$$

6.2.1 Switch functions for multi-mode operations

Although each power-split mode could be ideally selected for any overall transmission ratio τ, multi-mode PS-CVTs are designed so as to drive in the input-split mode for lower ratios and in the compound-split mode for higher ratios. In this way, the power recirculation in the electric unit is limited and compliance with the speed, torque, and power constraints of the electric MGs is ensured even if the electric unit is downsized [34,164]. Moreover, switching between modes is performed when the shafts involved in clutches operation have zero relative speed (see also Section 3.2.3). In this way, the plates of clutches are prevented

from slipping and a smooth synchronous mode shift is realised. In the case of Voltec II, the relative speed between the PG2 ring gear and MG1 is zero at the mechanical point $\tau_{\#i}$, when MG1 is stationary, similarly to the PG2 ring gear, which is either connected to MG1 by C1 or braked to the frame by C2. Therefore, the mechanical point $\tau_{\#i}$ is not only the overall speed ratio at which parallel operation can be performed, but also the ratio at which mode shift can occur, as shown in Fig. 6.3. Moreover, the functional parameters $\tau_{\#i}$ and $\tau_{o\#i}$ referred to the condition whereby the shaft *i* is stationary are the same in both input-split and compound-split mode. On the contrary, the values of $\tau_{\#o}$ and $\tau_{i\#o}$ referred to the condition whereby the shaft *o* is stationary are different (Table 5.2 and Fig. 6.3), since these speed ratios are affected by the state of the clutches on the shaft *i* (see Fig. 6.2).

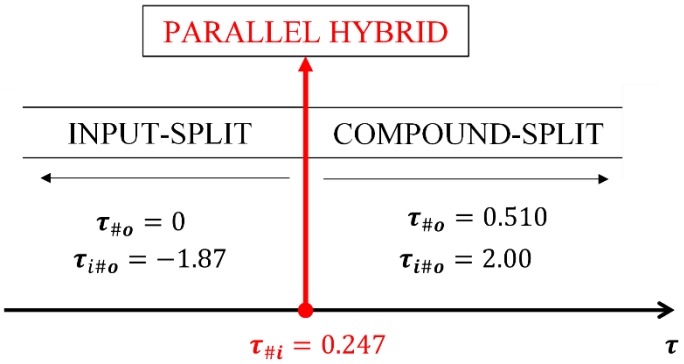

Fig. 6.3. Mode shift strategy in Voltec II based on the overall speed ratio τ.

The described mode shift strategy can be embedded in the parametric model for the power-split operation of Section 6.1, by introducing continuous switch functions to model the switching functional parameters $\tau_{\#o}$ and $\tau_{i\#o}$. The continuous switch is obtained by the following functions of the overall speed ratio τ:

$$\begin{aligned} \tau_{\#o} &= \frac{\tau_{\#o}^{CS} + \tau_{\#o}^{IS}}{2} + \frac{\tau_{\#o}^{CS} - \tau_{\#o}^{IS}}{\pi} \operatorname{atan}\left(N_1(\tau - \tau_{\#i})\right) \\ \tau_{i\#o} &= \frac{\tau_{i\#o}^{CS} + \tau_{i\#o}^{IS}}{2} + \frac{\tau_{i\#o}^{CS} - \tau_{i\#o}^{IS}}{\pi} \operatorname{atan}\left(N_2(\tau - \tau_{\#i})\right) \end{aligned} \tag{6.16}$$

where the apices IS and CS relate to the functional parameters of the input-split and compound-split mode, respectively. Moreover, to address also the fixed-ratio parallel mode within the same model, an additional set of switch functions is introduced:

$$\begin{aligned} f_{FR} &= \frac{1}{2} + \frac{2}{\pi^2} \operatorname{atan}\left(N_3(-(\tau_{\#i} - \Delta) + \tau)\right) \cdot \operatorname{atan}\left(N_3((\tau_{\#i} + \Delta) - \tau)\right) \\ f_{PS} &= \frac{1}{2} + \frac{2}{\pi^2} \operatorname{atan}\left(N_3((\tau_{\#i} - \Delta) + \tau)\right) \cdot \operatorname{atan}\left(N_3((\tau_{\#i} + \Delta) - \tau)\right) \end{aligned} \tag{6.17}$$

f_{FR} and f_{PS} are built so that the former is always zero except for a narrow neighbourhood of $\tau_{\#i}$ with a radius Δ, when parallel mode occurs; conversely, the latter is zero in the

neighbourhood of $\tau_{\#i}$ and 1 for any other τ, where power-split operations are involved. The parameters Δ, N_1, N_2, and N_3 must be selected to include $\tau_{\#o}$ and $\tau_{i\#o}$ switch within the range $\tau_{\#i} - \Delta \leq \tau \leq \tau_{\#i} + \Delta$ to avoid numerical errors in the solution of the MPC problem. Fig. 6.4 shows the trend of the switch functions of Eqs. (6.16)-(6.17).

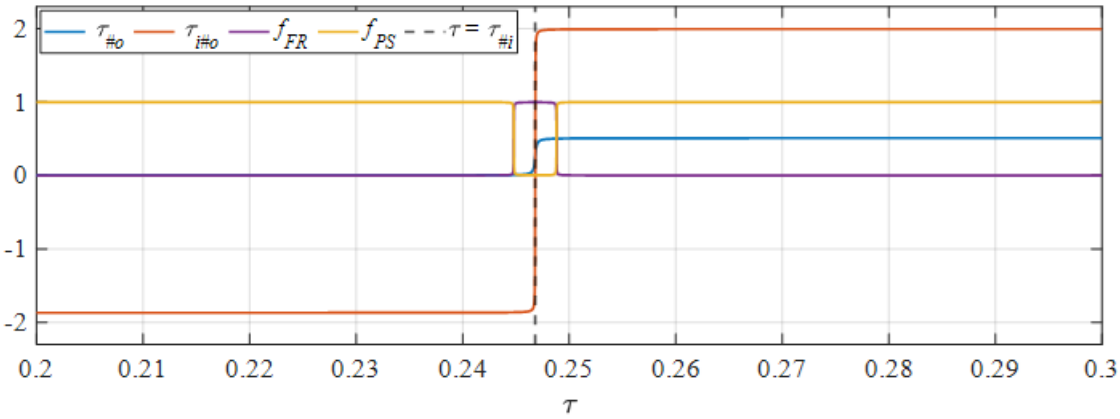

Fig. 6.4. Switch functions for the functional parameters and for power-split and parallel operation.

The switch functions (6.17) replace the speed relations of Eqs. (6.1) with the following ones:

$$\begin{aligned} \omega_i &= \omega_i^{FR} \cdot f_{FR} + \omega_i^{PS} \cdot f_{PS} \\ \omega_o &= \omega_o^{FR} \cdot f_{FR} + \omega_o^{PS} \cdot f_{PS} \end{aligned} \tag{6.18}$$

where ω_i^{PS} and ω_o^{PS} are those of Eqs. (6.1). Similar relations rule the accelerations instead of Eqs. (6.2).

6.2.2 *Transmission meshing losses*

The normalised PSU meshing losses of Voltec II were assessed in 5.2.2. In Eq. (6.19), they are expressed as a continuous function of the overall speed ratio τ and overall torque ratio $\Theta = T_{out}/T_{in}$ to be included in Eqs. (6.5) for MPC formulation.

$$\bar{p}_L = (1-\eta_1)\left|1 - \frac{\tau}{\tau_{\#i}(1-\psi_1)}\right| - \frac{1-\eta_2}{1-\psi_2}\left|\left(\Theta + \frac{1}{\tau_{\#i}}\right)\left[\frac{\tau_{\#o}}{\tau_{\#o}-\tau_{\#i}}(\tau - \tau_{\#i}) - \psi_2\tau\right]\right| - (1-\eta_{fd})|\tau\Theta| \tag{6.19}$$

The first two terms are PG1 and PG2 meshing losses, dependent on their constructive arrangement, Willis ratio, and ordinary efficiency, according to Table 5.4. The third term is the loss in the fixed-ratio final drive.

6.2.3 *ICE and MGs efficiency maps*

In contrast to the assessment procedure of the PSU meshing power losses, which is based on a physically consistent mathematical model that requires only the knowledge of the PSU constructive arrangement, the conversion power losses in the ICE and MGs are more often derived from experimental data. Thus, the efficiency of the actuators is available in the form

of maps with scattered data that must be fitted to derive the continuous functions necessary for implementing gradient-based algorithms. Therefore, the ICE and MGs efficiency maps of the Chevrolet Volt available in [35,162] are approximated by fifth-order polynomial functions of their respective speed and torque:

$$\eta_k(\omega_k, T_k) = \sum_{m=0}^{5} \sum_{n=0}^{5-m} p_{mn} {\omega_k}^m {T_k}^n \tag{6.20}$$

where $k = ICE, MG1, MG2$. Moreover, a similar fitting is required for the maximum torque of the ICE and MGs, as a function of their respective speed, by using a single-variable n-th order polynomial:

$$T_k^{max}(\omega_k) = \sum_{m=1}^{n+1} p_m {\omega_k}^{n+1-m} \tag{6.21}$$

A fourth-order polynomial was used for the ICE maximum torque, while a seventh-order polynomial was necessary for the MG1 and MG2 maximum torque. The fitting for the efficiency maps and maximum torque was performed by the MATLAB Curve Fitting toolbox. Fig. 6.5 shows the results of the interpolation.

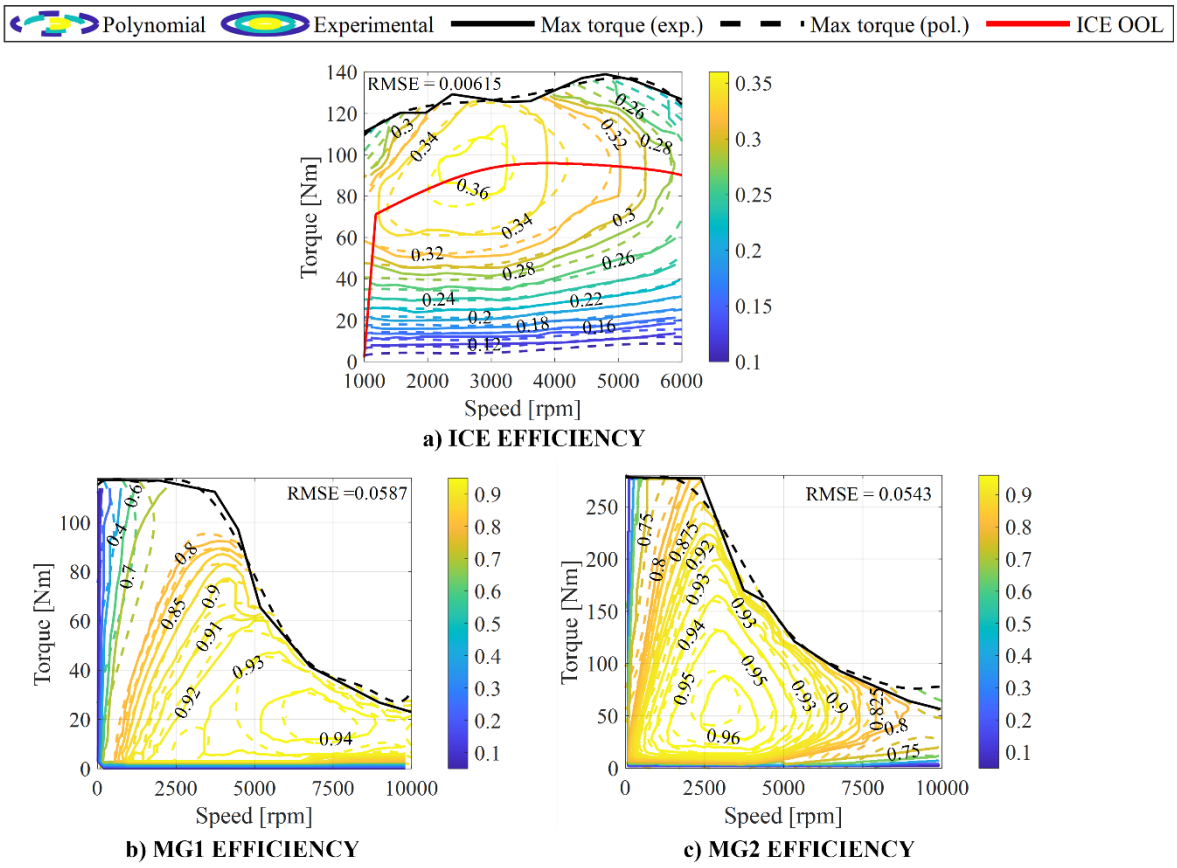

Fig. 6.5. Fitting results for actuators efficiency maps and maximum torques, with their respective root mean square error (RMSE).

6.3 Internal models definition by preliminary open-loop comparison

To reduce the length of the simulation campaign, a preliminary analysis in an open-loop simulation framework is carried out to define the internal models worthy of investigation in the MPC framework. The internal models considered in the preliminary analysis are derived from the baseline model of Section 6.1, including the PSU meshing losses of Eq. (6.19), the polynomial form for MGs efficiency, and the inertial load of the actuators according to Eqs. (6.8). Then, the complexity of the baseline model is reduced by modifying one of the three analysed factors at a time, according to Table 6.2.

Table 6.2. Internal models for open-loop preliminary analysis.

Internal Model	Inertial load	MGs efficiency	Meshing losses
OL_Baseline	Considered	Polynomial	Considered
OL_IdealMGE	Considered	$\eta_{MG1} = \eta_{MG2} = 1$	Considered
OL_ConstantMGE	Considered	$\eta_{MG2} = 0.87;\ \eta_{MG2} = 0.9$	Considered
OL_NoPSULosses	Considered	Polynomial	Neglected
OL_NoInertia	Neglected	Polynomial	Considered

6.3.1 Open-loop simulation framework

A preliminary comparison of the five internal models listed in Table 6.2 is carried out by implementing the open-loop simulation framework shown in Fig. 6.6. The seven driving cycles listed in Table 6.3 are used to simulate typical conditions in terms of vehicle speed and acceleration, as well as the resulting demanded torque [165]. A regenerative braking strategy is developed for the friction brakes, to prevent MGs saturation. During the deceleration phases, it assesses the resulting MGs torque values for the current demanded torque, considering the ICE idling operations. If the torque of one MG exceeds its maximum value for the current vehicle speed, this torque is saturated, and the resulting maximum torque T_{out} recoverable on the *out* shaft is computed by inverting the torque equations that can be derived from the formulations in Section 6.1. Then, a simplified rule-based strategy is implemented to establish ICE operation. The core concept of the rule-based strategy, illustrated in Fig. 6.7, is to limit the battery involvement to simulate a realistic response of the Chevrolet Volt powertrain during the charge-sustaining operation. Thus, the ICE power is set equal to the output power during vehicle traction and the ICE operating points are kept as close as possible to the ICE optimal operating line (OOL) shown in Fig. 6.5. The acceleration of the engine is assessed by deriving the actual speed, which in a backward-facing model is the desired speed. If the demanded power overcomes the maximum ICE power, the ICE works at the maximum power, and the difference must be compensated by

the battery; during regenerative braking, the ICE is kept idling and the recoverable mechanical energy is stored in the battery. The resulting ICE torque, speed, and acceleration are provided as input of each internal model defined by the equations of Sections 6.2-6.3 with the respective exceptions of Table 6.2. The internal model block simulates the PSU and electric unit operations and outputs the battery SOC, which is used as a benchmark index to compare the five internal models.

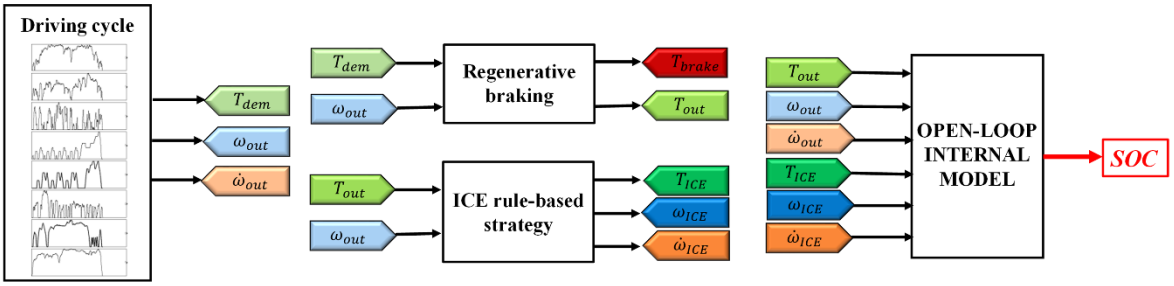

Fig. 6.6. Open-loop simulation framework for preliminary comparison.

Table 6.3. Characteristics of the simulated driving cycles from [165].

Driving cycle	Type	Distance [m]	Duration [s]	Average speed [km/h]
Artemis Urban	urban	4874	993	17.7
Artemis Road	mixed	17275	1082	57.5
Artemis Motorway130	extra-urban	28737	1068	96.9
NEDC	mixed	11017	1180	33.6
J10-15	urban	4165	660	22.7
UDDS	urban	11997	1369	31.6
HWFET	extra-urban	16503	765	77.7

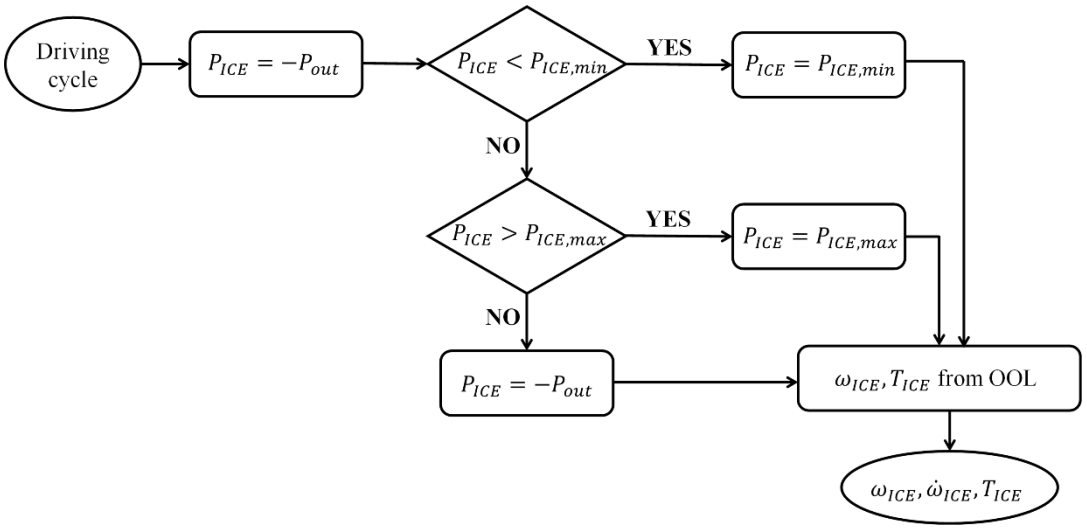

Fig. 6.7. Simplified rule-based strategy for ICE control in open-loop simulations.

6.3.2 *Results of open-loop comparison and MPC internal models definition*

This preliminary comparison in open-loop aims to assess the impact of PSU power losses, MGs efficiency and actuators inertial load on the simulated powertrain response. Since the ICE operations derived from the rule-based strategy are the same for each internal model, only battery SOC is observed to quantify the deviation of each internal model from the baseline through the following percentage variation:

$$|\Delta SOC|_{Baseline,IM_j} = \frac{\left|SOC_{IM_j} - SOC_{Baseline}\right|}{SOC_{Baseline}} \cdot 100 \tag{6.22}$$

where IM_j indicates the jth internal model. The comparison results are in Fig. 6.8, while Fig. 6.9 reports the trend of the battery SOC for each internal model in the Artemis driving cycles, by way of example.

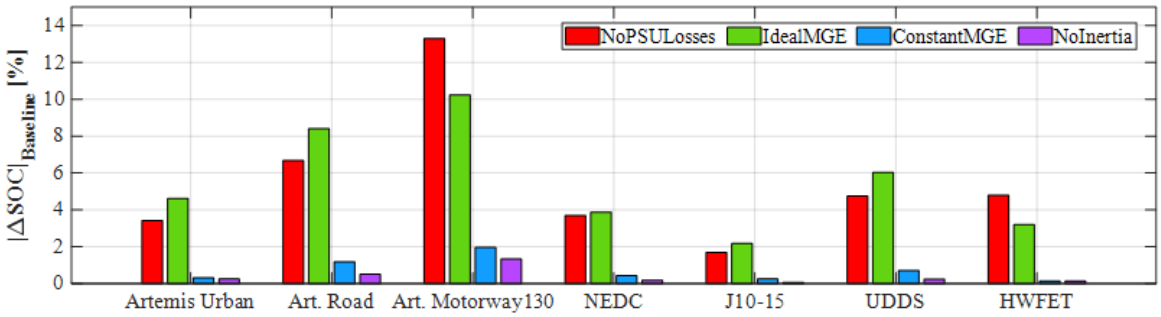

Fig. 6.8. SOC comparison resulting from the open-loop analysis in terms of variation from the Baseline SOC.

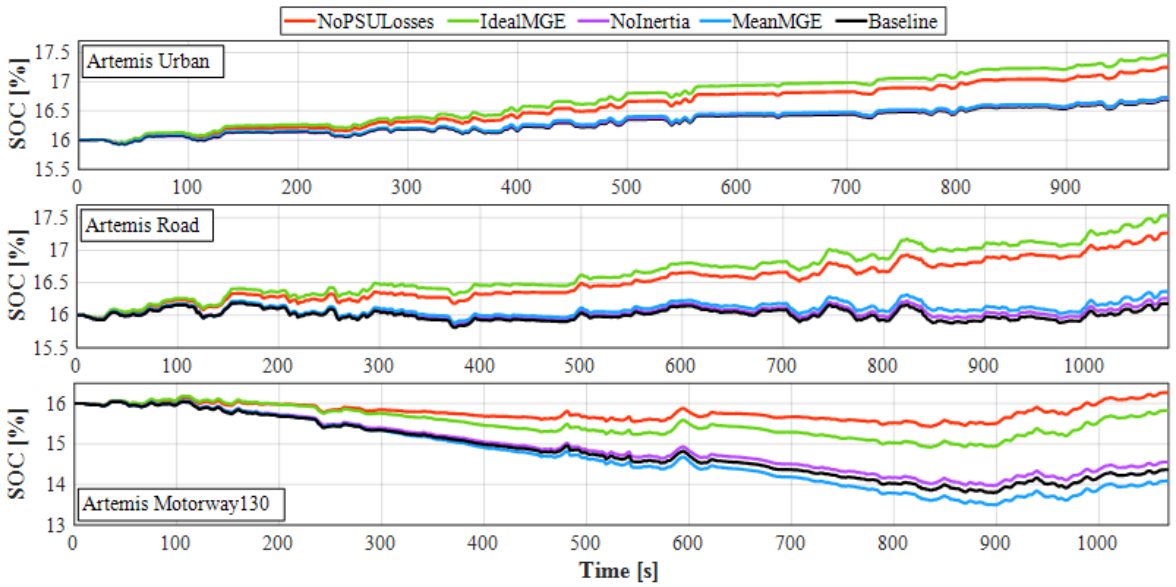

Fig. 6.9. SOC battery trend for Artemis driving cycles: open-loop comparison between the internal models of Table 6.2.

The results of Fig. 6.8 and Fig. 6.9 suggest that the highest deviation from the baseline model is achieved when a unitary efficiency is assumed for the MGs efficiency. Moreover,

neglecting PSU power losses implies a significant deviation as well, which is the largest in the high-speed driving cycles Artemis Motorway130 and HWFET. In both IdealMGE and NoPSULosses models, the final SOC is overestimated with respect to the baseline. On the contrary, omitting the actuators inertial load from the internal model does not result in significant SOC variation, especially in low-speed driving cycles. Similar considerations are valid for the internal model with a constant MGs efficiency in the place of polynomial maps.

Therefore, the results of this preliminary comparison suggest that it is worth investigating the impact of the PSU meshing losses in the MPC framework, while it is reasonable to neglect the actuators inertia to avoid computational complexity. Although the open-loop analysis reveals that a constant value could replace a polynomial model for the MGs efficiency, the influence of these two different approaches is deemed worthy of further analysis because, if the same trend is confirmed in the MPC framework, the traditional approach used in the literature based on the polynomial or experimental maps could be simplified into a constant efficiency, reducing the internal model complexity and thus the running time of the EMS solver. Given these considerations, the four internal models listed in Table 6.4 are considered in the MPC framework to assess the impact of PSU power losses and MGs efficiency.

Table 6.4. Internal models to compare in the MPC framework.

Internal Model	Inertial load	MGs efficiency	Meshing losses
MPC_IM1	Neglected	$\eta_{MG1} = 0.87;\ \eta_{MG2} = 0.9$	Neglected
MPC_IM2	Neglected	Polynomial	Neglected
MPC_IM3	Neglected	$\eta_{MG1} = 0.87;\ \eta_{MG2} = 0.9$	Considered
MPC_IM4	Neglected	Polynomial	Considered

6.4 MPC problem formulation

MPC-based EMS allows solving multi-input multi-output nonlinear problems with equality and/or inequality constraints. The formulation of the MPC optimal control problem requires the following state-space representation of the controlled system, with state vector $\boldsymbol{x}(t)$, output vector $\boldsymbol{y}(t)$, and control vector $\boldsymbol{u}(t)$, for given external inputs $\boldsymbol{w}(t)$:

$$\begin{cases} \dot{\boldsymbol{x}}(t) = f(\boldsymbol{x}, \boldsymbol{u}, \boldsymbol{w}) \\ \boldsymbol{y}(t) = g(\boldsymbol{x}, \boldsymbol{u}, \boldsymbol{w}) \end{cases} \tag{6.23}$$

When applied to power-split HEVs to solve the EMS problem, the formulation based on the powertrain model of Section 6.1 involves the following vectors if the inertial load of the actuators is neglected:

$$\begin{cases} \boldsymbol{x}(t) = \{SOC\} \\ \boldsymbol{u}(t) = \{\omega_{in}, T_{ICE}, T_{brake}\} \\ \boldsymbol{y}(t) = \{\dot{m}_{fuel}, SOC\} \\ \boldsymbol{w}(t) = \{\omega_{out}, T_{dem}\} \end{cases} \tag{6.24}$$

Thus, the nonlinear state-space equation is Eq. (6.14).

The goal of the MPC strategy is to establish the optimal control variables to minimise a cost function over a prediction horizon (PH). The cost function is defined as the sum of a first term penalising the ICE fuel rate, and a second term penalising the deviation of the battery SOC from a reference value:

$$J(\boldsymbol{x}, \boldsymbol{u}, \boldsymbol{w}, t) = \int_{t_o}^{t_0+PH} \left(q_1 \cdot \left|\dot{m}_{fuel}\right|^2 + q_2 \cdot \left|SOC - SOC_{ref}\right|^2 \right) dt \tag{6.25}$$

where q_1 and q_2 are the weights of the fuel rate and battery SOC deviation. The control variables optimisation must comply with the soft and hard constraints of the system, related to the battery SOC and power, and actuators speed and torque. Moreover, the mechanical braking torque, T_{brake}, must be positive to meet the adopted sign convention:

$$\begin{cases} SOC^{min} \leq SOC(t) \leq SOC^{max} \quad (soft) \\ P_{batt}^{min} \leq P_{batt}(t) \leq P_{batt}^{max} \\ \omega_k^{min} \leq \omega_k(t) \leq \omega_k^{max} \\ T_k^{min} \leq T_k(t) \leq T_k^{max} \\ T_{brake} \geq 0 \end{cases} \tag{6.26}$$

with $k = ICE, MG1, MG2$. A soft constraint is considered on the battery SOC to ensure a deviation of around $\pm 1\%$ from the 16% reference value. When the optimal sequence of control inputs over the prediction horizon is obtained, the control variables assessed for the first time step are applied to the plant; then, the prediction horizon is moved one step forward and the optimisation is repeated for the next time step.

The MPC optimal control problem was set by implementing the equations of Sections 6.1-6.2 that were modified according to Table 6.4 in the Automatic Control and Dynamic Optimization toolkit (ACADO). ACADO is an open-source framework to solve optimal control problems using a solver based on sequential quadratic programming, combining gradient-based algorithms and quadratic programming to iteratively solve the optimal control problem also in real time [166]. The multiple-shooting discretisation and the Gauss-Newton Hessian approximation were set in the ACADO programming. Then, from the C++ code developed in the ACADO toolkit for MATLAB, an S-function is exported and embedded into the backward-facing Simulink framework in Fig. 6.10.

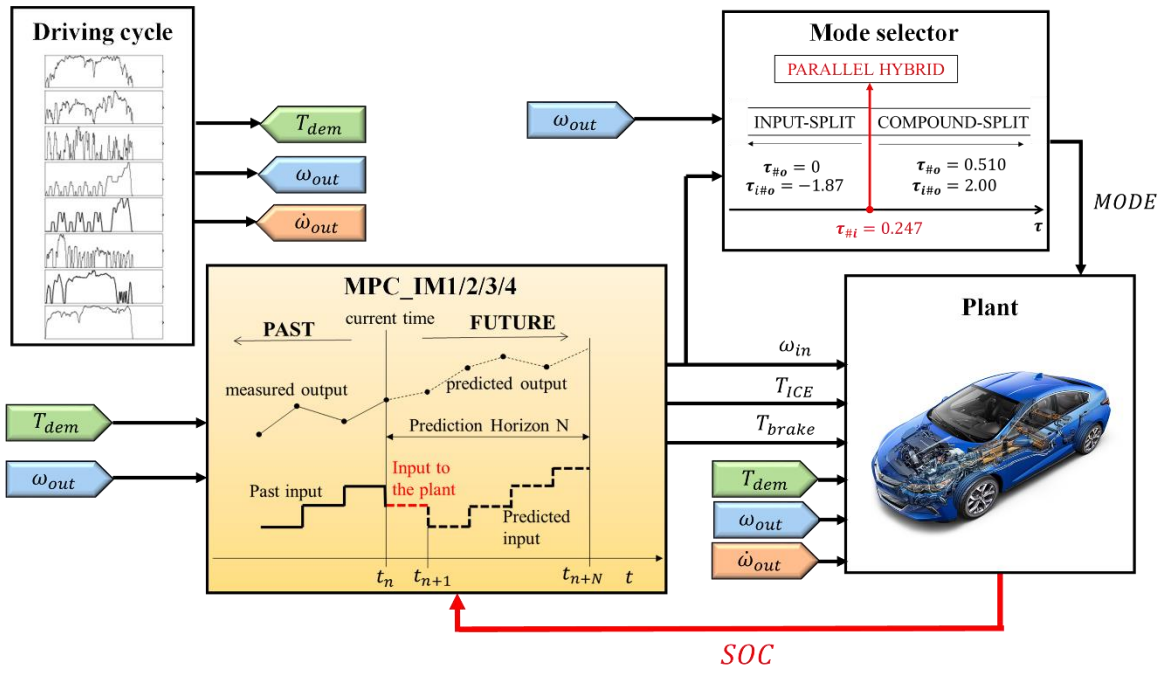

Fig. 6.10. Simulink backward-facing model for MPC EMS with integrated mode shift.

Embedding in the MPC internal model the universal formulation of Section 6.1 and the continuous switching formulation of Section 6.2.1 results in the following novelties: 1) a single controller is sufficient to deal with the EMS of any multi-mode power-spit powertrain, and 2) the possibility of performing a mode switch is integrated within the MPC framework, thus, there is no need of predefining the operating mode as input of the controller. The vehicle speed and demanded torque derived from the driving cycle are provided to the MPC block as external inputs to the controller. The MPC algorithm optimises the control variables, which include also the ICE speed, by initially supposing their first-attempt values and then changing them to pursue the minimisation of the cost function. For a given vehicle speed, the ICE speed affects the overall speed ratio, which determines the selected mode (Section 6.2.1). Thus, a first-attempt mode is implicitly supposed in the optimisation through the first-attempt ICE speed, but then the considered mode varies if a different engine speed is considered by the optimisation algorithm, thanks to the continuous switching formulation of Eqs. (6.16)-(6.17). Similarly, the optimal ICE speed returned by the MPC block determines the optimal transmission ratio and, thus, the selection of the optimal mode according to the strategy in Fig. 6.3. Therefore, the active mode is the result of the MPC optimisation. The optimal ICE operations, PSU mode, and eventual friction braking torque are used as input data to the plant. The resulting battery SOC is provided in feedback to the MPC.

A benchmark MPC controller is introduced to test the performance of the novel internal model with integrated mode shift modelled by switch functions. The benchmarking MPC framework, shown in Fig. 6.11 and referred to as Triple-MPC, relies on the typical approach

adopted in the literature based on multiple MPC controllers, one for each mode. Each controller is involved according to the current mode, which is selected on the basis of the demanded torque and vehicle speed by a mode selection map obtained from earlier offline analysis. In this case, the map provided by General Motors in [35] for the Chevrolet Volt operation is considered. Now the mode is a discrete external input to the MPC formulation, and not an optimised output. The internal model used for the IS and CS modes is formulated according to the same parametric approach of Section 6.1, by keeping constant values of the functional parameters in Table 5.2. The FR internal model is modified according to Eqs. (6.15); thus, the ICE speed is proportional to the vehicle speed instead of a control variable.

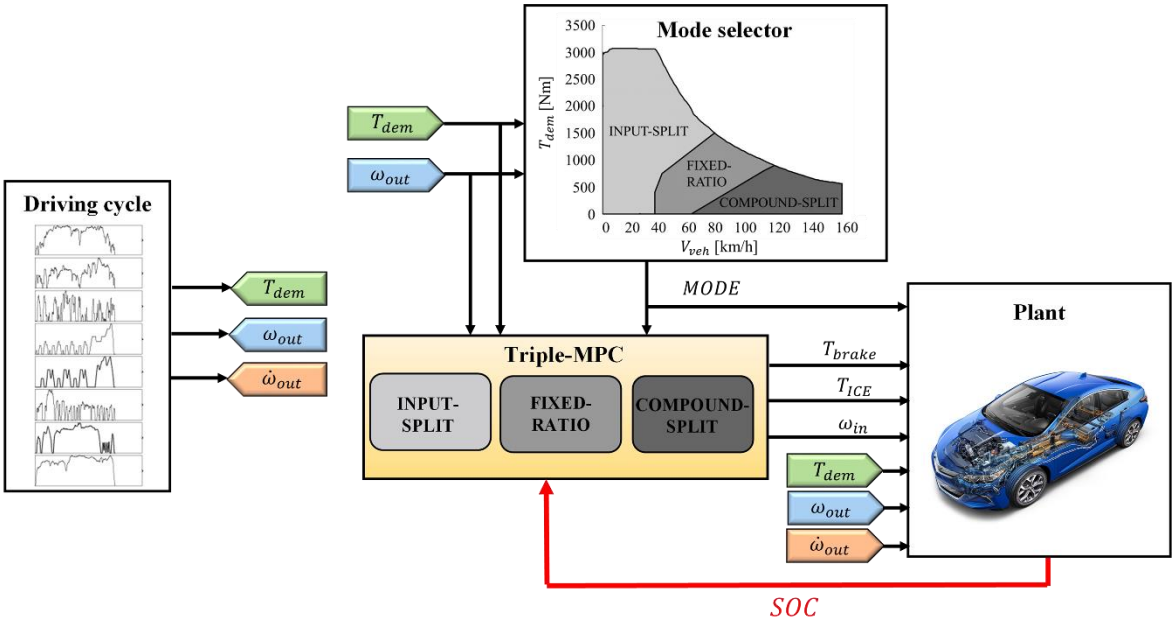

Fig. 6.11. Simulink backward-facing model for MPC EMS with pre-defined map for mode shift.

A typical MPC internal model based on the Willis formula and PG free body diagram would not have allowed an integrated continuous formulation of the mode switch. On the contrary, the universal parametric model offers the opportunity to integrate the mode switch in the MPC optimal control problem or use a different optimisation strategy for mode selection.

6.5 Results and discussion

The MPC framework of Fig. 6.10 was implemented in Simulink to compare the performance of the four internal models with different complexity (Table 6.4) for the driving cycles of Table 6.3. A sampling time of 1 s and a prediction horizon of 10 s were used for the MPC controller. A brute-force optimisation was carried out to fit the cost function weights; the best performance was achieved when the minimisation of the fuel consumption

was prioritised over the battery SOC variation through a weight one order of magnitude larger. A preview function was implemented to provide the MPC controller with future information on demanded torque and vehicle speed derived from the driving cycle.

To consider the different battery SOC at the end of the driving cycle, a fuel compensation term, m_{fuel}^{comp}, is added to the actual fuel consumption of the petrol engine, m_{fuel} [167]. The total equivalent consumption m_{fuel}^{eq} expressed in grams is:

$$m_{fuel}^{eq} = m_{fuel} + m_{fuel}^{comp} = m_{fuel} - \frac{(SOC_{end} - SOC_{ref})Q_{batt}V_{OC}\overline{BSFC}}{1000} \quad (6.27)$$

where m_{fuel} is the fuel consumption of the internal combustion engine in grams, SOC_{end} is the final battery SOC ranging from 0 to 1, SOC_{ref} is the reference SOC equal to 0.16, $\overline{BSFC}$ is the average brake specific fuel consumption of the engine expressed in g/kWh and equal to:

$$\overline{BSFC} = \frac{1}{\bar{\eta}_{ICE}H_{LHV}} \quad (6.28)$$

where $\bar{\eta}_{ICE}$ is the engine average efficiency over the driving cycle and $H_{LHV} = 0.01193$ kWh/g is the petrol lower heating value. The fuel consumption can be expressed in litres per 100 kilometres as follows:

$$FC = \frac{m_{fuel}^{eq}}{d\rho_{fuel}} * 100 \quad (6.29)$$

where d is the total distance covered by the driving cycle in km (Table 6.3) and $\rho_{fuel} = 743$ g/l is the petrol density.

The comparison between the four internal models of Table 6.4 is performed by considering the percentage variation from the most accurate internal models, i.e., IM4:

$$\Delta FC_{IM4,IM_j} = \frac{FC_{IM_j} - FC_{IM4}}{FC_{IM4}} \cdot 100 \quad (6.30)$$

with $j = 1,2,3$.

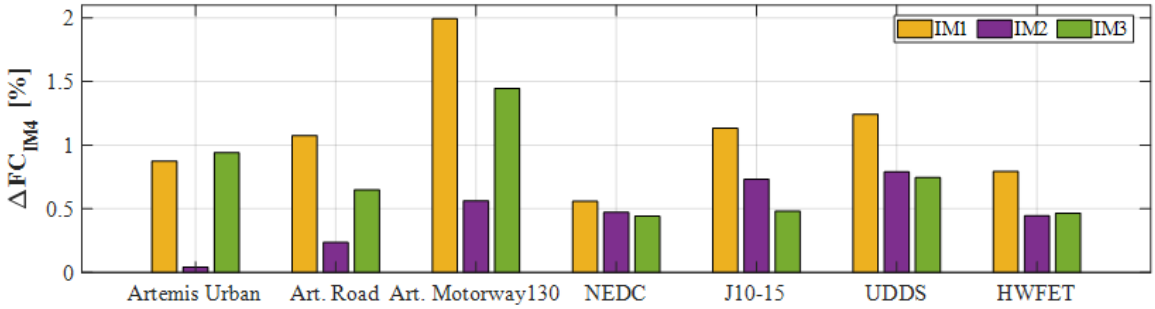

Fig. 6.12. Total fuel consumption: comparison of the simpler internal models versus IM4.

The results in Fig. 6.12 prove that the most accurate internal model IM4 always overperforms the other ones, since the percentage variation of Eq. (6.30) is positive in all the simulated driving cycles. Similarly, the simplest internal model IM1, which neglects the PSU meshing losses and considers a constant value for the MGs efficiency, leads to the highest fuel consumption, up to 2% more than IM4 in the Artemis Motorway130 cycle. The Artemis Urban is an exception, since IM3 has the worst performance.

The performance assessment of the internal models IM2 and IM3 is less intuitive. IM2 results in the lowest variation from IM4 in the Artemis and HWFET cycles, while IM3 is the second-best internal model after IM4 in the NEDC, J10-15, and UDDS cycles. It should be noted that IM3 differ from IM4 for MGs efficiency, considered constant in IM3; on the other hand, IM2 differ from IM4 for PSU meshing losses, neglected in IM2. Therefore, the higher the difference between IM4 and IM3, the more the MGs efficiency affects the MPC performance; on the contrary, the higher the difference between IM4 and IM2, the more the PSU meshing losses affect the MPC performance. Hence, the EMS outcomes are more affected by the MGs efficiency in the Artemis and HWFET cycles, while the PSU meshing losses are more impactful in the NEDC, J10-15, and UDDS cycles. Nonetheless, the comparison of IM4 and IM2 indicates that the influence of the sole PSU meshing losses is less than 1%. This is due to the fact that the Voltec II is a well-designed PSU, because the PGs synchronism is included within their actual working range [96]. Thus, the meshing losses are low for most operating conditions. Nevertheless, these results suggest that neglecting the PSU power losses during the design process does not significantly affect the MPC-based EMS performance; hence, in the first instance, the meshing power losses can be neglected during the identification of the optimal functional parameters. As a result, any non-existing transmission can be modelled by only functional parameters without the need to define the constructive layout first. Then, after selecting the optimal functional parameters, the arrangement of the PGs can be defined through the design chart, so that they operate synchronously within the desired range to pursue low meshing losses. However, including PSU meshing losses in the MPC internal model for the EMS implementation is advisable to enhance fuel saving.

The above considerations might seem to contradict the results of the preliminary open-loop comparison (Fig. 6.8), where the impact of the PSU meshing losses is significantly higher. Nonetheless, the consideration of the different principles underpinning the MPC strategy and the ICE rule-based strategy is essential for a fair comparison between the MPC and the open-loop framework. Indeed, although the rule-based strategy attempts to limit the SOC variation, no constraints are imposed on it, thus exceeding the desired ±1% range (Fig.

6.9). Moreover, the ICE operation is not affected by the internal model complexity in the open-loop framework. On the contrary, the MPC strategy instantaneously selects the best ICE operation to meet the constraint on the battery SOC, resulting into a total equivalent consumption affected by both fuel consumption and final SOC (Eq. (6.27)).

The actual ICE fuel consumption and final battery SOC are analysed to evaluate the impact of MGs efficiency and PSU meshing losses on the total equivalent consumption. The only Artemis Road results are reported in Fig. 6.13 for brevity. The graph shows that the engine fuel consumption is lower for IM4 and IM2, i.e., the internal models which include the polynomial MGs efficiency; on the contrary, the final battery SOC is higher if the PSU meshing losses are included in the IMs, i.e., in IM4 and IM3. The same trends for the ICE fuel consumption are detected for all the driving cycles except for Artemis Urban, where IM2 results in the lowest consumption, followed by IM4, IM1 and IM3. Regarding the battery SOC, the highest final value is always reached for IM4 or IM3, while IM2 and IM1 perform worse, according to the prediction of the open-loop analysis, whereby the PSU losses affect the battery SOC more than the MGs efficiency. Even a small difference in battery SOC affects the fuel compensation term in Eq. (6.27) because of the high energy storable in the battery and the low ICE efficiency. These results reveal the synergetic effect of including both polynomial MGs efficiency and PSU meshing losses in the MPC internal model, which leads to the IM4 best performance in terms of both fuel consumption reduction and final battery SOC increase.

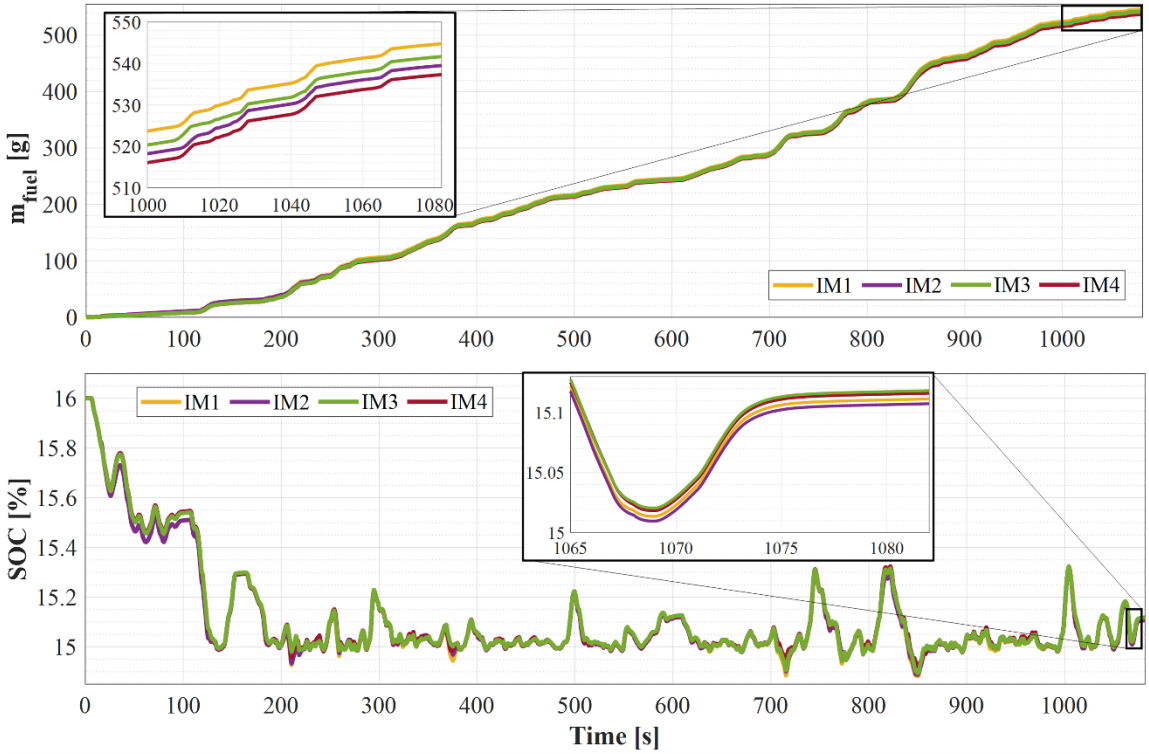

Fig. 6.13. ICE fuel consumption and battery SOC trends for each internal model in the Artemis Road cycle.

Lastly, the Triple-MPC framework of Fig. 6.11 was implemented to compare the performance of the integrated mode switch against the mode selection strategy based on offline optimisation. Fig. 6.14 shows the difference in fuel consumption per 100 km of the internal model IM4 and the Triple-MPC framework. The integrated mode switch of IM4 fails to achieve the best powertrain operations in two driving cycles, i.e., the Artemis Urban and Road. Instead, it performs slightly better than the offline mode optimisation in the remaining five cycles. Therefore, the performance of the two controllers is comparable. On the one hand, this implies that adopting the novel formulation for online EMS of power-split HEVs may be worthy only if the switch functions of Eqs. (6.16)-(6.17) do not excessively increase the computational effort. Thus, further investigation of real-time capability is necessary, but it goes beyond the scope of this work. On the other hand, the lack of the need for offline optimisation would significantly reduce the computational time necessary to compare several viable solutions, making the integrated mode switch strongly preferable in the design stage.

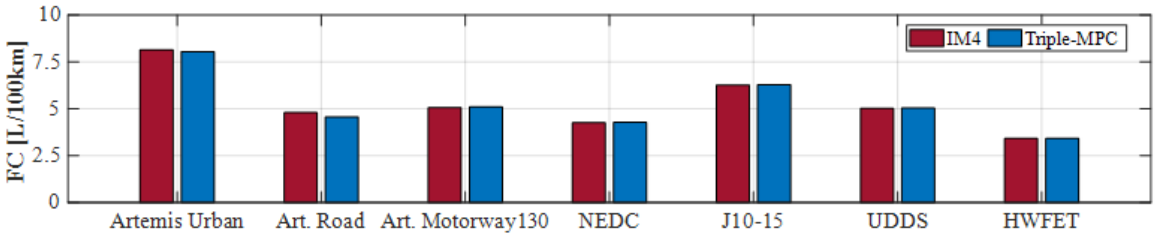

Fig. 6.14. IM4 with integrated mode switch versus Triple-MPC with offline mode optimisation strategy: fuel consumption comparison.

To complete the comparison between IM4 and the Triple-MPC, the speed profile, the selected mode, and the battery SOC in the Artemis Motorway130 are shown in Fig. 6.15. IM4 and Triple-MPC differ in selecting the fixed-ratio mode for low-medium speed at the beginning and end of the driving cycle, resulting in slightly different usage of the battery power. Minor differences have been detected also in the operating points of the ICE and MGs, as shown in Fig. 6.16. In particular, the more frequent selection of the input-split mode performed by the controller IM4 when the vehicle speed is steeply variable (see Fig. 6.15), results in a higher variation of the MG2 speed (see Fig. 6.16(b)), since it is kinematically coupled to the wheels in the input-split mode.

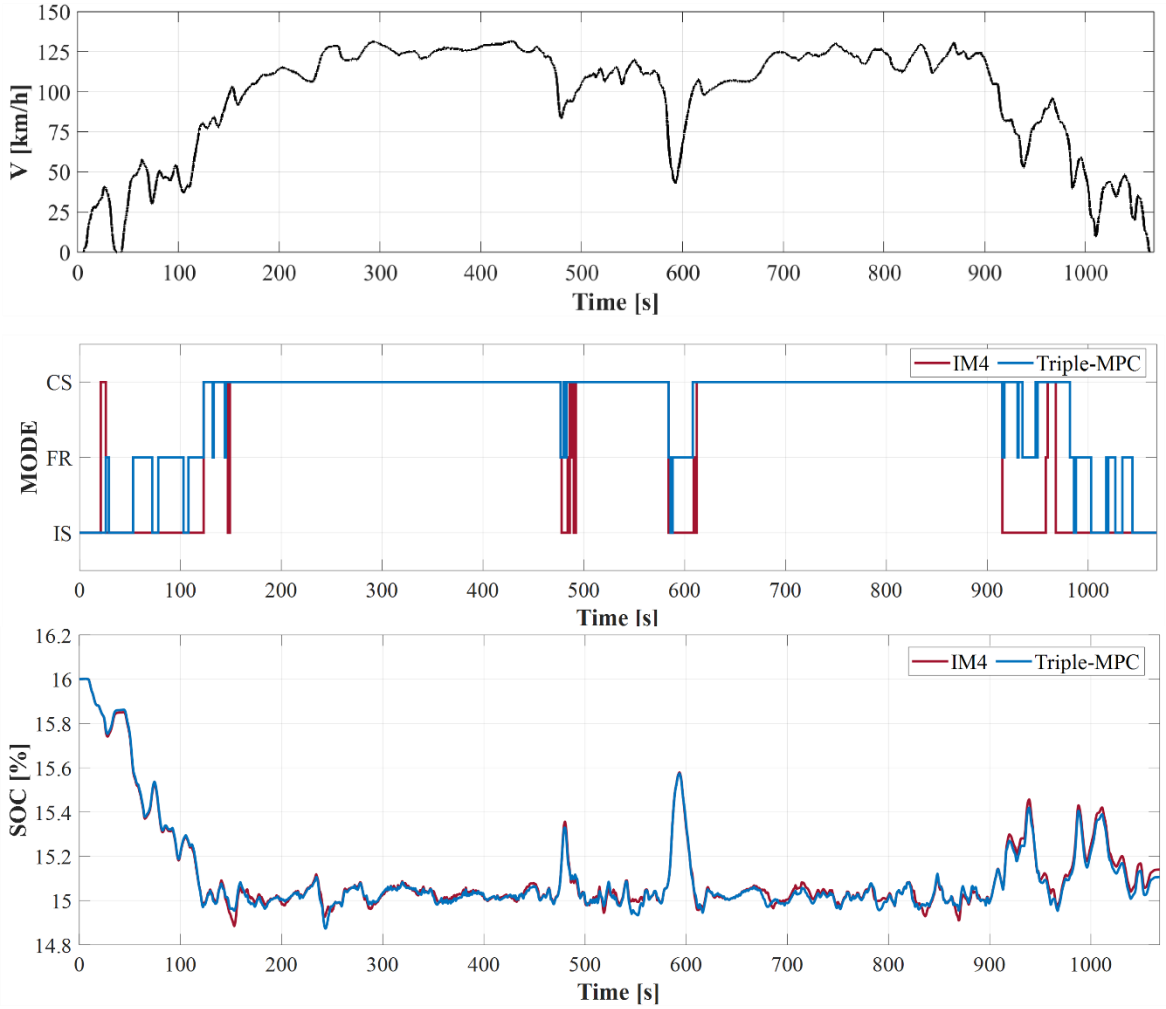

Fig. 6.15. IM4 with integrated mode switch versus Triple-MPC with offline mode optimisation strategy in the Artemis Motorway130 cycle: speed profile, mode, and battery SOC.

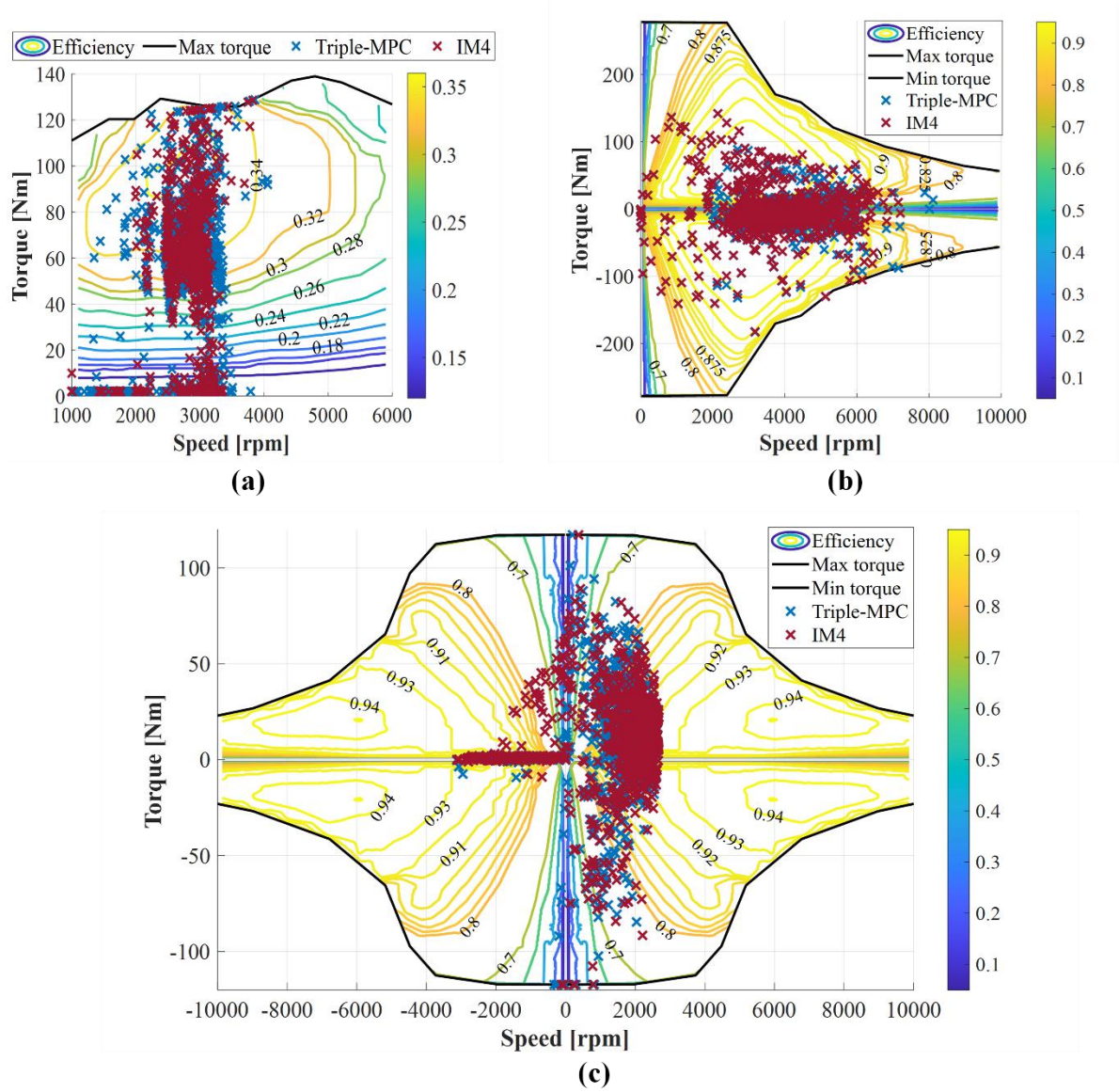

Fig. 6.16. IM4 with integrated mode switch versus Triple-MPC with offline mode optimisation strategy in the Artemis Motorway130 cycle: **(a)** ICE operations; **(b)** MG2 operations; **(c)** MG1 operations.

CONCLUSIONS

This research has expanded a unified parametric model for power-split continuously variable transmissions, which are the core unit of the most promising hybrid electric technology.

The speed, torque, and power ratios between any two shafts in the power-split unit depend on how the branches of the planetary gear trains are connected, as well as on the PGs constructive ratio. Moreover, any ordinary gear train and the connections between the PSU internal shafts with the actuators and the wheels must also be considered to model the whole power-split driveline. The speed of PG branches is ruled by the Willis equation, while the torque ratios are assessed by the free body diagram of the ring gear, sun gear, carrier, and planet gears in most of the models for PS-CVTs available in the literature. Nonetheless, modelling any power-split powertrain with this approach requires equations suitable only to the analysed PS-CVT; whenever the PSU constructive arrangement changes, even just in terms of the connections between shafts, a different set of equations must be considered.

The universal parametric model considered in this research has overcome the need for a case-specific formulation for PS-CVTs. Any PSU is modelled as a four-port device that some functional parameters can comprehensively characterise by ruling a set of universal equations for speed, torque and power ratios. Being speed ratios, these functional parameters are related to the Willis ratio of the PGs and the gear ratio of the OGs in the PSU. They are also affected by the state of any clutch included in a multi-mode PS-CVT arrangement. The strength of this parametric approach is the capability of modelling any PS-CVT relying on the same set of equations ruled by the functional parameters. The numerical values of the latter are the only difference among different PSUs, or between two modes of the same PSU. As a result, the wide variety of viable power-split transmissions can be addressed both in analysis and in the design phase through a unified mathematical treatment, which also includes a rapid assessment of the PSU meshing losses.

The main advancements of the research have concerned: 1) the introduction of a novel matrix approach for the identification of the functional parameters from the constructive layout of a PSU with any number of PGs and operating modes; 2) the extension of the formulation to the full-electric operation; 3) a design case study for hybridising an oil drilling rig; 4) the integration of the model within the vehicle energy management strategy.

In the analysis stage, the functional parameters can be identified from a constraint matrix

depending on the PSU constructive layout. Once the functional parameters are derived, the parametric model has enabled a rapid and comprehensive assessment of the PSU speed, torque and power ratios, including the consideration of the transmission meshing losses without any case-specific formulation. The model usability has been tested through an example of application on the multi-mode transmission of Cadillac CT6c, analysed in four power-split modes, three parallel modes, and four full-electric modes. The same analysis procedure relying on the same equations can be applied to any other PS-CVT.

A comprehensive assessment of any PS-CVT behaviour is performed by requiring only the a priori knowledge of the functional parameters, which are univocally defined for an existing PSU. However, the same set of functional parameters can be achieved by several constructive arrangements.

In the design stage, the functional parameters have to be defined yet. The parametric model enables a hierarchical and modular design procedure whereby each phase is decoupled from the others. Hence, once the ICE is selected, the designer can prioritise the sizing of the electric machines, the most expensive equipment, before defining the transmission constructive arrangement. In this respect, a strategy aimed at minimizing the motor-generators rated power is pursued. Then, the mechanical devices inside the PSU are synthesised, prioritising the selection of the PGs. The Willis ratio of the PGs, their synchronism, and connections can be selected by a design chart describing the power-split unit kinematics so as to avoid constructive complexity and improve mechanical efficiency. Lastly, the OGs necessary to meet the kinematics requirements are synthesised. Throughout the design procedure, the designer has complete control over the viable choices in each design stage, unlike in a computer-aided design process relying on automated algorithms based on topological models, such as the graph theory.

The modular parametric design procedure has been applied to hybridise an oil drilling rig to recover energy braking during the gravity-driven lowering phases. Moreover, further energy saving is obtained from the thermal unit downsizing and the possibility for the engine to continuously work at its most efficient operation. Although an energy management strategy is essential to select the ICE power size properly, two scenarios differing in engine power size have been investigated to probe how the engine selection affects the power size of the electric machines. In the first one, only one of the two engines deployed in the original drilling rig plant was kept in the hybrid layout, without any downsizing. As a result, the power required in the transmission output for hoisting operations was widely lower than the ICE operating point for most drilling rig functioning. This implied that such a high engine power is almost always unnecessary and causes an oversizing of the electric unit. Therefore,

a second scenario with a downsized engine was considered, which seemed preferable given the smaller electric unit resulting in lower costs, proving that the initial ICE sizing is crucial to optimise the hybridised powertrain in both energetical and cost-effective terms.

Therefore, significant efforts have been made to deploy the parametric model as a basis for the implementation of an energy management strategy. Firstly, the road load and the efficiency maps of ICE and electric MGs were introduced to shift from a dimensionless approach to a dimensional analysis of the powertrain response for a given vehicle speed and demanded torque. All the viable powertrain operating points are available as a set of operating maps containing the actuators functioning points, their efficiency, the meshing power losses in the transmission, the battery power, and the powertrain global efficiency. These data can be exploited for the development of the desired energy management strategy.

By way of example, a procedure for selecting the optimal operating points maximising the Chevrolet Volt global efficiency in steady-state power-split and full-electric driving was proposed. Then, the same procedure was adopted to analyse the transient operation of an output-split powertrain; this case study was used to compare two performance indices, i.e., the real powertrain global efficiency and an equivalent efficiency where ICE and MGs efficiency was normalised to the respective maximum value. The results showed the importance of properly handling the battery SOC to ensure the possibility of exploiting the electric unit as an energy exchanger, as well as the benefit of PGs synchronism to reduce friction losses. Moreover, the results suggested that considering the actual ICE efficiency, which is considerably lower than the MGs efficiency, would strongly penalise ICE operation, thus favouring battery power utilisation. However, this would lead to a charge-depleting drive that can suit PHEVs, not FHEVs. On the contrary, optimising the equivalent efficiency corresponds to maximising both ICE and MGs efficiency, thus resulting in a more charge-sustaining drive. Although these applications are far from an exhaustive control strategy, their outcome could be used as look-up tables to reduce the running time of an online EMS.

Lastly, the integration of the parametric model within a model predictive control EMS has been addressed. Thanks to the universal formulation ruled by the functional parameters that assume different values according to the constructive arrangement, switch functions were introduced to propose a novel integration of the mode shift within the receding horizon framework.

Moreover, the parametric model allowed the consideration of the transmission meshing losses in the MPC internal model, which are usually challenging to include because of the case-specific formulations required to assess losses in planetary gearing. Given the potential influence that the accuracy of the MPC internal model may have on the EMS performance,

a comparison of internal models with different complexity for power-split HEVs was proposed for the first time. The internal models to assess in the MPC framework were selected after a preliminary open-loop analysis. The simulations suggested that, besides the PSU meshing losses, the influence of electric machines efficiency was worthy of investigation, too, while the actuators inertial load is negligible. Thus, four internal models differing for null or variable PSU meshing losses and constant or polynomial-fitted MGs efficiency were compared for the charge-sustaining operation of the second generation of Chevrolet Volt. The results showed that the difference in fuel consumption between the simplest and the most complex internal model is 2% at most. In particular, considering or neglecting PSU meshing losses affects battery exploitation more than MGs efficiency, which, instead, has a higher impact on the engine operation. Furthermore, the novel MPC formulation with the integrated mode switch was compared with a benchmark EMS relying on a predetermined mode shift map, resulting in comparable performance.

Given that the improvement in fuel saving is relatively minor for the increased complexity of internal models, further analysis on real-time performance would help to understand if the new MPC formulation with variable meshing losses, polynomial MGs efficiency maps and integrated mode switch is worthy of onboard implementation. Nonetheless, for the same reason, the obtained results suggest that using a simplified internal model with ideal PSU and constant MGs efficiency does not involve a significant error in the estimation of overall fuel consumption. This may be useful during the design stage when the ultimate PSU constructive arrangement and the electric machines have not been selected yet.

The MPC formulation based on the parametric internal model presented in this research paves the path for the selection of the optimal functional parameters in the design stage. The strength of this approach is the possibility to simulate any existing and non-existing transmission, even multi-mode, by only varying the PSU main functional parameters and without requiring offline optimisation of the mode shift strategy. Thus, for a given vehicle, it is possible to simulate the MPC-based EMS by assuming upstream different values for the functional parameters, achieving a swift evaluation of how different functional parameters affect fuel consumption over a simulation of a typical driving scenario. As a result, the proposed MPC framework could be integrated with an optimisation algorithm for PSU functional parameters that can be selected according to the best vehicle performance and fuel saving. Then, the electric unit sizing and PSU synthesis could be performed according to the best functional parameters so as to pursue actuators downsizing and PGs synchronism. Lastly, the most complex internal model could be used to select the best powertrain arrangement among different viable solutions. Thanks to the utmost generality of the

described design approach, it can be adopted for any power-split powertrain, not only in the automotive field. Such an automated design approach would not be possible with a traditional PSU model relying on case-specific equations, because a variation of the internal model would be required for any change in the PSU.

The deployment of the analysed MPC framework in the design stage is still under development and requires further research to optimise the search for the best functional parameters in single-mode and multi-mode operations. Furthermore, the modular design process adopted in this research befits any single-mode shunt or compound power-split transmission with up to two planetary gear sets. Hence, future developments include the extension of the modular design process to multi-mode transmissions with any number of PGs. The integration of an EMS within the design process appears unavoidable for the ICE and electric unit sizing.

Other future developments will involve the introduction of the relationships between the PSU meshing losses and the inertial loads within a PSU direct dynamic model, and the investigation of how different objective functions affect the EMS and/or the sizing of the powertrain components.

REFERENCES

[1] Directorate-General for Mobility and Transport (European Commission), EU transport in figures – Statistical pocketbook 2021, Publications Office, 2021. https://doi.org/doi/10.2832/27610.

[2] European Commission, Commission proposal on the revision of Regulation (EU) 2019/631 setting CO2 emission performance standards for new passenger cars and for new light commercial vehicles, n.d. https://eur-lex.europa.eu/legal-content/EN/TXT/?uri=CELEX:52021PC0556.

[3] European Automobile Manufacturers' Association (ACEA), ACEA Pocket Guide 2023-2024, 2023. https://www.acea.auto/files/ACEA_Pocket_Guide_2023-2024.pdf.

[4] S. Statharas, Y. Moysoglou, P. Siskos, G. Zazias, P. Capros, Factors Influencing Electric Vehicle Penetration in the EU by 2030: A Model-Based Policy Assessment, Energies 2019, Vol. 12, Page 2739. 12 (2019) 2739. https://doi.org/10.3390/EN12142739.

[5] Q. Ali, M.L. Di Silvestre, P. Lombardi, E.R. Sanseverino, G. Zizzo, The Role of Renewable Energy Generation in Electric Vehicles Transition and Decarbonization of Transportation Sector, Proc. - 2023 IEEE Int. Conf. Environ. Electr. Eng. 2023 IEEE Ind. Commer. Power Syst. Eur. EEEIC / I CPS Eur. 2023. (2023). https://doi.org/10.1109/EEEIC/ICPSEUROPE57605.2023.10194766.

[6] E. Gryparis, P. Papadopoulos, H.C. Leligou, C.S. Psomopoulos, Electricity demand and carbon emission in power generation under high penetration of electric vehicles. A European Union perspective, Energy Reports. 6 (2020) 475–486. https://doi.org/10.1016/J.EGYR.2020.09.025.

[7] C. Mi, M.A. Masrur, Hybrid Electric Vehicles: Principles and Applications with Practical Perspectives, Second Edi, John Wiley & Sons Ltd., 2017. https://onlinelibrary.wiley.com/doi/book/10.1002/9781118970553.

[8] T.J. Böhme, B. Frank, Hybrid Systems, Optimal Control and Hybrid Vehicles, 2017. http://link.springer.com/10.1007/978-3-319-51317-1.

[9] L. Guzzella, A. Sciarretta, Vehicle propulsion systems: Introduction to modeling and optimization, Springer-Verlag Berlin Heidelberg, 2013. https://doi.org/10.1007/978-3-642-35913-2.

[10] Y. Yang, K.A. Ali, J. Roeleveld, A. Emadi, State-of-the-art electrified powertrains - hybrid, plug-in, and electric vehicles, Int. J. Powertrains. 5 (2016) 1–29. https://doi.org/10.1504/ijpt.2016.075181.

[11] M. Ehsani, Y. Gao, S.E. Gay, A. Emadi, Modern Electric, Hybrid Electric, and Fuel Cell Vehicles: Fundamentals, Theory, and Design, CRC Press LLC, 2005.

[12] D.D. Tran, M. Vafaeipour, M. El Baghdadi, R. Barrero, J. Van Mierlo, O. Hegazy, Thorough state-of-the-art analysis of electric and hybrid vehicle powertrains: Topologies and integrated energy management strategies, Renew. Sustain. Energy Rev. 119 (2020) 109596. https://doi.org/10.1016/J.RSER.2019.109596.

[13] K.V. Singh, H.O. Bansal, D. Singh, A comprehensive review on hybrid electric vehicles: architectures and components, J. Mod. Transp. 27 (2019) 77–107. https://doi.org/10.1007/s40534-019-0184-3.

[14] C.C. Chan, The state of the art of electric, hybrid, and fuel cell vehicles, Proc. IEEE. 95 (2007) 704–718. https://doi.org/10.1109/JPROC.2007.892489.

[15] V. Krithika, C. Subramani, A comprehensive review on choice of hybrid vehicles and power converters, control strategies for hybrid electric vehicles, Int. J. Energy Res. 42 (2018) 1789–1812. https://doi.org/10.1002/er.3952.

[16] W. Zhuang, S. Li (Eben), X. Zhang, D. Kum, Z. Song, G. Yin, F. Ju, A survey of powertrain configuration studies on hybrid electric vehicles, Appl. Energy. 262 (2020) 114553. https://doi.org/10.1016/j.apenergy.2020.114553.

[17] K.C. Prajapati, R. Patel, R. Sagar, Hybrid vehicle: A study on technology, Int. J. Eng. Res. Technol. 3 (2014) 1076–1082.

[18] W. Enang, C. Bannister, Modelling and control of hybrid electric vehicles (A comprehensive review), Renew. Sustain. Energy Rev. 74 (2017) 1210–1239. https://doi.org/https://doi.org/10.1016/j.rser.2017.01.075.

[19] X. Xu, P. Dong, Y. Liu, H. Zhang, Progress in Automotive Transmission Technology, Automot. Innov. 1 (2018) 187–210. https://doi.org/10.1007/s42154-018-0031-y.

[20] M.A. Hannan, F.A. Azidin, A. Mohamed, Hybrid electric vehicles and their challenges: A review, Renew. Sustain. Energy Rev. 29 (2014) 135–150. https://doi.org/10.1016/j.rser.2013.08.097.

[21] D.S. Cardoso, P.O. Fael, A. Espírito-Santo, A review of micro and mild hybrid systems, Energy Reports. 6 (2020) 385–390. https://doi.org/10.1016/j.egyr.2019.08.077.

[22] S.M. Lukic, J. Cao, R.C. Bansal, F. Rodriguez, A. Emadi, Energy Storage Systems for Automotive Applications, IEEE Trans. Ind. Electron. 55 (2008) 2258–2267. https://doi.org/10.1109/TIE.2008.918390.

[23] E.D. Tate, M.O. Harpster, P.J. Savagian, The electrification of the automobile: From conventional hybrid, to plug-in hybrids, to extended-range electric vehicles, SAE Tech. Pap. (2008). https://doi.org/10.4271/2008-01-0458.

[24] A.N. Duhon, K.S. Sevel, S.A. Tarnowsky, P.J. Savagian, Chevrolet Volt Electric Utilization, SAE Int. J. Altern. Powertrains. 4 (2015) 269–276. https://doi.org/10.4271/2015-01-1164.

[25] X. Zeng, J. Wang, Analysis and design of the power-split device for hybrid systems, Springer, Singapore, 2017. https://doi.org/10.1007/978-981-10-4272-0.

[26] H. Naunheimer, B. Bertsche, J. Ryborz, W. Novak, P. Fietkau, Automotive transmissions:

Fundamentals, selection, design and application, Springer, 2011. https://doi.org/10.1007/978-3-642-16214-5.

[27] N. Srivastava, I. Haque, A review on belt and chain continuously variable transmissions (CVT): Dynamics and control, Mech. Mach. Theory. 44 (2009) 19–41. https://doi.org/10.1016/J.MECHMACHTHEORY.2008.06.007.

[28] C. Sieg, F. Küçükay, Benchmarking of Dedicated Hybrid Transmissions, Vehicles. 2 (2020) 100–125. https://doi.org/10.3390/vehicles2010006.

[29] L. Wang, Y. Cui, F. Zhang, G. Li, Architectures of planetary hybrid powertrain system: Review, classification and comparison, Energies. 13 (2020). https://doi.org/10.3390/en13020329.

[30] H. Chen, L. Li, A. Lange, F. Küçükay, Innovative Dedicated Hybrid Transmission Concepts in the Next Generation of Hybrid Powertrains, SAE Int. J. Altern. Powertrains. 8 (2019) 75–88.

[31] M.A. Miller, A.G. Holmes, B.M. Conlon, P.J. Savagian, The GM "Voltec" 4ET50 Multi-Mode Electric Transaxle, SAE Int. J. Engines. 4 (2011) 1102–1114. https://doi.org/10.4271/2011-01-0887.

[32] W. Zhuang, X. Zhang, Y. Ding, L. Wang, X. Hu, Comparison of multi-mode hybrid powertrains with multiple planetary gears, Appl. Energy. 178 (2016) 624–632. https://doi.org/10.1016/j.apenergy.2016.06.111.

[33] N. Kim, J. Kwon, A. Rousseau, Trade-off between multi-mode powertrain complexity and fuel consumption, EVS 2010 - Sustain. Mobil. Revolut. 25th World Batter. Hybrid Fuel Cell Electr. Veh. Symp. Exhib. (2010).

[34] B. Conlon, Comparative analysis of single and combined hybrid electrically variable transmission operating modes, SAE Tech. Pap. 114 (2005) 1265–1275. https://doi.org/10.4271/2005-01-1162.

[35] B.M. Conlon, T. Blohm, M. Harpster, A. Holmes, M. Palardy, S. Tarnowsky, L. Zhou, The Next Generation "voltec" Extended Range EV Propulsion System, SAE Int. J. Altern. Powertrains. 4 (2015) 248–259. https://doi.org/10.4271/2015-01-1152.

[36] A.G. Holmes, M.R. Schmidt, Hybrid electric powertrain including a two-mode electrically variable transmission, 2002.

[37] A. Holmes, J. Liu, D. Ames, V. Neelakantan, K. Rahman, T. Grewe, General Motors Electric Variable Transmission for Cadillac CT6 Sedan, SAE Tech. Pap. (2016). https://doi.org/10.4271/2016-01-1150.

[38] Z. Zhao, P. Tang, H. Li, Generation, Screening, and Optimization of Powertrain Configurations for Power-Split Hybrid Electric Vehicle: A Comprehensive Overview, IEEE Trans. Transp. Electrif. 8 (2022) 325–344. https://doi.org/10.1109/TTE.2021.3105244.

[39] F. Buchsbaum, F. Freudenstein, Synthesis of kinematic structure of geared kinematic chains and other mechanisms, J. Mech. 5 (1970) 357–392. https://doi.org/10.1016/0022-

2569(70)90068-6.

[40] J.R. Gomà Ayats, U. Diego-Ayala, J. Minguella Canela, F. Fenollosa, J. Vivancos, Hypergraphs for the analysis of complex mechanisms comprising planetary gear trains and other variable or fixed transmissions, Mech. Mach. Theory. 51 (2012) 217–229. https://doi.org/10.1016/j.mechmachtheory.2011.07.011.

[41] H. Pei, X. Hu, Y. Yang, X. Tang, C. Hou, D. Cao, Configuration optimization for improving fuel efficiency of power split hybrid powertrains with a single planetary gear, Appl. Energy. 214 (2018) 103–116. https://doi.org/10.1016/j.apenergy.2018.01.070.

[42] H. Pei, X. Hu, Y. Yang, H. Peng, L. Hu, X. Lin, Designing Multi-Mode Power Split Hybrid Electric Vehicles Using the Hierarchical Topological Graph Theory, IEEE Trans. Veh. Technol. 69 (2020) 7159–7171. https://doi.org/10.1109/TVT.2020.2993019.

[43] V.R. Shanmukhasundaram, Y. V.D. Rao, S.P. Regalla, Enumeration of displacement graphs of epicyclic gear train from a given rotation graph using concept of building of kinematic units, Mech. Mach. Theory. 134 (2019) 393–424. https://doi.org/10.1016/j.mechmachtheory.2019.01.005.

[44] X. Zhou, D. Qin, D. Rotella, M. Cammalleri, Hybrid electric vehicle powertrain design: Construction of topologies and initial design schemes, Springer International Publishing, 2019. https://doi.org/10.1007/978-3-030-03320-0_6.

[45] H.T. Ngo, H. Sen Yan, Configuration synthesis of parallel hybrid transmissions, Mech. Mach. Theory. 97 (2016) 51–71. https://doi.org/10.1016/j.mechmachtheory.2015.11.002.

[46] W. Yang, H. Ding, A. Kecskeméthy, Automatic structural synthesis of non-fractionated 2-DOF planetary gear trains, Mech. Mach. Theory. 155 (2021) 104125. https://doi.org/10.1016/j.mechmachtheory.2020.104125.

[47] H. Ngo, H. Yan, Configuration synthesis of series-parallel hybrid transmissions, Proc. Inst. Mech. Eng. Part D J. Automob. Eng. 230 (2016) 664–678. https://doi.org/10.1177/0954407015591405.

[48] M. Du, L. Yang, A basis for the computer-aided design of the topological structure of planetary gear trains, Mech. Mach. Theory. 145 (2020) 103690. https://doi.org/10.1016/j.mechmachtheory.2019.103690.

[49] C. Münzer, B. Helms, K. Shea, Automatically Transforming Object-Oriented Graph-Based Representations Into Boolean Satisfiability Problems for Computational Design Synthesis, J. Mech. Des. 135 (2013). https://doi.org/10.1115/1.4024850.

[50] P. Dong, S. Zuo, T. Liu, X. Xu, W. Guo, Y. Liu, H. Wu, S. Wang, A matrix-based method for searching configurations of planetary gear trains, Mech. Mach. Theory. 180 (2023) 105161. https://doi.org/10.1016/j.mechmachtheory.2022.105161.

[51] F. Yang, J. Feng, H. Zhang, Power flow and efficiency analysis of multi-flow planetary gear trains, Mech. Mach. Theory. 92 (2015) 86–99. https://doi.org/10.1016/j.mechmachtheory.2015.05.003.

[52] D.R. Salgado, J.M. Del Castillo, Analysis of the transmission ratio and efficiency ranges of the four-, five-, and six-link planetary gear trains, Mech. Mach. Theory. 73 (2014) 218–243. https://doi.org/10.1016/j.mechmachtheory.2013.11.001.

[53] X. Zhang, C.T. Li, D. Kum, H. Peng, Prius + and volt -: Configuration analysis of power-split hybrid vehicles with a single planetary gear, IEEE Trans. Veh. Technol. 61 (2012) 3544–3552. https://doi.org/10.1109/TVT.2012.2208210.

[54] W. Wang, R. Song, M. Guo, S. Liu, Analysis on compound-split configuration of power-split hybrid electric vehicle, Mech. Mach. Theory. 78 (2014) 272–288. https://doi.org/10.1016/j.mechmachtheory.2014.03.019.

[55] T. Ke, H. Ding, C. Gong, M. Geng, Configuration synthesis of nine-speed automatic transmissions based on structural decomposition, Mech. Mach. Theory. 164 (2021) 104421. https://doi.org/10.1016/J.MECHMACHTHEORY.2021.104421.

[56] J. Gao, T. Zhang, H. Yu, C. Wang, H. Cheng, F. Ge, A New Strategy to Optimize the Economy Performance of the New Power-Split Hybrid Transmission Platform CHS-HT2800, SAE Tech. Pap. 2018-April (2018) 1–12. https://doi.org/10.4271/2018-01-1016.

[57] T. Barhoumi, H. Kim, D. Kum, Automatic generation of design space conversion maps and its application for the design of compound split hybrid powertrains, J. Mech. Des. Trans. ASME. 140 (2018) 1–12. https://doi.org/10.1115/1.4039451.

[58] H. Kim, T. Barhoumi, D. Kum, Comprehensive Design Methodology of Compound-Split Hybrid Electric Vehicles: Introduction of the Compound Lever as a Design Tool, IEEE Access. 7 (2019) 84744–84756. https://doi.org/10.1109/ACCESS.2019.2925146.

[59] H.L. Benford, M.B. Leising, The lever analogy: A new tool in transmission analysis, SAE Trans. (1981) 429–437.

[60] H. Yang, S. Cho, N. Kim, W. Lim, S. Cha, Analysis of planetary gear hybrid powertrain system part 1: Input split system, Int. J. Automot. Technol. 8 (2007) 771–780.

[61] H. Yang, B. Kim, Y. Park, W. Lim, S. Cha, Analysis of planetary gear hybrid powertrain system part 2: output split system, Int. J. Automot. Technol. 10 (2009) 381–390.

[62] X. Chen, J. Jiang, L. Zheng, H. Tang, X. Chen, Study and analysis of a multi-mode power split hybrid transmission, World Electr. Veh. J. 11 (2020). https://doi.org/10.3390/WEVJ11020046.

[63] W. Lee, J. Park, N. Kim, Analysis of Transmission Efficiency of a Plug-In Hybrid Vehicle Based on Operating Modes, Int. J. Precis. Eng. Manuf. - Green Technol. 8 (2021) 165–175. https://doi.org/10.1007/s40684-019-00147-9.

[64] Y.G. Liao, M.Y. Chen, Analysis of multi-speed transmission and electrically continuous variable transmission using lever analogy method for speed ratio determination, Adv. Mech. Eng. 9 (2017) 1–12. https://doi.org/10.1177/1687814017712948.

[65] N. Kim, S. Choi, J. Jeong, R. Vijayagopal, K. Stutenberg, A. Rousseau, Vehicle level control analysis for Voltec powertrain, World Electr. Veh. J. 9 (2018) 1–12.

https://doi.org/10.3390/wevj9020029.

[66] H. Peng, D. Qin, J. Hu, C. Fu, Synthesis and analysis method for powertrain configuration of single motor hybrid electric vehicle, Mech. Mach. Theory. 146 (2020) 103731. https://doi.org/10.1016/J.MECHMACHTHEORY.2019.103731.

[67] X. Zhang, S. Eben Li, H. Peng, J. Sun, Efficient exhaustive search of power-split hybrid powertrains with multiple planetary gears and clutches, J. Dyn. Syst. Meas. Control. Trans. ASME. 137 (2015). https://doi.org/10.1115/1.4031533.

[68] C.-T. Chung, C.-H. Wu, Y.-H. Hung, A design methodology for selecting energy-efficient compound split e-CVT hybrid systems with planetary gearsets based on electric circulation, Energy. 230 (2021) 120732. https://doi.org/10.1016/j.energy.2021.120732.

[69] X. Zhang, H. Peng, J. Sun, A near-optimal power management strategy for rapid component sizing of multimode power split hybrid vehicles, IEEE Trans. Control Syst. Technol. 23 (2015) 609–618. https://doi.org/10.1109/TCST.2014.2335060.

[70] S.S. Volpe, G. Carbone, M. Napolitano, E. Sedoni, Design optimization of input and output coupled power split infinitely variable transmissions, J. Mech. Des. Trans. ASME. 131 (2009) 1110021–11100211. https://doi.org/10.1115/1.3179145.

[71] E. Ince, M.A. Guler, Design and Analysis of a Novel Power-Split Infinitely Variable Power Transmission System, J. Mech. Des. Trans. ASME. 141 (2019). https://doi.org/10.1115/1.4041783.

[72] P.G. Anselma, Y. Huo, J. Roeleveld, A. Emadi, G. Belingardi, Rapid optimal design of a multimode power split hybrid electric vehicle transmission, Proc. Inst. Mech. Eng. Part D J. Automob. Eng. 233 (2019) 740–762. https://doi.org/10.1177/0954407017750789.

[73] O.H. Dagci, H. Peng, J.W. Grizzle, Hybrid electric powertrain design methodology with planetary gear sets for performance and fuel economy, IEEE Access. 6 (2018) 9585–9602. https://doi.org/10.1109/ACCESS.2018.2796939.

[74] D.C. Talbot, A. Kahraman, A. Singh, An Experimental Investigation of the Efficiency of Planetary Gear Sets, J. Mech. Des. 134 (2012). https://doi.org/10.1115/1.4005599.

[75] D. Talbot, A. Kahraman, A methodology to predict power losses of planetary gear sets, in: Int. Gear Conf. 2014 26th–28th August 2014, Lyon, 2014: pp. 625–635. https://doi.org/10.1533/9781782421955.625.

[76] A. Kahraman, D.R. Hilty, A. Singh, An experimental investigation of spin power losses of a planetary gear set, Mech. Mach. Theory. 86 (2015) 48–61. https://doi.org/10.1016/j.mechmachtheory.2014.12.003.

[77] C. Nutakor, A. Kłodowski, J. Sopanen, A. Mikkola, J.I. Pedrero, Planetary gear sets power loss modeling: Application to wind turbines, Tribol. Int. 105 (2017) 42–54. https://doi.org/10.1016/J.TRIBOINT.2016.09.029.

[78] J.M. del Castillo, The analytical expression of the efficiency of planetary gear trains, Mech. Mach. Theory. 37 (2002) 197–214. https://doi.org/https://doi.org/10.1016/S0094-

114X(01)00077-5.

[79] M. Velardocchia, E. Bonisoli, E. Galvagno, A. Vigliani, A. Sorniotti, Efficiency of Epicyclic Gears in Automated Manual Transmission Systems, SAE Tech. Pap. 2007-Septe (2007). https://doi.org/10.4271/2007-24-0139.

[80] E.L. Esmail, E. Pennestrì, A. Hussein Juber, Power losses in two-degrees-of-freedom planetary gear trains: A critical analysis of Radzimovsky's formulas, Mech. Mach. Theory. 128 (2018) 191–204. https://doi.org/10.1016/j.mechmachtheory.2018.05.015.

[81] F. Bottiglione, S. De Pinto, G. Mantriota, Infinitely Variable Transmissions in neutral gear: Torque ratio and power re-circulation, Mech. Mach. Theory. 74 (2014) 285–298. https://doi.org/10.1016/j.mechmachtheory.2013.12.017.

[82] A.K. Gupta, C.P. Ramanarayanan, Analysis of circulating power within hybrid electric vehicle transmissions, Mech. Mach. Theory. 64 (2013) 131–143. https://doi.org/10.1016/j.mechmachtheory.2013.01.011.

[83] D. Rotella, M. Cammalleri, Power losses in power-split CVTs: A fast black-box approximate method, Mech. Mach. Theory. 128 (2018) 528–543. https://doi.org/10.1016/j.mechmachtheory.2018.06.011.

[84] S. De Pinto, G. Mantriota, Power Flows in Compound Transmissions for Hybrid Vehicles, Machines. 7 (2019) 19. https://doi.org/10.3390/MACHINES7010019.

[85] M. De Carlo, G. Mantriota, Electric vehicles with two motors combined via planetary gear train, Mech. Mach. Theory. 148 (2020) 103789. https://doi.org/10.1016/J.MECHMACHTHEORY.2020.103789.

[86] F. Bottiglione, S. De Pinto, G. Mantriota, A Simple Approach for Hybrid Transmissions Efficiency, Recent Res. Environ. Geol. Sci. (2014) 386–391.

[87] F. Bottiglione, G. Mantriota, Power Flows and Efficiency of Output Compound e-CVT, Int. J. Veh. Technol. 2015 (2015) 136437. https://doi.org/10.1155/2015/136437.

[88] G. Mantriota, G. Reina, Dual-Motor Planetary Transmission to Improve Efficiency in Electric Vehicles, Machines. 9 (2021) 58. https://doi.org/10.3390/machines9030058.

[89] G. Mantriota, G. Reina, A. Ugenti, Performance Evaluation of a Compound Power-Split CVT for Hybrid Powertrains, Appl. Sci. 2021, Vol. 11, Page 8749. 11 (2021) 8749. https://doi.org/10.3390/APP11188749.

[90] E.L. Esmail, E. Pennestrì, M. Cirelli, Power-Flow and Mechanical Efficiency Computation in Two-Degrees-of-Freedom Planetary Gear Units: New Compact Formulas, Appl. Sci. 2021, Vol. 11, Page 5991. 11 (2021) 5991. https://doi.org/10.3390/APP11135991.

[91] G. Mantriota, E. Pennestrì, Theoretical and Experimental Efficiency Analysis of Multi-Degrees-of-Freedom Epicyclic Gear Trains, Multibody Syst. Dyn. 9 (2003) 389–408. https://doi.org/10.1023/A:1023319515306.

[92] E. Pennestrì, P.P. Valentini, A review of formulas for the mechanical efficiency analysis of two degrees-of-freedom epicyclic gear trains, J. Mech. Des. Trans. ASME. 125 (2003) 602–

608. https://doi.org/10.1115/1.1587157.

[93] E. Pennestrì, F. Freudenstein, A systematic approach to power-flow and static-force analysis in epicyclic spur-gear trains, J. Mech. Des. Trans. ASME. 115 (1993) 639–644. https://doi.org/10.1115/1.2919238.

[94] E. Pennestrì, L. Mariti, P.P. Valentini, V.H. Mucino, Efficiency evaluation of gearboxes for parallel hybrid vehicles: Theory and applications, Mech. Mach. Theory. 49 (2012) 157–176. https://doi.org/10.1016/j.mechmachtheory.2011.10.012.

[95] M. Cammalleri, D. Rotella, Functional design of power-split CVTs: An uncoupled hierarchical optimized model, Mech. Mach. Theory. 116 (2017) 294–309. https://doi.org/10.1016/j.mechmachtheory.2017.06.003.

[96] D. Rotella, M. Cammalleri, Direct analysis of power-split CVTs: A unified method, Mech. Mach. Theory. 121 (2018) 116–127. https://doi.org/10.1016/j.mechmachtheory.2017.10.006.

[97] M.F. M. Sabri, K.A. Danapalasingam, M.F. Rahmat, A review on hybrid electric vehicles architecture and energy management strategies, Renew. Sustain. Energy Rev. 53 (2016) 1433–1442. https://doi.org/10.1016/j.rser.2015.09.036.

[98] C.M. Martinez, X. Hu, D. Cao, E. Velenis, B. Gao, M. Wellers, Energy Management in Plug-in Hybrid Electric Vehicles: Recent Progress and a Connected Vehicles Perspective, IEEE Trans. Veh. Technol. 66 (2017) 4534–4549. https://doi.org/10.1109/TVT.2016.2582721.

[99] F. Zhang, X. Hu, R. Langari, D. Cao, Energy management strategies of connected HEVs and PHEVs: Recent progress and outlook, Prog. Energy Combust. Sci. 73 (2019) 235–256. https://doi.org/10.1016/j.pecs.2019.04.002.

[100] Y. Zhu, X. Li, Q. Liu, S. Li, Y. Xu, A comprehensive review of energy management strategies for hybrid electric vehicles, Mech. Sci. 13 (2022) 147–188. https://doi.org/10.5194/MS-13-147-2022.

[101] S. Onori, L. Serrao, G. Rizzoni, Hybrid Electric Vehicles Energy Management Strategies, Springer, London, 2016.

[102] M.F. M. Sabri, K.A. Danapalasingam, M.F. Rahmat, A review on hybrid electric vehicles architecture and energy management strategies, Renew. Sustain. Energy Rev. 53 (2016) 1433–1442. https://doi.org/https://doi.org/10.1016/j.rser.2015.09.036.

[103] A. Panday, H.O. Bansal, A review of optimal energy management strategies for hybrid electric vehicle, Int. J. Veh. Technol. 2014 (2014) 160510. https://doi.org/10.1155/2014/160510.

[104] A. Sciarretta, L. Guzzella, Control of Hybrid Electric Vehicles, IEEE Control Syst. Mag. 27 (2007) 60–70.

[105] F. Zhang, L. Wang, S. Coskun, H. Pang, Y. Cui, J. Xi, Energy management strategies for hybrid electric vehicles: Review, classification, comparison, and outlook, Energies. 13 (2020) 1–35. https://doi.org/10.3390/en13133352.

[106] A. Biswas, A. Emadi, Energy management systems for electrified powertrains: State-of-the-

art review and future trends, IEEE Trans. Veh. Technol. 68 (2019) 6453–6467. https://doi.org/10.1109/TVT.2019.2914457.

[107] P. Zhang, F. Yan, C. Du, A comprehensive analysis of energy management strategies for hybrid electric vehicles based on bibliometrics, Renew. Sustain. Energy Rev. 48 (2015) 88–104. https://doi.org/10.1016/j.rser.2015.03.093.

[108] Q. Xue, X. Zhang, T. Teng, J. Zhang, Z. Feng, Q. Lv, A comprehensive review on classification, energy management strategy, and control algorithm for hybrid electric vehicles, Energies. 13 (2020). https://doi.org/10.3390/en13205355.

[109] A.M. Ali, D. Söffker, Towards optimal power management of hybrid electric vehicles in real-time: A review on methods, challenges, and state-of-the-art solutions, Energies. 11 (2018) 1–24. https://doi.org/10.3390/en11030476.

[110] J.M. Maciejowski, Predictive Control: With Constraints, Prentice Hall, 2002.

[111] Y. Huang, H. Wang, A. Khajepour, H. He, J. Ji, Model predictive control power management strategies for HEVs: A review, J. Power Sources. 341 (2017) 91–106. https://doi.org/10.1016/j.jpowsour.2016.11.106.

[112] X. Lü, S. Li, X.H. He, C. Xie, S. He, Y. Xu, J. Fang, M. Zhang, X. Yang, Hybrid electric vehicles: A review of energy management strategies based on model predictive control, J. Energy Storage. 56 (2022) 106112. https://doi.org/10.1016/J.EST.2022.106112.

[113] U. Montanaro, S. Dixit, S. Fallah, M. Dianati, A. Stevens, D. Oxtoby, A. Mouzakitis, Towards connected autonomous driving: review of use-cases, Veh. Syst. Dyn. 57 (2019) 779–814. https://doi.org/10.1080/00423114.2018.1492142.

[114] J. Theunissen, A. Tota, P. Gruber, M. Dhaens, A. Sorniotti, Preview-based techniques for vehicle suspension control: a state-of-the-art review, Annu. Rev. Control. 51 (2021) 206–235. https://doi.org/10.1016/J.ARCONTROL.2021.03.010.

[115] V. Vidal, P. Stano, G. Tavolo, M. Dhaens, D. Tavernini, P. Gruber, A. Sorniotti, On Pre-Emptive In-Wheel Motor Control for Reducing the Longitudinal Acceleration Oscillations Caused by Road Irregularities, IEEE Trans. Veh. Technol. 71 (2022) 9322–9337. https://doi.org/10.1109/TVT.2022.3172172.

[116] A. Scamarcio, C. Caponio, M. Mihalkov, P. Georgiev, J. Ahmadi, K.M. So, D. Tavernini, A. Sorniotti, Predictive anti-jerk and traction control for V2X connected electric vehicles with central motor and open differential, IEEE Trans. Veh. Technol. (2022). https://doi.org/10.1109/TVT.2022.3143497.

[117] W. Golebiewski, K. Prajwowski, K. Danilecki, M. Lisowski, K.F. Abramek, Reducing the Fuel Consumption of an Hybrid Electric Vehicle with the Use of Model Predictive Control - Case Study, IEEE Trans. Veh. Technol. (2023). https://doi.org/10.1109/TVT.2023.3266829.

[118] C. Sun, S.J. Moura, X. Hu, J.K. Hedrick, F. Sun, Dynamic Traffic Feedback Data Enabled Energy Management in Plug-in Hybrid Electric Vehicles, IEEE Trans. Control Syst. Technol. 23 (2015) 1075–1086. https://doi.org/10.1109/TCST.2014.2361294.

[119] C. Sun, X. Hu, S.J. Moura, F. Sun, Velocity Predictors for Predictive Energy Management in Hybrid Electric Vehicles, IEEE Trans. Control Syst. Technol. 23 (2015) 1197–1204. https://doi.org/10.1109/TCST.2014.2359176.

[120] C. Le Xiang, F. Ding, W. Da Wang, W. He, Y.L. Qi, MPC-based energy management with adaptive Markov-chain prediction for a dual-mode hybrid electric vehicle, Sci. China Technol. Sci. 60 (2017) 737–748. https://doi.org/10.1007/s11431-016-0640-2.

[121] C. Xiang, F. Ding, W. Wang, W. He, Energy management of a dual-mode power-split hybrid electric vehicle based on velocity prediction and nonlinear model predictive control, Appl. Energy. 189 (2017) 640–653. https://doi.org/10.1016/j.apenergy.2016.12.056.

[122] J. Guo, H. He, C. Sun, ARIMA-based road gradient and vehicle velocity prediction for hybrid electric vehicle energy management, IEEE Trans. Veh. Technol. 68 (2019) 5309–5320. https://doi.org/10.1109/TVT.2019.2912893.

[123] J. Oncken, B. Chen, Real-Time Model Predictive Powertrain Control for a Connected Plug-In Hybrid Electric Vehicle, IEEE Trans. Veh. Technol. 69 (2020) 8420–8432. https://doi.org/10.1109/TVT.2020.3000471.

[124] Z. Chen, H. Hu, Y. Wu, Y. Zhang, G. Li, Y. Liu, Stochastic model predictive control for energy management of power-split plug-in hybrid electric vehicles based on reinforcement learning, Energy. 211 (2020). https://doi.org/10.1016/j.energy.2020.118931.

[125] B. Zhang, J. Zhang, F. Xu, T. Shen, Optimal control of power-split hybrid electric powertrains with minimization of energy consumption, Appl. Energy. 266 (2020) 114873. https://doi.org/10.1016/J.APENERGY.2020.114873.

[126] J. Oncken, K. Sachdeva, H. Wang, B. Chen, Integrated Predictive Powertrain Control for a Multimode Plug-in Hybrid Electric Vehicle, IEEE/ASME Trans. Mechatronics. 26 (2021) 1248–1259. https://doi.org/10.1109/TMECH.2021.3061287.

[127] W. Wang, X. Guo, C. Yang, Y. Zhang, Y. Zhao, D. Huang, C. Xiang, A multi-objective optimization energy management strategy for power split HEV based on velocity prediction, Energy. 238 (2022) 121714. https://doi.org/10.1016/J.ENERGY.2021.121714.

[128] D. Yang, T. Liu, D. Song, X. Zhang, X. Zeng, A real time multi-objective optimization Guided-MPC strategy for power-split hybrid electric bus based on velocity prediction, Energy. 276 (2023). https://doi.org/10.1016/J.ENERGY.2023.127583.

[129] X. Yang, C. Jiang, M. Zhou, H. Hu, Bi-level energy management strategy for power-split plug-in hybrid electric vehicles: A reinforcement learning approach for prediction and control, Front. Energy Res. 11 (2023) 183. https://doi.org/10.3389/FENRG.2023.1153390/BIBTEX.

[130] N. Yang, S. Ruan, L. Han, H. Liu, L. Guo, C. Xiang, Reinforcement learning-based real-time intelligent energy management for hybrid electric vehicles in a model predictive control framework, Energy. 270 (2023) 126971. https://doi.org/10.1016/J.ENERGY.2023.126971.

[131] J. Zhang, T. Shen, Real-Time Fuel Economy Optimization with Nonlinear MPC for PHEVs,

IEEE Trans. Control Syst. Technol. 24 (2016) 2167–2175. https://doi.org/10.1109/TCST.2016.2517130.

[132] K. Yu, H. Yang, X. Tan, T. Kawabe, Y. Guo, Q. Liang, Z. Fu, Z. Zheng, Model Predictive Control for Hybrid Electric Vehicle Platooning Using Slope Information, IEEE Trans. Intell. Transp. Syst. 17 (2016) 1894–1909. https://doi.org/10.1109/TITS.2015.2513766.

[133] W. Wang, C. Xiang, H. Liu, S. Jia, A model-predictive-control-based power management strategy for a power-split electromechanical transmission, Proc. Inst. Mech. Eng. Part D J. Automob. Eng. 230 (2016) 1987–2001. https://doi.org/10.1177/0954407016630911.

[134] X. Li, L. Han, H. Liu, W. Wang, C. Xiang, Real-time optimal energy management strategy for a dual-mode power-split hybrid electric vehicle based on an explicit model predictive control algorithm, Energy. 172 (2019) 1161–1178. https://doi.org/10.1016/j.energy.2019.01.052.

[135] H. Wang, J. Oncken, B. Chen, Receding horizon control for mode selection and powertrain control of a multi-mode hybrid electric vehicle, IEEE Veh. Technol. Conf. 2019-Septe (2019). https://doi.org/10.1109/VTCFALL.2019.8891382.

[136] R. Yang, X. Yang, W. Huang, S. Zhang, Energy Management of the Power-Split Hybrid Electric City Bus Based on the Stochastic Model Predictive Control, IEEE Access. 9 (2021) 2055–2071. https://doi.org/10.1109/ACCESS.2020.3047113.

[137] Z. Chen, H. Gu, S. Shen, J. Shen, Energy management strategy for power-split plug-in hybrid electric vehicle based on MPC and double Q-learning, Energy. 245 (2022) 123182. https://doi.org/10.1016/J.ENERGY.2022.123182.

[138] F. Ju, N. Murgovski, W. Zhuang, X. Hu, Z. Song, L. Wang, Predictive energy management with engine switching control for hybrid electric vehicle via ADMM, Energy. 263 (2023) 125971. https://doi.org/10.1016/J.ENERGY.2022.125971.

[139] M. Cammalleri, A. Castellano, Analysis of hybrid vehicle transmissions with any number of modes and planetary gearing : kinematics, power flows, mechanical power losses, Mech. Mach. Theory. 162 (2021) 104350. https://doi.org/10.1016/j.mechmachtheory.2021.104350.

[140] A. Castellano, D. Leone, M. Cammalleri, Design of a Hybrid Electric Power-Split Transmission for Braking Energy Recovery in a Drilling Rig, Designs. 6 (2022) 74. https://doi.org/10.3390/designs6050074.

[141] A. Castellano, M. Cammalleri, Global Efficiency of Power-Split Hybrid Electric Powertrain, in: Mech. Mach. Sci., Quaglia G., Gasparetto A., Petuya V., Carbone G. (eds) Proceedings of I4SDG Workshop 2021. I4SDG 2021. Mechanisms and Machine Science, vol 108. Springer, Cham., 2022: pp. 502–511. https://doi.org/10.1007/978-3-030-87383-7_54.

[142] A. Castellano, M. Cammalleri, Power losses minimization for optimal operating maps in power-split HEVs: A case study on the Chevrolet Volt, Appl. Sci. 11 (2021) 7779. https://doi.org/10.3390/app11177779.

[143] A. Castellano, M. Cammalleri, Optimal operation of power-split hybrid electric powertrain:

comparison between two performance indices, Int. J. Mech. Control. 23 (2022) 3–14.

[144] A. Castellano, P. Stano, U. Montanaro, M. Cammalleri, A. Sorniotti, Model predictive control for multimode power-split hybrid electric vehicles : Parametric internal model with integrated mode switch and variable meshing losses, Mech. Mach. Theory. 192 (2024) 105543. https://doi.org/10.1016/j.mechmachtheory.2023.105543.

[145] A.G. Holmes, M.R. Schmidt, D. Klemen, B.M. Conlon, Three mode electrically-variable transmission, 2010.

[146] A. Khan, T. Grewe, J. Liu, M. Anwar, A. Holmes, R. Balsley, The GM RWD PHEV Propulsion System for the Cadillac CT6 Luxury Sedan, SAE Tech. Pap. (2016). https://doi.org/10.4271/2016-01-1159.

[147] S. Jurkovic, K.M. Rahman, P.J. Savagian, Electric traction motors for Cadillac CT6 plugin hybrid-electric vehicle, ECCE 2016 - IEEE Energy Convers. Congr. Expo. Proc. (2016) 1–9. https://doi.org/10.1109/ECCE.2016.7855030.

[148] D. Rotella, M. Cammalleri, D. Qin, X. Zhou, A simple method for the design of hybrid electric power-split cvts: A case study, Springer International Publishing, 2019. https://doi.org/10.1007/978-3-030-03320-0_8.

[149] W.C. Lyons, G.J. Plisga, M.D.B.T. Lorenz, Standard Handbook of Petroleum and Natural Gas Engineering, Gulf Professional Publishing, 2016.

[150] A. Ismail, W. Moustafa, New hybrid drill bit with innovative technology improves drilling efficiency in challenging Jordanian drilling project, Soc. Pet. Eng. - SPE Saudi Arab. Sect. Tech. Symp. Exhib. (2014). https://doi.org/10.2118/172169-MS.

[151] P. Yadav, R. Kumar, S.K. Panda, C.S. Chang, An Improved Harmony Search algorithm for optimal scheduling of the diesel generators in oil rig platforms, Energy Convers. Manag. 52 (2011) 893–902. https://doi.org/10.1016/J.ENCONMAN.2010.08.016.

[152] D. Pavković, A. Sedić, Z. Guzović, Oil drilling rig diesel power-plant fuel efficiency improvement potentials through rule-based generator scheduling and utilization of battery energy storage system, Energy Convers Manag. 121 (2016) 194–211. https://doi.org/10.1016/j.enconman.2016.05.022.

[153] E. Chupin, K. Frolov, M. Korzhavin, O. Zhdaneev, Energy storage systems for drilling rigs, J. Pet. Explor. Prod. Technol. 12 (2022) 341–350. https://doi.org/10.1007/S13202-021-01248-5/TABLES/2.

[154] M. Bilgin, J. Donen, V. Scaini, M. Snijder, World's first hybrid drilling rig, SPE/IADC Drill. Conf. Proc. 2020-March (2020) 0–3. https://doi.org/10.2118/199573-ms.

[155] Z. Lujun, An energy-saving oil drilling rig for recovering potential energy and decreasing motor power, Energy Convers. Manag. 52 (2011) 359–365. https://doi.org/10.1016/J.ENCONMAN.2010.07.009.

[156] X. Dai, K. Wei, X. Zhang, Analysis of the peak load leveling mode of a hybrid power system with flywheel energy storage in oil drilling rig, Energies. 12 (2019).

https://doi.org/10.3390/en12040606.

[157] A.-M. LUPAȘCU (OPREA), V.-M. IONESCU, I. POTÂRNICHE, V. NĂVRĂPESCU, A.-A. SĂPUNARU, Increase of energy efficiency of electrically driven drilling installations by valorising the braking regime of the draw works upon descending the pipe line, EMERG - Energy. Environ. Effic. Resour. Glob. 6 (2020) 33–40. https://doi.org/10.37410/emerg.2020.3.03.

[158] A.T. Hamada, M.F. Orhan, An overview of regenerative braking systems, J. Energy Storage. 52 (2022) 105033. https://doi.org/10.1016/j.est.2022.105033.

[159] Drillmec mobile rigs., (n.d.). https://www.drillmec.com/en/onshore/mobile-rigs (accessed May 14, 2022).

[160] A. Tota, E. Galvagno, M. Velardocchia, On the Power-Weighted Efficiency of Multimode Powertrains: A Case Study on a Two-Mode Hybrid System, in: 2022: pp. 522–531. https://doi.org/10.1007/978-3-030-87383-7_56.

[161] A. Tota, E. Galvagno, L. Dimauro, A. Vigliani, M. Velardocchia, Energy management strategy for hybrid multimode powertrains: Influence of inertial properties and road inclination, Appl. Sci. 11 (2021) 11752. https://doi.org/10.3390/app112411752.

[162] S. Jurkovic, K. Rahman, N. Patel, P. Savagian, Next Generation Voltec Electric Machines; Design and Optimization for Performance and Rare-Earth Mitigation, SAE Int. J. Altern. Powertrains. 4 (2015) 336–342. https://doi.org/10.4271/2015-01-1208.

[163] W. Zhuang, X. Zhang, D. Li, L. Wang, G. Yin, Mode shift map design and integrated energy management control of a multi-mode hybrid electric vehicle, Appl. Energy. 204 (2017) 476–488. https://doi.org/10.1016/j.apenergy.2017.07.059.

[164] P. Mattsson, Continuously Variable Split-Power Transmissions with Several Modes, 1996.

[165] E.G. Giakoumis, Driving and engine cycles, Driv. Engine Cycles. (2016) 1–408. https://doi.org/10.1007/978-3-319-49034-2/COVER.

[166] B. Houska, H.J. Ferreau, M. Diehl, ACADO toolkit—An open-source framework for automatic control and dynamic optimization, Optim. Control Appl. Methods. 32 (2011) 298–312. https://doi.org/10.1002/OCA.939.

[167] Y. Liu, J. Li, M. Ye, D. Qin, Y. Zhang, Z. Lei, Optimal Energy Management Strategy for a Plug-in Hybrid Electric Vehicle Based on Road Grade Information, Energies. 10 (2017). https://doi.org/10.3390/en10040412.